THE ROLE OF LARGE SCALE FLOWS IN MOLECULAR CLOUD FORMATION IN SPIRAL GALAXIES

Felipe Gerardo Ramon Fox

A Thesis Submitted for the Degree of PhD
at the
University of St Andrews

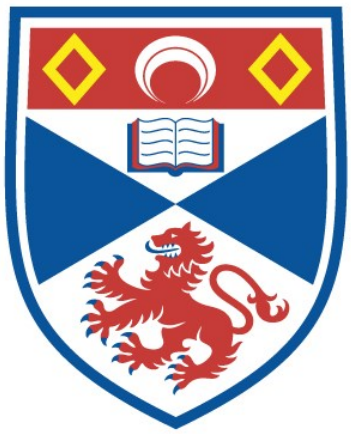

2019

The Role of Large Scale Flows in Molecular Cloud Formation in Spiral Galaxies

Felipe Gerardo Ramon Fox

University of
St Andrews

This thesis is submitted in partial fulfilment for the degree of

Doctor of Philosophy (PhD)

at the University of St Andrews

June 2018

Candidate's declaration

I, Felipe Gerardo Ramon Fox, do hereby certify that this thesis, submitted for the degree of PhD, which is approximately 45,600 words in length, has been written by me, and that it is the record of work carried out by me, or principally by myself in collaboration with others as acknowledged, and that it has not been submitted in any previous application for any degree.

I was admitted as a research student at the University of St Andrews in September 2014.

I, Felipe Gerardo Ramon Fox, received assistance in the writing of this thesis in respect of grammar and spelling, which was provided by William Lucas.

I received funding from an organisation or institution and have acknowledged the funder(s) in the full text of my thesis.

Date Signature of candidate

Supervisor's declaration

I hereby certify that the candidate has fulfilled the conditions of the Resolution and Regulations appropriate for the degree of PhD in the University of St Andrews and that the candidate is qualified to submit this thesis in application for that degree.

Date Signature of supervisor

Permission for publication

In submitting this thesis to the University of St Andrews we understand that we are giving permission for it to be made available for use in accordance with the regulations of the University Library for the time being in force, subject to any copyright vested in the work not being affected thereby. We also understand, unless exempt by an award of an embargo as requested below, that the title and the abstract will be published, and that a copy of the work may be made and supplied to any bona fide library or research worker, that this thesis will be electronically accessible for personal or research use and that the library has the right to migrate this thesis into new electronic forms as required to ensure continued access to the thesis.

I, Felipe Gerardo Ramon Fox, have obtained, or am in the process of obtaining, third-party copyright permissions that are required or have requested the appropriate embargo below.

The following is an agreed request by candidate and supervisor regarding the publication of this thesis:

Printed copy

No embargo on print copy.

Electronic copy

No embargo on electronic copy.

Date Signature of candidate

Date Signature of supervisor

Underpinning Research Data or Digital Outputs

Candidate's declaration

I, Felipe Gerardo Ramon Fox, understand that by declaring that I have original research data or digital outputs, I should make every effort in meeting the University's and research funders' requirements on the deposit and sharing of research data or research digital outputs.

Date Signature of candidate

Permission for publication of underpinning research data or digital outputs

We understand that for any original research data or digital outputs which are deposited, we are giving permission for them to be made available for use in accordance with the requirements of the University and research funders, for the time being in force.

We also understand that the title and the description will be published, and that the underpinning research data or digital outputs will be electronically accessible for use in accordance with the license specified at the point of deposit, unless exempt by award of an embargo as requested below.

The following is an agreed request by candidate and supervisor regarding the publication of underpinning research data or digital outputs:

No embargo on underpinning research data or digital outputs.

Date Signature of candidate

Date Signature of supervisor

Collaboration Satemtent

The work presented in this thesis was produced by me during my time as a Ph. D. student at the University of St Andrews between September 2014 and June 2018. The main tool I used was the code sphNG, which is a smoothed particle hydrodynamics code originally developed by Willy Benz and now maintained and available with permission from Matthew Bate and Daniel Price. Some sections in Chapter 2 involve slight modifications to the code. The code sphNG is usually acknowledged in the literature by the paper "Modelling accretion in protobinary systems", M. R. Bate, I. A. Bonnell and N. M. Price, 1995, MNRAS, pp. 362-376.

Chapter 5 is based on a paper which has been published in a refereed scientific journal. As my supervisor, Ian Bonnell, gave scientific advice on the work in all chapters I have written. All the text in this thesis and all figures have been made by me from data produced during my own work, except several figures in the introduction which are obtained from third-party sources.

Some results of Chapter 3 have been shared with Duncan Forgan to be used for testing a code for identifying spiral structure and these results have been published in "Classifying and modelling spiral structures in hydrodynamic simulations of astrophysical discs", Forgan, D. H.; Ramón-Fox, F. G.; Bonnell, I. A., 2018, MNRAS, 476, 2384, but the work of this chapter has been entirely my own.

The results of Chapter 4 have been produced by me but have not been published yet.

The results of Chapter 5 have been published on the paper "Streaming Motions and Kinematic Distances to Molecular Clouds", Ramón-Fox, F. G. and Bonnell, I. A., 2018, MNRAS, 474, 2028. For this chapter, I analysed simulations performed by Ian Bonnell, and developed my own tools to obtain the results in the paper. I produced all the results of the analysis and wrote

a paper.

The results of Chapter 6 have been produced by me but have not been published yet.

I have had discussions with Will Lucas, Guillaume Laibe, Diego Falceta-Gonçalves, Claudia Cyganowski and Duncan Forgan on the science involved.

Abstract

Star formation begins on the large scales of a galaxy and takes place on the smallest scales. As the interstellar gas flows into a spiral arm, it forms a shock where the change in density, coupled to self-gravity and thermal instabilities, leads to the formation of high density structures where molecular clouds grow. It is important to understand the role of large-scale flows in assembling these clouds. This work explores the gas flows in spiral arms to understand its role on molecular cloud formation comparing between grand-design and flocculent galaxies.

A set of high-resolution smoothed particle hydrodynamics (SPH) simulations are used. One simulation evolves the gas in a potential including a halo, stellar disc, and spiral arms. The second simulation evolves the gas in an N-body stellar disc and bulge within a fixed halo potential. The first and second models are representative of grand-design and flocculent galaxies, respectively. The third simulation is a high-resolution simulation of a region of gas flowing in a spiral arm based on the simulations of Bonnell et al. (2013), which follows in more detail the local cloud dynamics. In the global models, the mass resolution is about $45M_{\odot}$ per gas particle and in the spiral simulation, about $0.6M_{\odot}$.

The results show that in both the grand-design and flocculent models, the gas is shocked as it flows through an arm. The N-body model shows flow characteristics qualitatively similar to the spiral potential model but with more variations due to the potentials arm-to-arm variations. Clouds are identified using a friends-of-friends algorithm to catalogue clumps above a given density threshold. These have non-negligible streaming motions and their properties are consistent with observed mass-radius and size-velocity dispersion relations.

Acknowledgements

I am very grateful to Prof. Ian Bonnell for his help and advise during the course of my PhD. He is always enthusiastic and open to help in every aspect of the postgraduate life. I also wish to thank the people of the Star Formation Group for their help and discussions during my experience in the PhD. This work was supported by the ERC ECOGAL project under grant number 291277. I also thank the University of St. Andrews for supporting me with a St. Leonards Scholarship. I also wish to acknowledge support from St. Andrews for giving me access to the machines Wardlaw, Kennedy and Cygnus. I am also grateful to the DiRAC team at the University of Leicester for their support with the Complexity machine. I would also like to thank the examiners for their valuable work in reading this thesis.

I wish to particularly thank my parents, my sister, and all my family both in Mexico and the UK for motivating me during this time. I wish to thank all my friends, but specially, Nina, Lisa, Maya, Inna, Annelies, Carolina, Roberto, Bert, Romas, Mario, and of course, to all the great colleagues in the offices that I have shared a space with. At the Physics and Astronomy Department, I would also like to thank Dr. Vivienne Wild and Dr. Anne-Marie Weijmans for their help during my PhD. I also want to thank Dr. Duncan Forgan, Dr. Guillaume Laibe, and Dr. Diego Falceta-Gonçalves for their valuable input and discussions. I cannot thank enough Dr. Sarah Ragan also for her help and support at the last stages. I also thank Dr. Héctor Aceves and Dr. Takamitsu Miyaji for hosting me several times at IA-UNAM Ensenada in Mexico during my PhD.

I want to thank Dr. Irina Leonhardt, Poppy Nicholson, Lesley Aitken, Linda Cousins, and Dimali Vithanage for their help and support with administrative work. I also want to thank the Aikido Club of the University for teaching me a fantastic art and for the great time that I had training with you.

Contents

List of Figures

List of Tables

1

Introduction

1.1 Molecular Clouds and Star Formation in Spiral Galaxies

1.1.1 Star Formation from a Galactic Perspective

Star formation is a process of significant importance for galactic evolution. In a broad sense, the warm, low density gas in a galaxy needs to be cooled and transformed into high density gas where stars can form (e. g. Stahler & Palla 2004; Burkert 2017). Once stars form, they start injecting energy to the surrounding medium. Eventually, the most massive stars explode as supernovae, which injects a large amount of energy ($\sim 10^{51}$ erg) into the nearby gas (e. g. Klessen & Glover 2016; Dale 2015). At the same time, this process enriches the surrounding medium with heavier elements, which determines the chemical evolution of the galaxy (e. g. Audouze & Tinsley 1976). This creates a gas cycle in a galaxy, which drives its long term evolution (e. g. Molinari et al. 2014). Understanding this process in the context of galaxy evolution will have implications in explaining the evolution of star formation over cosmic time scales (e. g. Madau & Dickinson 2014).

Observationally, star formation in galaxies has been characterised by the relationship between the gas surface density $\Sigma_{\rm gas}$ and the star formation rate (SFR) per unit area $\Sigma_{\rm SFR}$, usually written as

$$\Sigma_{\rm SFR} \propto \Sigma_{\rm gas}^{N}, \tag{1.1}$$

and known as the Kennicutt-Schmidt (KS) relation. Schmidt (1959) proposed this form and found that $N \approx 2$ from Milky Way observations. The analysis of young stellar objects in dense cores in a sample of molecular clouds in the Milky Way by Heiderman et al. (2010) finds that $N \approx 1.1$. For a sample of external galaxies, Kennicutt (1989) obtained $N \approx 1.3$. Later, Kennicutt (1998b) reported that $N \approx 1.4$, after analysing a larger sample of galaxies. This relation is also observed for galaxies at higher redshifts. For example, Daddi et al. (2010) report that $N \approx 1.42$ for galaxies with redshift (z) within 0.5 and 1.5; Bouché et al. (2007) find that $N \approx 1.71$ for objects near $z = 2$; Genzel et al. (2010) obtain $N \approx 1.1$ for more distant galaxies, near $z = 3.5$. Many of this studies take into account the total gas surface density (neutral plus molecular H_2); however, Wong & Blitz (2002) find a close to linear correlation when only the molecular gas surface density is considered. The KS relation has been interpreted in terms of the expected star formation rate given a free-fall time of the local gas (e. g. Elmegreen 2002), in terms of spiral arm shocks triggering star formation (Bonnell et al., 2013), as well as in terms of observational effects and errors when comparing star formation and gas quantities averaged over a given area (e. g. Kruijssen & Longmore 2014).

The KS relation characterises star formation from a global perspective for a large range of galaxies (e. g. Kennicutt 1998a), but depends on processes that occur on the smallest scales. Comprehending the relation between star formation and gas density requires a good understanding of molecular clouds. Star formation takes place in dense regions or cores inside molecular gas clouds (e. g. Dobbs et al. 2014; Klessen & Glover 2016) (described in more detail in §1.1.3 and §1.1.4). Their dynamical properties are important for the conditions leading to star formation. However, these objects cannot be viewed as isolated objects as their growth and properties may depend on the larger-scale structure, such as spiral arms and bars, and dynamics of a galaxy (e. g. Schinnerer et al. 2013; Hughes et al. 2013; Dobbs et al. 2014; Meidt et al. 2018). Spiral arms can play an important role in the formation of molecular clouds (e. g. Dobbs & Baba 2014; Dobbs et al. 2014). Then, a global picture of star formation needs to account for the processes operating from the large scales down to the small scales of a galaxy and explain how this influences the triggering of star formation within molecular

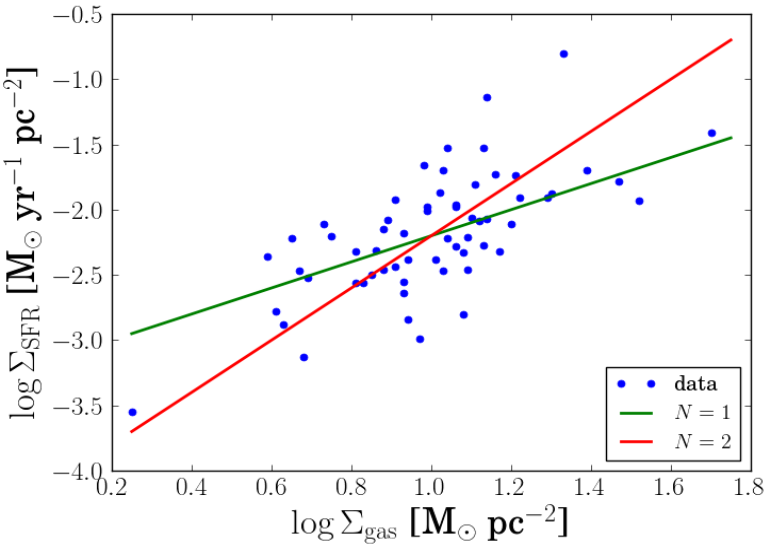

Figure 1.1: Star formation surface density versus total gas surface density data points taken from Kennicutt (1998b). The green and red lines correspond to the Kennicutt-Schmidt relation (equation 1.1) with $N = 1$ and $N = 2$, respectively. Schmidt (1959) originally found $N = 2$, but other works have found values ranging between 1 and 2.

clouds. Before introducing molecular clouds, a brief overview of the interstellar medium is presented in the next section.

1.1.2 The Interstellar Medium Components: an overview

The interstellar medium (ISM) can be understood both in terms of its chemical composition as well as its thermal phases (e. g. Lequeux 2005; Osterbrock & Ferland 2005). In terms of chemical composition, the ISM is a mixture of gas and and dust. The most abundant element is hydrogen, followed by helium. Hydrogen can be neutral as well as ionised depending on the local temperature and radiation conditions (e. g. Osterbrock & Ferland 2005). It is also composed of several molecules: molecular hydrogen (H_2), carbon monoxide (CO), carbon-hydrogen (CH), carbon monosulfide (CS), cyanide (CN) compunds, hydrogen cyanide (HCN), hydroxyl (OH) compounds, ammonia (NH_3) (e. g. De Becker 2013).

The ISM can be broadly divided in the following thermal phases: the cold neutral medium (CNM) and dense molecular, which has the densest gas ($n \sim 10^1 - 10^6$ cm^{-3}) and typical temperatures around $T \approx 10 - 100$ K; the warm neutral medium (WNM) and warm ionised medium (WIM), which has lower densities ($n \sim 10^{-1} - 10^4$ cm^{-3}) and higher temperatures around $T \approx 10^4$ K; and the hot ionised medium (HIM), which has the lowest densities ($n \sim$

10^{-3}) cm^{-3} and highest temperatures around $T \approx 10^6$ K (e. g. Goldsmith et al. 1969; McKee & Ostriker 1977; Cox 2005). The different thermal phases of the ISM are summarised in Table 1.1.

Phase	T [K]	n [cm^{-3}]	Properties
Hot Ionised (HIM)	$\gtrsim 10^6$	10^{-3}	Heated by shocks and collisional ionisation Cooled by adiabatic expansion; X-ray emission Traced with UV, X-ray and radio observations
Warm Ionised (WIM)	$\sim 10^4$	$10^{-1} - 10^4$	Heated by photoionisation Cooled by line, free-free, and fine structure emission Traced by optical (lines) and radio observations
Warm Atomic (WNM)	$5000 - 10^4$	0.6	Warm neutral medium (HI) Heated from dust photoelectric effect Ionisation by background radiation and cosmic rays Cooling by line emission and fine structure lines Traced by HI 21-cm line and Optical, UV absorption lines
Cold Atomic (CNM)	$50 - 100$	$20 - 50$	Heated by dust photoelectric effect Ionisation by background radiation and cosmic rays Cooled by fine structure lines Traced by HI 21-cm emission, optical and UV absorption lines
Diffuse Molecular	~ 50	10^2	Cooled by fine structure lines Observed with HI 21-cm emission; absoprtion, optical and UV lines
Dense Molecular (MM)	$10 - 50$	$10^3 - 10^6$	Cooled by CO, CI fine structure line Traced by CO 2.6-mm and dust FIR emission

Table 1.1: Phases of the Interstellar Medium. Based on information from Draine (2011); Lequeux (2005); Pettitt (2015).

The phases exist in pressure equilibrium and the thermal energy is regulated by cooling and heating mechanisms. Cooling results mainly from fine structure lines, molecular transitions, and collisional lines. These processes operate at different temperatures depending on the excitation temperature of the transition (e. g. Dyson & Williams 1997; Wolfire et al. 1995; Koyama & Inutsuka 2000). Heating results from the photoelectric effect, ionisation by cosmic rays and strong radiation, and shock heating (e. g. Goldsmith et al. 1969; Wolfire et al. 1995; Koyama & Inutsuka 2000). Supernova feedback can drive gas to the hottest phase as well (e. g. Cox & Smith 1974; McKee & Ostriker 1977). The net energy gained or lost is quantified by the function (e. g. Lequeux 2005):

$$L(n,T) = n^2\Lambda(T) - n\Gamma, \tag{1.2}$$

where L is the general loss function, n is the number density, Λ is the cooling function, and Γ is the heating function. If $L > 0$, cooling dominates; if $L = 0$, the medium is in equilibrium; if $L < 0$, heating dominates. The behaviour of this function is shown in the temperature-density and pressure-density diagrams of Figure 1.2 assuming the cooling and heating functions in Koyama & Inutsuka (2000). In the bottom panel of Figure 1.2, the pressure decreases with density between 10^0 and 10^1 cm^{-3} and this is a region of an unstable gas phase as any slight perturbation out of equilibrium would quickly cool or heat and move to the parts of the curves with positive slope.

The neutral hydrogen is usually traced by the 21-cm transition, which provides information of its spatial distribution and a galaxy's rotation curve (e. g. Walter et al. 2008; Kalberla & Kerp 2009; Sofue 2017). The ionised hydrogen can be found either in H_{II} regions surrounding young O and B stars that emit sufficiently energetic radiation to ionise the nearby gas (Strömgren, 1939). Additionally, it may be found in a hot diffuse distribution surrounding the galaxy known as the corona. This gas may be the result of gas heated by supernova explosions (e g Lequeux 2005; Draine 2011).

Molecular hydrogen (H_2) is an abundant molecule, but its direct detection is very difficult because the high symmetry of the molecule does not allow $\Delta J = \pm 1$ transitions. Higher transitions such as $\Delta J = \pm 2$ are possible, but have an excitation temperature of 500 K (e g. Rybicki & Lightman 2004). The temperatures in molecular clouds are too low to excite this transition (Timmermann et al., 1996). The formation of H_2 is usually explained with the following mechanism: dust grains function as a catalyst for H atoms to bond and form the molecule (Hollenbach & Salpeter, 1971; Gould & Salpeter, 1963), however the entire process is not fully understood yet. This requires high density environments that can shield the molecule from strong UV radiation. H_2 is one of the main components of molecular clouds and it is expected to play an important role in the star formation process as it exists in the densest parts of star forming clouds (e. g. Habart et al. 2005; Dobbs et al. 2014; Klessen & Glover 2016).

Carbon monoxide (CO) is also an abundant molecule that plays an important role in tracing molecular clouds. It is mainly observed at $\lambda = 2.6$ mm, which corresponds to the $J = 1 \rightarrow 0$ transition. Other transitions such as the $J = 2 \rightarrow 1$ are also used. The CO is assumed to trace the H_2 distribution, but the information derived about it depends the conversion factor $X_{\rm CO} = 2 \times 10^{20} \mathrm{molecules\,cm^{-2}\,(K\,km\,s^{-1})^{-1}}$ (e. g. Heyer & Dame 2015). Recent simulations

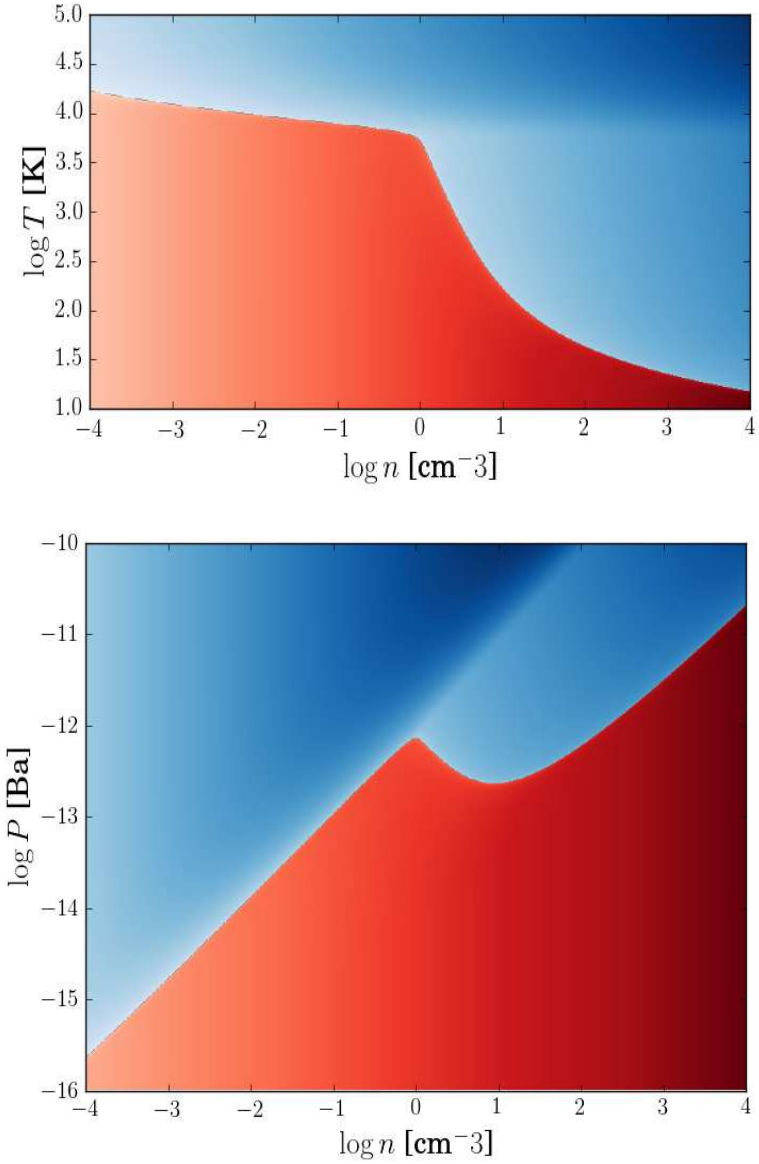

Figure 1.2: Top panel: temperature-density map of the general loss function of equation (1.2) using the cooling function Λ of Koyama & Inutsuka (2000) and a constant Γ term. The red and blue regions correspond to where the heating and cooling terms dominate and the colour scales with the magnitude of the function. The line where the regions meet corresponds to the equilibrium point ($n^2\Lambda = n\Gamma$). Bottom panel: pressure-density map of the general loss function similar to the top panel.

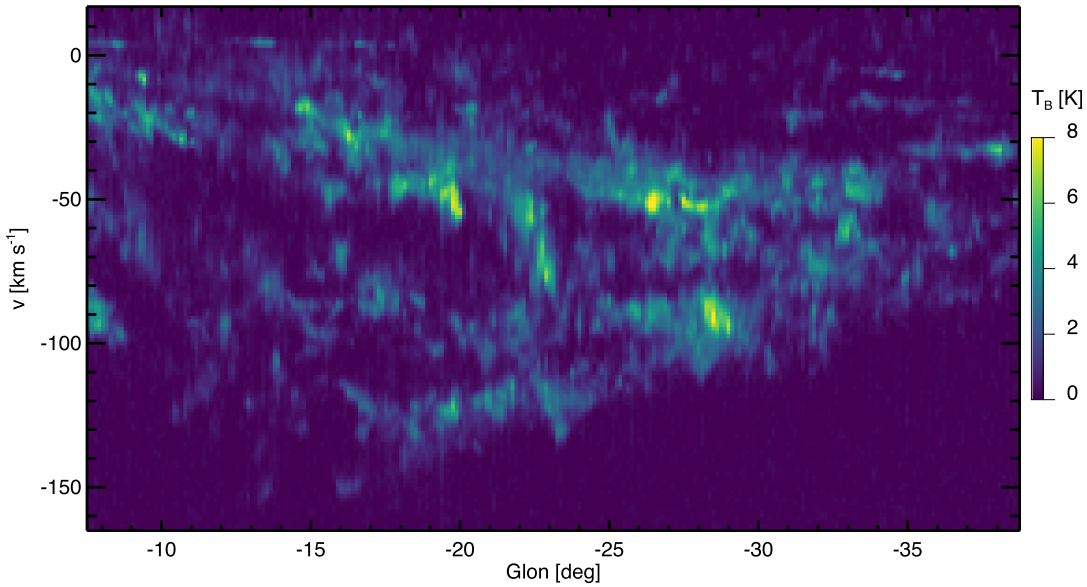

Figure 1.3: Example of an l-v_{los} map made from CO observations in the plane of the Milky Way. Molecular clouds are expected to be associated with the peaks in this map. Image taken from Miville-Deschênes et al. (2017). (© AAS. Reproduced with permission. https://doi.org/10.3847/1538-4357/834/1/57)

by Smith et al. (2014) also show that there may be a significant fraction of diffuse CO that is not necessarily associated with H_2 clouds. Nevertheless, this is still the most common tracer of molecular clouds and the dense gas phase in both Milky Way and extragalactic surveys.

1.1.3 Molecular Clouds: Overview of Observational Identification

Observations of Molecular Clouds

This subsection briefly overviews the concept of a cloud in observations and the main properties derived (more details are also provided in the introductory section of Chapter 6). Molecular clouds have been studied since the early CO observations of Solomon et al. (1979, 1987); Dame et al. (1986) (for a review, see Heyer & Dame 2015). The data in these surveys is a four-parameter space containing the emission intensity I_{CO} or antenna temperature (T), the line-of-sight velocity v_{los}, and the Galactic longitude and latitudes, (l, b) respectively. Solomon et al. (1979) originally proposed to define clouds as closed intensity surfaces in a position-position-velocity (PPV) map, namely a (l, b, v_{los}) space. Dame et al. (1986) proposed a method that keeps only data above a certain antenna temperature threshold to produce an integrated (l, v_{los}) map (see Figure 1.3 for an example), where clouds are identified based on data peaks.

Systematic cloud identification methods such as CLUMPFIND (Williams et al., 1994) and CPROPS (Rosolowsky & Leroy, 2006) were later developed. These search for clouds in a PPV

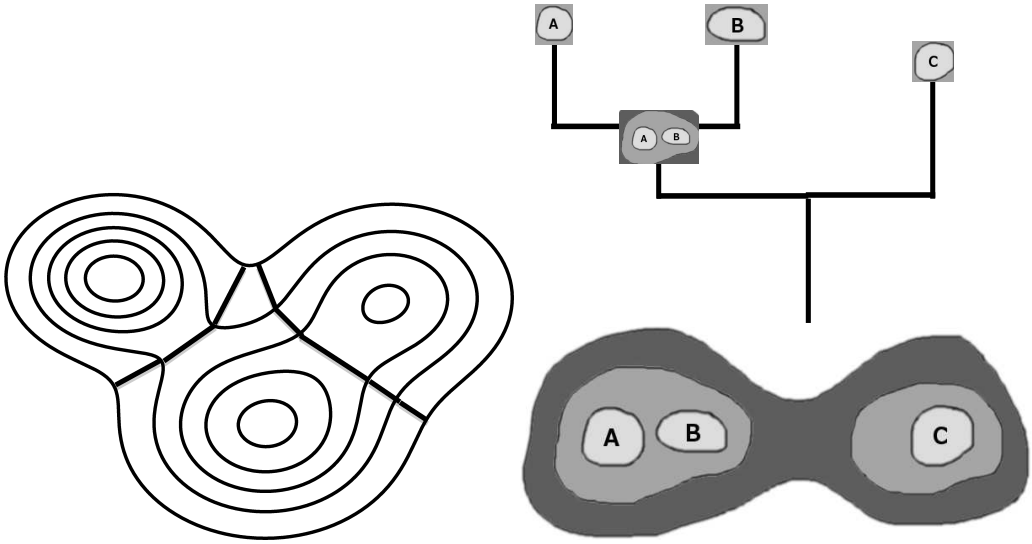

Figure 1.4: The left panel illustrates the way CLUMPFIND (Williams et al., 1994) classifies structures in an isocontour map. In this method, peaks are tagged as the centre of independent clumps and a friends-of-friends algorithm is applied to the regions of common isocontours in order to establish the division. The right panel illustrates the concept of dendograms in classifying structures. Substructure is classified in different branches. The clump centres become the leaves of the dendogram.

set by identifying peaks as a clump's approximate centre and defining its geometry in terms of antenna temperature isocontours. CLUMPFIND identifies peaks and breaks down different structures by applying a friends-of-friends algorithm at the point where a common isocontour surrounds different clumps (see the left panel of Figure 1.4). On the other hand, CPROPS rescales the temperature data to reduce the interference of small internal substructure in the classification of larger structures and the segmentation of common isocontours is determined by checking if the characteristic sizes along the clump's axes vary by a given fraction. A third technique applies dendograms and clustering analysis to classify clouds in a hierarchical structure (Colombo et al., 2015) (see the right panel of Figure 1.4).

Some characteristic properties of molecular clouds are: mass, size, and velocity dispersion. Cloud masses (M_c) are usually derived from the total CO luminosity of the cloud and the H_2 mass is calculated via the $X_{\rm CO}$ conversion factor (e. g. Solomon et al. 1987). The most massive clouds can have up to $M_c \sim 10^5 - 10^6$ solar masses and are known as Giant Molecular Clouds (GMCs) (e. g. Dobbs et al. 2014; Heyer & Dame 2015). Sizes (R_c) are usually calculated based on the apparent angular size of the cloud and the estimated distance, which is usually derived from the galaxy's circular velocity (Solomon et al., 1987; Rosolowsky & Leroy, 2006; Roman-Duval et al., 2010; Heyer & Dame, 2015). The internal dynamics are characterised by the velocity dispersion σ_v, which is usually derived from the observed line width in the cloud's

spectrum (e. g. Solomon et al. 1987; Rosolowsky & Leroy 2006. Data from different Milky Way surveys show that typical sizes can be in the range of a few 10 pc and velocity dispersions in the range of $\approx 0.1- \approx 10$ km s^{-1} (Larson, 1981; Heyer et al., 2009; Roman-Duval et al., 2010; Heyer & Dame, 2015; Miville-Deschênes et al., 2017).

According to Heyer & Dame (2015), the typical density and temperature in molecular clouds can be measured via the ratio of intensities of the CO $J = 2-1$ and $J = 1-0$ lines: $R = I(2-1)/I(1-0)$. Combining $J = 2-1$ observations by (Sakamoto et al., 1997; Yoda et al., 2010) and $J = 1-0$ by (Cohen et al., 1986; Dame et al., 2001) provide a rough idea of the conditions in different regions. Regions where $R > 1$, have number densities $n \approx 10^4-10^5$ cm^{-3} and a typical temperature $T \approx 40$ K. These are found near HII regions and supernova remnants. Areas with R in the range between $0.7-1.0$ have $n \approx 250-10^5$ cm^{-3} and $T \approx 10-50$ K, and regions with $R < 0.7$ have $n \approx 100-500$ cm^{-3} and $T = 10-40$ K (Heyer & Dame, 2015). These are just overall values, as there may be cloud-to-cloud variations of these quantities.

It is interesting to study, from both observational and theoretical perspectives, the mass function and size distributions as these relate to the geometrical nature of the ISM (e. g. fractal Elmegreen & Falgarone 1996) and reflect the effect of different formation mechanisms (Rosolowsky, 2005; Dobbs, 2008; Dobbs et al., 2014) (discussed in §1.2). Observations show that the mass scales with velocity dispersion (e. g. Solomon et al. 1987) as well as with radius: $M_c \propto R_c^2$ (e g. Elmegreen & Falgarone 1996; Roman-Duval et al. 2010). An interesting result is the scaling between size and velocity dispersion: $\sigma_v \propto R_c^n$ (e. g. Larson 1979, 1981). Larson (1981) found that $n \approx 0.38$ and interpreted this behaviour in terms of turbulent motions in the ISM (see Figure 1.5). Recent surveys show that the velocity dispersion is more strongly correlated between with the product of the size and surface density Σ_c: $(\sigma_v \propto (\Sigma_c R_c)^{1/2})$; which would result for clouds in approximate virial equilibrium (Heyer et al., 2009; Dobbs et al., 2014). A more detailed discussion on the observed properties of molecular clouds for both Milky Way and some extragalactic sources is provided in §6.1 of Chapter 6.

Molecular Clouds from a Galactic Perspective

Molecular clouds and star forming regions tend to be associated with spiral arms (e. g. Elmegreen & Elmegreen 1983; Elmegreen 2002; Dobbs & Baba 2014). In the Milky Way, this concept has been used to trace the spiral structure of the Galaxy (e. g. Cohen et al. 1980; Heyer et al. 2009;

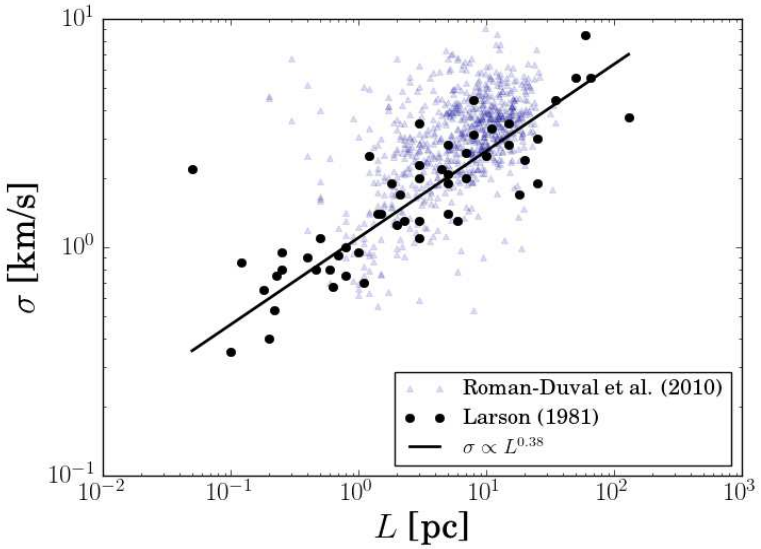

Figure 1.5: Size-velocity dispersion for molecular clouds and star forming regions. The black dots correspond to data from Larson (1981) and the light blue triangles to data from molecular clouds identified in the CO survey of Roman-Duval et al. (2010). The black line is the fit found by Larson (1981).

Roman-Duval et al. 2010). However, the recovered positions are obtained by a kinematic distance, assuming that the gas is moving in circular orbits. This may introduce significant errors in the distance (as will be discussed in Chapter 5), which affects studies that attempt to study cloud populations with respect to the Galaxy's spiral arm structure.

Extragalactic observations offer a better opportunity to compare the position of molecular clouds with respect to the stellar spiral arms. Hughes et al. (2013) compared CO observations available in the literature of M51, a grand-design galaxy with a strong 2 armed pattern, and of M33 a flocculent galaxy. Figure 1.6 shows optical pictures of both these galaxies. M51 data shows that the CO emission is well associated with spiral arms. On the other hand, similar data for M33 shows that this emission is irregularly distributed over the the disc. Figure 1.7 shows the CO maps of these galaxies as shown in Hughes et al. (2013). A similar result is obtained from the CO(2-1) observations of M33 by Druard et al. 2014. Hughes et al. (2013) conclude that the peak intensities as well as the velocity dispersion tends to be higher in M51 than in M33. A previous study by Rosolowsky et al. (2003) of molecular clouds in M33 finds that the properties are not very different to those in the Milky Way. However, a study of clouds in the spiral M64 by Rosolowsky & Blitz (2005) shows differences with respect to Local Group galaxies. A detailed analysis of M51 by Colombo et al. (2014a) shows that there are

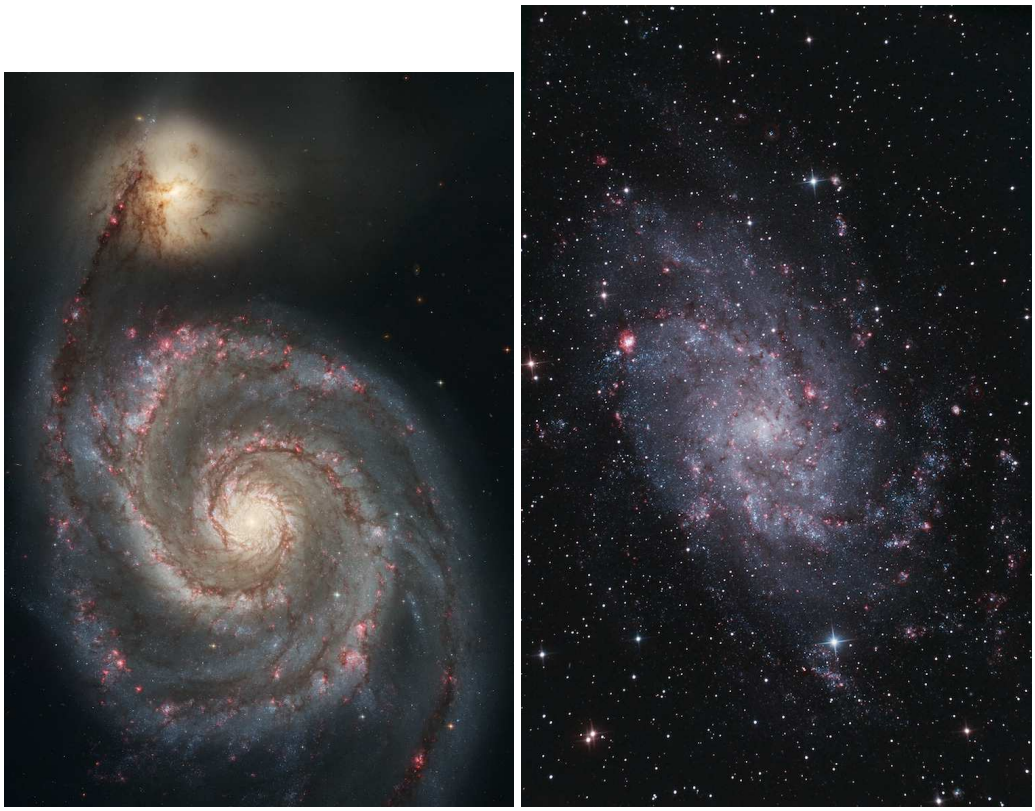

Figure 1.6: Left panel: optical image of the grand-design galaxy M51 also known as the Whirlpool Galaxy (Image Credit: NASA/ESA/S. Beckwith (STSCI), and the Hubble Heritage Team (STScI/AURA)). Right panel: optical image of the flocculent galaxy M33 also known as the Triangulum Galaxy (Image Credit: A. Meleg). M51 shows a strong spiral arm pattern, which is traced by dark dust and gas lanes. Although M33 has spiral structure in the stellar component, the structure is patchier. Both dust and gas tend to have a more irregular distribution.

differences in the properties of molecular clouds in various regions of the galaxy and the clouds with higher masses and velocity dispersions tend to be associated with the inner region and the strongest spiral arms.

The above results indicate that molecular cloud properties have some dependence on the environment, which suggests that the formation mechanisms (discussed in §1.2) also have a similar dependence. This motivates numerical simulations that explore in more detail the role of different spiral arm morphologies in the formation of molecular clouds.

1.1.4 From the large-scales to molecular clouds to stars

Observations of spiral galaxies (e. g. THINGS survey, Walter et al. 2008) show that there is a significant amount of neutral hydrogen distributed over large scales. This gas needs to be cooled driven to high densities to form molecular clouds and eventually stars. On the large scales,

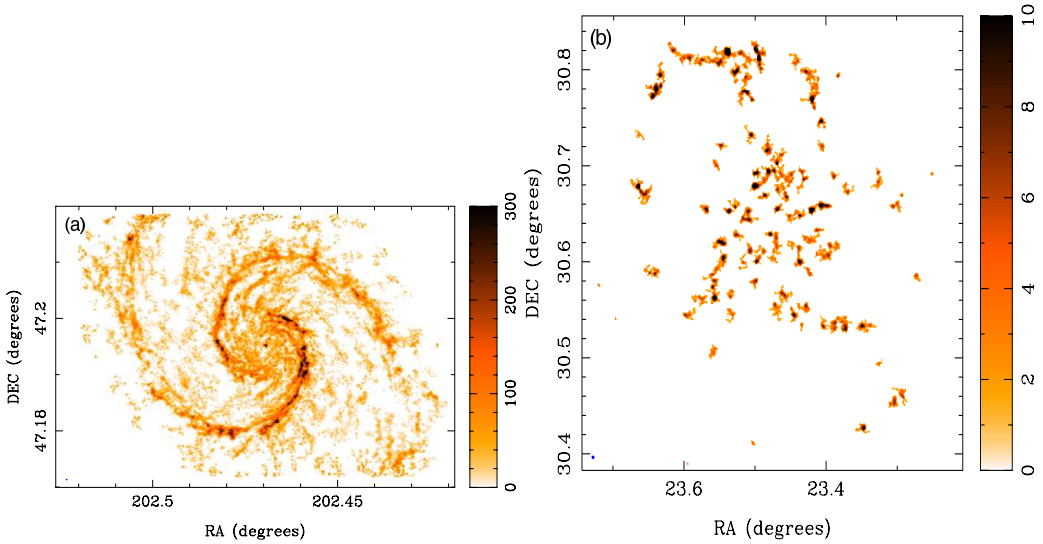

Figure 1.7: The left and right panels show CO maps for M51 and M33, respectively. The CO emission is clearly associated with the spiral arms in M51 whereas in M33 it has a more irregular distribution, not showing any trend with spiral structure. These images are taken from Hughes et al. (2013), but the data are based on different sources: M51: Schinnerer et al. (2013); Pety et al. (2013); M33: Rosolowsky et al. (2007) (© AAS. Reproduced with permission. https://doi.org/10.1088/0004-637X/779/1/46)

several mechanisms have been proposed: large-scale gravitational instabilities (e. g. Goldreich & Lynden-Bell 1965b; Elmegreen 2002) and spiral arm shocks (e. g. Roberts 1969). On smaller scales, cloud collisions (e. g. Casoli & Combes 1982; Dobbs 2008) and colliding flows (e. g. Audit & Hennebelle 2005; Heitsch et al. 2005; Vázquez-Semadeni et al. 2007). These mechanisms are discussed in detail in §1.2 and the remainder of this section presents a brief overview of star formation in molecular clouds.

Once a molecular cloud is formed, the gas must be transformed into stars. This requires the formation of dense cores. In a broad sense, to form solar-mass stars, these contract gravitationally from scales of $\sim$ 1 pc to $\sim 10^4$ AU. If there is an initial rotation of the cloud it collapses to a rotating disc because of angular momentum. At this point, the central object can still accrete gas from its surroundings. A protostar forms in the centre of the disc and the surrounding gas envelope after $\approx 10^4 - 10^5$ yr. The object also develops bipolar jets. After 10^5—10^6 yr, it evolves into a T-Tauri system and eventually makes its way through the pre-main sequence and enters the main sequence (Stahler & Palla, 2004; Ward-Thompson & Whitworth, 2011; Klessen & Glover, 2016).

From a galactic perspective, star formation is usually quantified by the star formation rate (SFR), which is usually traced by diagnostics such as UV emission, H_α emission, forbidden lines such as O_{II} particularly for higher redshifts, and Far Infrared Emission (Kennicutt, 1998b).

These are combined with population synthesis models that fit the observed spectral energy distributions assuming a certain star formation history (e. g. Bruzual A. & Charlot 1993). For spiral galaxies, the global SFR can reach up to values of $\approx 20\ M_\odot\,\mathrm{yr}^{-1}$ in spirals rich in gas, which is still low compared to starburst galaxies which can have a SFR as high as $10^2\ M_\odot\,\mathrm{yr}^{-1}$ (Kennicutt, 1998b). For the Milky Way, the global SFR is around $2\ M_\odot\,\mathrm{yr}^{-1}$ (Dobbs et al., 2014). The star formation rate also appears to be sensitive to the spiral arm morphology (low versus high spiral arm pitch angles) (Kennicutt, 1998b). For individual clouds in the Milky Way, for example, Lada et al. 2010 estimate cloud SFRs based on the number of young stellar objects. They find that the SFR is correlated wit the cloud's mass and ranges between 3×10^{-6} $M_\odot\,\mathrm{yr}^{-1}$ and $7.15 \times 10^{-4}\ M_\odot\,\mathrm{yr}^{-1}$.

The star formation efficiency (SFE) can be quantified by the ratio of the mass of formed stars to the total mass in the system: $\epsilon_\star = M_\star/(M_{\mathrm{gas}} + M_\star)$, where $M_\star$ is the mass of stars formed and M_{gas} is the gas mass (e. g. Dobbs et al. 2014). Another way is to calculate it in terms of the efficiency per free-fall time: $\epsilon_{\mathrm{ff}} = \dot{M}_\star/(M_{gas}/\tau_{\mathrm{ff}})$, where τ_{ff} is the free-fall time given by $\tau_{\mathrm{ff}} \sim 1/(G\rho)^{1/2}$, where ρ is the gas density (e. g. Dobbs et al. 2014). In general, observations show that star formation efficiencies in molecular clouds are generally low, which suggests that there are additional mechanisms controlling the star formation activity of the cloud (e. g. Evans et al. 2009; Heiderman et al. 2010). Evans et al. (2009) find that $\epsilon_\star \sim 10^{-2}$ and $\epsilon_{\mathrm{ff}} \sim 10^{-2}$ as well. Some observations show that ϵ_{ff} can be as low as 10^{-3} (for a review, see Dobbs et al. 2014).

The low efficiency suggests that there are some mechanisms controlling the star formation rate on small scales.Turbulence as well as magnetic fields have been proposed as supporting mechanisms against collapse (Mac Low & Klessen, 2004; Dobbs et al., 2014). Turbulent motions can be driven either by external or internal mechanisms. External injection can be driven by gas accretion from the surrounding medium or by colliding flows (e. g. Klessen & Hennebelle 2010). Internal injection can be driven by outflows from protostellar objects (Banerjee et al., 2007) and supernova feedback (Padoan et al., 2016). These mechanisms are a source of additional kinetic energy that may increase the overall support of the cloud. However, turbulent compressions inside the cloud may drive the formation of locally high-density regions where stars can form (Mac Low & Klessen, 2004; Klessen & Glover, 2016). This additional support may explain the observed low SFEs.

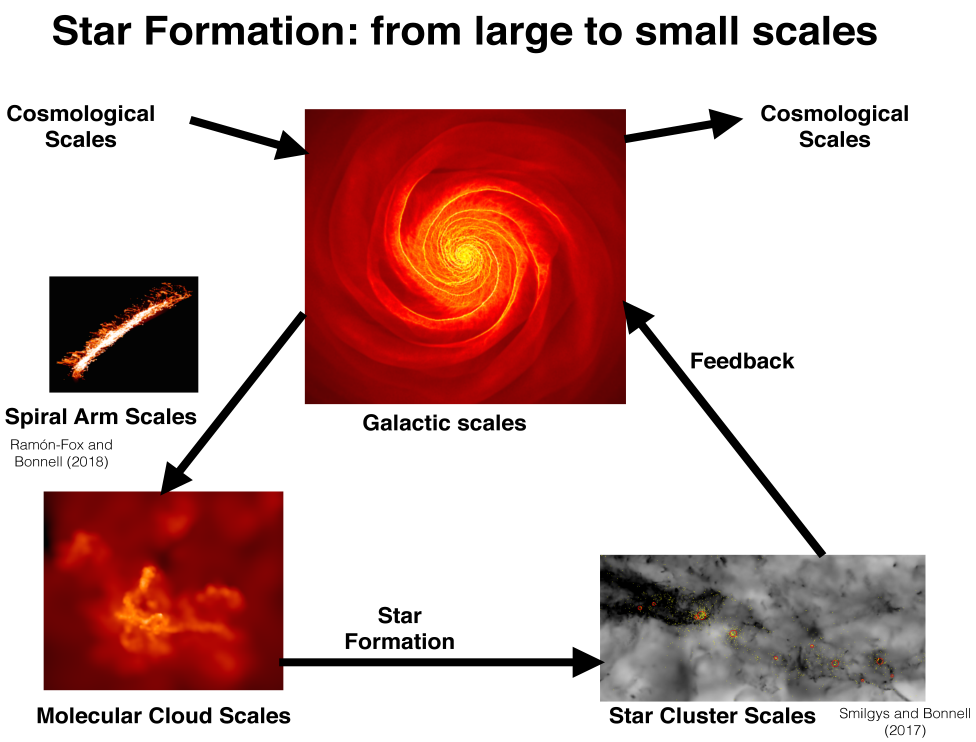

Figure 1.8: The star formation process through different scales viewed from the perspective of simulations. A galaxy can accrete gas from the larger cosmological scales, then the large-scale distribution of gas within the galaxy must be driven to the dense gas at smaller scales where molecular clouds can form. Star formation takes place in dense structures within molecular clouds. The new stars can inject energy during their lives and the most massive can inject more through supernova explosions. These mechanisms have been studied rather separately in simulations. Images taken from: Ramón-Fox & Bonnell (2018); Smilgys & Bonnell (2017)).

These processes are part of a global cycle that regulates star formation in a galaxy (see Figure 1.8). However, the mechanisms have been studied rather separately in different simulations. For example, the larger scales are studied in galaxy-scale simulations (e. g. Dobbs 2008; Smith et al. 2014). The intermediate and smaller scales have been studied in zoom-in simulations of gas flowing through spiral arms (e. g. Bonnell et al. 2013; Smilgys & Bonnell 2017). Star formation itself and feedback have been studied in smaller scale simulations with rather idealised initial conditions (e. g. Bate 2018; Dale et al. 2012; Iffrig & Hennebelle 2015). It is important to develop simulations and models that permit the study these mechanisms from a global galactic perspective.

1.2 Molecular Cloud Formation Mechanisms

1.2.1 Spiral arm shocks and Gravitational Instabilities

The large-scale mechanisms that are usually invoked to explain the formation of molecular clouds are spiral arm shocks and gravitational instabilities, which are explained in more detail in the following sections.

Spiral Arm Shocks

Spiral arm shocks were originally investigated by Fujimoto (1966) and Roberts (1969) in the context of spiral arms behaving a quasi-stationary density waves (Lindblad, 1960; Lin & Shu, 1964). In this model, spiral arms are viewed as density waves with a fairly constant amplitude that rotate with a constant angular speed, known as the pattern speed (Ω_p). The point where the stars and gas rotate at the same rate as the arm is known as the corotation radius.

In the spiral arm shock model, the gas flows into the spiral arm and gains a higher velocity due to the local additional force exerted by the arm. The flow can become supersonic and eventually form strong shocks that drive the gas density to higher values than those in the typical inter-arm regions. Simulations by Fujimoto (1966) found that the density contrast can be up to a factor of 4 in the shock region and that the arm drives non-circular streaming motions of the order of 15 $\mathrm{km\,s^{-1}}$. The position of the shock region relative to the arm is sensitive to the pattern speed and the inter-arm spacing.

Roberts (1969) also developed several models exploring the response of an isothermal gas to an imposed spiral potential and found that it can lead to the formation of large-scale shocks along spiral arms in both leading and trailing spiral arms. In this model, the spiral potential increases the gas velocity normal to the arm as it enters the arm and sharply changes to lower values after the shock. The velocity tangent to the arm tends to decrease and then increases after the shock. The density increases sharply at the shock and then decreases gradually after this point. The shock is usually located before the potential minimum (see Figure 1.9). For the parameters assumed in the Roberts (1969) model and a constant gas velocity dispersion, the ratio of peak density to average density varies with location in a galaxy and tends to increase with decreasing radius. In some cases, the peak density in the shock can be as high as 10 for the inner regions of the galaxy, but depends on the assumed velocity dispersion. Roberts

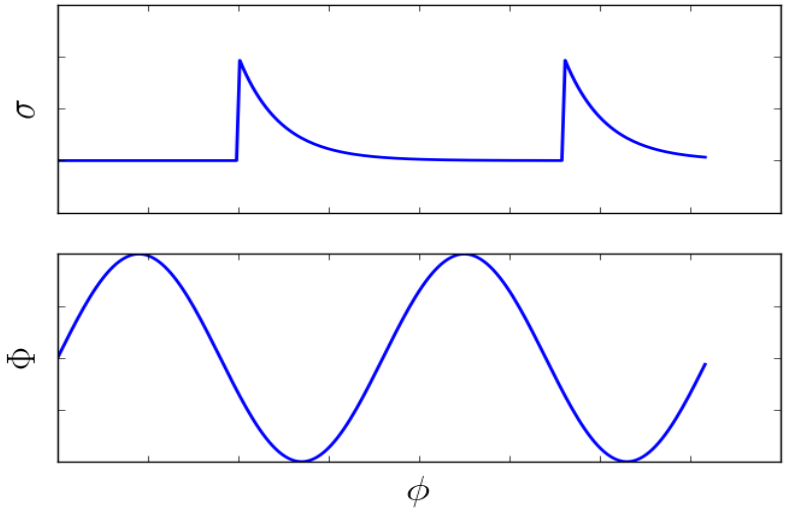

Figure 1.9: Qualitative behaviour of the shock model of Roberts (1969). The upper and lower panels show the gas surface density σ and spiral potential Φ as a function of azimuth ϕ. This model predicts that the shock forms before the gas reaches the potential minimum of the spiral.

(1969) argues that the large-scale shocks can drive gas to sufficiently high densities where self-gravity can allow clouds to collapse and lead to star formation.

Shu et al. (1972) also explored the formation of large-scale shock formation in terms of a two-phase ISM considering cold clouds surrounded by a warm medium. Their results show that cold gas clouds experience a much stronger compression than the inter-cloud medium. Their velocity solutions show a qualitatively similar behaviour to the Roberts (1969) model. A limitation in the shock models is that the gas-self gravity is usually not included. Lubow et al. (1986) shows that when self-gravity is included, it increases the gas response to the perturbation but tends to reduce the formation of gas shocks.

The shock scenario has been widely studied in more recent numerical simulations. Several hydrodynamical simulations by Bonnell et al. (2006); Dobbs & Bonnell (2006); Dobbs et al. (2012); Bonnell et al. (2013); Forgan & Bonnell (2018) show that clumpy inter-arm gas passing through spiral arm shocks can lead to the formation of cloud structures with kinematics that satisfy observed relations between the velocity dispersion and cloud size (e. g. Larson 1981). These simulations have assumed a well behaved spiral arm perturbation based on the model of Cox & Gómez (2002). Gittins & Clarke (2004) have shown that the position of the shock relative to the arm varies with radius and can be used to estimate the corotation radius of spiral galaxies. The results are also sensitive to the number of arms. Clarke & Gittins (2006)

showed that in N-body simulations, the gas tends to settle in the potential wells of the arms. On the other hand Wada (2008), developed galactic-scale simulations including heating and cooling mechanisms as well as supernova feedback and finds that the gas in the arms does not necessarily form regular hydrodynamic shocks, which makes the picture more complex. Lee (2014) has shown that the shock position is sensitive to the effect of self-gravity and magnetic fields using a prescribed spiral potential. Additionally, many shock simulations have not taken into account the more transient and varying structure occurring in dynamic arms, which may be associated with flocculent galaxies. In this sense, Baba et al. (2016) have compared the gas dynamics between potential-based and dynamic (N-body) spiral arms using the same code and large-scale galactic model. In the dynamic arms, the offset between maximum stellar density is less pronounced than in the potential-based model. This may be a consequence of gas falling from both side of the arms, which according to N-body and hydrodynamics simulations of Wada et al. (2011). Similar differences in gas flow properties have been studied in the simulations of Pettitt et al. (2017). A limitation of these simulations, is that the resolution may not be high enough to study shock features in spiral arms.

Gravitational Instabilities

The gravitational instability scenario has been developed to explain the formation of giant molecular clouds and the largest agglomerations of molecular gas. The gravitational stability of a disc is characterised by the Toomre (1964) parameter: $Q = \sigma_R \kappa / 3.36 G\Sigma$, where σ_R is the radial velocity dispersion, κ is the epicyclic frequency, G is the gravitational constant, and Σ is the surface density. When applied to gas, $\sigma_R \rightarrow c_s$ and $3.36 \rightarrow \pi$, where c_s is the sound speed. When $Q < 1$, instabilities can form in the disc. The gravitational instability scenario has two different variants. One variant is the overall growth of large-scale gravitational instabilities in a rotating gas disc in a galactic potential (e. g. Goldreich & Lynden-Bell 1965a,b). Another variant is to assume a large-scale spiral arm perturbation and include the effect of gas self-gravity in the local flow solution (e. g. Balbus & Cowie 1985).

Goldreich & Lynden-Bell (1965a) analysed the growth of gravitational instabilities in a thin disc with a uniform rotation, and later expanded this analysis to include differentially rotating discs (Goldreich & Lynden-Bell, 1965b). According to Goldreich & Lynden-Bell (1965a), spiral arms in the gas disc can be viewed as the overlapping of smaller instabilities in the gas disc. When $\pi G \rho_{\rm avg} / 4\Omega^2$, where $\rho_{\rm avg}$ is the average density and Ω is the orbital angular fre-

quency, falls between 1.8 and 0.7 instabilities in the disc can grow and eventually make the medium brake into several fragments (Goldreich & Lynden-Bell, 1965a). In a later paper, Goldreich & Lynden-Bell (1965b) expanded this analysis to include differentially rotating discs and found that shear has an important effect in the growth of perturbations. From this point of view, molecular clouds would result from the massive clumps that result after these spiral perturbations fragment.

According to the mechanism proposed in Elmegreen (1979) and Cowie (1981), as cold cloudlets and their surrounding medium flow through a spiral arm, the gas density increases due to compression effects. This may trigger gravitational instabilities that can lead to the formation of giant molecular clouds. Balbus & Cowie (1985) developed a mathematical description of this scenario assuming that gas flows through a spiral arm in a similar way as in the Roberts (1969) model but including the effect of self-gravity. Their results show that gravitational instabilities can lead to the formation of massive gas clouds regularly spaced. They estimate masses of $\sim 10^6\ M_\odot$ and typical separations of $\sim 10^2$ pc. This analysis was only limited to perturbations growing normal to the arm. In a later paper, Balbus (1988) expanded the analysis for perturbations growing in more directions and obtained similar results. The key point of this model is that it predicts the formation of massive clouds with regular separations in spiral arms, and may explain why massive molecular clouds and star formation regions are associated to spiral arms. Gravitational instabilities have been invoked to develop models of star formation in the context of galaxy formation and evolution (e. g. Silk 1997).

The formation of molecular clouds by self-gravity has also been studied in simulations. Numerical simulations of gaseous discs including self-gravity, heating and cooling functions, and a multiphase ISM have shown that clumps resembling molecular clouds can be formed from gravitational instabilities even without including an underlying spiral potential (e. g. Wada & Norman 1999; Tasker & Bryan 2008; Tasker & Tan 2009). However, the process may be sensitive to the surface density of the gas disc (Tasker & Tan, 2009).The simulations by Dobbs et al. (2011a) also show that clouds can form without an underlying spiral potential. However, they compare this case with simulations with varying strengths of a spiral potential and show that spiral arms have an effect on forming longer lived and more strongly gravitationally bound clouds.

Other works have also assessed the formation of clouds in simulations including gas self-

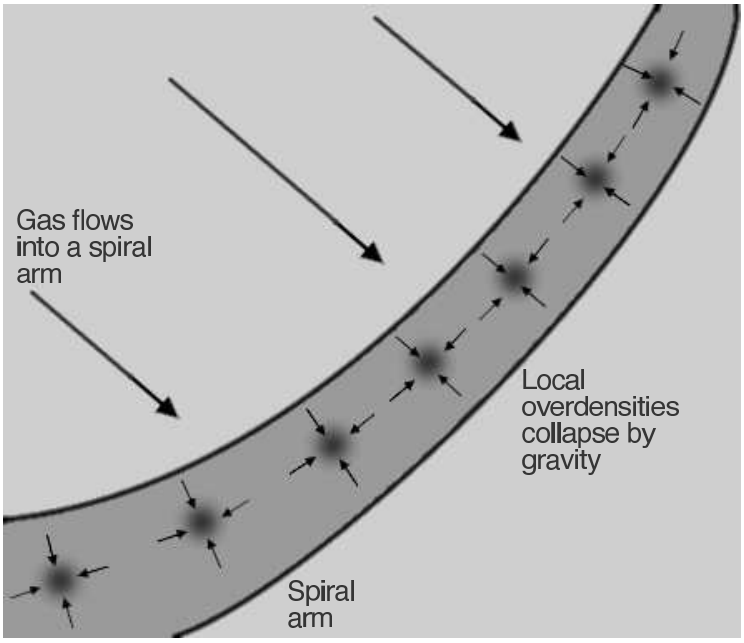

Figure 1.10: In the gravitational instability scenario, the higher density regions in the spiral arm can collapse by their self-gravity to form dense clouds along the arm. This model predicts that the inter-cloud distance is fixed and depends on the local gas properties. The cloud's form a structure resembling a "beads-on-a-string" pattern.

gravity and the effect of spiral arms, both as prescribed potentials (e. g. Wada 2008; Dobbs et al. 2006; Dobbs 2008; Dobbs et al. 2012) or naturally developing an N-body stellar disc (e. g. Kim & Ostriker 2002; Clarke & Gittins 2006; Dobbs & Bonnell 2008; Wada et al. 2011; Baba et al. 2017). These works produce more complex morphologies in the gas clouds and the cold gas distribution that may be more representative of spiral galaxies; however, they may be still limited by the low resolution used in the gas. Both the earlier models (Cowie, 1981) as recent simulations both with spiral arms (Dobbs, 2008) as well as without them (Tasker & Tan, 2009; Bournaud et al., 2010; Dobbs et al., 2012), show that cloud collisions and interactions may be another important formation mechanism, which is described in the next subsection.

1.2.2 Cloud Collisions and Agglomeration

Cloud collisions and agglomeration are other mechanisms that can explain the formation of massive clouds that has been proposed since early works such as Scoville & Hersh (1979); Hausman (1982) and Cowie (1981). Scoville & Hersh (1979) developed a model to explain the formation of giant molecular clouds via the collisions and merging of smaller clouds. However, the model assumes that massive clouds that collide always merge. Cowie (1981) proposed that clouds formed in the spiral arm due to gravitational instabilities can also merge to form

larger clouds, which may be aided by the overall compression of the surrounding medium as it passes through the arm. A problem with this model is that it requires large timescales (more than 10^2 Myr) given the observed velocity dispersion of molecular clouds (Blitz & Shu, 1980). Additionally, simulations of individual collisions show that the process is sensitive to the masses and orbital configurations, the most unstable cases resulting from head-on collisions (e. g. Lattanzio et al. 1985), which may not be the most frequent case.

Several simulations support this picture by showing that spiral arms in fact increase the probability and frequency of collisions between smaller molecular clouds. For example, Casoli & Combes (1982) developed a Monte Carlo method to study the effects of collisions for an ensemble of clouds. Their results show that the spiral arm can increase the effect of this mechanism in the necessary timescales. On the other hand, full hydrodynamical simulations by Tasker & Tan (2009) show that even without an imposed spiral potential, collisions between clouds can be as frequent as 0.2 per orbit. However, their simulations assumed that the ISM is dominated by high surface density gas. Simulations by (Dobbs, 2008) show that gas self-gravity increases the effects of collisions and cloud interactions. However, it has some dependance on the strength of the spiral arm perturbation.

Cloud collisions are important at intermediate scales (from a few 100pc to a kpc) because they operate mainly within spiral arms where clouds are fairly close to each other and can also explain the formation of molecular clouds with masses in the range of $10^5 - 10^6\ M_\odot$. This mechanism can also explain the observed mass distribution (e. g. Hausman 1982; Das & Jog 1996; Williamson & Thacker 2012) and the angular momentum distribution of clouds (Dobbs, 2008; Tasker & Tan, 2009; Dobbs et al., 2011a).

1.2.3 Colliding flows

On the smallest scales, in the range of $1-100$ pc, colliding or converging flows play an important role in the formation of small molecular clouds. Such flows may be triggered by expanding supernova shells. One case occurs when two nearby expanding bubbles will produce a locally converging flow in the region where the shells collide, as shown in Figure 1.11. These produces a locally strong compression that increases the local gas density as shown in simulations by Dawson et al. (2015). Another case can happen when a single supernova expansion drives gas to a higher or a lower vertical position with respect to the galaxy's midplane. The gas eventually falls back to the mid-plane, which will produce a locally converging flow. The converging

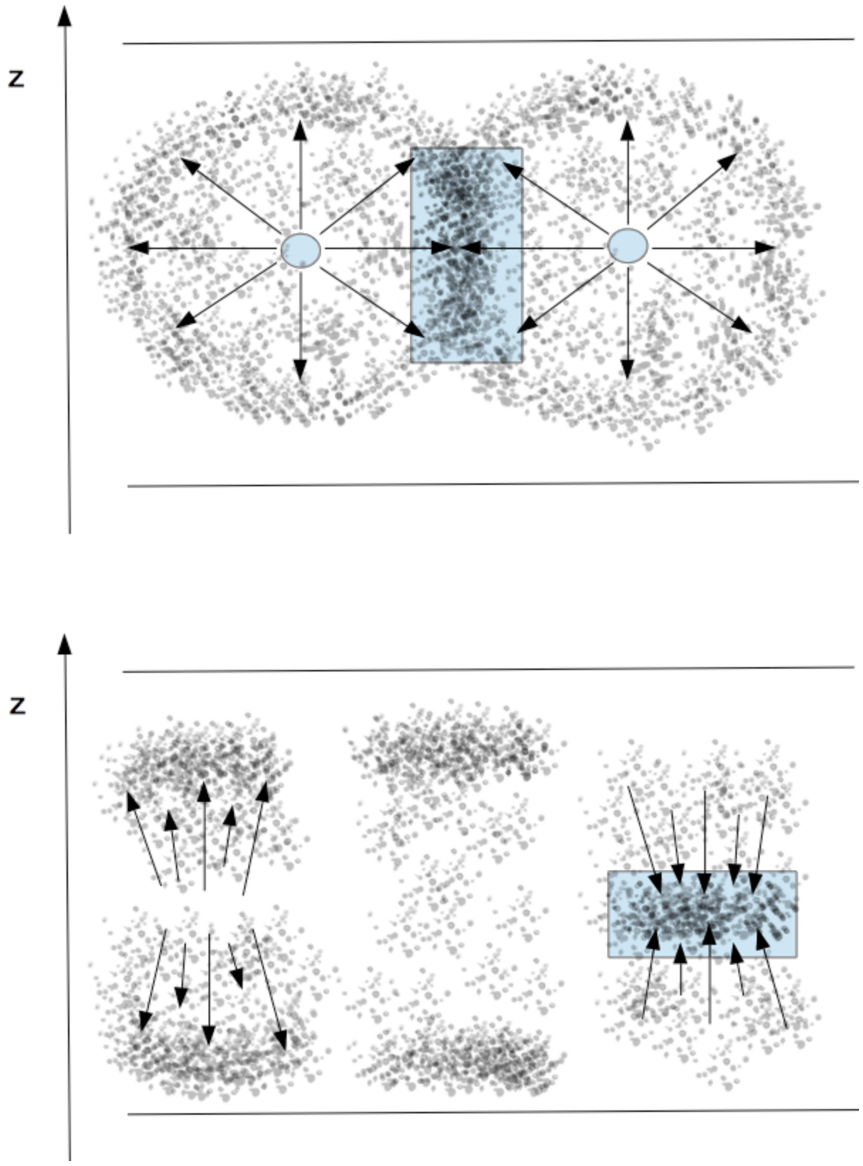

Figure 1.11: In the colliding flows scenario, a dense region is formed at the area (blue box) where opposite flows produced by two nearby expanding shells interact as shown in the top panel. The expanding shells can also drive strong vertical flows, which moves the gas to higher positions with respect to the galaxy's mid-plane. Eventually, these vertical motions stop and the gas falls back to the mid-plane. The bottom panel shows that as the gas converges in the mid-plane, a region of high-density is formed (blue box).

flow needs to be coupled to efficient cooling in order to reach the densities for molecular cloud formation (Koyama & Inutsuka, 2000; Heitsch et al., 2005; Vázquez-Semadeni et al., 2007). This mechanism can explain the formation of clouds with masses around 10^4 $M_\odot$ (Dobbs et al., 2014).

1.2.4 Molecular Cloud Lifetimes

The life time of a molecular is usually compared to the following timescales: the free-fall time: $t_{\rm ff}$ and the crossing time $t_c = L/\sigma_v$ (e. g. Dobbs et al. 2014; Heyer & Dame 2015). In early works, the lifetimes of molecular clouds where expected to be larger than 10^8 yr (Scoville & Hersh, 1979). (Koda et al., 2009) also estimate a timescale larger than 100 Myr based on the properties of clouds in M51. These are typically larger than the expected free-fall time given the cloud densities (Dobbs et al., 2014).

Shorter lifetimes in the range of 10−30 Myr are estimated based on the amount of molecular gas found in Galactic, young open clusters. Kawamura et al. (2009) and Fukui et al. (1999) estimated lifetimes based on the presence of stellar clusters in molecular clouds in the Large Magellanic Cloud. They estimate a total lifetime of ≈ 25 Myr. Estimates from Milky Way star forming regions suggest a timescale of ∼ 10 Myr (Dobbs et al., 2014).

Stellar feedback and supernovae are proposed mechanisms that could disrupt molecular clouds (e. g. Dale 2015). Galaxy-scale simulations by Dobbs & Pringle (2013) show that clouds can be disrupted by shear and feedback. Their results show that feedback is more important on smaller scales and shear dominates on the larger scales. The latter is important particularly when clouds are leaving spiral arms and near the centre of the galaxy where the gradient of the rotation curve is larger. Iffrig & Hennebelle (2015) performed simulations of supernova exploding within as well and outside molecular clouds and show that the mass loss is sensitive to the location of the explosion, but has an important effect. The main causes of molecular cloud disruption are still not fully understood (Heyer & Dame, 2015).

1.3 Towards a more global modelling

1.3.1 Overview of Recent Simulations Studying Molecular Cloud Formation

Molecular cloud formation and evolution has been studied in a wide range of smoothed particle hydrodynamics (SPH), mesh and adaptive mesh refinement (AMR) simulations, which are different in terms of the gas representation. SPH is Lagrangian, which models the gas a as a particle distribution and the fluid properties are calculated following the particles' motions. The spatial resolution adapts to the local mass density. AMR is an Eulerian methodology that solves the hydrodynamics equations in a mesh. In high-density regions, the cells are locally

refined into a smaller grid of much higher resolution also providing an adaptive resolution. This subsection summarises some recent simulations using these methodologies.

SPH Examples

Dobbs et al. (2006) showed that spiral arms can drive the formation formation of dense gas features resembling clouds, assuming an isothermal gas and a prescribed spiral potential. A similar result was obtained by Dobbs & Bonnell (2008) using an active potential, but still assuming an isothermal gas and no gas self-gravity. Using a spiral potential, Dobbs (2008) explored the formation of molecular clouds in low and high surface density environments as well as in different temperature regimes. Self-gravity and magnetic fields were included, but the gas was still assumed to be isothermal and only an annular subregion of a galaxy was modelled. Dobbs (2008) found that collisions and agglomeration are important in forming molecular clouds at low surface density environments and self-gravity is more important in higher-surface density environments, even for warm gas. Collisions also explain the formation of retrogradely rotating clouds.

The Dobbs (2008) model has been further explored by Dobbs et al. (2008), which showed that cooling in shocks formed in spiral arms can lead to the formation of molecular clouds, even without self-gravity. Although this had already been studied by Koyama & Inutsuka (2000, 2002); Heitsch et al. (2008), it had not been simulated in a galactic context. However, these simulations reach a resolution of a few hundred solar masses and are still focused on an annular region of the galaxy assuming a constant surface density profile. Furthermore, Dobbs et al. (2011b) and Dobbs et al. (2011a) developed galaxy scale simulations including feedback to study the properties of molecular clouds under these conditions. It shows that when the spiral potential is varied, molecular clouds form and gather in these structures. However, the spiral potential was assumed to be fixed and the resolution was limited to a few $\sim 10^3\ M_\odot$. Hopkins et al. (2011) developed N-body simulations including SPH to simulate self-consistent spiral structure and the effect of feedback. They show the latter can disrupt molecular clouds and return gas to the warm phase. Also using N-body models and SPH, Williamson & Thacker (2012) studied the effect of cloud collisions and found that they are relevant to the long-term evolution of the galaxy. Although this work developed a large-scale model, it did not include feedback and the resolution was limited to giant molecular clouds.

Dobbs et al. (2012) explored the effect of different galaxy models: no spiral arms, fixed

spiral arms, and flocculent (with an N-body stellar disc), in the formation of molecular clouds including feedback. They show that is possible to form molecular clouds in all scenarios. By tracking particle histories, they find that the gas that will form clouds already has higher densities than the overall ISM within 10 Myr before forming the cloud. This work aims at addressing cloud formation from a galactic perspective, but the resolution is still a few 10^3 $M_\odot$ and the disc is modelled by $\approx 10^6$ particles. They also test a case where the resolution is a few 10^2 $M_\odot$ using 8×10^6 particles.

Another example of a large-scale simulation is that of Dobbs & Pringle (2013) which included heating, cooling, gas self-gravity and feedback in a steady $m = 2$ spiral potential down to a resolution of 312 $M_\odot$, which followed in more detailed the evolution of molecular clouds. They find that some massive clouds tend to form from the coalescence of smaller clouds both in the arm and inter-arm regions and that the evolution is very complex and different for various mass ranges. This makes the definition of a lifetime very difficult.

A simulation including heating and cooling of an annular section of a galaxy in an $m = 4$ spiral potential was developed by Bonnell et al. (2013), which had a resolution down to ≈ 40 $M_\odot$. This simulation explores the effect of spiral shocks in driving star formation. A particular development in Bonnell et al. (2013) is that it takes subregions of the galaxy and resamples them which a higher number of particles to follow its evolution in higher detail to study conditions for star formation, while taking into account information from the larger scales. This idea has been followed in the simulations of Dobbs (2015); Smilgys & Bonnell (2016, 2017); Duarte-Cabral & Dobbs (2016, 2017), which have allowed to follow the evolution of molecular clouds in higher detail.

In particular, Duarte-Cabral & Dobbs (2016) use a section of a galaxy resampled from the simulation of Dobbs & Pringle (2013). It includes self-gravity, heating and cooling, and simple chemistry for H_2 and CO. Instantaneous feedback is included for dense gas above 500 cm^{-3}. The mass resolution is 3.85 $M_\odot$. Clouds are identified in position-position-position (PPP) space as well as in position-position-velocity (PPV) using synthetic observations. The clouds are defined by the H_2 or CO density, rather than using the total gas density. They find that cloud properties traced in 3D by CO gas agree with those traced by H_2, and that CO provides a good marker for high density H_2, but not for the total molecular gas. They find that clouds identified by H_2 in the spiral arm have a higher velocity dispersion than inter-arm ones. On the

other hand, the inter-arm region is dominated by large filaments with lengths of $\sim 100^2$ pc. With the same simulation, Duarte-Cabral & Dobbs (2017) find that the large filaments in the inter-arm region eventually make their way into the spiral arm, but tend to evolve into more complex structures as they interact with the local gas structures. They find that they have a tendency to be aligned with the arm just before reaching the potential's minimum.

Using *N*-body simulations, Hopkins et al. (2012) explored the effect of feedback in the evolution of molecular clouds in Milky Way-sized models but at a fairly low resolution. Williamson et al. (2014) explored the effect of feedback in the number of clouds as a function of time and the star formation rate, but their resolution was limited to $1.3 \times 10^4\ M_\odot$. Ward et al. (2016) also used galaxy-scale simulations, with a resolution of $\approx 440\ M_\odot$, which showed that properties such as the mass and the dispersion vary with galactic position. Baba et al. (2016) and Baba et al. (2017) have focused on the gas dynamics and the formation of molecular clouds comparing the gas dynamics in steady arms (potential based) with that in *N*-body models. The resolution is down to a few $10^3\ M_\odot$. In particular, Baba et al. (2017) find that for dynamic spiral arms, there is not an evolutionary cloud sequence across the arm. They find that molecular clouds tend to be in collapse rather than in a virial state and that both the large-scale structure as well as feedback are important factors in cloud evolution.

Recently, Pettitt et al. (2018) studied the formation and evolution of molecular clouds in simulations of an interacting system aimed to be compared with M51. It includes heating, cooling, star formation and feedback, but the resolution is still limited. It verifies several scaling-relations of molecular cloud properties and also shows that the more massive clouds associate with spiral arms.

Mesh and AMR Examples

Some simulations started by considering a box with size of 10 pc to kpc to focus on the smallest scales. For example, Slyz et al. (2005) simulated a cubic region with a length of 1.28 kpc with periodic boundaries using an AMR code. It included gas self-gravity, star formation and feedback from stellar winds and supernovae (SNe), but did not include the large-scale galactic potential. Their results showed that self-gravity produces a high-density tail in the gas PDF and that both gravity and SNe are important for injecting kinetic energy into the medium. However, it lacks the large-scale effects of galactic structure and rotation. This mode of simulation was further explored by Glover & Mac Low (2007a,b), but extending its vertical

length. They included chemistry networks to study the role of gravity and turbulence in the formation of H_2. Local box simulations have also been used by Heitsch et al. (2008) to study the role of colliding flows in forming molecular clouds. These are assumed to be produced by large-scale effects such as expanding shells or spiral arms, but these may still be rather idealised initial conditions.

Hennebelle & Iffrig (2014) have used AMR simulations of a kpc-sized box including heating, cooling, self-gravity, star formation, SNe feedback, magnetic fields, and the vertical force of the galactic potential. The results show that SNe exploding within dense clouds reduce the star formation activity. Magnetic fields also tend to reduce the star formation rate. However, this simulation did not include the effect of galactic rotation. Hennebelle (2018) extended this simulation to a resolution below pc scales to study the connection between large and small scales in a specific environment and focusing on the formation of dense clumps. Colling et al. (2018) added the effect of shear due to galactic rotation and H_{II} feedback and shows that as the shear is increased, the SFR is decreased.

Another example is the vertical ISM simulations by Walch et al. (2015). This is an AMR simulation using a box 0.5 kpc by 0.5 kpc by 10 kpc. It includes self-gravity, heating, cooling, magnetic fields, time-dependent H_2 and CO chemistry with self-shielding, star formation and SNe feedback, and the vertical component of the galactic potential. It shows that the formation of H_2 is sensitive to the SN rate and that magnetic fields have a small effect on the disc structure, but do delay the formation of molecular hydrogen. Although these simulations study in more detail the connection between small and large scales, they lack the connection with structure such as the spiral arms and the broader galactic context.

Several global-scale examples have also been studied in AMR simulations. For example, Tasker & Bryan (2006) studied 3D models of gas discs embedded in static dark matter haloes. Their simulation included self-gravity, a cooling curve down to 300 K, star formation and SNe feedback. The spatial resolution is 50 pc. It starts with a purely gaseous disc and the stellar component gradually forms from it. This study shows that the molecular clouds can form by gravitational instabilities and merge to form larger clouds. Their lifetime is sensitive to the feedback. They obtain a two-phase medium dominated by cold gas (80% in mass). However, the disc develops a rather irregular structure lacking clear spiral arms. The model is further explored by Tasker & Bryan (2008), which adds a heating term, and explores the differences

between a two-phase medium and an isothermal (10^4 K) medium. It shows that the latter assumption leads to a formation of artificially larger clumps and that background heating has a non-negligible effect on the long term evolution of the ISM.

Tasker & Tan (2009) developed further simulations with similar physics as the above, but without feedback and heating, and down to a resolution of 7.8 pc to study the formation of molecular clouds in the context of a Milky Way sized galaxy. Their results show that collisions can be important and that they occur in typical timescales of 1/5 of the Galaxy's orbital period. The recovered cloud properties are in good agreement with observed relations and depend on the balance between gravitational instabilities as well as collisions and interactions between clouds. Tasker (2011) finds that by adding star formation and photoelectric heating, the fragmentation of the medium is decreased. More filamentary structures of cold gas are formed, surrounded by warmer gas. The fraction of retrogradely rotating clouds decreases and rate of collisions increases to about 1/4 of the orbital period. In a third paper, Tasker et al. (2015) explore the effect of feedback in molecular cloud evolution and find that it does not necessarily destroy the cloud. However, these works have not considered the effect of large-scale spiral arm structure.

Shetty & Ostriker (2006) perform simulations of an isothermal warm disc with self-gravity and with an imposed spiral potential. Without the potential, self-gravity drives the formation of structure. With the potential, it drives the formation of dense structures and if it is strong enough, the structures form a "beads on a string" pattern. This simple model produces clouds with masses up to 10^7 $M_\odot$. Shetty & Ostriker (2008) extended the simulation to include SNe feedback. They find masses up to 10^6 $M_\odot$ and that the injected turbulence produces a wider ranger of masses compared to previous simulations. However, they did not include a 3D treatment of the hydrodynamics.

Agertz et al. (2009) produced galaxy-scale AMR simulations including self-gravity, cooling down to 300K, a star formation prescription based on the free-fall time scale, and SNe feedback. Their resolution is around 24 pc and 6 pc. In general, their models produce a multiphase ISM where cold structures coexisting with the surrounding warm gas. The SNe drive a hot phase. As in Tasker & Tan (2009), cloud evolution depends on gravitational interaction and collisions. Agertz et al. (2009) conclude that both self-gravity and SNe inject turbulence. The first is more important where the SFR per area is low, and the converse is true for the

second mechanism. However, this simulation did not include spiral arms or stellar discs.

Similarly, Bournaud et al. (2010) performed an AMR simulation of a Large Magellanic Cloud type galaxy, including self-gravity, heating and cooling, and SN feedback, which allowed a resolution down to 0.8 pc and a mass resolution of $5 \times 10^3\ M_\odot$. The simulation shows that gravitational instabilities lead to the formation of molecular clouds and this drives turbulence down to the substructures inside GMCs. The authors explain that gravity, hydrodynamics, and adequate thermal modellling are sufficient to develop a realistic representation of the ISM. Feedback has an important effect on longer timescales. This simulation also not included the effect of large-scale structure such as spiral arms.

Renaud et al. (2013) extended the methods of Bournaud et al. (2010) to model a Milky Way type galaxy including a live stellar disc. The spatial resolution reaches 0.05 pc in a cubic box with a length of 100 kpc. It shows that dense clouds are forming along spiral arms in a "beads on a string" arrangement. Clouds are mainly formed by gravitational collapse and reach masses of $\sim 10^6\ M_\odot$. Their masses tend to decrease with time. Some spiral arms tend to have spurs and a Kelvin-Helmholtz instability is generated in the strongest arms. On the other hand, the simulation of Fujimoto et al. (2014) explores the effect of galactic environment by simulating a barred galaxy with a dominant $m = 2$ pattern and finds some differences between the populations identified in the bar region, in the arms, and in the outer disc.

Grisdale et al. (2018) used an AMR simulation similar to the Renaud et al. (2013) simulation but adding metallicity to study the properties of molecular clouds. The resolution is 4.6 pc. An interesting analysis of this work is that it compares the cloud identification based on a 3D method in position-position-position (PPP) space based on a density threshold and a 2D method in position-position-velocity (PPV) space, analogous to observers. It shows that the 3D method tends to steepen the scaling relations between molecular properties. In this sense, Pan et al. (2015) and Khoperskov et al. (2016) have made a similar analysis using mesh-based simulations. Pan et al. (2015) conclude that the results of the 3D-PPP and 2D-PPV agree for most clouds while Khoperskov et al. (2016) conclude the opposite. Note that although they use the same basic concepts, they do not use exactly the same identification methods. In addition, Pan et al. (2015) support their results by matching the clouds identified by both methods and perform a cloud-by-cloud comparison. However, more analysis is needed to clarify this opposing views.

Aims of this Work

The cloud formation mechanisms operate on different scales and modelling the entire process of molecular cloud formation requires models that take into account the larger-scale structure of a galaxy. It is possible that the different formation processes combine to some extent in galaxies. This idea is motivated by recent extragalactic observations that show that molecular cloud properties vary between different parts of a galaxy and also between different galaxies (Hughes et al., 2013; Colombo et al., 2014b), which brings the question of whether this may reflect an environmental dependence of the formation mechanisms. To explore this effect, analytic approximations to understand the effect of the large-scale structure in molecular cloud dynamics has been developed by Meidt et al. (2018). This is interesting as it takes into account a theoretical framework that quantifies the effect of spiral arms in driving gas motions, but it is still necessary to develop and improve full hydrodynamic simulations that model the galaxy in a more self-consistent manner. To include all the detailed physics due to stellar evolution in a galactic context also requires simulations with higher resolution.

The nature of the spiral arms may play an important effect in the formation of molecular clouds. A recent work by Baba et al. (2016) performed hydrodynamical simulations comparing the differences between the flows driven by a rigid, rotating spiral arms and those of the dynamic arms of an N-body simulation. Their results show that the rigid arm has a tendency to drive radial streaming motions whereas the dynamic arms tend to produce tangential streaming motions. Observations by Meidt et al. (2013) of M51 show that the gas has significant streaming motions, which may have a stabilising effect on some clouds. It is interesting to explore how the gas motions driven by the spiral arm affect the formation of molecular clouds. Although some works have addressed the problem of molecular clouds in spiral arms, it is still important to develop simulations that compare the differences between rigid arms and more dynamic arms. The motivation for this work is to develop galaxy scale hydrodynamical simulations comparing a rigid spiral arm simulation with an N-body simulation including heating and cooling mechanisms as well as gas self-gravity. The aim is to characterise the flows in the different spiral arm models and explore the differences that arise in the molecular cloud properties. A detailed outline is presented in the next section.

1.4 Thesis Outline

Chapter 2 provides an outline of the numerical techniques used for modelling N-body systems and for simulating hydrodynamics using the smoothed particle hydrodynamics method (SPH), which are the techniques used for simulating the model galaxies. A description of the included thermal physics is also given. Chapter 3 provides an overview of the tools used to setup an N-body representation of a galaxy. For the N-body model, the code of McMillan & Dehnen (2007) is used to generate initial conditions and for the spiral potential model, the potential of Cox & Gómez (2002) is used, both are described in detail in this chapter. Then, the method for initialising the gas is described.

Chapter 4 presents results of the large scale gas dynamics in both the spiral potential and the N-body simulation, focusing on the streaming motions and velocity dispersions driven by the spiral arms. Chapter 5 presents results of the gas dynamics of a region of gas resampled from the simulations of Bonnell et al. (2013). Cold gas clouds are identified and their kinematics with respect to the spiral arm are studied. These results are used to assess the error in the kinematic distance method. Chapter 6 presents an analysis of the molecular cloud properties identified in the simulations. Chapter 7 summarises the conclusions and the future work.

2

Numerical Techniques

Galaxies are composed of a large number of stars, gas reservoirs and, in the context of the ΛCDM cosmology, massive dark matter halos (e. g. Sparke & Gallagher 2000). A global galaxy simulation requires to model processes operating on a wide range of length and time scales. For this reason, it is necessary to apply numerical techniques to perform simulations in a reasonable amount of computational time. The methods for simulating galaxies have been derived from approaches to solve the classical gravitational N-body problem (Binney & Tremaine, 2008). In addition, several hydrodynamics schemes have been developed to include gas dynamics in galaxy simulations such as Eulerian mesh-based codes (e. g. Stone & Norman 1992; Bryan et al. 2014), particle-based Lagrangian methods such as Smoothed Particle Hydrodynamics (SPH) (e. g. Gingold & Monaghan 1977; Springel 2005; Schaller et al. 2016; Price et al. 2017), and more recent developments such as moving-mesh codes (e. g. Springel 2010; Vandenbroucke & De Rijcke 2016). In this work, simulations are performed with the code sphNG (Bate et al., 1995), which has the capability to perform N-body simulations with hydrodynamics using the SPH method.

This chapter presents an overview of the numerical methods used in galaxy simulations, focusing on those implemented in sphNG. It is divided as follows: §2.1 reviews the methods for calculating gravitational forces in large N-body systems; §2.2 introduces the SPH method; §2.3 briefly describes the time integration scheme; §2.4 overviews the thermal physics included in the code; §2.5 describes the sink particle creation procedures.

2.1 N-body Techniques

2.1.1 Direct Summation Approach

The N-body problem can be stated as follows: what are the equations of motion for an arbitrary N number of particles that are subject to a mutual inter-particle force? In the case of galaxy simulations, the inter-particle force is the classical Newtonian gravity. For an isolated particle system, this can be expressed as:

$$\mathbf{F}_i = -\sum_{j\neq i}^{N} G m_i m_j \frac{\mathbf{r}_i - \mathbf{r}_j}{\left|\mathbf{r}_i - \mathbf{r}_j\right|^3}, \tag{2.1}$$

where $\mathbf{F}_i$ is the force on the i-th particle due to all the other particles in the system, $\mathbf{r}_i$ and $\mathbf{r}_j$ are the i-th and j-th particle positions, respectively; m_i and m_j are the particle masses and G is the gravitational constant. This assumes that the particles behave like point masses.

The i-th particle's acceleration is $\mathbf{a}_i = \mathbf{F}_i/m_i$ by Newton's second law and the particles' motions are determined by integrating:

$$\frac{\mathrm{d}\mathbf{v}_i}{\mathrm{d}t} = \mathbf{a}_i(\mathbf{r}_i), \tag{2.2}$$

$$\frac{\mathrm{d}\mathbf{r}_i}{\mathrm{d}t} = \mathbf{v}_i, \tag{2.3}$$

where $\mathbf{v}_i$ is the particle's velocity. The integration can be performed by methods such as the leap-frog method, kick-drift-kick schemes (e. g. Springel 2005) as well as Runge-Kutta methods. In sphNG, the integration is performed with a second-order Runge-Kutta method. More details are provided in §2.3. Equations (2.1), (2.2) and (2.3) are a general outline of the N-body problem. However, the approach to solve it, depends on the number of particles. For example, for $N = 2$ the particle motion has an analytic solution. However, just by increasing the number to $N = 3$ the problem becomes much more complex (e. g. Hut 1983; Heggie

2005).

A problem with equation (2.1) is that the force diverges as $\mathbf{r}_i - \mathbf{r}_j \to 0$. This implies that very close particle pairs will receive strong accelerations resulting in large integration errors if the particle's time step is not adjusted accordingly. However, adapting the time step depending on the acceleration can lead a simulation to become impractically slow as the step becomes too small. These close interactions also produce an artificial heating, which reflects on artificially higher velocity dispersions in a stellar disc (e. g. Binney & Tremaine 2008). A modification to help alleviate this problem is to "soften" the force by introducing a softening parameter ϵ in equation (2.1), which becomes:

$$\mathbf{F}_i = -\sum_{j \neq i}^{N} G m_i m_j \frac{\mathbf{r}_i - \mathbf{r}_j}{\left(\left|\mathbf{r}_i - \mathbf{r}_j\right|^2 + \epsilon^2\right)^{3/2}}. \tag{2.4}$$

This force actually corresponds to that derived from a Plummer potential (Plummer, 1911). In simulations it is commonly known as the Plummer softening (e. g. Barnes 1994). This can be interpreted as particles with mass densities following the Plummer profile interacting by their mutual gravitational force. The Plummer acceleration is effectively reduced at small radii compared to the Newtonian case as shown in Figure 2.1. However, this is not the only choice and other softening formulations have been explored in Athanassoula et al. (2000); Dehnen (2001). The code sphNG allows to use either a Plummer softening or a cubic-spline adaptive softening, the latter choice is convenient for SPH codes (Price & Monaghan, 2004). More details are given in section §2.2.3.

The summation approach requires N^2 operations to compute the forces on all the particles. This makes it impractical for large systems such as galaxies, but it is adequate for simulating few-body problems such as planetary systems, binary systems or stellar clusters.

2.1.2 Hierarchical Tree Codes

In large-scale systems such as galaxies, the gravitational force can be split in two components:

$$\mathbf{F} = \mathbf{F}_{\text{short-range}} + \mathbf{F}_{\text{long-range}}, \tag{2.5}$$

where $\mathbf{F}_{\text{short-range}}$ is the force exerted by nearby particles and $\mathbf{F}_{\text{long-range}}$ is the force resulting from the overall mass distribution, as shown in Figure 2.2 (e. g. Aguilar 1991; Binney &

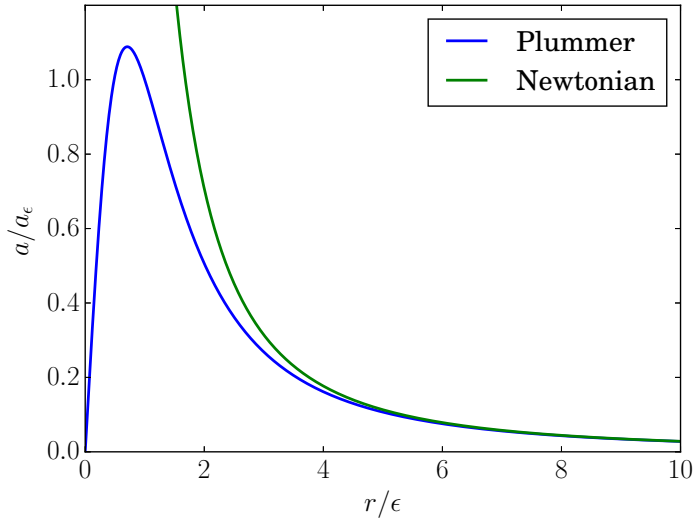

Figure 2.1: The acceleration due to the Plummer force softening (blue line) compared to the Newtonian case (green line). The radial coordinate has been scaled by the softening length ϵ and the acceleration by the Plummer acceleration at $r = \epsilon$, which is denoted by a_ϵ. At large radii both accelerations match but at small radii the Plummer acceleration decreases and approaches 0 as $r \to 0$.

Tremaine 2008). For example, consider a particle near the edge of a galaxy sampled by a large number of particles. The gravitational force on this particle can be approximated by first calculating the long-range force $\mathbf{F}_{\text{long-range}}$ using the potentials of the halo, disc, and bulge and then, computing the short-range force $\mathbf{F}_{\text{long-range}}$ by adding the forces exerted by neighbours up to a certain radius from the particle of interest. This certainly reduces the number of operations compared to a direct summation. However, in a fully dynamic simulation, the density profiles may evolve with time and non-axisymmetric features such as spiral arms and bar features with transient behaviours may develop. This requires a generalised approach that does not assume a particular geometry or mass density profile.

Barnes & Hut (1986) as well as Press (1986) developed an algorithm for calculating gravitational forces produced by generalised particle distributions that takes advantage of the multipole expansion of the gravitational field to approximate the force. In this expansion, the high-order terms decay rapidly with distance r, allowing to calculate the long-range force with only the low-order terms (e. g. Barnes 1996; Binney & Tremaine 2008). This algorithm divides the particle system into a series of regions. The gravitational force is then calculated from the approximate potential of these regions rather than using equation (2.4). The idea of this method is to systematically divide a particle distribution in order to calculate gravitational forces.

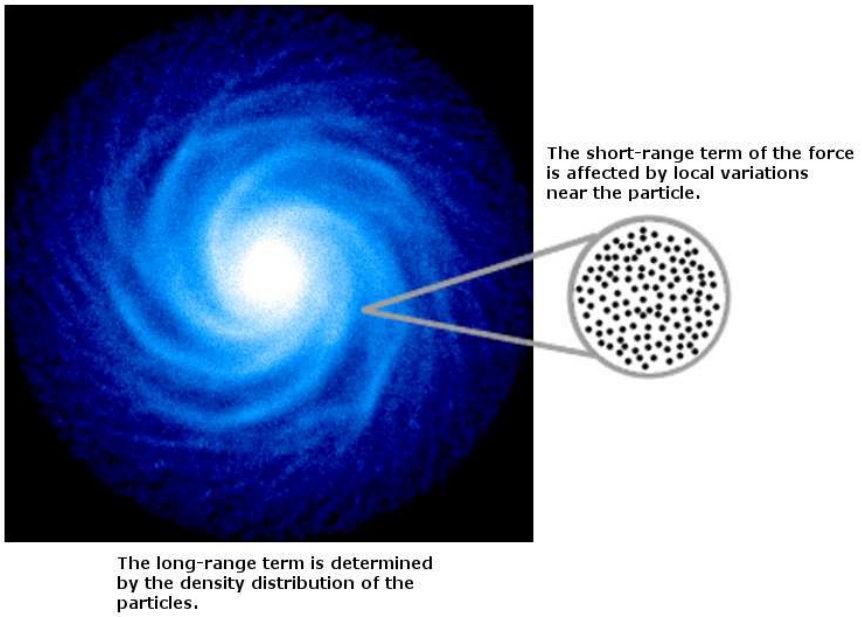

Figure 2.2: The force on a particle can be split in two terms: the short-range term, which depends on the nearest neighbours of the particle and it is affected by local variations in the neighbourhood, and the long-range term, which depends on the overall mass density distribution. A tree code takes advantage of this concept to calculate the long-range force using an approximation based on a tree-structure decomposition of the particle distribution rather than summing the forces over all particles.

The Barnes & Hut (1986) algorithm first creates a root cell enclosing the entire particle distribution, which is subdivided recursively until there is only one particle per cell. For a 3D cell, this results in 8 subdivisions. This builds a hierarchical tree structure of cells where each individual particle is in the smallest cells. Then, to calculate the force on a given particle, the algorithm examines the cell structure starting from the root. It checks if $d > l/\theta$ is satisfied, which is known as the opening criterion; in this inequality: d is the distance between the particle and the cell's centre of mass, l is the cell's side length, and θ is the opening angle. If the opening criterion is satisfied, then the force exerted by that cell is calculated and added to the total; if not, the next subdivisions are examined and tested. The number of operations scales as $N \ln N$ (Barnes & Hut, 1986). Tests show that $\theta \approx 0.5 - 0.7$ is an adequate range of values for the opening angle (Barnes & Hut, 1986, 1989; Hernquist, 1987). This methodology has been widely implemented in galaxy simulations.

sphNG uses a tree code based on the Press (1986) algorithm as described in Benz et al. (1990a); Bate (1995). In this method, the tree is constructed in an inverted fashion where the lower level contains all the particles in the simulation. For each particle, the code searches for the nearest mutual neighbour and each pair forms a node in the second level. Then, for each of these nodes, the code searches for the nearest mutual pairs in the second-level plus

any particles that remain unpaired. This generates the third level in the tree. The process is repeated until the structure is completed. Each node stores its centre of mass, which is used as its location, and the quadrupole moment of the pair that was used to construct it. This version also scales as $N \ln N$ and uses the opening-angle criterion to determine if the node or individual particles are to be used in the calculation. In sphNG, the opening angle is set to 0.5. This tree code version avoids artificial tessellations in clumpy regions and is more efficient in the gravitational force calculation compared to other versions (Benz et al., 1990a).

2.1.3 Combined Approaches

Some codes have developed methods where the long-range forces are calculated from tree codes and short-range forces are calculated using the direct summation approach. This is useful for cases where close-encounters are important. The code sphNG uses this approach, more details of the implementation are given in §2.2. Other N-body with hydrodynamics codes also have followed this approach (e. g. Springel 2005)

2.2 Smoothed Particle Hydrodynamics

In the smoothed particle hydrodynamics (SPH) method, a fluid is sampled by an ensemble of particles that carry information of the local properties of the fluid such as mass density and internal energy. Fluid quantities are calculated by expressions involving the sum of quantities contributed by neighbouring particles weighted by a smoothing kernel function. The equations of hydrodynamics are expressed in these terms. This provides a numerical method applicable to a wide variety of geometries and easily coupled to N-body algorithms. It was first proposed in Lucy (1977) and Gingold & Monaghan (1977) for simulations of stellar structure and further developed by Monaghan & Lattanzio (1985).

This method has been widely implemented in astrophysics; see for example Benz et al. (1990b); Bate et al. (1995) for applications in binary systems; see Benz et al. (1989) for simulations of the Earth-Moon formation; see Rice et al. (2014) for simulations of planet formation; Price & Bate (2007) for simulations of star formation with magnetic fields; Friedli & Benz (1993, 1995); Lee et al. (1999); Foyle et al. (2008); Grand et al. (2012) for applications in the secular evolution of disc galaxies. It has been widely applied in simulations of star formation in a galactic context as in Bonnell et al. (2013); Dobbs & Pettitt (2014); Dobbs (2015) as well as in cosmological simulations (e. g. Springel 2005; Schaye et al. 2015). SPH

is reviewed with more detail in Monaghan (2005); Rosswog (2009); Springel (2010); Price (2012).

In this section, a brief overview of SPH is presented focusing on the formulation implemented in the code sphNG. In §2.2.1 the equations of hydrodynamics are briefly introduced. §2.2.1 introduces the concept of kernel functions and interpolation, which are the basis of the SPH method. Then, §2.2.3 describes the equations of hydrodynamics in SPH terms.

2.2.1 Equations of Hydrodynamics

The equations of hydrodynamics are statements of mass conservation, Newton's second law, and the conservation of energy applied to fluids. Their derivation has been widely discussed in the literature. This subsection follows the derivation of Clarke & Carswell (2007).

It is possible to describe the dynamics of a fluid in two ways. The first one, is to determine how the fluid properties vary with time in a fixed point in space, which is known as the Eulerian description. The second one, takes a finite element of mass and the fluid properties are measured in a comoving volume that evolves with the motion of this element. This is known as the Lagrangian description. The SPH method is Lagrangian because it follows mass elements. This will be described with more detail in the following sections.

For a given fluid quantity f, the Eulerian and Lagrangian descriptions are related by:

$$\frac{\mathrm{D}f}{\mathrm{D}t} = \frac{\partial f}{\partial t} + \mathbf{v}\cdot\nabla f, \tag{2.6}$$

where the operator $\mathrm{D}/\mathrm{D}t$ is the derivative in the Lagrangian description, $\partial/\partial t$ is the partial derivative of f with respect to time, $\mathbf{v}$ is the fluid velocity and ∇f is the gradient of the quantity in the Eulerian description.

Continuity Equation

For a given volume, the variation of mass with time depends on the mass flux across its surface:

$$\frac{\mathrm{d}}{\mathrm{d}t}\left[\int_V \rho\, dV'\right] = -\oiint_S \rho\mathbf{v}\cdot d\mathbf{A}\,, \tag{2.7}$$

where ρ is the mass density, $\mathbf{v}$ is the velocity, dV' and $d\mathbf{A}$ are the differential volume and surface area, respectively. With the divergence theorem, it is possible to transform the previous

equation to the continuity equation in Eulerian form:

$$\frac{\partial \rho}{\partial t} + \nabla \cdot (\rho \mathbf{v}) = 0. \tag{2.8}$$

The Lagrangian form is derived by using $\nabla \cdot (\rho \mathbf{v}) = \rho(\nabla \cdot \mathbf{v}) + \mathbf{v} \cdot \nabla \rho$, rearranging terms, and substituting $D\rho/Dt = \frac{\partial \rho}{\partial t} + \mathbf{v} \cdot \nabla \rho$:

$$\frac{D\rho}{Dt} + \rho(\nabla \cdot \mathbf{v}) = 0 \, . \tag{2.9}$$

Momentum Equation

The momentum equation results from applying Newton's second law to a fluid element, which can be written as (e. g. Clarke & Carswell 2007:

$$\left(\frac{D}{Dt} \int_V \rho \mathbf{v} dV' \right) \cdot \mathbf{n} = - \int_S P\mathbf{n} \cdot d\mathbf{A} + \int_V \rho \mathbf{g} \cdot \mathbf{n} dV' \, , \tag{2.10}$$

where P is the pressure, $\mathbf{g}$ are external or body forces, and $\mathbf{n}$ is a unit vector. The LHS is the rate of change of the momentum of the fluid element and the RHS is the net force due to pressure and external forces.

With the divergence theorem, the pressure term becomes:

$$\int_S P\mathbf{n} \cdot d\mathbf{A} = \int_V \nabla \cdot (P\mathbf{n}) dV' \, . \tag{2.11}$$

Substituting $\nabla \cdot (P\mathbf{n}) = \mathbf{n} \cdot \nabla P + P(\nabla \cdot \mathbf{n}) = \mathbf{n} \cdot \nabla P$, this is expressed as

$$\int_V \nabla \cdot (P\mathbf{n}) dV' = \int_V \nabla P \cdot \mathbf{n} dV' \, . \tag{2.12}$$

Substituting Equation (2.12) in Equation (2.10) and reducing the integration volume to a small element δV, the momentum equation reduces to

$$\frac{D(\rho \mathbf{v} \delta V)}{Dt} \cdot \mathbf{n} = (-\nabla P + \rho \mathbf{g}) \cdot \mathbf{n} \delta V \, . \tag{2.13}$$

The LHS can be expressed as

$$\frac{D(\rho \mathbf{v} \delta V)}{Dt} \cdot \mathbf{n} = \left(\frac{D(\rho \delta V)}{Dt} \mathbf{v} + \rho \delta V \frac{D\mathbf{v}}{Dt} \right) \cdot \mathbf{n} \,, \tag{2.14}$$

This is written in terms of the Lagrangian Derivative (following constant mass elements), thus the first term is zero because the mass in the fluid element is conserved. With the remaining term, equation (2.13) is reduced to:

$$\rho \frac{D\mathbf{v}}{Dt} = -\nabla P + \rho \mathbf{g} \,, \tag{2.15}$$

which is the Lagrangian form [1] [2]. This shows that the fluid motion results from pressure gradients and external body forces.

For completeness, the Eulerian form is derived by substituting the Lagrangian derivative for $\mathbf{v}$ in equation (2.15):

$$\rho \left(\frac{\partial \mathbf{v}}{\partial t} + \mathbf{v} \cdot \nabla \mathbf{v} \right) = -\nabla P + \rho \mathbf{g} \tag{2.16}$$

Energy Equation

The fluid's total energy per unit volume is

$$E = \rho \left(\frac{1}{2} |\mathbf{v}|^2 + \Phi + u \right) = \rho e \tag{2.17}$$

where Φ is the gravitational potential, u is the specific internal energy, and e is the specific total energy. The Lagrangian derivative of this equation yields

$$\frac{DE}{Dt} = \rho \frac{De}{Dt} + \frac{D\rho}{Dt} e \,. \tag{2.18}$$

The first term is

$$\frac{De}{Dt} = \mathbf{v} \cdot \frac{D\mathbf{v}}{Dt} + \frac{D\Phi}{Dt} + \frac{Du}{Dt} \,. \tag{2.19}$$

[1] In ideal MHD, the term $\mathbf{j} \times \mathbf{B}$ appears where $\mathbf{j}$ is the current density and $\mathbf{B}$ is the magnetic field. This term contains the effects of magnetic 'pressure' and 'tension'. See Clarke & Carswell (2007) for a discussion.

[2] If the fluid's viscosity becomes relevant, a term depending on the stress tensor should also be added, leading to the Navier-Stokes equations (Clarke & Carswell, 2007). See Clarke & Carswell (2007) for a detailed derivation and discussion.

Substituting $e = E/\rho$ in the second term gives

$$\frac{D\rho}{Dt}e = \frac{E}{\rho}\frac{D\rho}{Dt}. \tag{2.20}$$

With the first law of thermodynamics $du = dq - PdV$, where du is the change in specific internal energy, dq is the heat and PdV is the work done by the gas, it is possible to express the term Du/Dt in equation (2.19) as:

$$\frac{Du}{Dt} = \dot{Q} - P\frac{Dv}{Dt}, \tag{2.21}$$

where $\dot{Q}$[3] represents any heating/cooling mechanisms affecting the fluid element, and $v = 1/\rho$ is the specific volume. The second term in Equation (2.21) becomes

$$\frac{Dv}{Dt} = -\frac{1}{\rho^2}\frac{D\rho}{Dt}\ , \tag{2.22}$$

and

$$\frac{Du}{Dt} = \dot{Q} + \frac{P}{\rho^2}\frac{D\rho}{Dt}\ . \tag{2.23}$$

Substituting equation (2.23) in equation (2.19) and the resulting expression for De/Dt in equation (2.18) yields a Lagrangian form of the energy equation:

$$\frac{DE}{Dt} = \frac{E}{\rho}\frac{D\rho}{Dt} + \rho\left(\mathbf{v}\cdot\frac{D\mathbf{v}}{Dt} + \frac{D\Phi}{Dt} + \dot{Q} + \frac{P}{\rho^2}\frac{D\rho}{Dt}\right) \tag{2.24}$$

Transformation to the Eulerian form requires additional manipulation and substitution of terms from the continuity and momentum equations (see Clarke & Carswell (2007) for a detailed derivation). For completeness, the Eulerian form is shown:

$$\frac{\partial E}{\partial t} + \nabla\cdot[(E+P)\mathbf{v}] = \rho\left(\dot{Q} + \frac{\partial\Phi}{\partial t}\right) \tag{2.25}$$

Closure of the system requires an equation of state for the fluid (e. g. $P = P(\rho, T)$) depending on the physics of the gas. See Clarke & Carswell (2007) for a detailed derivation and discussion.

[3] In some derivations, $\dot{Q}$ is explicitly written with a negative sign to imply cooling. Here $\dot{Q} < 0$ would represent cooling and $\dot{Q} > 0$ heating.

2.2.2 SPH Kernel Estimates

Kernel Estimates

One of the basic fluid quantities is the mass density ρ. For a fluid modelled by an ensemble of particles, the simplest way for calculating this is to pick a particle and draw a sphere of radius R around it. Then, add the particle masses in the region and divide by its volume. Mathematically,

$$\rho = \frac{\sum_{i=1}^{N} m_i}{\frac{4}{3}\pi R^3}, \tag{2.26}$$

where m_i is the particle mass. Price (2012) gives a similar example. According to Gingold & Monaghan (1982), for particles with equal masses, the mass density is proportional to the local particle density and the latter can be interpreted as a probability distribution function. Thus, the ensemble of particles can be viewed as a discrete sample of this function (Gingold & Monaghan, 1982). With this idea, it is possible to apply the kernel estimation methods developed by Whittle (1958), Rosenblatt (1956), Parzen (1962) to estimate the shape of the probability function given a discrete number of samples following this distribution. In SPH this becomes a kernel estimate of a fluid quantity f, which is written as (e. g. Monaghan 2005):

$$f_I(\mathbf{r}) = \int_V f(\mathbf{r}')W(\mathbf{r}-\mathbf{r}',h)dV', \tag{2.27}$$

where f_I is the interpolated [4] value and f is the actual quantity; W is the kernel function which depends on the smoothing length h; V is the volume of integration.

The kernel function must satisfy the following (Monaghan, 2005):

1. It must be a normalised function:

$$\int_{-\infty}^{\infty} W(\mathbf{r},h)dV = 1\ . \tag{2.28}$$

2. In the limit $h \to 0$, it should approach the Dirac delta function:

$$\lim_{h\to 0} W(\mathbf{r}-\mathbf{r}',h) = \delta(\mathbf{r}-\mathbf{r}')\ . \tag{2.29}$$

[4] In some contexts (e. g. Monaghan 2005), equation (2.27) is referred as a kernel interpolation. This meaning has its roots in the works of Whittle (1958), Rosenblatt (1956), and Parzen (1962) that derived a method to estimate the shape of a probability distribution given a small number of samples. Instead of calculating a histogram, a kernel density estimator was used to obtain an interpolating function of the PDF.

The interpolated function is equal to the original function when the δ function is substituted in equation (2.27).

3. The kernel must provide compact support (see Figure 2.3), that is that $W(r > r_c, h) = 0$, where r_c is the compact support radius (e. g. Monaghan 2005).

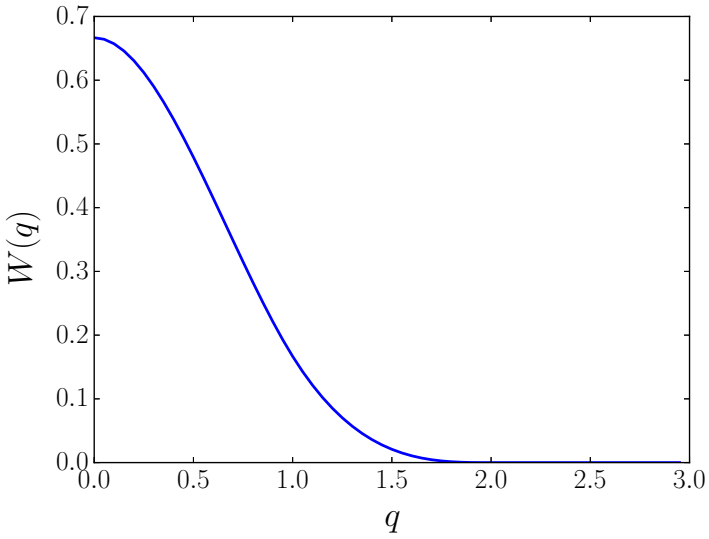

Figure 2.3: The cubic-spline kernel (equation 2.42) as a function of $q = r/h$. The function is zero for $q > 2$. This is an example of a function satisfying the kernel properties described in this section.

Additionally, if $W(\mathbf{r}, h)$ is even and sharply peaked, then $f_I(\mathbf{r})$ is an accurate approximation of $f(\mathbf{r})$ to second order in h (Benz et al., 1990b).

For a given set of particles sampling the fluid, equation (2.27) can be expressed as

$$f_I(\mathbf{r}_a) = \sum_{b=1}^{N} f(\mathbf{r}_b) W(\mathbf{r}_a - \mathbf{r}_b, h) \Delta V_b \ , \tag{2.30}$$

where $\mathbf{r}_a$ is the particle's position where the quantity f is being calculated. The summation is carried only on the neighbouring particles. Since $\Delta V_b = m_b/\rho_b$, equation (2.30) becomes (e. g. Monaghan (2005))

$$f_I(\mathbf{r}_a) = \sum_{b=1}^{N} f(\mathbf{r}_b) W(\mathbf{r}_a - \mathbf{r}_b, h) \frac{m_b}{\rho_b} \ , \tag{2.31}$$

where m_b is the particle's mass, and ρ_b is the density. Setting $f(\mathbf{r}) = \rho(\mathbf{r})$ in equation (2.31),

results in

$$\rho_a = \sum_{b=1}^{N} m_b W(\mathbf{r}_a - \mathbf{r}_b, h) \, . \tag{2.32}$$

In SPH, the density at $\mathbf{r}_a$ is then a weighted sum of the mass of neighbouring particles (e. g. Monaghan 2005; Price 2012). The simple density estimate given in equation (2.26) corresponds to using a box-shaped kernel function in equation (2.32). Once the density is specified, all other quantities in SPH can be calculated with equation (2.31). The method for setting an appropriate smoothing length is described in §2.2.3.

In some cases, as in the momentum equation, it is necessary to evaluate the gradient of a function. In terms of a kernel estimate, ∇f is:

$$\nabla f(\mathbf{r})_I = \int_V \nabla f(\mathbf{r}') W(\mathbf{r} - \mathbf{r}', h) dV' \, . \tag{2.33}$$

Integrating by parts (e. g. Lucas 2015), this becomes

$$\nabla f(\mathbf{r})_I = \int_S f(\mathbf{r}') W(\mathbf{r} - \mathbf{r}', h) \hat{\mathbf{n}} dS + \int_V f(\mathbf{r}') \nabla W(\mathbf{r} - \mathbf{r}', h) dV' \, . \tag{2.34}$$

If W has compact support or approaches 0 at infinity, the first term of this integral vanishes and the interpolating integral becomes

$$\nabla f(\mathbf{r})_I = \int_V f(\mathbf{r}') \nabla W(\mathbf{r} - \mathbf{r}', h) dV' \, , \tag{2.35}$$

and in SPH form,

$$\nabla f(\mathbf{r}_a) = \sum_{b=1}^{N} f(\mathbf{r}_b) \nabla_a W(\mathbf{r}_a - \mathbf{r}_b, h) \frac{m_b}{\rho_b} \tag{2.36}$$

Equation (2.36) has the problem that it is non-vanishing when $f(\mathbf{r})$ is constant. An expression eliminating this problem is (Monaghan, 2005)

$$\nabla f(\mathbf{r}_a) = \sum_{b=1}^{N} \frac{m_b}{\rho_b} (f(\mathbf{r}_b) - f(\mathbf{r}_a)) \nabla_a W(\mathbf{r}_a - \mathbf{r}_b, h) \, . \tag{2.37}$$

The divergence can be obtained with good accuracy by solving for $\nabla \cdot \mathbf{v}$ in $\rho \nabla \cdot \mathbf{v} = \nabla(\rho \mathbf{v}) -$

$\mathbf{v}\cdot\nabla\rho$; in SPH terms, this becomes (Monaghan, 1992; Springel, 2010):

$$\nabla\cdot\mathbf{v}_a=\sum_{b=1}^{N}(\mathbf{v}_b-\mathbf{v}_a)\cdot\nabla_a W(\mathbf{r}_a-\mathbf{r}_b,h)\ . \tag{2.38}$$

See Monaghan (2005); Springel (2010); Price (2012) for a discussion of the previous equations.

Examples of Kernel Functions

Different kernels have been proposed and used in the SPH literature. Gingold & Monaghan (1977) proposed a Gaussian kernel:

$$W(r,h)=\frac{1}{h\sqrt{\pi}}e^{-r^2/h^2} \tag{2.39}$$

where $r=|\mathbf{r}-\mathbf{r}'|$. This is advantageous as it provides a very good density estimate, however the lack of compact support makes it a computationally expensive choice (Gingold & Monaghan, 1982; Price, 2012). Lucy (1977) proposed the kernel

$$W(r,h)=\begin{cases}\frac{105}{16\pi h^3}(1+3(r/h))(1-(r/h))^3 & \text{if } 0\le r\le h\\ 0 & \text{if } r>h,\end{cases} \tag{2.40}$$

which does provide compact support.

Functions derived from the Schoenberg (1946) splines have been implemented in more recent SPH codes. In general, these are defined by a Fourier transform of the form

$$M_n(x,h)=\frac{1}{2\pi}\int_{-\infty}^{\infty}\left(\frac{\sin(kh/2)}{kh/2}\right)^n\cos(kx)dk\ . \tag{2.41}$$

M_2 corresponds to a triangle-shaped function, M_4 is the cubic-spline, M_5 the quartic-spline and M_6 the quintic spline, which have also been explored in SPH (e. g. Price 2012).

The cubic-spline M_4 and has been widely implemented in SPH, which is (e. g. Price 2004):

$$W(q,h)=\frac{\sigma}{h^\nu}\begin{cases}(2-q)^3-4(1-q)^3, & \text{if } 0\le q\le 1,\\ (2-q)^3, & \text{if } 1\le q\le 2,\\ 0, & \text{if } q>2,\end{cases} \tag{2.42}$$

where $q = |\mathbf{r} - \mathbf{r}'|/h$, ν is the number of dimensions, and σ is a normalisation constant:

$$\sigma = \begin{cases} 1/6, & \text{if } \nu = 1, \\ 15/(14\pi), & \text{if } \nu = 2, \\ 1/(4\pi), & \text{if } \nu = 3. \end{cases} \tag{2.43}$$

This is kernel advantageous as it provides good density estimates at a reasonable computational cost and compact support and is the one implemented in sphNG (e. g. Price 2012). Another family of kernels recently explored in SPH is the Wendland (1995) polynomial families, which also have compact support and are interesting for properties that will be described in the next subsection. Several kernels are plotted in Figure 2.4.

Choice of Kernel and Error Analysis

The choice of a kernel has to take into account the accuracy of the kernel in estimating the density, forces, and derivatives of quantities in SPH (e. g. Price 2012). A common problem in many SPH simulations is the formation of pairs of nearby particles, which is known as the pairing instability (e. g. Schuessler & Schmitt 1981; Benz et al. 1990b). These affects codes using kernels of the spline family. Dehnen & Aly (2012) show that a necessary condition to avoid the pairing instability is that the Fourier transform of the kernel is always positive. The spline-kernels do not satisfy this condition, but the Gaussian and Wendland kernels do satisfy it. The latter may be a better choice because they provide compact support.

It is possible to test different kernels by performing an error analysis. The error in the density estimate can be analysed by computing the density estimate in a uniform particle distribution for which the actual density is known. The error in the first derivative can be analysed by checking the following normalisation:

$$S1 = \int (x - x') \frac{\partial W}{\partial x} dx' = \sum_b (x_a - x_b) \frac{\partial W_{ab}}{\partial x_a} = 1. \tag{2.44}$$

Likewise, the second derivative satisfies the following normalisation:

$$S2 = \frac{1}{2} \int (x - x')^2 \frac{\partial^2 W}{\partial x^2} dx' = \frac{1}{2} \sum_b (x_a - x_b)^2 \frac{\partial^2 W_{ab}}{\partial x_a^2} = 1. \tag{2.45}$$

A 1-D analysis was performed to compare the cubic-spline and Wendland C4 kernels. The

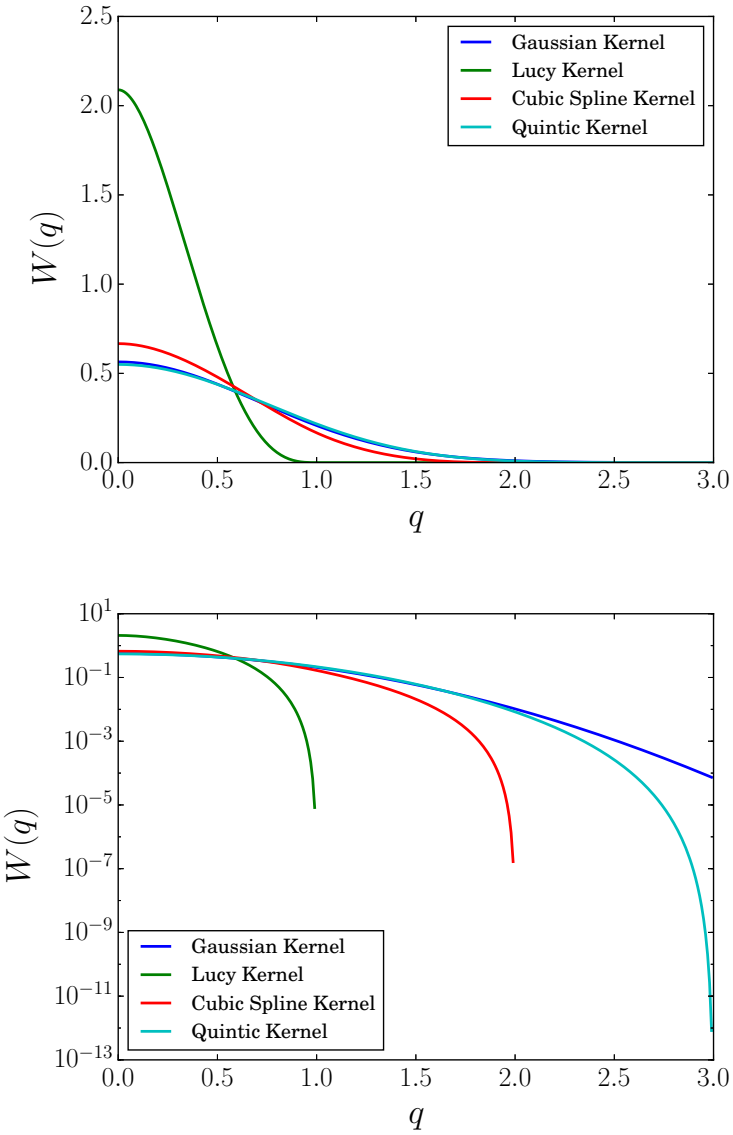

Figure 2.4: Examples of different Kernel functions. The lower panel provides a better visualisation of the compact support radius of each kernel.

relative error in density is shown in Figure 2.5. The error in $S1$, which tests the first derivative is shown in Figure 2.6. The error in $S2$, which tests the second derivative is shown in Figure 2.7. Although the Wendland C4 kernel does avoid the pairing instability because of its properties, the cubic-spline has a reasonable performance in terms of SPH quantity estimates without being too computationally expensive (higher-order splines and the Wendland functions involve higher order polynomials that increase the computational cost). There may be better kernels in terms of quantity estimate, but the cubic-spline is a standard choice for its computational advantage. This is the kernel implemented in sphNG.

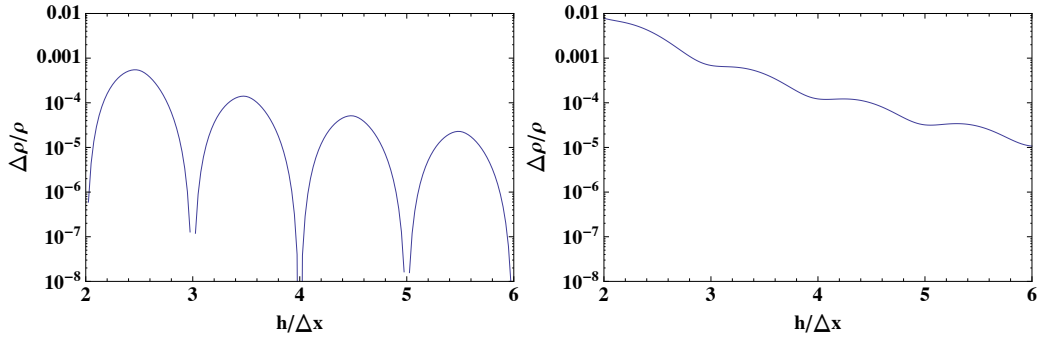

Figure 2.5: Relative error in the density calculation as a function of $h/\Delta x$ for the cubic-spline kernel (left panel) and the Wendland C4 (right panel).

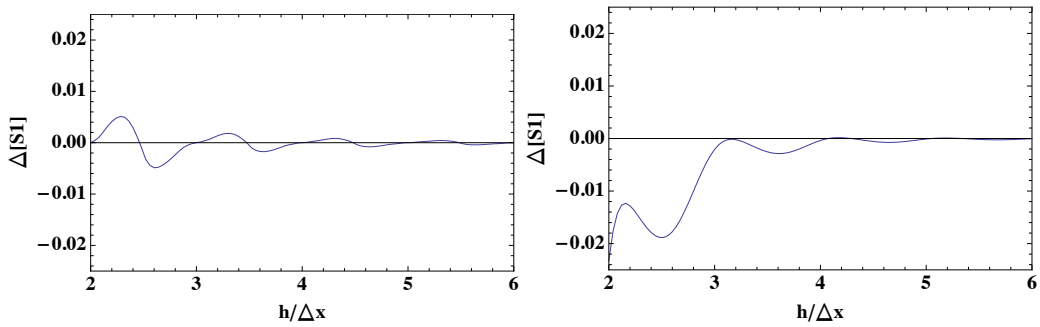

Figure 2.6: Relative error in the normalisation $S1$ as a function of $h/\Delta x$ for the cubic-spline kernel (left panel) and the Wendland C4 (right panel).

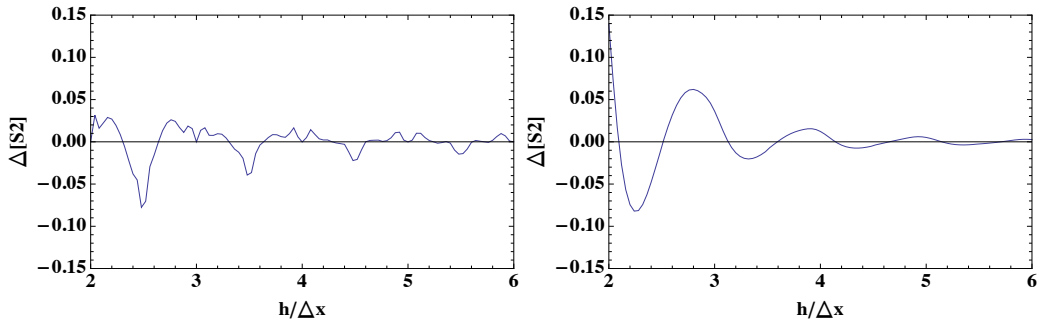

Figure 2.7: Relative error in the normalisation $S2$ as a function of $h/\Delta x$ for the cubic-spline kernel (left panel) and the Wendland C4 (right panel).

2.2.3 Equations of Hydrodynamics in SPH

Continuity Equation

This subsection introduces the equations of hydrodynamics in SPH form. Recalling equation (2.32), the density is given by

$$\rho_a = \sum_b m_b W_{ab}, \tag{2.46}$$

where $W_{ab} = W(\mathbf{r}_a - \mathbf{r}_b, h)$. This satisfies the continuity equation (equation 2.9), which in SPH terms is expressed as

$$\frac{D\rho_a}{Dt} = \sum_b m_b(\mathbf{v}_a - \mathbf{v}_b)\cdot\nabla_a W_{ab}\ . \tag{2.47}$$

See Price (2004, 2012) for a derivation.

Momentum Equation

It is possible to derive the momentum equation in SPH for either by applying the kernel integral of equation (2.27) to both sides of the momentum equation (see Benz et al. 1990b). Another method is to derive the equations of motion from the Lagrangian and the Euler-Lagrange equations (Springel & Hernquist, 2002; Price, 2004; Springel, 2010), which is the one described in this subsection. In hydrodynamics, the Lagrangian can be expressed as (Eckart, 1960; Morrison, 1998):

$$L = \int \left(\frac{1}{2}\rho\mathbf{v}^2 - \rho u\right) dV\ , \tag{2.48}$$

which in SPH terms becomes (Price, 2004)

$$L = \sum_b m_b \left[\frac{1}{2}\mathbf{v}_b^2 - u_b\right]\ . \tag{2.49}$$

Substituting L in the Euler-Lagrange equations,

$$\frac{\mathrm{d}}{\mathrm{d}t}\left(\frac{\partial L}{\partial \mathbf{v}_a}\right) - \frac{\partial L}{\partial \mathbf{r}_a} = 0, \tag{2.50}$$

and using $\frac{\partial u_b}{\partial \rho_b} = P_b/\rho_b^2$, it is possible to derive the equations of motion [5]:

$$\frac{\mathrm{d}\mathbf{v}_a}{\mathrm{d}t} = -\sum_b m_b \left(\frac{P_a}{\rho_a^2} + \frac{P_b}{\rho_b^2} \right) \nabla_a W_{ab} \,. \tag{2.51}$$

This is symmetric in a and b, thus SPH explicitly conserves linear and angular momenta. Benz et al. (1990b) arrives at the same result, but using the kernel integral method.

Energy Equation

In the absence of dissipation, the first law of thermodynamics can be written as

$$\frac{Du}{Dt} = \frac{P}{\rho^2} \frac{D\rho}{Dt} \,. \tag{2.52}$$

From the continuity equation, this becomes

$$\frac{Du}{Dt} = -\left(\frac{P}{\rho} \right) \nabla \cdot \mathbf{v} \,. \tag{2.53}$$

In SPH, this is

$$\frac{Du_a}{Dt} = \frac{P_a}{\rho_a^2} \sum_b m_b (\mathbf{v}_a - \mathbf{v}_b) \cdot \nabla_a W_{ab} \tag{2.54}$$

where u_a is the specific internal energy.

The total energy is,

$$E = \sum_a m_a \left(\frac{1}{2} \mathbf{v}_a^2 + u_a \right) \,. \tag{2.55}$$

Since the Lagrangian is not an explicit function of time, the Hamiltonian is equal to the energy of the system (Price, 2004). Taking the Lagrangian time derivative,

$$\frac{DE}{Dt} = \sum_a \left(\mathbf{v}_a \cdot \frac{D\mathbf{v}_a}{Dt} + \frac{Du_a}{Dt} \right) \,, \tag{2.56}$$

which becomes

$$\frac{DE}{Dt} = \sum_a m_a \frac{De_a}{Dt} \,, \tag{2.57}$$

$$\frac{DE}{Dt} = \sum_a m_a \left[\sum_b m_b \left(\frac{P_a}{\rho_a^2} \mathbf{v}_b + \frac{P_b}{\rho_b^2} \mathbf{v}_a \right) \cdot \nabla_a W_{ab} \right] \,. \tag{2.58}$$

[5] see Price (2004) for a derivation. Although gravitational forces do not explicitly appear here, the relevant term can be added to the equation. See Hernquist & Katz (1985) for a description.

This is an expression of the energy equation in SPH. A detailed discussion is provided in Monaghan (1992); Price (2004); Monaghan (2005).

Including self-gravity in the momentum equation

For SPH gas particles, the gravitational force between two particles is obtained by treating the kernel function as a density distribution $\rho(r,h)$. The integral over this function gives the particle's mass. The potential Φ produced by this density distribution is obtained from the Poisson equation for a spherically symmetric system (Benz et al., 1990b):

$$\frac{1}{r^2}\frac{\mathrm{d}}{\mathrm{d}r}\left(r^2\frac{\mathrm{d}\Phi}{\mathrm{d}r}\right) = 4\pi G\rho(r), \tag{2.59}$$

which results in acceleration of the form

$$\mathbf{g}_{ab} = -\frac{GM(|\mathbf{r}_{ab}|)}{|\mathbf{r}_{ab}|^2}\frac{\mathbf{r}_{ab}}{|\mathbf{r}_{ab}|}, \tag{2.60}$$

where

$$M(|\mathbf{r}_{ab}|) = 4\pi\int_0^{|\mathbf{r}_{ab}|} r'^2\rho(r')dr' = 4\pi\int_0^{|\mathbf{r}_{ab}|} r'^2 m_a W(r',h)dr' \tag{2.61}$$

The kernel function W needs to be such that the above integral converges to a finite value as $\mathbf{r}_{ab} \to \infty$. This should be true for any kernel function that satisfies the normalisation condition. In addition, a compact support radius ensures that this integral converges. For separations larger than the kernel length the acceleration follows the Newtonian case; for smaller separations the force is softened because it only considers the mass integrated up to $|\mathbf{r}_{ab}|$. Thus, as $\mathbf{r}_{ab} \to 0$, $M(|\mathbf{r}_{ab}) \to 0$ which leads to a non-diverging force for small separations (see Figure 2.8).

The total acceleration on a particle can be expressed as (Benz et al., 1990b)

$$\mathbf{g}_a = -\sum_{b=1}^{N}\frac{GM(|\mathbf{r}_{ab}|)}{|\mathbf{r}_{ab}|^2}\frac{\mathbf{r}_{ab}}{|\mathbf{r}_{ab}|}. \tag{2.62}$$

This force calculation scales as N^2. Therefore, the gravitational force for a self-gravitating gas in sphNG is computed by combining a short-range component calculated by using equation (2.62) only for neighbours within a kernel and a along-range component calculated using a tree code (Bate, 1995; Lucas, 2015) (see §2.1). Equation (2.62) corresponds to a force

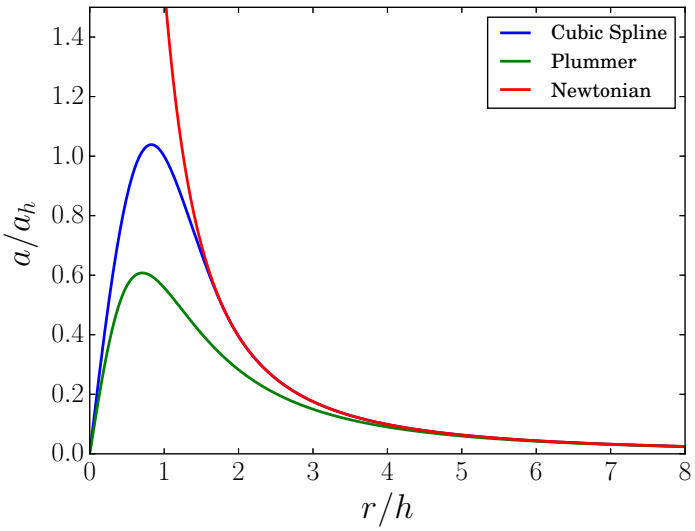

Figure 2.8: The acceleration for the cubic-spline softened form compared to the Plummer and Newtonian cases. The radial coordinate is scaled by the smoothing length h and the vertical axes by a_h, which is the kernel softened acceleration at $r = h$. The spline form gives a better approximation of the Newtonian force at smaller radii compared to the Plummer case. The acceleration still approaches to zero as $r \to 0$.

softened by the kernel function; sphNG also allows to use a Plummer softening for gas particles if desired.

Artificial Viscosity

A problem with the SPH equations introduced above is that these are only applicable to inviscid flows and cannot properly describe shocks (e. g. Benz et al. 1990b). In a viscous fluid, there will be a certain dissipation of kinetic energy into heat. In astrophysical applications, the viscosity is usually very low and dissipation is expected to occur mostly in shocks (Benz et al., 1990b). In SPH, it is necessary to include a mechanism that incorporates the transfer of kinetic energy into thermal energy in shocks and avoids particle interpenetration that can occur in shock regions.

As described in Benz et al. (1990b), two types of viscosity terms are combined to incorporate an artificial viscosity in SPH. The bulk viscosity:

$$\Pi_l = -\alpha \rho l c_s \nabla \cdot \mathbf{v}, \tag{2.63}$$

and the von Neumann-Richtmyer viscosity:

$$\Pi_q = \beta \rho l^2 (\nabla \cdot \mathbf{v})^2, \tag{2.64}$$

where α and β are free parameters, l is a characteristic scale length over which the shock spreads, and c_s is the speed of sound. These terms are sensitive to the local velocity divergence. However, instead of using the SPH form of the divergence to evaluate these equations, the following quantity is introduced (e. g. Monaghan & Gingold 1983; Benz et al. 1990b):

$$\mu_{ab} = \frac{h(\mathbf{v}_{ab} \cdot \mathbf{r}_{ab})}{|\mathbf{r}_{ab}|^2 + \epsilon h^2}, \tag{2.65}$$

where $\mathbf{v}_{ab} = \mathbf{v}_a - \mathbf{v}_b$, and $\mathbf{r}_{ab} = \mathbf{r}_a - \mathbf{r}_b$, h is the smoothing length, and ϵh^2 is a term introduced to avoid large values of μ for small particle separations. This is an estimate of the velocity divergence at particle a due to a nearby particle b and helps to dampen velocity fluctuations on scales smaller than h (Benz et al., 1990b).

The artificial viscosity term is usually expressed as (e. g. Benz et al. 1990b; Bate 1995):

$$\Pi_{ab} = \begin{cases} \frac{-\alpha c_{ab} \mu_{ab} + \beta \mu_{ab}^2}{\rho_{ab}}, & \text{if } \mathbf{r}_{ab} \cdot \mathbf{v}_{ab} \leq 0, \\ 0, & \text{if } \mathbf{r}_{ab} \cdot \mathbf{v}_{ab} > 0, \end{cases} \tag{2.66}$$

However, as pointed in Balsara (1995), it has been shown that this formulation generates larger entropy values in shear flows. Balsara (1995) proposed the following modification to alleviate this problem:

$$\mu'_{ij} = \frac{f_i + f_j}{2} \mu_{ij}, \tag{2.67}$$

where f_i is a function of the local divergence and curl of the velocity field,

$$f_i = \frac{|\langle \nabla \cdot \mathbf{v} \rangle_i|}{|\langle \nabla \cdot \mathbf{v} \rangle_i| + |\langle \nabla \times \mathbf{v} \rangle_i| + 0.0001 c_i / h}. \tag{2.68}$$

The momentum equation including the artificial viscosity term is

$$\frac{\mathrm{D}\mathbf{v}_a}{\mathrm{D}t} = -\sum_b m_b \left(\frac{P_a}{\rho_a^2} + \frac{P_b}{\rho_b^2} + \Pi_{ab} \right) \nabla_a W_{ab}. \tag{2.69}$$

The code sphNG implements the artificial viscosity of equation (2.66) and has the option

to include the modification of equation (2.67).

Artificial Conductivity

Some works have shown that, although the artificial viscosity improves shock capturing in simulations, SPH still has problems in treating flow discontinuities and instabilities such as the Kelvin-Helmholtz instability (e. g. Agertz et al. 2007; Price 2008). To improve this, an artificial viscosity is added Price (2008):

$$\frac{\mathrm{D}u_a}{\mathrm{D}t} = -\sum_b \alpha_u v_{\mathrm{sig}}(u_a - u_b)\frac{\mathbf{r}_{ab}}{|\mathbf{r}_{ab}|}\cdot\nabla_a W_{ab}, \tag{2.70}$$

where u is the specific internal energy, $\mathbf{r}_{ij}$ is the separation vector between particles, and v_{sig} is defined as the signal velocity. The latter may be interpreted as a characteristic speed for the transmission of quantities between particles, and it can be calculated with (Monaghan, 1997):

$$v_{\mathrm{sig}} = \frac{1}{2}(c_a + c_b - \beta\mathbf{v}_{ab}\cdot\frac{\mathbf{r}_{ab}}{|\mathbf{r}_{ab}|}), \tag{2.71}$$

where c_a and c_b are the sound speed given the properties of each particle, $\mathbf{v}_{ab}$ is the relative velocity between particles. Other forms have been proposed. For example, Wadsley et al. (2008) use the form $v_{\mathrm{sig}} = \mathbf{v}_{ab}\cdot\mathbf{r}_{ab}/|\mathbf{r}_{ab}|$. Price (2008) proposed the form:

$$v_{\mathrm{sig}} = \sqrt{\frac{|P_a - P_b|}{\bar{\rho}_{ab}}}, \tag{2.72}$$

where P_a and P_b are the pressures of the particle pair and $\bar{\rho}_{ab}$ is the average density. The artificial conductivity term improves the capability to treat discontinuities in the thermal energy across a discontinuity in the fluid (e. g. Price 2008, 2012). The code sphNG has the option to include artificial conductivity in a simulation.

Defining Smoothing Lengths in SPH

The SPH equations described so far have been written in terms of a constant smoothing length h. However, it is desirable to allow this quantity to vary as a function of the fluid's local conditions. The smoothing length can be expressed as (e. g. Benz et al. 1990b; Monaghan 1992; Price 2012)

$$h_a = \eta\left(\frac{m_a}{\rho_a}\right)^{1/3}, \tag{2.73}$$

for the three-dimensional case; η is a numerical parameter depending on the mean particle separation. However, this requires that the density is known:

$$\rho(\mathbf{r}_a, h_a) = \sum_b m_b W(\mathbf{r}_{ab}, h_a). \tag{2.74}$$

Substituting the previous expression in equation (2.73) results in an equation which can be solved for h_a using numerical root-finding algorithms (e. g. Price 2012). The derivative with respect to ρ of equation (2.73) is

$$\frac{\mathrm{d}h}{\mathrm{d}\rho} = -\frac{1}{3}\frac{h}{\rho}, \tag{2.75}$$

which means that the Newton-Raphson method can be implemented to solve equations (2.73) and (2.74) simultaneously. However, if this method fails to converge, it is possible to reach a solution via the bisection method, but with a possibly longer time to converge (e. g. Price 2012; Lucas 2015). This iterative scheme has the property that the mass inside the kernel is kept roughly constant. Because particle masses are equal, it is equivalent to say that the number of neighbouring particles is kept constant (Price, 2012). The code sphNG uses this method to set the smoothing lengths of particles in a simulation.

2.2.4 Grad-h formalism

A variable smoothing length requires new terms that depend on ∇h in the equations of SPH. These terms ensure that they are still conservative (Nelson & Papaloizou, 1993). It is possible to obtain the grad-h factor Ω by deriving equation (2.73) with respect to time, leads to

$$\frac{\mathrm{d}\rho_a}{\mathrm{d}t} = \sum_b m_b \mathbf{v}_{ab} \cdot \nabla_a W_{ab} + \frac{\partial h_a}{\partial \rho_a}\frac{\mathrm{d}\rho_a}{\mathrm{d}t}\sum_b \frac{\partial W_{ab}}{\partial h_a}. \tag{2.76}$$

Solving for $\mathrm{d}\rho_a/\mathrm{d}t$, yields:

$$\frac{\mathrm{d}\rho_a}{\mathrm{d}t} = \frac{1}{\Omega_a}\sum_b m_b \mathbf{v}_{ab} \cdot \nabla_a W_{ab}(h_a), \tag{2.77}$$

where

$$\Omega_a = 1 - \frac{\partial h_a}{\partial \rho_a}\sum_b m_b \frac{\partial W_{ab}(h_a)}{\partial h_a}. \tag{2.78}$$

The above term is the basis of the gradh-h formalism. See Nelson & Papaloizou (1993); Monaghan (2002); Springel & Hernquist (2002); Price & Monaghan (2004) for a detailed discus-

sion. In this formalism, the momentum equation becomes:

$$\frac{\mathrm{D}\mathbf{v_a}}{\mathrm{D}t} = -\sum_b m_b \left[\frac{P_a}{\Omega_a \rho_a^2} \nabla_a W(\mathbf{r}_{ab}, h_a) + \frac{P_b}{\Omega_b \rho_b^2} \nabla_a W(\mathbf{r}_{ab}, h_b) + \Pi_{ab} \nabla_a W_{ab} \right], \tag{2.79}$$

and the energy equation is written as

$$\frac{\mathrm{D}u_a}{\mathrm{D}t} = \frac{P_a}{\Omega_a \rho_a^2} \Sigma_b m_b \mathbf{v}_{ab} \cdot \nabla_a W(r_{ab}, h_a). \tag{2.80}$$

The version of sphNG used in this work includes the grad-h terms.

2.3 Time Integration Method

Runge-Kutta-Fehlberg Integration

The code sphNG uses a Runge-Kutta-Fehlberg method to integrate the equations previously described with respect to time. Following Lucas (2015), this method can be summarised as follows. Let $y(t)$ be a given fluid quantity of interest. Its derivative can be expressed as a function of time and y: $y' = f(t, y)$. For a given step with size Δt, the initial quantities are:

$$y_0' = f_0 = f(t_0, y_0). \tag{2.81}$$

Then, the quantities for a time step $\Delta t/2$ are obtained,

$$f_1 = f(t_0 + \frac{1}{2}\Delta t, y_0 + \frac{1}{2}\Delta t f_0). \tag{2.82}$$

The integration up to a step of size Δt is then calculated as:

$$y_1 = y_0 + \frac{1}{256}\Delta t f_0 + \frac{255}{256}\Delta t f_1. \tag{2.83}$$

The process is repeated for each subsequent step until a desired final time. This is essentially a first-order Runge-Kutta method (Lucas, 2015).

As described in Lucas (2015), it is possible to calculate the following

$$f_2 = f(t_0 + \Delta t, y_0 + \frac{1}{256}\Delta t f_0 + \frac{255}{256}\Delta t f_1), \tag{2.84}$$

which is essentially f_0 at the beginning of the new step. However, the key point is that this quantity can be used to estimate the truncation error of the method. Following the notation in Lucas (2015), let $\hat{y}_1$ be:

$$\hat{y}_1 = y_0 + \frac{1}{256}\Delta t f_0 + \frac{255}{256}\Delta t f_1 + \frac{1}{512}\Delta t f_2. \tag{2.85}$$

The truncation error of this integration may be estimated as (Lucas, 2015):

$$\Delta y_{\mathrm{TE}} = y_1 - \hat{y}_1 = \frac{1}{512}(f_0 - f_2)\Delta t \tag{2.86}$$

In order to adapt the time step depending on the error at a given time, it is possible to express the ratio of the next time step size δt_2 to the current δt_1 as:

$$\frac{\Delta t_2}{\Delta t_1} = \sqrt{\frac{\epsilon}{|\Delta y_{\mathrm{TE}}|}}, \tag{2.87}$$

where ϵ is a tolerance parameter, which may be chosen in the range of $10^{-5} - 10^{-6}$. Given the error in the integration and the tolerance parameter, the time step size can be adjusted accordingly (Lucas, 2015)

Additional Time Step Criteria

In a simulation, additional time step criteria need to be applied to ensure that the hydrodynamics are being integrated with an adequate time step. One criterion is the Courant-Friedrich-Lewy condition, which is expressed as:

$$\Delta t_{C,a} = \frac{\zeta h_a}{c_{s,a} + h_a|\nabla \cdot \mathbf{v}|_a + 1.2(\alpha c_s + \beta h_a|\nabla \cdot \mathbf{v}|_a)}, \tag{2.88}$$

where $c_{s,a}$ is the sound speed for particle a, α and β are the artificial viscosity parameters, and ζ is a constant. In sphNG, $\zeta = 0.3$ (Lucas, 2015). The CFL condition ensures that the time steps are sufficiently small to allow information to be correctly transmitted between particles.

The second criterion depends on the local force exerted on a given particle, which can be applied to both gas as well as stellar particles. It is expressed as

$$\Delta t_{F,i} = \zeta \sqrt{\frac{h_i}{|\mathbf{a}_i|}} \tag{2.89}$$

For a given particle, the time step used will be the smallest resulting from the RK truncation error, the CFL and force conditions. These conditions are implemented in sphNG to allow the time step to adapt to the local conditions of each particle (Lucas, 2015).

Time Step Limiter

A problem with an adaptive time step scheme is that momentum and energy are not properly conserved in a simulation. To understand this behaviour, consider two particles interacting with one having a larger step than the second one. For example, assume that the second particle has a step a factor of 4 smaller than the first. The second particle updates its quantities more frequently than the first. The first particle will update its quantities after the second particle has already moved 4 steps. This results in an asymmetry in the force calculation that breaks the conservation of momentum (e. g. Lucas 2015). Although the error checking and time step criteria previously described still ensure that the error is low, it is important to ensure that momentum and energy are reasonably preserved within numerical limits.

The code sphNG implements the time step limiter developed by Lucas (2015), which is motivated by the limiter schemes developed by Saitoh & Makino (2009) and Durier & Dalla Vecchia (2012). The limiter aims to maintain a factor of 4 difference in the steps of two neighbouring particles a and b:

$$\Delta t_a \leq 4\Delta t_b. \tag{2.90}$$

Although Saitoh & Makino (2009) originally proposed an arbitrary factor, they argue that tests showed that a factor of 4 produced the best results as larger values produced steps that violated the CFL condition (equation 2.88). Due to the time step distribution that occurs in a simulation, the limiter can have strong and weak cases. In the strong case, a particle on a longer time step (higher bin), which may not be active when particles on lower steps are being integrated, has to be checked and the step should be reduced if necessary. This allows particles on longer steps to react quickly to changes in neighbouring particles. In the weak case, the particle only checks itself at the same pace as it evolves (Lucas, 2015).

In sphNG, the strong limiting is applied at the force calculation subroutines which loop over the neighbours of a given particle. In this case, the time step will change when the particle is in between the beginning and end of a step (see Figure 2.9). For this reason, two cases may occur: 1) the change takes place before the half-step calculations of the RK method for

this particle; 2) the change takes place after this half-step point (Lucas, 2015). If a particle is strongly limited, it is tagged, removed from the current bin and placed in the one associated to the new step. When the new bin is updated, the particle's quantities are integrated using a different scheme. In case 1, the particle is updated with the Euler method to the point of synchronisation with the new bin at its next advance step. In case 2, a modified version of the RK method that takes into account the fraction of time step required to complete the update is applied. This takes advantage of the already known half-step information, which provides a computational advantage (Lucas, 2015). In the weak limiting case, the particle step is modified at the end of the previous step. Therefore, it can be placed in a new bin immediately Lucas (2015). The time step limiter implemented in sphNG has been tested with Sedov explosion in Lucas (2015) showing a significant improvement in the density evolution compared to the non-limiter version. For a more detailed description of the implementation see Lucas (2015).

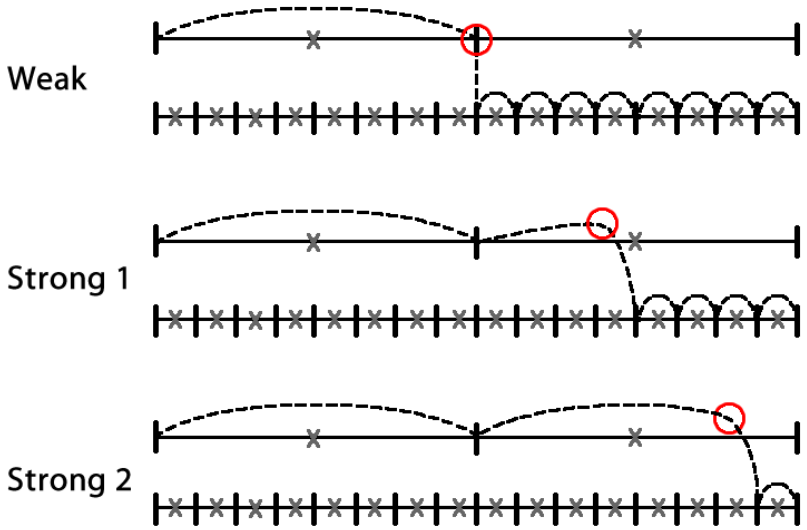

Figure 2.9: In the weak limiter, the change is applied at the end of the previous step. In the strong limiting case 1, the change needs to be applied before the half-step prediction of the RK method. In the strong case 2, the change needs to be applied after the half-step prediction. Figure from Lucas (2015).

2.4 Thermal Physics

2.4.1 Gas Equation of State

For most astrophysical applications, it is possible to model the gas physics using an ideal gas law which can be expressed as

$$P = \frac{k_B T}{\mu m_{\rm H}} \rho, \tag{2.91}$$

where P is the gas pressure, k_B is the Boltzmann constant, T is the gas temperature, μ is the mean molecular weight, and $m_{\rm H}$ is the hydrogen mass. The mean molecular weight is given by

$$\mu = \left(\sum_i \frac{X_i}{A_i} \right)^{-1}, \tag{2.92}$$

where X_i is the mass fraction of a species i, and A_i is the mass in terms of $m_{\rm H}$. The sound speed, can be calculated from $c_s^2 = \partial P / \partial \rho$, which gives:

$$c_s = \sqrt{\frac{k_B T}{\mu m_{\rm H}}}. \tag{2.93}$$

This allows to write the pressure as

$$P = c_s^2 \rho. \tag{2.94}$$

If the gas is monatomic, the specific internal energy is

$$u = \frac{3}{2} \frac{k_B T}{\mu m_{\rm H}} = \frac{3}{2} c_s^2. \tag{2.95}$$

With this expressions, it is possible to express the pressure as

$$P = \frac{3}{2} \rho u, \tag{2.96}$$

which is the actual equation used in the code to calculate the pressure as ρ and u are the quantities evolved. To some extent, it is possible to approximate the medium as a monatomic gas as the H_2 molecule requires higher temperatures than in typical clouds to excite rotational and vibrational modes (e. g. Habart et al. 2005). The simulation also does no follow chemical networks that include the formation of molecules and assumes a neutral, atomic medium based on solar abundances. This may be oversimplified for a realistic ISM, but still allows the formation of the cold and warm phases and allows to explore the contribution of different cloud formation mechanisms depending on hydrodynamics, gravity and the large-scale structure of the galaxy. The code sphNG does include modules for simple H_2 and CO chemistry (Dobbs et al., 2008), but this is left for future work.

In sphNG, the simplest equation of state (EOS) is to use is the isothermal EOS, which is simply equation (2.91) with a constant temperature. This assumes that the gas maintains a constant specific internal energy as a function of time. This can be interpreted as a gas where

any process that increases the internal energy is quickly radiated. Several of the simulations used in this work are evolved using an isothermal EOS, which will be described in more detail in chapter 3.

The code is also able to simulate an adiabatic gas following the ideal gas EOS. In this case, the internal energy evolution explicitly includes the change due to work on the gas pdV. If the gas expands, it will lose internal energy and the converse is true if the gas is compressed. In the adiabatic case, the total energy of the gas is conserved. The code also includes terms that account for the change of internal energy due to shocks. For completeness, it is added that sphNG also allows the user to implement a polytropic equation of state ($P \propto \rho^{\gamma}$), however it is not used in this work.

2.4.2 Including Cooling and Heating Mechanisms

It is possible to run simulations in sphNG that include the effect of cooling and heating. A brief overview of the mechanisms included and the method implemented to update the internal energy is given in this subsection. In general, the rate of change of energy can be expressed as, following the notation in Lucas (2015):

$$n\dot{u}_{\rm total} = n^2\Lambda + n\Gamma + n\dot{u}_{\rm hydro}, \tag{2.97}$$

where n is the number density $n = \rho/(\mu m_{\rm H})$, Λ is the cooling function, Γ is the heating function, and $\dot{u}_{\rm hydro}$ is a contribution due to work done on the gas: $\dot{u}_{\rm hydro} > 0$ in compression and $\dot{u}_{\rm hydro} < 0$ in expansion; it also includes changes produced in shocks.

In this work, the cooling function of Koyama & Inutsuka (2002) is used, which is

$$\frac{\Lambda(T)}{\Gamma} = 10^7 \exp\left(\frac{-114800}{T+1000}\right) + 0.014\sqrt{T}\exp\left(-\frac{92}{T}\right)[\mathrm{cm}^3], \tag{2.98}$$

where T is in Kelvin, Λ is in units of $\mathrm{erg\,s^{-1}\,cm^3}$, and Γ depends on the background radiation field and is set to $2\times10^{-26}\ \mathrm{erg\,s^{-1}}$ as specified in Koyama & Inutsuka (2002). The equilibrium density, temperature and pressure for this heating and cooling terms is shown in Figure 2.10.

The internal energy is evolved using the semi-implicit method of Vázquez-Semadeni et al.

(2007), which starts from writing equation (2.97) as:

$$n^2\Lambda = n\Gamma + n\dot{u}_{\rm hydro}. \tag{2.99}$$

Note that in the original Vázquez-Semadeni et al. (2007) implementation, the $n\dot{u}_{\rm hydro}$ is not directly included. However, this has been added to sphNG (Lucas, 2015). The following step is to determine the cooling time-scale,

$$\tau_\Lambda = \left| \frac{u - u_{\rm eq}}{n\Lambda(T) - \dot{u}_{\rm hydro} - \Gamma} \right| \tag{2.100}$$

This requires that the equilibrium thermal energy $u_{\rm eq}$ is specified, which can be calculated as follows. The equilibrium number density $n_{\rm eq}$ is obtained from

$$n_{\rm eq} = \frac{\Gamma}{\Lambda(T_{\rm eq})}, \tag{2.101}$$

where $T_{\rm eq}$ is the equilibrium temperature. The resulting equilibrium curve is shown in Figure 2.10. In the code, a set of values of $(T_{\rm eq}, n_{\rm eq})$ is tabulated and the equilibrium temperature is obtained by an interpolation technique given the gas density. Then, the equilibrium internal energy is evaluated from $u_{\rm eq} = u(T_{\rm eq})$. The internal energy is then updated by

$$u_{\rm new} = u_{\rm eq} + (u - u_{\rm eq}) \exp\left(-\frac{\Delta t}{\tau_\Lambda}\right), \tag{2.102}$$

where $u_{\rm new}$ is the updated value and Δt is the time step. If the time step is short compared to the cooling time, the above reduces to (Vázquez-Semadeni et al., 2007):

$$u_{\rm new} = u - \Delta t(n^2\Lambda - n\Gamma). \tag{2.103}$$

When the cooling time is very short, then the exponential term in equation (2.102) tends to unity if $\Delta t \gg \tau_\Lambda$ and the updated energy is essentially the equilibrium value. This method allows gas that is heating or cooling very quickly to reach the equilibrium value without decreasing the time step significantly, which could make the computational time much longer (Vázquez-Semadeni et al., 2007; Lucas, 2015).

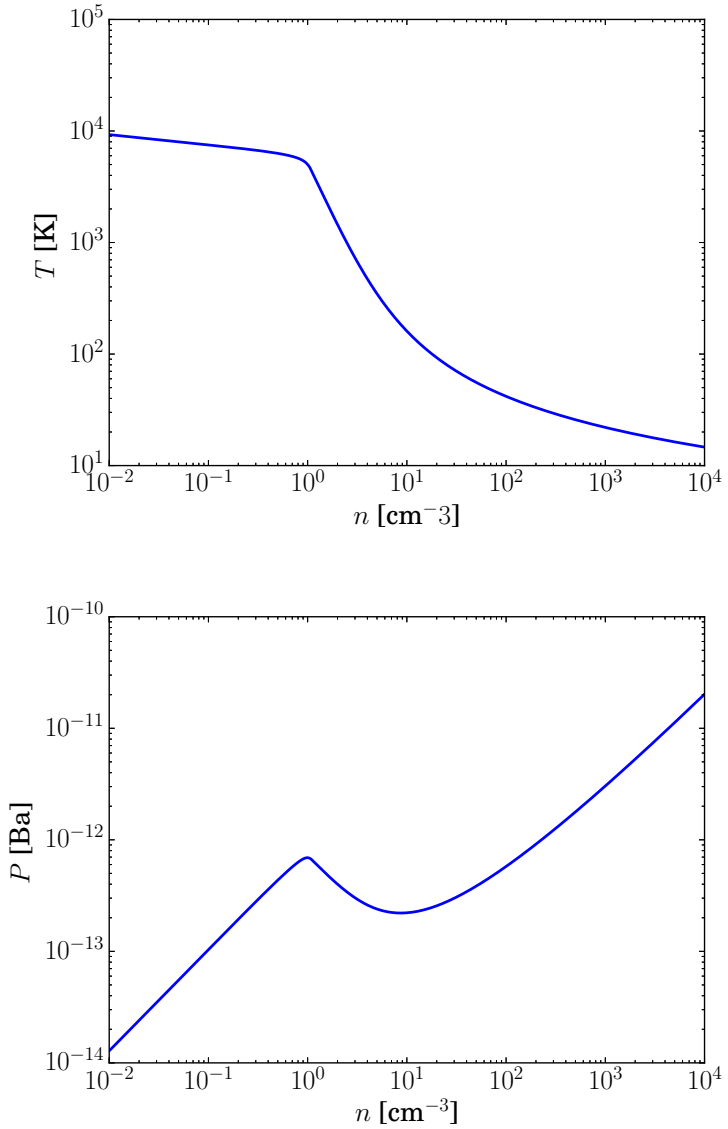

Figure 2.10: The top panel shows the equilibrium density-temperature plot and the lower panel shows the pressure-density plot for the cooling and heating terms used in Koyama & Inutsuka (2002).

2.5 Sink Particle Creation

This section first describes, in §2.5.1, the procedure for introducing sink particles in a simulation in sphNG.

2.5.1 Sink Particles

The code sphNG allows to create sink particles dynamically in a simulation. These particles are point masses that act as tracers of star formation activity and can accrete gas from their

vicinity. Another advantage of these particles is that they essentially kill the densest gas in a simulation, which has the smallest time steps and usually make a simulation run slower.

The following parameters are required for sink particle creation: a critical density ρ_{critical}, which is expressed as a multiple of the mean gas density in the initial conditions; a critical radius R_{critical} that should be set to be a small scale in the simulation; inner and outer accretion radii, $R_{\text{acc,inner}}$ and $R_{\text{acc,outer}}$ (Bate et al., 1995; Lucas, 2015).

If the density of a gas particle is above ρ_{critical}, the code performs a series of tests to determine if a sink particle should be created. First, the particle's smoothing length must be less than $0.5R_{\text{critical}}$ and all its neighbours must be at the current time step. If this is satisfied, further tests are performed. Let E_{therm} be the thermal energy, E_{grav} the gravitational potential energy and E_{rot} the rotational energy measured about the densest particle, then: 1) $E_{\text{therm}}/|E_{\text{grav}}| < 0.5$ to ensure that it is not thermally supported; 2) $(E_{\text{therm}} + E_{\text{rot}})/|E_{\text{grav}}| < 1$, which ensures that rotation also does not dominate; 3) $E_{\text{therm}} + E_{\text{rot}} + E_{\text{grav}} < 0$ to make sure that the region is bound; 4) the divergence of the particles' acceleration must be negative as this avoids creating sinks in regions under tidal disruption or just going through some transient effects (Bate et al., 1995; Lucas, 2015).

If these tests are passed, a sink particle is created at the centre of mass and with the centre of mass velocity of the particles within R_{critical} that where tested. The angular momentum is also added to the new particle. These steps ensure that linear and angular momentum are conserved.

Particles in the vicinity of a sink can be accreted provided that they fall within the outer accretion radius $R_{\text{acc,outer}}$ and pass several tests: 1) the particle has to be gravitationally bound; 2) the particle's specific angular momentum measured with respect to the sink must be less than that for a circular orbit with a radius equal to $R_{\text{acc,outer}}$; 3) when there are several sinks nearby, the particle must be accreted by the particle to which it is more tightly bound. If a particle falls within the inner accretion radius, it is automatically accreted. The sink gains the mass and linear momentum, and angular momentum of the accreted particles and its position is shifted to the centre of mass of the gas particle and sink. Appendix A describes a supernova injection method attached to this sink particles. It is presented as an appendix as its implementation is left for future work.

3

Model Galaxies

The following chapter introduces the theoretical background for modelling galaxies in numerical simulations and describes the models used in this work. The discussion is focused in spiral galaxies. §3.1 introduces an overview of observed density profiles in spiral galaxies. §3.2 describes the methodology for modelling a spiral galaxy in a simulation §3.3 presents the method for including a gaseous component in the model galaxy; §3.1.2 describes the physical parameters of the models used in this work. §3.4 summarises the results of testing the models in isolated evolution.

3.1 Modelling a Galaxy

3.1.1 Modelling the Mass Distribution in Disc Galaxies

Density Profile, Circular Velocity and Gravitational Potential

The density distribution can be expressed as the sum of the density profiles of its components:

$$\rho = \rho_{\rm dm} + \rho_{\rm d} + \rho_{\rm b} + \rho_{\rm gas}, \tag{3.1}$$

where $\rho_{\rm dm}$, $\rho_{\rm d}$, $\rho_{\rm b}$, and $\rho_{\rm gas}$ are the dark matter, stellar disc, bulge, and gas density profiles, respectively; $\rho_{\rm d}$ may include terms accounting for spiral arms and a central bar.

From Poisson's equation,

$$\nabla^2\Phi = 4\pi G\rho, \tag{3.2}$$

where Φ is the total gravitational potential and G is the gravitational constant, it is possible to express the total galactic potential as the sum of the potential of its individual components:

$$\Phi = \Phi_{\rm dm} + \Phi_{\rm d} + \Phi_{\rm b} + \Phi_{\rm g}, \tag{3.3}$$

where $\Phi_{\rm dm}$ is the dark matter potential, $\Phi_{\rm d}$ is the stellar disc potential, $\Phi_{\rm b}$ is the bulge potential, and $\Phi_{\rm g}$ is the potential of the gas distribution.

A useful quantity for characterising the potential is the circular velocity v_c, given by:

$$v_c^2(R) = R\frac{\partial\Phi}{\partial R} \tag{3.4}$$

where R is the galactocentric radius. This is interpreted as the velocity that a particle requires to follow a circular orbit of radius R. Substituting equation (3.3) in the above equation gives the circular velocity as the sum of the squares of the individual components' circular velocity:

$$v_c(R)^2 = v_{c_{\rm dm}}^2 + v_{c_{\rm d}}^2 + v_{c_{\rm b}}^2 + v_{c_{\rm g}}^2, \tag{3.5}$$

where $v_{c_{\rm dm}}$, $v_{c_{\rm d}}$, $v_{c_{\rm b}}$, $v_{c_{\rm g}}$ are the circular velocities of the dark matter halo, stellar disc, bulge and gas, respectively. The above equations establish the connection between the galaxy's mass density, gravitational potential, and circular velocity.

Stellar Disc and Spiral Arm Intensity Profiles

In spiral galaxies, observations show that the surface brightness of stellar discs follows an exponential profile:

$$I_d(R) = I_d(0)\exp(-R/R_d), \tag{3.6}$$

where $I_d(0)$ is the central intensity and R_d is the scale radius (e. g. de Vaucouleurs 1959; Freeman 1970; van der Kruit & Freeman 2011). In the vertical direction, Milky Way studies suggest an exponential decay (Jurić et al., 2008). In observations of edge-on galaxies, van der Kruit & Searle (1981) fitted the profile

$$I_d(R,z) = I_d(0)\exp\left(-\frac{R}{R_d}\right)\mathrm{sech}^2\left(\frac{z}{z_0}\right), \tag{3.7}$$

where z_0 is the vertical scale height. This was motivated by earlier works suggesting that the disc can be modelled as an isothermal sheet with a constant vertical velocity dispersion and scale height (e. g. Freeman 1978). This is also supported by the theoretical work by Camm (1950), which derives the sech^2 from applying the Collisionless Boltzmann Equation (equation 3.21) to a self-gravitating plane stellar system

The surface brightness of the spiral arms is usually expressed as a Fourier sum (e. g. Saraiva Schroeder et al. 1994):

$$\frac{I(R,\phi)}{\bar{I}(R)} = \sum_{m=1}^{\infty} A_m(R)e^{im(\phi-\phi_m)}, \tag{3.8}$$

where $\bar{I}(R)$ is the average intensity at a radius R, m is the spiral mode and A_m its amplitude; ϕ_m is a phase shift. The shape of the arms is usually characterised by a logarithmic curve, which has the form:

$$r(\phi) \propto e^{\tan\alpha\phi}, \tag{3.9}$$

where α is the pitch angle, a measure of the arm's "openness". More detailed models incorporate this into equation (3.8) in order to fit α to surface brightness profiles (e. g. Seigar et al. 2005). An example of a logarithmic spiral arm model is given in Figure 3.1. These profiles suggest similar functions for the actual mass density profiles $\rho(R,z)$. Although this may not be directly extracted from extragalactic observations, Milky Way star count studies find density profiles in good agreement with the mathematical forms of equations (3.6) and (3.7) (Bahcall & Soneira, 1980; Jurić et al., 2008).

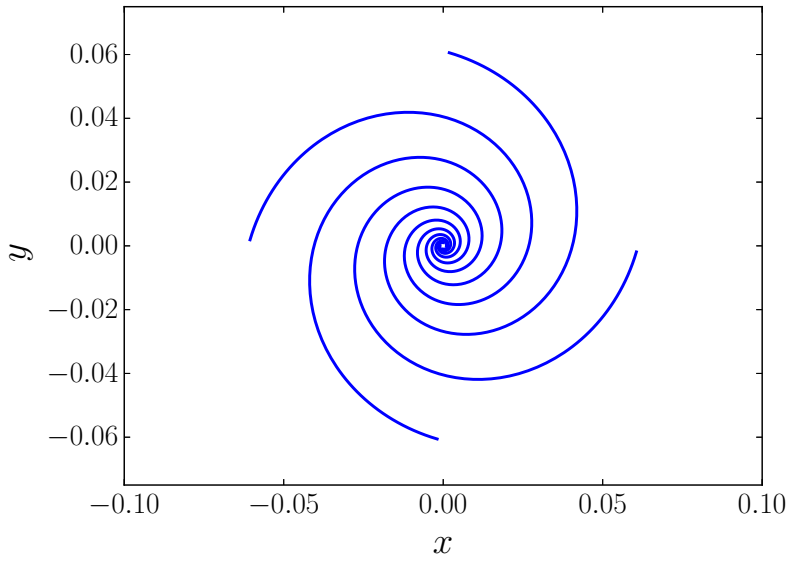

Figure 3.1: Logarithmic spiral arm model for a perturbation with $N = 4$ arms and a pitch angle $\alpha = 15°$. Positions are in arbitrary units.

Bulge

The bulge surface brightness is usually modelled by a Sérsic (1963) profile:

$$I_b(R) = I_{b_e} \exp\left(-b_n\left[(R/R_e)^{1/n} - 1\right]\right), \tag{3.10}$$

where I_{b_e} is the intensity at the effective radius R_e and b_n is a constant depending on the parameter n. The disc and bulge parameters are usually obtained by finding the best-fit parameters for the surface brightness profiles (e. g. Binney & Merrifield 1998; van der Kruit & Freeman 2011). Figure 3.2 shows an example of the bulge and disc intensity profiles.

Gas Disc

Milky Way observations show that the HI distribution in the inner galaxy ($R < 12.5$ kpc) has a roughly constant surface density ($\Sigma \approx 10\,\mathrm{M_\odot\,pc^{-2}}$) and in the outer galaxy it can be modelled by an exponential profile (Kalberla & Dedes, 2008). The molecular gas, traced by CO observations, tends to have a more pronounced radial decay. From Milky Way data described in Heyer & Dame (2015), the surface density tends to be low in the inner regions and reaches a peak value of $\approx 5\,\mathrm{M_\odot\,pc^{-2}}$ around $R = 5$ kpc and then decays with distance.

Using data from the CO HERACLES and HI THINGS surveys, Bigiel & Blitz (2012) select a

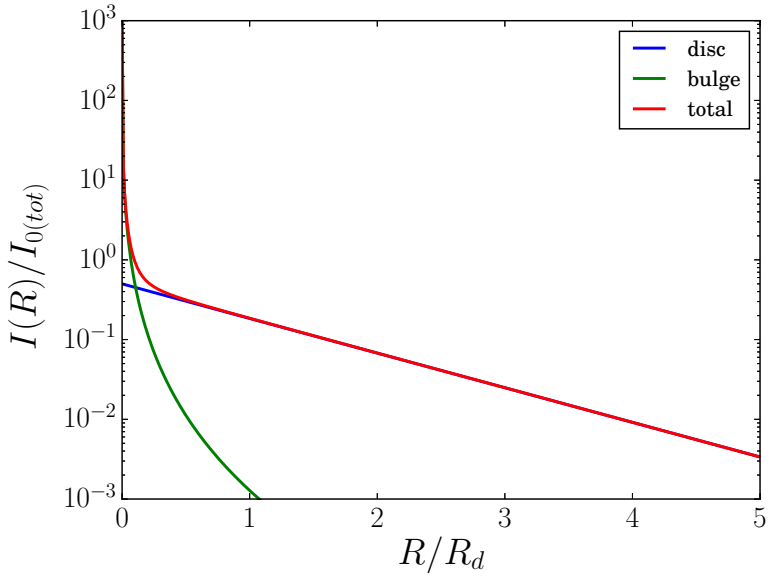

Figure 3.2: Example of the intensity profiles of the exponential disc and the Sersic profile normalised to the total central intensity. The radius is scaled to the disc's scale length R_d. The bulge usually appears as a central cusp feature in intensity profiles.

sample of 33 local galaxies and analyse the HI, molecular, and combined surface density profiles. Their results show that the HI distribution tends to be rather flat with surface densities varying between $1-10\,M_\odot\,pc^{-2}$. The molecular gas has an exponential decay with central densities reaching values of up to $100\,M_\odot\,pc^{-2}$. The combined HI plus molecular surface density profile is fitted by an exponential which, according to Bigiel & Blitz (2012), seems to be a property of many galaxies. Druard et al. (2014) find a similar trend in the local spiral M33. These results suggest that an exponential surface density profile is a reasonable model for the gas in a disc galaxy.

In terms of kinematics, gas observations provide a measurement of the circular velocity of a galaxy as gas is expected to be in rotational equilibrium. For a sample of nearby galaxies, typical circular velocity values are in the range of $v_c \approx 100-300\ km\,s^{-1}$ (Sofue & Rubin, 2001). Circular velocity data is useful for extracting information about the mass distribution of the different galaxy components via equations (3.4) and (3.5). The more massive the galaxy, the higher the circular velocity.

Dark Matter Halo

The dark matter profile has been more challenging to address observationally. Its existence is inferred from the flatness of galaxy rotation curves measured at large radii. Rotation curve studies using the decomposition of equation (3.5) have shown that the circular velocity calculated with the observed matter distribution is not sufficient to fit the measured velocities. This suggests that an additional "dark" component is needed to explain the observed rotation curves (e. g. Zwicky 1937; Rubin et al. 1980; Sofue & Rubin 2001; Sofue et al. 2009; Sofue 2017).

Galactic dark matter profiles have been explored in cosmological N-body simulations. The density profile is assumed to follow the two-power functional form (following the notation of Binney & Tremaine 2008):

$$\rho(r) = \frac{\rho_0}{(r/r_s)^{\alpha}(1 + r/r_s)^{\beta-\alpha}}, \tag{3.11}$$

where ρ_0 is the central density, r_s is a scale radius, and α and β are constants. Cosmological simulations by Navarro et al. (1997) found a profile with $\alpha = 1$ and $\beta = 3$, which has a central cusp in the density. However, Einasto (1965, 1969) also proposed the profile

$$\rho(r) = \rho_e \exp\left(-d_n\left[(r/r_e)^{1/n} - 1\right]\right). \tag{3.12}$$

The above equation follows the notation of Merritt et al. (2006), where r_e is the effective radius and ρ_e is the density at $r = r_e$; d_n is a constant that depends on the parameter n. Merritt et al. (2006) find that the Einasto profile also provides a very good fit to the density profiles of a set of halos derived from cosmological N-body simulations. Other works have assumed simpler models such as the (Plummer, 1911) profile (e. g. Revaz et al. 2009). From an observational point of view, a given dark matter profile is assumed and it is characterised from best-fit parameters of rotation curves (e. g. Hague & Wilkinson 2015; Sie Kam et al. 2015).

3.1.2 Physical Parameters of Model Galaxies

In this work, the large-scale dynamics are studied in a global model based on the local galaxy M33. The small-scale dynamics are analysed in a simulation of a region of gas flowing into a spiral arm of a Milky Way model derived from Bonnell et al. (2013), which has resolution

to explore the small scale dynamics and to compare the results with the global model. This subsection very briefly summarises the physical parameters of M33 and the Milky Way.

M33 Physical Parameters

M33 is an interesting galaxy because it has a relatively flocculent morphology and is nearly face on, which has allowed a number of surveys of gas and star formation properties in different parts of the object (e. g. Gratier et al. 2010; Druard et al. 2014).

Early photometric studies found that the stellar surface brightness follows an exponential profile with $R_d = 1.2 \pm 0.2$ kpc, and identified a central bulge-like component following a $(R/R_e)^{1/4}$ profile with $R_e = 2.0$ kpc (Regan & Vogel, 1994). Recent works find updated values: $R_d = 1.7$ kpc (Seigar, 2011) and $R_d = 1.8$ kpc (Sie Kam et al., 2015). In terms of stellar mass, Corbelli & Salucci (2000) find $M_d = (3.4 \pm 0.8) \times 10^9 M_\odot$ from a rotation curve analysis. Corbelli (2003) find a value in the range $M_d \approx (3-6) \times 10^9 M_\odot$; Corbelli et al. (2014) constrain the value to $M_d = 4.9^{+0.5}_{-0.7} \times 10^9 M_\odot$, which still falls in the range of earlier works.

In terms of spiral structure, de Vaucouleurs et al. (1991) classified it as a SA(s)cd which means no central bar, no ring structures and relatively loose arms. Puerari (1993) suggested an inner two-armed structure up to a projected radius of 28 arcmin and more chaotic structure at larger radii. CO maps show fairly irregular structure (Hughes et al., 2013).

It is a relatively gas rich galaxy. For example, Corbelli & Salucci (2000) report that the atomic hydrogen mass is $M_{HI} \approx 1.8 \times 10^9 M_\odot$ and the molecular gas mass is $M_{H2} \approx 1.9 \times 10^8 M_\odot$. Another study suggests that the total gas mass (atomic+molecular) is $M_{\rm gas} \approx 3 \times 10^9 M_\odot$, with a radial scale length slightly larger than that of the stellar disc (Corbelli, 2003).

There is some discussion about the presence of a bulge and bar. Regan & Vogel (1994) find a clear bulge component and Stephens & Frogel (2002) show that the central stellar population is different to the disc and is consistent with bulge properties. Hernández-López et al. (2009) suggest that existence of a central bar with a scale of length of ≈ 0.8 kpc, but this is sensitive to projection effects. The bulge mass is estimated to be $M_b = (1.14 \pm 0.14) \times 10^8 M_\odot$, with a Sérsic index $n = 1$ and effective radius $R_e = 0.39 \pm 0.03$ kpc, which corresponds to a bulge-to-disc ratio $B/D = 0.03$ (Seigar, 2011).

A dark matter halo component is included in models fitting the rotation curve, which tops at around 120 $\mathrm{km\,s^{-1}}$. Corbelli & Salucci (2000) show that $M_h > 5 \times 10^{10} M_\odot$ and, assuming

a (Navarro et al., 1997) profile, the concentration parameter, which is defined as $c = R_v/R_s$ where R_v is the virial radius, is $c \approx 5$. Seigar (2011) find that: $M_h = (2.2 \pm 0.1) \times 10^{11} M_\odot$ and $c = 4.0 \pm 1.0$, and a scale radius $R_h \approx 39$ kpc assuming also a NFW profile. Corbelli et al. (2014) find higher values: $M_h = 3.9^{+1.0}_{-0.6} \times 10^{11} M_\odot$ and $c = 10 \pm 1$ for a NFW profile, which agrees with the mass found by Seigar (2011). Hague & Wilkinson (2015) also find that a NFW profile fits the rotation curve with $R_s \approx 32.6$ kpc. Constraining the halo parameters of M33 is still an ongoing line of research (Sie Kam et al., 2015).

The final choice of parameters are presented in sections 3.2.3 and 3.2.2. This work does not seek to build a model exactly reproducing M33. The aim is to use this as a model galaxy with realistic parameters that produces a flocculent morphology.

Milky Way Physical Parameters

The spiral arm simulation is described in Chapter 5. The model galaxy has physical parameters representative of the Milky Way, briefly reviewed below.

The stellar disc's density is assumed to follow an exponential profile (e. g. Bahcall & Soneira 1980; van der Kruit & Freeman 2011). Results compiled in the review of van der Kruit & Freeman (2011) suggest that the scale radius R_d is in the range $3-6$ kpc; Binney & Tremaine (2008) give a value of $R_d = 2.5 \pm 0.5$ kpc; the model of Klyping et al. (2002) estimate a value in the range of $3.0-3.5$ kpc. Churchwell et al. (2009) find that $R_d = 3.9 \pm 0.6$ kpc based on observations of red-clump giants. The stellar disc mass is estimated to be in the range $(3.5-6) \times 10^{10} M_\odot$ (Klyping et al., 2002); (Sofue et al., 2009) find that $M_d \approx 6.5 \times 10^{10} M_\odot$. In terms of gas content, the HI mass is estimated as $M_{HI} \approx 8 \times 10^9 M_\odot$ and the warm ionised gas mass is $\approx 2 \times 10^9 M_\odot$ (Kalberla & Kerp, 2009). The molecular gas mass, according to the model of Kalberla & Kerp (2009), is calculated to be $\approx 2.5 \times 10^9 M_\odot$; Heyer & Dame (2015) estimate that the total H_2 mass is $M_{H_2} = (1.0 \pm 0.3) \times 10^9 M_\odot$. Regarding the bulge, Sofue et al. (2009) find a mass $M_b \approx 1.8 \times 10^{10} M_\odot$, modelled by an $(r/R_e)^{1/4}$ profile with $R_e = 0.5$ kpc. Klyping et al. (2002) and Portail et al. (2015) also estimate that $M_b \sim 10^{10} M_\odot$.

The spiral arms of the Milky Way are usually modelled by 4 long arms with a pitch angle in the range $10-15°$ (Vallée, 2005, 2017). Information on the spiral arms is obtained either from tracing molecular gas with kinematic distances (e. g. Roman-Duval et al. 2009), using trigonometric parallaxes of massive star forming regions (e. g. Reid et al. 2009), which are

more reliable than the kinematic estimate (see Chapter 5)), or by fitting dynamical models to features in $l-v$ (galactic longitude – velocity diagrams) (e. g. Englmaier 2000).

The Milky Way rotation curve is mostly flat at large radii with values between $200-220$ $\mathrm{km\,s^{-1}}$. Circular velocity fitting models by Sofue et al. (2009) decomposing the bulge, disc and halo, estimate that the halo mass integrated up to 20 kpc is $1.24\times10^{11}M_{\odot}$; Klyping et al. (2002) find a halo mass in the range of $(1-2)\times10^{12}M_{\odot}$.

The Milky Way simulations analysed in this work are based on the parameters of Dobbs et al. (2006), which assumes a nearly flat rotation curve at 220 $\mathrm{km\,s^{-1}}$. More details are given in §3.2.3 and Chapter 5.

3.2 Methods for Setting up Galaxy Simulations

This section introduces the two main approaches to set up a galaxy simulation. One method is to generate initial conditions for an N-body simulation as described in §3.2.1 and §3.2.2. Another approach, outlined in §3.2.3, is to model the galactic potential by specifying an axisymmetric potential representing the overall dark matter and stellar components and adding a spiral arm perturbation.

3.2.1 The Distribution Function and Collisionless Systems

To set up an N-body simulation, it is desirable to generate particle distributions with density profiles representative of observed galaxies. In this case, the spiral arms grow naturally and the model can be tuned to produce either grand-design galaxies or flocculent discs. However, such simulations may be computationally expensive. An N-body model requires knowledge of the system's distribution function to sample the particles' positions and velocities.

A problem in building N-body models is to obtain particle distributions that are representative of a galaxy's observed matter distribution and kinematics and that remain stable for several galactic rotations in a simulation. As a star orbits a galaxy, its path is gradually modified by interactions with neighbouring stars. This occurs on a relaxation timescale,

$$t_r \approx \frac{0.1N}{\ln N} t_c, \tag{3.13}$$

which depends on the number of particles N and the crossing time $t_c = L/v$; v is a character-

istic particle velocity and L is the scale of the system.

For self-gravitating systems, the relaxation time introduces a distinction between collisional and collisionless particle systems. For galaxies, $t_r \gg t_c$ and much larger than their typical ages, thus it is possible to treat them as collisionless systems. This implies that the Collisionless Boltzmann Equation can be used to find a distribution function for generating initial conditions for N-body models. This is described in more detail in this subsection.

The Distribution Function

A system's dynamical state is described by its phase-space coordinates: $(\mathbf{q}, \mathbf{p})$, where $\mathbf{q}$ and $\mathbf{p}$ are the generalised position and momentum vectors, respectively. A particle system can be represented in phase-space by the distribution function (DF) $f(\mathbf{q}, \mathbf{p})$, which is defined such that the number of particles δN in an element of hypervolume $\mathrm{d}^3\mathbf{q}\mathrm{d}^3\mathbf{p}$ is (e. g. Binney and Tremaine 2008):

$$\delta N = f(\mathbf{q}, \mathbf{p})\mathrm{d}^3\mathbf{q}\mathrm{d}^3\mathbf{p}. \tag{3.14}$$

The mass density as a function of position is obtained by multiplying equation (3.14) by the particle mass and integrating with respect to $\mathbf{p}$,

$$\rho(\mathbf{q}) = \int mf(\mathbf{q}, \mathbf{p})\mathrm{d}^3\mathbf{p}. \tag{3.15}$$

Then, integrating this with respect to $\mathbf{q}$ gives the system's total mass.

The Collisionless Boltzmann Equation

If collisions are neglected and mass conservation is assumed, it is possible to obtain (e. g. Binney & Tremaine 2008):

$$\frac{\partial f}{\partial t} + \nabla_{\mathbf{X}} \cdot (f\dot{\mathbf{X}}) = 0, \tag{3.16}$$

where $\mathbf{X} = (\mathbf{q}, \mathbf{p})$ is the state vector. This is an expression for the CBE and is analogous to the continuity equation. When collisions are not negligible, source and sink terms should be included in the right-hand-side of equation (3.16). By expanding the divergence and using the Lagrangian derivative, it can be rewritten as:

$$\frac{\mathrm{D}f}{\mathrm{D}t} + f\nabla_{\mathbf{X}} \cdot \dot{\mathbf{X}} = 0. \tag{3.17}$$

For a Hamiltonian system,

$$\dot{\mathbf{p}} = -\frac{\partial H}{\partial \mathbf{q}},\ \dot{\mathbf{q}} = \frac{\partial H}{\partial \mathbf{p}}, \tag{3.18}$$

from which

$$\nabla_{\mathbf{X}} \cdot \dot{\mathbf{X}} = \nabla_{\mathbf{q}} \cdot \dot{\mathbf{q}} + \nabla_{\mathbf{p}} \cdot \dot{\mathbf{p}} = \frac{\partial}{\partial \mathbf{q}} \frac{\partial H}{\partial \mathbf{p}} - \frac{\partial}{\partial \mathbf{p}} \frac{\partial H}{\partial \mathbf{q}} = 0 \tag{3.19}$$

This reduces equation (3.17) to

$$\frac{\mathrm{D}f}{\mathrm{D}t} = 0 \tag{3.20}$$

which means that the DF is constant along a particle's path (Binney and Tremaine 2008). Given that $\dot{\mathbf{X}} = (\dot{\mathbf{q}}, \dot{\mathbf{p}}) = (\dot{\mathbf{q}}, -\nabla_{\mathbf{q}}\Phi)$, equation (3.16) becomes:

$$\frac{\partial f}{\partial t} + \dot{\mathbf{q}} \cdot \left(\frac{\partial f}{\partial \mathbf{q}}\right) - \left(\frac{\partial \Phi}{\partial \mathbf{q}}\right) \cdot \left(\frac{\partial f}{\partial \mathbf{p}}\right) = 0. \tag{3.21}$$

Implications of the CBE for the N-body problem

With the Hamiltonian $H = 1/2v^2 + \Phi(\mathbf{x})$, the CBE can be expressed in Cartesian positions and velocities (e. g. Binney & Tremaine 2008):

$$\frac{\partial f}{\partial t} + \mathbf{v} \cdot \left(\frac{\partial f}{\partial \mathbf{x}}\right) - \left(\frac{\partial \Phi}{\partial \mathbf{x}}\right) \cdot \left(\frac{\partial f}{\partial \mathbf{v}}\right) = 0. \tag{3.22}$$

This is a first-order linear partial differential equation and its behaviour can be studied with the method of characteristics (e. g. Courant & Hilbert 1962). Given a first-order linear PDE of the form

$$\sum_{i=1}^{n} K_i \frac{\partial f}{\partial x_i} = L, \tag{3.23}$$

where $K_i = K_i(x_i, ..., x_n)$, $L = L(x_i, ..., x_n)$, f is the function of interest, and $\frac{\partial}{\partial x_i}$ is the partial derivative with respect to the i-th variable, the characteristic curves are given by

$$\frac{\mathrm{d}x_i}{\mathrm{d}s} = K_i(x_1, ..., x_n), \tag{3.24}$$

which are a function of a parameter s. The solution to this system of differential equations gives the behaviour of the solution along a curve.

To picture the idea, equation (3.23) is written as

$$\sum_{i=1}^{n} K_i \frac{\partial f}{\partial x_i} - L = 0, \tag{3.25}$$

which can be expressed as the dot product of a vector of the coefficients and L in the last component $\langle K_1, ..., K_n, L\rangle$ and of derivatives with a -1 in the last component: $\langle \partial f/\partial x_1, ..., \partial f/\partial x_n, -1\rangle$. The last vector is essentially the normal to the solution surface, so the first has to be tangent to this surface. This means that the characteristic curves trace the surface of the solution.

Applying this method to the CBE means that the coefficients for the spatial derivatives $(\partial/\partial x_i)$ are the velocities v_i, and for the velocity derivatives $(\partial/\partial v_i)$ the coefficients are the local acceleration components expressed as $\partial\Phi/\partial x_i$. The coefficient for $\partial f/\partial t$ is 1, which means that the characteristics can be parametrised in terms of time. Then, the characteristic curves become

$$\frac{\mathrm{d}x_i}{\mathrm{d}t} = v_i, \tag{3.26}$$

$$\frac{\mathrm{d}v_i}{\mathrm{d}t} = a_i = -\frac{\partial\Phi}{\partial x_i}, \tag{3.27}$$

$$\frac{\mathrm{d}f}{\mathrm{d}t} = 0 \tag{3.28}$$

where i corresponds to each coordinate (x, y, z). The first two sets of equations are simply the equations of motion of the particles subject to the potential Φ. The third equation states that f is constant along a curve, which is another statement of equation (3.20) (e. g. King 1990; Dosch & Zank 2016).

This result has an important implication for the N-body problem. It shows that integrating the equations of motion of an ensemble of particles sampled from a given DF as an N-body simulation is a method for solving the CBE (Binney & Tremaine, 2008). This means that if the DF of a galaxy model is specified, it can be used to generate the initial conditions for an N-body simulation of this system. The question becomes how to specify such a DF and determine if it will be in equilibrium.

Equilibrium solutions of the CBE

A given DF satisfying the CBE may not necessarily be a steady-state solution. An isolated galaxy can be assumed to be in a steady-state (King, 1990). For this reason, in galaxy simulations it

is of interest to find a steady-state DF.

As described in Courant & Hilbert (1962), a PDE of the form of equation (3.23) has a solution that depends only on $n-1$ parameters

$$C_i = G_i(x_i, ..., x_n), \tag{3.29}$$

where n is the number of independent variables. The function G_i remains constant along the characteristic curves and the solution to the PDE can be expressed as a function depending on these integrals: $F(G_1, ..., G_{n-1})$.

For the CBE, $x_i \rightarrow (\mathbf{x}, \mathbf{v})$ and G becomes a function of position and velocity that is constant along the particle's path. Such quantities are the integrals of motion of the orbit. Then, a distribution function that satisfies the CBE can be expressed as a function of the integrals of motion (e. g. King 1990).

The Jeans (1915) theorem provides a useful result for specifying an equilibrium DF. It states that any DF that depends only on the integrals of motion will be a steady-state solution of the CBE. The strong Jeans theorem says that for a galaxy with a potential that allows orbits such that most of these are regular, then the DF can be expressed in terms of three independent isolating integrals of motion (see Binney & Tremaine (2008) for a discussion).

This provides a useful principle for specifying a DF for modelling particle distributions in terms of integrals such as the energy, the angular momentum, or the vertical component of the angular momentum. However, its application for full galaxy models is not straightforward and has been widely studied in the literature. For example, Shu (1969) presented a DF for a razor-thin disc as a model for stellar discs. A more detailed disc DF is proposed in Dehnen (1999). Hernquist (1990) obtained a DF for a density profile assumed to be representative of spherical systems such as galactic bulges. Osipkov (1979) and Merritt (1985) explored DFs for spherical systems applicable to galactic halos. Examples of full galaxy models based on combinations of the individual DFs for the bulge, disc, and halo have been proposed in Kuijken & Dubinski (1995) and McMillan & Dehnen (2007), to mention some examples.

3.2.2 N-body Model

In this work, the approach of McMillan & Dehnen (2007) for generating initial conditions for an N-body model of a galaxy is used. This method is implemented in the code mkgalaxy developed by McMillan & Dehnen (2007). This is publicly available via the NEMO website (Teuben, 1995)[1]. The steps of this method are summarised in the following subsections.

Halo and Bulge Initialisation

The bulge and halo densities are described by a spherically symmetric two-power model given by

$$\rho(r) = \frac{\rho_0}{x^{\gamma_0}(x^\eta + 1)^{(\gamma_\infty - \gamma_0)/\eta}} T(r/r_t), \tag{3.30}$$

where $x = r/r_s$; r_s is a scale radius, γ_0 and γ_∞ are the profile's inner and outer slopes (in $\log\rho$ vs. $\log r$), η is a parameter controlling the transition from the inner to the outer profile. $T(r/r_t)$ is a truncation function scaled by the length r_t useful for profiles with a non-converging integrated mass such as the NFW profile. The standard values used in McMillan & Dehnen (2007) for the halo density are $\gamma_0 = 1$, $\gamma_\infty = 3$, $\eta = 1$, which produces a NFW profile; and for the bulge, $\gamma_0 = 1$, $\gamma_\infty = 4$, $\eta = 1$, which produces a Hernquist (1990) profile. These parameters are used in the present work. Figure 3.3 shows these functions normalised to the central density.

The rotation curve for the NFW profile is given by

$$v_{c\,h}^2(r) = \left(\frac{GM_h}{R_h}\right)\left(\frac{1}{g(c)}\right)\frac{\ln(1+x_h) - x_h/(1+x_h)}{x_h}, \tag{3.31}$$

where M_h is the halo mass, R_h the scale radius, $x_h = r/R_h$ and $g(c) = \ln(1+c) - c/(1+c)$, and c is the concentration parameter. The rotation curve for the Hernquist (1990) profile is

$$v_{c\,b}^2(r) = \frac{GM_b}{R_b}\frac{x_b}{(1+x_b)^2} \tag{3.32}$$

where M_b is the bulge mass, R_b the scale radius, $x_b = r/R_b$. Model parameters are specified based on approximately fitting M33's circular velocity.

McMillan & Dehnen (2007) sample the particle velocities from a DF based on the models

[1] NEMO – A Stellar Dynamics Toolbox, website by P. Teuben: teuben.github.io/nemo/

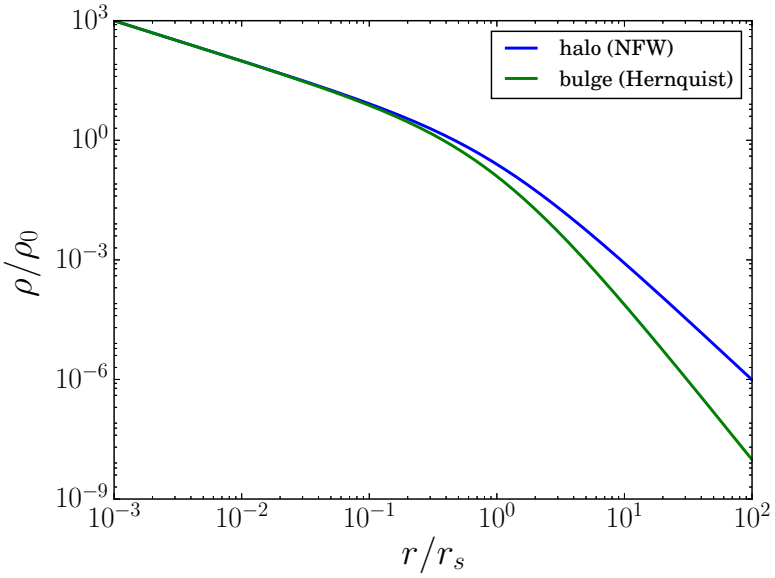

Figure 3.3: Density profiles for the target halo and bulge models used in this work. The density is normalised to the central density and the radius to the scale radius. The transition between the inner and outer slopes occurs around $r = r_s$.

of Cuddeford (1991); Osipkov (1979); Merritt (1985). These extend the Eddington (1916) inversion method, where the DF is obtained from an integral depending on the density profile, to allow an anisotropic velocity dispersion in a spherical particle system. This is motivated by works suggesting non-isotropic kinematics in bulges (e. g. Hernquist 1993)

The Cuddeford (1991) DF is written as:

$$f(\mathscr{E}, L) = L^{2\alpha} f(Q), \tag{3.33}$$

where $Q = \mathscr{E} - L^2/(2r_a^2)$, r_a is the anisotropy radius and $\mathscr{E} = \Psi - 1/2v^2$, which is defined as the relative energy; $\Psi = -\Phi(r) + \Phi_0$ is the relative potential where Φ is the gravitational potential and Φ_0 is an arbitrary constant. As described by Cuddeford (1991), the density is given by the DF integral with respect to velocity, written as:

$$\rho_2(\Psi) = \lambda(\alpha) \int_0^{\Psi} (\Psi - Q)^{\alpha+1/2} f(Q) dQ, \tag{3.34}$$

where

$$\lambda(\alpha) = 2^{\alpha+3/2} \pi^{3/2} \frac{\Gamma(\alpha+1)}{\Gamma(\alpha+3/2)}, \tag{3.35}$$

and

$$\rho_2 = \frac{(1+(r/r_a)^2)^{\alpha+1}}{r^{2\alpha}}\rho \tag{3.36}$$

Because the integral of $f(\mathscr{E}, L)$ is a double integral, the function $\lambda(\alpha)$ results from evaluating the integral with respect to L, and ρ_2 results from variable substitutions to write the integral in the form equation (3.34).

By deriving the reduced density ρ_2 with respect to Ψ, it is possible to transform equation (3.34) into an Abel integral equation which can be inverted (e. g. Eddington 1916) to obtain (Cuddeford, 1991; McMillan & Dehnen, 2007):

$$f(Q) = \frac{\sin[(n-1/2-\alpha)\pi]}{\pi\lambda(\alpha)\eta(\alpha)}\frac{\mathrm{d}}{\mathrm{d}Q}\int_0^Q \frac{\mathrm{d}^n\rho_2}{\mathrm{d}\Psi^n}\frac{d\Psi}{(Q-\Psi)^{\alpha+3/2-n}}, \tag{3.37}$$

where

$$\eta(\alpha) = \begin{cases} (\alpha+1/2)(\alpha-1/2)...(\alpha+3/2-n) & \text{if } \alpha > -1/2 \\ 1 & \text{if } -1 < \alpha \leq -1/2, \end{cases} \tag{3.38}$$

The system's anisotropy is measured by the parameter of Binney (1980), which for the above formulation becomes (Cuddeford, 1991; McMillan & Dehnen, 2007):

$$\beta(r) = 1 - \frac{\sigma_t^2}{\sigma_r^2} = \frac{r^2 - \alpha r_a^2}{r^2 + r_a^2} \tag{3.39}$$

where σ_t and σ_r are the tangential and radial velocity dispersions. This shows that α controls the distribution's anisotropy.

According to McMillan & Dehnen (2007), this approach is advantageous in several ways: 1) the DF derived in Equation (3.37) is exact for a spherical particle distribution and will maintain the density profile in a simulation; 2) it does not assume a local Gaussian velocity distribution and velocities are directly sampled from the DF; 3) deriving the DF via the inversion method provides a powerful tool for generating distributions for different density profiles; 4) the DF is derived from a phase-space integration, which makes it applicable to multi-component spherical systems, this allows each component to be treated individually provided that the relative potential Ψ refers to the total potential of the multi-component system.

In the method of McMillan & Dehnen (2007), the halo and bulge are initialised using the

DF in equation (3.37), where the relative potential includes the total potential of the galaxy. For the halo and bulge, the potential can be evaluated exactly for the chosen profiles. The contribution of the disc is calculated with the mono-pole term of the corresponding multi-pole expansion. Positions are sampled from the radial density profile using a sampling technique based on inverting the cumulative mass function. Velocities are sampled using an acceptance-rejection method.

Once the halo and bulge particle distributions are ready, these are allowed to evolve in the disc's potential, which is gradually grown until its full form is attained. The particle distribution is evolved further in time to allow it to settle (McMillan & Dehnen, 2007).

Disc Initialisation

In the method of McMillan & Dehnen (2007), the stellar disc density is represented by a radial exponential profile and a vertical isothermal sheet:

$$\rho(R,z) = \frac{M_d}{4\pi R_d^2 z_d} \exp\left(-\frac{R}{R_d}\right) \mathrm{sech}^2\left(\frac{z}{z_d}\right), \tag{3.40}$$

where M_d is the disc's mass R_d is the scale radius and z_d is the scale height. This profile produces an exponential surface density profile:

$$\Sigma(R) = \int_{-\infty}^{\infty} \rho(R,z)dz = \frac{M_d}{2\pi R_d^2} \exp\left(-\frac{R}{R_d}\right), \tag{3.41}$$

which is consistent with the observational profiles described in §3.1.1.

The rotation curve for the above surface density profile is given by

$$v_{c\,d}^2 = \frac{2GM_d}{R_d}\left(\frac{R}{R_d}\right)^2 \left[I_0\left(\frac{R}{R_d}\right)K_0\left(\frac{R}{R_d}\right) - I_1\left(\frac{R}{R_d}\right)K_1\left(\frac{R}{R_d}\right)\right], \tag{3.42}$$

where I_n and K_n are modified Bessel functions of the first and second kind, respectively (Binney & Tremaine, 2008). The disc, bulge, and halo parameters are determined by ensuring that the model total rotation curve ($v_c^2 = v_{c\,d}^2 + v_{c\,b}^2 + v_{c\,h}^2$) reasonably fits the galaxy of interest and are given as input to the code mkgalaxy.

The disc stability is characterised by the Toomre (1964) parameter:

$$Q(R) = \frac{\sigma_R(R)\kappa(R)}{3.36G\Sigma(R)}, \tag{3.43}$$

where σ_R is the radial velocity dispersion, $\kappa(R)$ is the epicyclic frequency:

$$\kappa^2(R) = R\frac{\mathrm{d}\Omega^2}{\mathrm{d}R} + 4\Omega^2, \tag{3.44}$$

where $\Omega = v_c(R)/R$ is the angular frequency. The radial dispersion σ_R is assumed to follow an exponential profile:

$$\sigma_R \propto \exp\left(-\frac{R}{R_\sigma}\right), \tag{3.45}$$

where R_σ is the scale radius of the dispersion profile and a value is specified for $Q(R_\sigma)$. This choice produces a radial dispersion profile more consistent with observations of disc galaxies. For the vertical velocity dispersion σ_z, it is assumed to follow the profile of an isothermal sheet, and it is derived from:

$$\sigma_z^2(R) = \pi G z_d \Sigma(R), \tag{3.46}$$

The vertical scale height of the disc is assumed to be constant with radius.

The disc DF is based on the one proposed in Dehnen (1999) and is expressed as:

$$f_d(E_\parallel, E_\perp, L_z) = \frac{\Omega(R_{E_\parallel})\tilde{\Sigma}(R_{E_\parallel})}{(2\pi)^{3/2}\kappa(R_{E_\parallel})}\frac{1}{z_d\sigma_z(R_{E_\parallel})}\exp\left(-\frac{E_\perp}{\sigma_z^2(R_\parallel)}\right)\frac{1}{\tilde{\sigma}_R^2(R_{E_\parallel})}\exp\left(\frac{\Omega(R_{E_\parallel})[L_z - L_c(R_{E_\parallel})]}{\tilde{\sigma}_R^2(R_{E_\parallel})}\right), \tag{3.47}$$

where $R_{E_\parallel}$ is the radius of the circular orbit with energy $E_\parallel$, L_c is this orbit's angular momentum, and L_z is the vertical angular momentum. $R_{E_\parallel}$ approximates the mean orbital radius, which according to McMillan & Dehnen (2007) is a better definition that ensures that the radial profiles better resemble the target ones. This DF has the advantage that the target surface density and radial velocity dispersion profile are explicitly introduced through $\tilde{\Sigma}(R)$ and $\tilde{\sigma}_R(R)$.

As described by McMillan & Dehnen (2007), planar velocity components are sampled with an iterative approach where a radial position is first sampled from the radial density profile and the orbital energy $E_\parallel$ is evaluated. Then, a random value of L_z is sampled from the range accessible to that radius and the orbit is integrated for a radial period to evaluate the factor $\kappa(R)/\omega_R$, which is used to determine the number of particles sampled per orbit. Once this is determined, positions and velocities in cylindrical coordinates are sampled. This process is

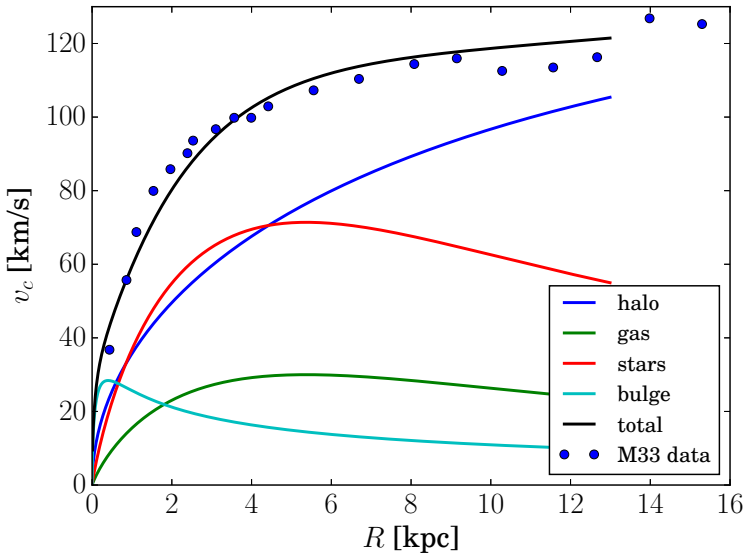

Figure 3.4: Model rotation curve for the M33 model based on the parameters of Table 3.1 compared to observational data extracted from (Corbelli & Salucci, 2000; Seigar, 2011).

repeated until the total number of particles is sampled. This is repeated until the radial surface density and velocity dispersion profiles are an acceptable match to the target profiles. Finally, the vertical positions and velocities are sampled from an isothermal sheet with constant z_d. Once the final disc population is obtained, it is inserted into the halo and bulge distribution and the model is ready for evolution.

Model Parameters

The parameters for the N-body model are based on those reviewed in §3.1.2 for M33. After several tests, the values shown in Table 3.1 were selected. The total disc's mass is divided into an 85% in stellar mass and 15% in gas mass. The rotation curve is shown in Figure 3.5.

3.2.3 Analytic Potential Model

Another approach for performing galaxy simulations is to specify a galaxy's potential using analytic expressions representing the contribution from the different components and allow either test particles or gas to move in this potential. It offers the advantage of focusing the computational efforts in the gas dynamics.

Table 3.1: Model Parameters Representative of M33 for N-body Model

Disc	
Profile	exp-sech^2
$M_d(10^9\,M_\odot)$	9.0
R_d(kpc)	2.5
z_d(kpc)	0.2
$Q(R_r)$	1.5
$m(R = 7\text{kpc})$	5.6
$T(R = 2R_d)(Myr)$	284
f_g	15%
$f_\star$	85%
Bulge	
Profile	Hernquist
$M_b(10^8\,M_\odot)$	3.0
R_b(kpc)	0.4
Halo	
Profile	NFW
$M_h(10^{11}\,M_\odot)$	5.7
R_h(kpc)	33.8
c	4.0

The potential of a galaxy is modelled by the combination of two terms:

$$\Phi_{\text{galaxy}} = \Phi_{\text{axysymmetric}} + \Phi_{\text{spiral arm}} \tag{3.48}$$

where the first term corresponds to the potential of the overall axisymmetric stellar and dark matter distribution and the second corresponds to the spiral arms.

In this work, the axisymmetric component is represented by a logarithmic potential:

$$\Phi(R,z) = \frac{1}{2}v_0^2 \ln\left(R^2 + (z/z_q)^2 + R_c^2\right), \tag{3.49}$$

where R_c is a characteristic radius, z_q is a vertical scale factor, and v_0 is a velocity parameter. The rotation curve for this potential is:

$$v_c(R) = v_0 \frac{R}{\sqrt{R^2 + R_c^2}}, \tag{3.50}$$

which shows that v_0 is the circular velocity at $R >> R_c$. This potential produces a rotation curve that is mostly flat for $R > R_c$.

The spiral arm perturbation uses the potential of Cox & Gómez (2002), which is expressed as:

$$\Phi(R,\phi,z) = -4\pi G H \rho_0 \exp\left(-\frac{r-r_0}{R_s}\right) \sum_n \left(\frac{C_n}{K_n D_n}\right) \cos(n\Gamma(R,\phi,t)) \left(\operatorname{sech}\left(\frac{K_n}{\beta_n} z\right)\right)^{\beta_n}, \quad (3.51)$$

where H is the scale height, ρ_0 is the density at the fiducial radius r_0, R_s is a radial scale length. C_n is a constant coefficient in the summation and K_n, D_n and β_n are calculated as follows (Cox and Gomez 2002):

$$K_n = \frac{nN}{r \sin\alpha}, \quad (3.52)$$

$$\beta_n = K_n H(1 + 0.4 K_n H), \quad (3.53)$$

$$D_n = \frac{1 + K_n H + 0.3(K_n H)^2}{1 + 0.3 K_n H}, \quad (3.54)$$

where N is the number of arms, and α is the pitch angle. The arm is assumed to be logarithmic with a constant pitch angle and its temporal dependence is described by the term $\Gamma(R,\phi,t)$, which is written as:

$$\Gamma(R,\phi,t) = N\left(\phi + \Omega_p t - \phi_p(r_0) - \frac{\ln(r/r_0)}{\tan\alpha}\right), \quad (3.55)$$

where Ω_p is the pattern speed and $\phi_p(r_0)$ is a phase shift.

Model Parameters

For the M33 model, the potential was chosen such that it approximately represented the amplitude of the potential in the spiral arms of the evolved N-body model described in §3.2.2. The parameters are summarised in Table 3.2. The rotation curve is shown in Figure 3.5.

For the Milky Way spiral arm simulation, the parameters are described in more detail in Dobbs (2007) and Bonnell et al. (2013). The assumed MW parameters are briefly summarised here. The overall galactic potential is modelled with $v_0 = 220$ km s^{-1}, $Rc = 1$ kpc, and $z_q = 0.7$. The spiral potential is assumed to have $N = 4$ arms, $\alpha = 15\,^\circ$, and $\Omega_p = 20$ km s^{-1} kpc^{-1}. The corotation radius for this model is $R_{\rm corot} = 11$ kpc. This simulation is discussed in Chapter 5.

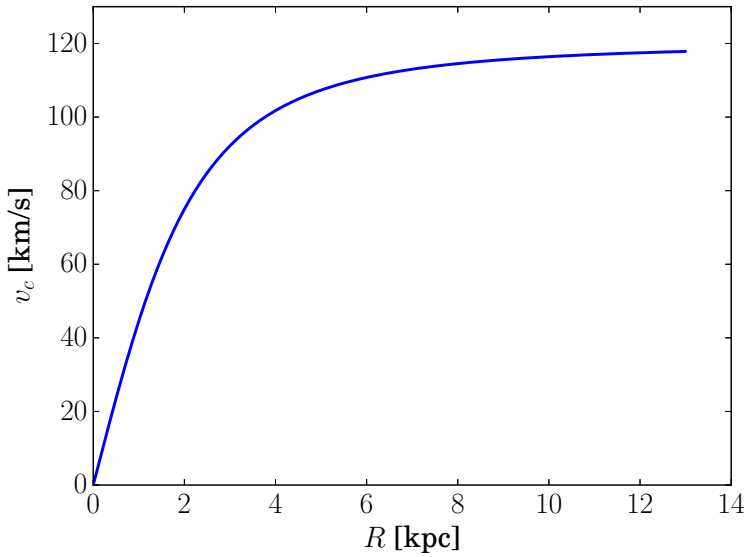

Figure 3.5: Logarithmic potential rotation curve for the M33 model using the parameters of Table 3.2.

3.3 Setting up the Gas Initial Conditions

3.3.1 Gas Equilibrium Conditions

Initially, the gas should as close as possible to rotational support in the radial direction and hydrostatic balance in the vertical direction. For an axisymmetric disc, these conditions are:

$$v_{c(\mathrm{gas})}^2 = \frac{R}{\rho_g}\frac{\partial P}{\partial R} + R\frac{\partial \Phi}{\partial R}, \tag{3.56}$$

$$\frac{1}{\rho_g}\frac{\partial P}{\partial z} + \frac{\partial \Phi}{\partial z} = 0, \tag{3.57}$$

for the radial and vertical components respectively. In these equations, $\rho_g = \rho_g(R,z)$ is the gas density, P is the gas pressure and Φ is the gravitational potential. The term $v_{c(\mathrm{gal})}^2 = R\frac{\partial \Phi}{\partial R} = v_{ch}^2 + v_{cd}^2 + v_{cb}^2 + v_{cg}^2$ in equation (3.56) is the potential's circular velocity including contribution of the gas self-gravity (v_{cg}^2). An equation of state (EOS) is needed to close this system of equations. For simplicity, an isothermal EOS is assumed:

$$P = \left(\frac{k_B T}{\mu m_p}\right)\rho_g, \tag{3.58}$$

Table 3.2: Model Parameters for M33 Spiral Potential

Galaxy Potential	
v_0 km s^{-1}	120.0
R_c(kpc)	2.5
z_q	0.7
Spiral Potential	
ρ_0 (M$_\odot$ pc^{-3})	0.05
r_0 (kpc)	5.6
R_s (kpc)	2.5
H (kpc)	0.2
N	4
$\alpha(^\circ)$	15
Ω_p km s^{-1} kpc^{-1}	23
$R_{\rm corot}$ (kpc)	4.58
$\phi_p(r_0)$	0
Gas Disc	
Profile	exp-sech^2
$M_g(10^9\,M_\odot)$	1.35
R_d(kpc)	2.5

where k_B is the Boltzmann constant, T is the temperature, μ is the mean molecular weight and m_p is the proton mass. The sound speed is

$$c_s^2 = \frac{\partial P}{\partial \rho_g} = \frac{k_B T}{\mu m_p}, \tag{3.59}$$

which makes it possible to write the pressure as $P = c_s^2 \rho_g$.

Rotational Equilibrium Condition

Rewriting Equation (3.56) in terms of the galaxy's circular velocity and the gas density and substituting the EOS gives:

$$v_{c(\rm gas)}^2 = v_{c(\rm gal)}^2 + c_s^2 \frac{R}{\rho_g}\frac{\partial \rho_g}{\partial R} \tag{3.60}$$

Observations show that the gas density falls with increasing radius, which means that $\frac{\partial \rho_g}{\partial R} < 0$. This means that the gas has to orbit at a lower orbital velocity compared to that required by the gravitational potential to compensate for the outward pressure force produced by the radial density gradient.

Solving the Vertical Balance Equation

Wang et al. (2010) propose a method for obtaining the density profile for a gas to remain in hydrostatic balance including the self-gravity of the gas. Substituting $P = c_s^2 \rho_g$ in the condition for vertical balance equation (3.57) gives:

$$\frac{c_s^2}{\rho_g}\frac{\partial \rho_g}{\partial z} = -\frac{\partial \Phi_{\text{tot}}}{\partial z}, \tag{3.61}$$

where $\Phi_{\text{tot}} = \Phi_g + \Phi_{\text{gal}}$ is the total gravitational potential, Φ_g is the potential of the gas and Φ_{gal} is the potential from other galaxy components. The function $\rho_g(z)$ is obtained by integrating this equation with respect to z and the final expression is:

$$\rho_g(R,z) = \rho_g(R,0)\exp\left(-\frac{1}{c_s^2}[\Phi_{\text{tot}}(R,z) - \Phi_{\text{tot}}(R,0)]\right). \tag{3.62}$$

According to Wang et al. (2010), if the disc is assumed to be thin, it is possible to write the Poisson equation for the gas component as:

$$\frac{\mathrm{d}^2\Phi_g}{\mathrm{d}z^2} = 4\pi G\rho_g. \tag{3.63}$$

Equations (3.62) and (3.63) form a system of equations where the unknowns are Φ_g and ρ_g. Substituting equation (3.62) in the above one results in:

$$\frac{\mathrm{d}^2\Phi_g}{\mathrm{d}z^2} = 4\pi G\rho_g(R,0)\exp\left(-\frac{1}{c_s^2}[\Phi_{\text{tot}}(R,z) - \Phi_{\text{tot}}(R,0)]\right). \tag{3.64}$$

Following Wang et al. (2010), the potential difference in the exponential term can be written as:

$$\Phi_{\text{tot}}(R,z) - \Phi_{\text{tot}}(R,0) = [\Phi_g(R,z) + \Phi_{\text{gal}}(R,z)] - [\Phi_g(R,0) + \Phi_{\text{gal}}(R,0)]. \tag{3.65}$$

With the substitutions:

$$\Delta\Phi_g(R,z) = \Phi_g(R,z) - \Phi_g(R,0),\ \Delta\Phi_{\text{gal}}(R,z) = \Phi_{\text{gal}}(R,z) - \Phi_{\text{gal}}(R,0), \tag{3.66}$$

equation (3.65) reduces to:

$$\Phi_{\text{tot}}(R,z) - \Phi_{\text{tot}}(R,0) = \Delta\Phi_g(R,z) + \Delta\Phi_{\text{gal}}(R,z). \tag{3.67}$$

Because the potential difference $\Delta\Phi_g$ determines $\rho_g(R,z)$, it is possible to write equation

(3.64) as (e. g. Wang et al. 2010):

$$\frac{\mathrm{d}^2\Delta\Phi_g}{\mathrm{d}z^2} = 4\pi G\rho_g(R,0)\exp\left(-\frac{1}{c_s^2}[\Delta\Phi_g(R,z)+\Delta\Phi_{\mathrm{gal}}(R,z)]\right). \tag{3.68}$$

For a given surface density profile $\Sigma(R)$, the mid-plane density $\rho_g(R,0)$ is expressed as:

$$\rho_g(R,0) = \frac{\Sigma(R)}{\int_{-\infty}^{\infty}\exp\left(-\frac{1}{c_s^2}[\Delta\Phi_g(R,z)+\Delta\Phi_{\mathrm{gal}}(R,z)]\right)dz}. \tag{3.69}$$

In summary, the method has the following steps: 1) substitute equation (3.62) in the Poisson Equation to solve for the potential difference of the gas $\Delta\Phi_g$; 2) substitute $\Delta\Phi_g$ back in equation (3.62) and obtain the vertical gas density profile; 3) use equation (3.69) to fix the mid-plane density in terms of the surface density profile. To find a solution, this requires that the mid-plane density is specified. However, this depends on the unknown $\Delta\Phi_g$ in equation (3.69). To overcome this problem, it is necessary to give an initial guess of the mid-plane density and iterate these steps until it converges (Wang et al., 2010).

The problem has an analytic solution for an infinite and uniform self-gravitating isothermal sheet (Spitzer, 1942). However, for more complex potentials and gas distributions this has to be approached by numerical methods. In this work, a 4th Order Runge-Kutta (RK4) method is applied to solve equation (3.68) for the potential difference of the gas and to obtain the gas density profile. The integral in equation 3.69 is also evaluated numerically. A `Python` code was written to implement the RK4 method and to take advantage of the integration tools available in `numpy` [2]. The approach taken to implement it in a SPH simulation is described in the following subsections.

3.3.2 Steps for Initialising the Gas in the N-body Model

Specify the Target Density Profile

Observations give information of the gas surface density Σ_g, which relates to density $\rho_g(R,z)$ by

$$\Sigma_g(R) = \int_{-\infty}^{\infty}\rho_g(R,z)dz. \tag{3.70}$$

[2]Detailed documentation for the `numpy` library may be obtained from: http://www.numpy.org .

Observations suggest that the gas surface decays exponentially:

$$\Sigma_g(R) = \Sigma_{0g} \exp\left(-R/R_g\right), \tag{3.71}$$

where Σ_{0g} is the central surface density and R_g is the radial scale length. This constrains the radial gas distribution, but does not completely specify $\rho_g(R,z)$. It is possible to gain some information by solving the vertical balance equation to find the vertical density profile as described in §3.3.1. This section describes the steps for obtaining the gas vertical profile in the potential of a combined disc-halo-bulge galaxy model and including the self-gravity of the gas.

In this model, the stellar disc follows the exponential-sech^2 profile given in equation (3.40). Its potential, according to Binney & Tremaine (2008) and Cuddeford (1993), can be expressed as:

$$\Phi_d(R,z) = -\frac{4G\Sigma_0}{R_d} \int_{-\infty}^{\infty} \mathrm{sech}^2(z'/z_d)dz' \int_0^{\infty} \sin^{-1}\left(\frac{2a}{\sqrt{+}+\sqrt{-}}\right) aK_0(a/R_d)da, \tag{3.72}$$

where Σ_0 is the central surface density, R_d is the scale radius, z_d is the scale height; K_0 is a modified Bessel function of the second kind. The symbols $\sqrt{+}$ and $\sqrt{-}$ are equal to $\sqrt{z^2+(a+R)^2}$ and $\sqrt{z^2+(a-R)^2}$, respectively. These integrals may be evaluated numerically to calculate $\Phi_d(R,z)$. A `Python` script was developed for this purpose using the `numpy` library.

The halo is modelled by a NFW potential expressed as:

$$\Phi_h(r) = -\frac{GM_h}{R_h}\left(\frac{1}{\ln(1+c)-c/(1+c)}\right)\frac{\ln(r/R_h+1)}{r/R_h} + K, \tag{3.73}$$

where M_h is the halo mass, c is the concentration parameter, R_h is the scale radius. K is a constant resulting from the truncation of the density profile given by:

$$K = \frac{GM_h}{R_h}\left[\left(\frac{1}{\ln(1+c)-c/(1+c)}\right)\frac{\ln(1+c)}{c} - \frac{1}{c}\right]. \tag{3.74}$$

The bulge is represented by a Hernquist (1993) profile given by:

$$\Phi_b(r) = -\frac{GM_b}{R_b}\frac{1}{1+r/R_b}, \tag{3.75}$$

where M_b is the mass and R_b the scale radius. The parameters in Table 3.1 are used to evaluate

these potentials.

The vertical hydrostatic balance equation is solved for a fixed set of radii. To incorporate the numerical calculation of $\Phi_d(R,z)$ in this method, equation (3.72) is evaluated for a finite set of z values keeping R fixed at the radius where the vertical profile is being obtained. Then, an interpolating function is used to calculate $\Phi_d(R,z)$ as a function of z. The galaxy's total potential $\Phi_{\rm gal}$ is calculated to by adding the disc, halo, and bulge contributions. This is used in equations (3.62), (3.68) and (3.69) to obtain the vertical density profile at that radius. This is repeated for all the radii in the given set.

Figure 3.6 shows the vertical profiles obtained at different radii assuming $T = 10^4$ K. The left plot shows the actual solution (solid lines) compared to a $\mathrm{sech}^2(z/z_d)$ model fitted to the solution (dashed lines). The right plot shows the difference between the actual solution and the fitted model. This shows that the solution is not very different to an isothermal profile. The difference tends to increase with z and is larger near the centre.

With increasing radius, the solution becomes closer to the isothermal sheet. Because ρ_g depends on the vertical potential difference, this is highest near the galaxy's centre as the potential is dominated by the disc. In the outer galaxy, the dominant potential is produced by the spherical halo and the equipotential surfaces approach a sphere. This makes the vertical difference $\Delta\Phi_{\rm gal}$ very small near the galactic plane at large radii. Thus the solution at large radii is dominated by the gas potential.

The mid-plane density decreases with radius, as shown in Figure 3.7, and the scale-height tends to grow with radius to almost a kpc near the galaxy's edge (see left panel of Figure 3.7). Near the centre, the gas distribution is more compact due to the stronger vertical force. The scale height is also sensitive to the temperature. For lower temperatures, it decreases due to the reduced gas pressure.

Generating a particle distribution with this method would require repeating the process at each particle's radial position. This would be computationally expensive for a large particle distribution. However, the fact that the actual vertical profile is not very different to the isothermal sheet profile provides a certain advantage. The idea is to first solve the vertical balance equation for a set of radii and use the solution to generate an interpolating function of the scale height as a function of radius $z_d(R)$. The next step is to sample a particle's vertical coordinate assuming a local vertical profile of the form $\mathrm{sech}^2(z/z_d(R))$, scaled by the local z_d.

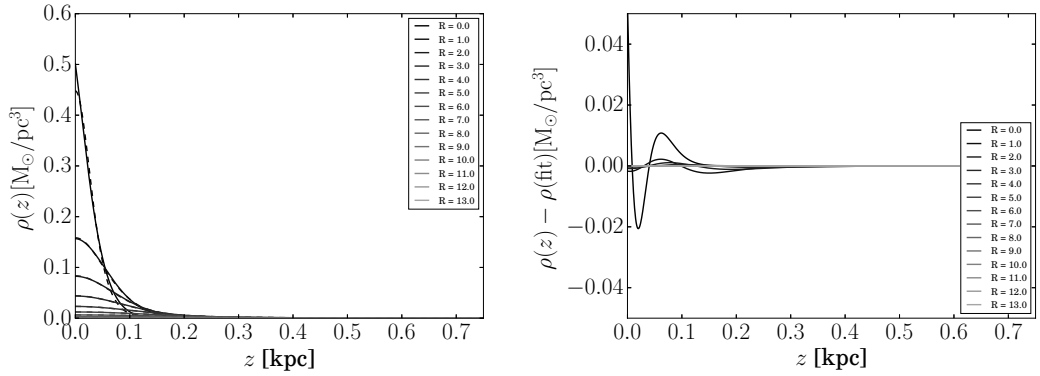

Figure 3.6: Left panel: density profile derived from the hydrostatic balance equation (solid line) compared to the best-fit $\mathrm{sech}^2(z)$ (dashed curve) for the full halo+disc+bulge model potential. The figure shows that the latter is not a bad approximation to the actual solution. Right panel: difference between the actual solution and the best-fit $\mathrm{sech}^2(z)$ profile, the difference is larger near the center and closer to the mid-plane.

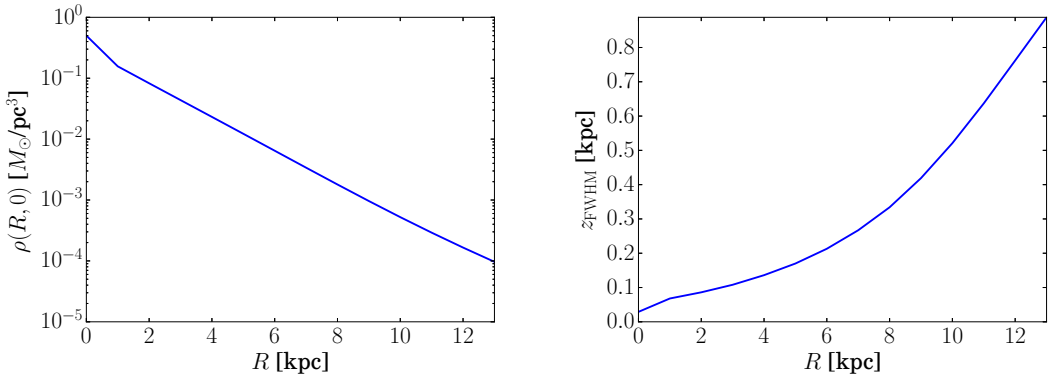

Figure 3.7: Left panel: gas mid-plane density as a function of radius for the full halo+disc+bulge model. Right-panel: vertical full-width at half maximum of the density profile as a function of radius. This measures the variation of the scale height of the disc with radius (flaring).

This is only an approximation, but it provides an advantage over just assuming an initial constant scale height and letting the gas relax. It can reduce some spurious effects produced by gas collapsing in the galaxy's central regions and expanding in the outer parts. This may be a convenient approach for initialising flaring discs for SPH simulations.

Setting Gas Particles in the N-body Model

First, an N-body model of galaxy consisting of a disc, bulge, and halo is generated using the method of §3.2.2. The disc is given a total mass corresponding to the sum of the gas and stellar masses: $M_{\rm disc} = M_{\rm gas} + M_\star$. The disc's total number of particles also satisfies $N_{\rm disc} = N_{\rm gas} + N_\star$, where $N_{\rm gas}$ and $N_\star$ are gas and stellar particle numbers, respectively.

The gaseous component is initialised by sampling $N_{\rm gas}$ particles from the original disc. The gas particle mass is then $m_g = M_{\rm gas}/N_{\rm gas}$. The remaining particles are allocated to the stellar disc with a particle mass given by $m_\star = M_\star/N_\star$. After this procedure, the disc has two separate components, but the total mass is preserved. This assumes that the gas and stellar discs have the same scale radius.

The initial N-body disc is sampled from a sech^2 profile with a constant scale height $z_{d\rm orig}$. Following the previous section's results, the flaring disc profile is set by scaling the gas particles' vertical positions by the transformation:

$$z' = \frac{z_d(R)}{z_{d\rm orig}} z, \tag{3.76}$$

where z' is the new coordinate and z is the original one. The radial and azimuthal coordinates of the particles are unchanged. In places where $z_d(R) < z_{d\rm orig}$ the distribution will become more compact, while it becomes thicker where $z_d(R) > z_{d\rm orig}$.

This vertical re-scaling preserves the radial surface density profile. This can be shown by expressing the density profile as

$$\rho_g(R,z) = \frac{\Sigma_0}{2z_d(R)} \exp\left(-R/R_d\right) \mathrm{sech}^2\left(z/z_d(R)\right), \tag{3.77}$$

where z_d explicitly depends on the radius. Substituting this in equation (3.70) gives the expo-

nential radial profile. The cumulative mass function can be written as:

$$M_{\rm cum} = \int_0^R \int_0^\phi \int_{-\infty}^z \frac{\Sigma_0}{2z_d(R')} \exp\left(-R'/R_d\right) \mathrm{sech}^2\left(z'/z_d(R')\right) dz' d\phi' R' dR', \tag{3.78}$$

which can be rearranged as:

$$M_{\rm cum} = \int_0^\phi d\phi' \int_0^R \Sigma_0 \exp\left(-R'/R_d\right) \left\{ \int_{-\infty}^z \frac{1}{2z_d(R')} \mathrm{sech}^2\left(z'/z_d(R')\right) dz' \right\} R' dR'. \tag{3.79}$$

For a constant z_d, the previous triple-integral can be split into three separate integrals and into three independent cumulative functions from which is possible to sample the particle's coordinates.

For a general $z_d(R)$, the radial and vertical positions are coupled in equation (3.79). However, it is still possible to devise a method analogous to the case of a constant z_d. To evaluate the total mass, the integration limits in equation (3.79) are set to $\phi = 2\pi$, $R \to \infty$, and $z \to \infty$. The innermost integral with respect to z is first evaluated. Because z_d is only a function of R, it can be taken as a constant and the inner integral results in:

$$\int_{-\infty}^{\infty} \frac{1}{2z_d(R')} \mathrm{sech}^2\left(z'/z_d(R')\right) dz' = 1. \tag{3.80}$$

Thus, equation (3.79) reduces to an integral over the surface density and can be split in two independent integrals from which to sample ϕ and R. Then, z is just sampled from the local vertical function at the sampled R.

This result can be visualised as follows. It is possible to generate a razor-thin disc with an exponential radial profile by sampling an arbitrary number of R and ϕ positions, all with $z = 0$. If the particles are only displace vertically, the volume density will vary but the surface density profile remains unchanged. If the particles are vertically displaced according to a flaring profile, $\Sigma_g(R)$ will be preserved.

Assign Gas Particle Velocities

At this point the gas and stellar particles have the velocities originally assigned by the initial conditions generator. The appropriate gas velocities need to be assigned. Equation (3.60) shows that $v^2_{\rm (gas)}$ has an additional term due to the radial pressure gradient. For an exponential profile, this becomes $-c_s^2 R/R_g$, where R_g is the scale length. For an M33-sized galaxy and

$c_s = 10\ \mathrm{km\,s^{-1}}$, this term results in a decrease of $\approx 2.5\ \mathrm{km\,s^{-1}}$ at large radii. This is not a large difference and the correct calculation of this term requires the SPH gas density for each particle, which is unavailable at this point. For simplicity the particles are assigned the local circular velocity at their position. The stellar particles are left with the kinematics given by the initial conditions generated with `mkgalaxy`.

Once the gas vertical positions and circular velocities are assigned, the galaxy is allowed to evolve for some time to allow the spiral structure to form. For the simulations in this work, the N-body halo is not used and it is replaced by the corresponding fixed potential. This choice directs the computational efforts to the disc dynamics.

3.3.3 Steps for Initialising the Gas in the Fixed Potential Model

Specify the Target Density Profile

In this section, the vertical profile is obtained for the logarithmic potential model considering both the cases without and with gas self-gravity. The potential is evaluated using the parameters in Table 3.2. In some cases, fixed-potential simulations without the gas self-gravity are useful to study the large-scale gas dynamics as it avoids small time steps required to follow collapsing clumps.

The gas surface density profile is assumed to decay exponentially. It is assumed to be isothermal at $T = 10^4$ K. In the absence of self-gravity, it is sufficient to use equations (3.62) and (3.69) to specify the vertical density profile. The result is shown in Figure 3.8 and the full solution including self-gravity is shown in Figure 3.9. In both figures, the left plot shows the actual solution (solid lines) compared to a $\mathrm{sech}^2(z/z_d)$ model fitted to the solution (dashed lines). The right plot shows the difference between the actual solution and the fitted model. These results show that the solution is not very different to an isothermal profile regardless of whether the gas self-gravity is included or not.

Figure 3.10 (left panel) shows the mid-plane density as a function of radius for the case without self-gravity and Figure 3.11 (left panel) shows the case with self-gravity. For both cases, the density decays exponentially, but it tends to be higher with self-gravity.

Figure 3.10 (right panel) and 3.11 (right panel) show the scale height as a function of radius for the no self-gravity and self-gravity solutions, respectively. The first has a clearly flaring

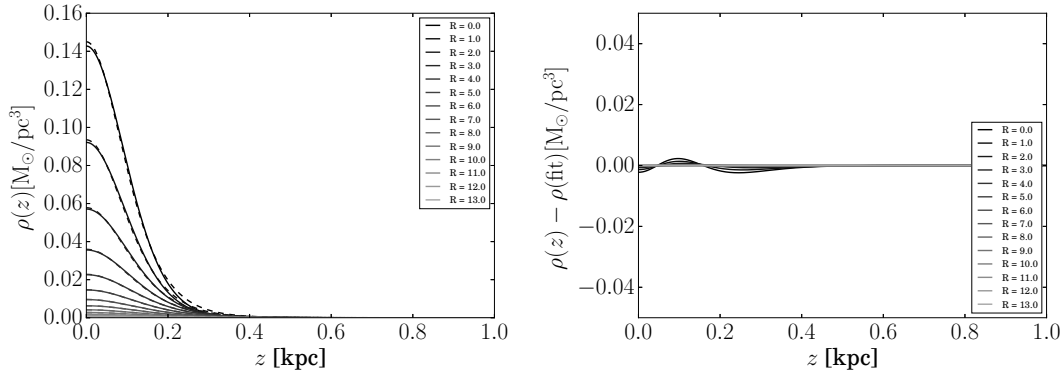

Figure 3.8: Left panel: density profile derived from the hydrostatic balance equation (solid line) compared to the best-fit $\mathrm{sech}^2(z)$ (dashed curve) for the logarithmic potential model with no gas self-gravity. The figure shows that the latter is not a bad approximation to the actual solution. Right panel: difference between the actual solution and the best-fit $\mathrm{sech}^2(z)$ profile, the difference is larger near the center and closer to the mid-plane.

profile, whereas the second has a distribution with a flatter profile. As the radius increases the solution approaches the isothermal profile. As described in §3.3.2, this data is used to build an interpolating function for $z_d(R)$ and the vertical positions are sampled assuming a local vertical sech^2 profile.

Specify the Velocity Distribution

The gas is assumed to orbit at the local circular velocity. For this model using the M33 parameters and $c_s = 10\ \mathrm{km\,s^{-1}}$, the $-c_s^2 R/R_g$ term results in a difference of $\approx 2.5\ \mathrm{km\,s^{-1}}$ at large radii. As the gas disc will be subject to the spiral perturbation, the disc will have to adjust to this potential, which will introduce some radial and azimuthal velocity variations. For this reason, the gas is initialised using only the circular velocity given by the galaxy's mass distribution and is allowed to settle in the potential. As the vertical density profile is derived from hydrostatic balance, the initial v_z is set to zero. However, it is possible to assign a velocity dispersion both in the plane and vertical directions if desired.

Sample the Density Distribution and Assign Particle Velocities

This case requires to generate a new disc. The particle positions are sampled using a Monte Carlo method based on probability functions derived from the cumulative mass function (CMF).

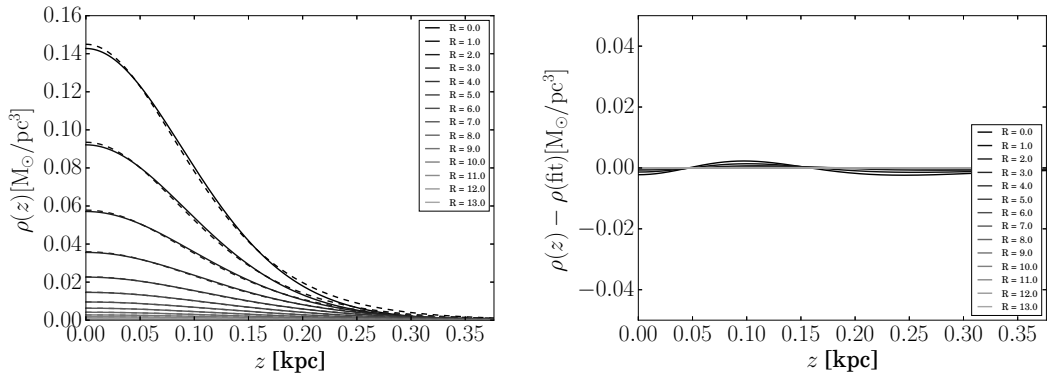

Figure 3.9: Left panel: gas mid-plane density as a function of radius for the logarithmic potential model with gas self-gravity. Right-panel: vertical full-width at half maximum of the density profile as a function of radius. This measures the variation of the scale height of the disc with radius (flaring).

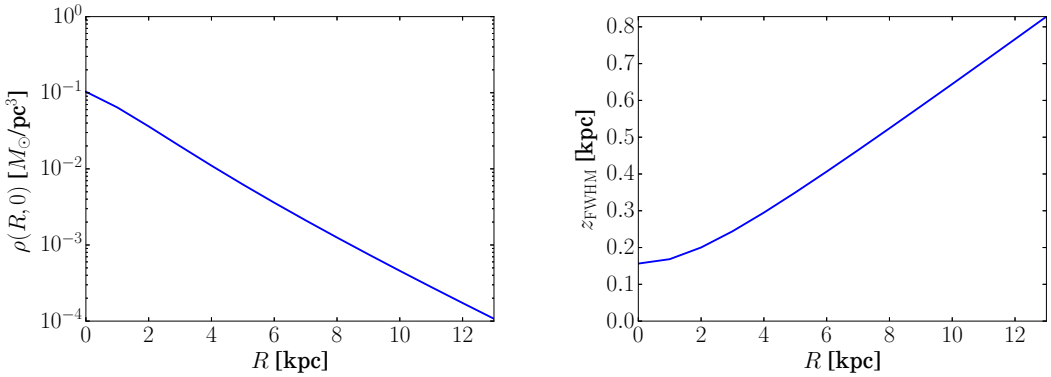

Figure 3.10: Left panel: density profile derived from the hydrostatic balance equation (solid line) compared to the best-fit $\mathrm{sech}^2(z)$ (dashed curve) for the logarithmic potential with no gas self-gravity. The figure shows that the latter is not a bad approximation to the actual solution. Right panel: difference between the actual solution and the best-fit $\mathrm{sech}^2(z)$ profile, the difference is larger near the center and closer to the mid-plane.

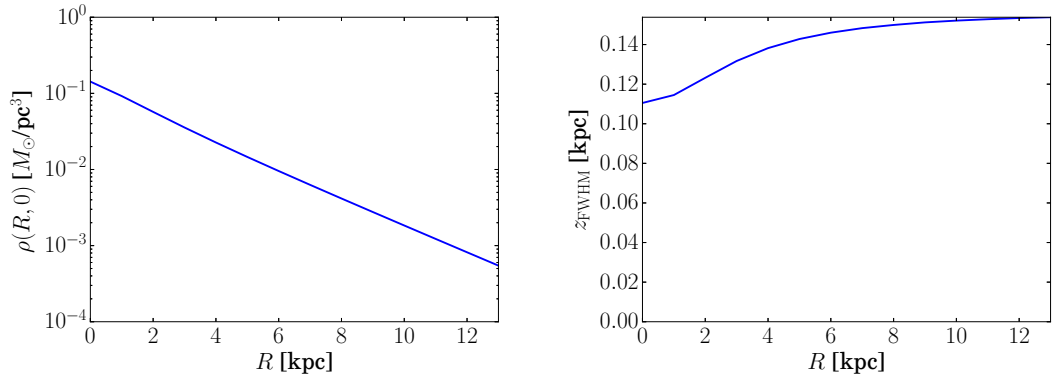

Figure 3.11: Left panel: gas mid-plane density as a function of radius for the logarithmic potential model with gas self-gravity. Right-panel: vertical full-width at half maximum of the density profile as a function of radius. This measures the variation of the scale height of the disc with radius (flaring).

For the density profile in equation (3.77) in §3.3.2, the CMF is:

$$M_{\rm cum} = \int_0^{\phi} d\phi' \int_0^{R} \Sigma_0 \exp\left(-R'/R_d\right) \left\{ \int_{-\infty}^{z} \frac{1}{2z_d(R')} \mathrm{sech}^2\left(z'/z_d(R')\right) dz' \right\} R' dR'. \tag{3.81}$$

As shown in equation (3.80), when evaluating the integral with respect to z', the function $z_d(R)$ can be taken as a constant. For the limits $\pm\infty$, this integral is normalised. This allows to write three separate probability distribution functions (PDF) to sample the coordinates.

With this result, it is possible to define a cumulative probability function (CDF) for each coordinate. For R, the CDF becomes:

$$F(R) = \frac{\int_0^R \exp\left(-R'/R_g\right) R' dR'}{\int_0^{\infty} \exp\left(-R'/R_g\right)) R' dR'} = 1 - \exp\left(-R/R_g\right)(R/R_g + 1). \tag{3.82}$$

For ϕ the CDF is:

$$\Phi(\phi) = \frac{\int_0^{\phi} d\phi'}{\int_0^{2\pi} d\phi'} = \frac{\phi}{2\pi}. \tag{3.83}$$

For z, the CDF is:

$$Z(z) = \frac{\int_{-\infty}^{z} \frac{1}{2z_d} \mathrm{sech}^2\left(z'/z_d\right) dz'}{\int_{-\infty}^{\infty} \frac{1}{2z_d} \mathrm{sech}^2\left(z'/z_d\right) dz'} = \frac{1 + \tanh(z/z_d)}{2}. \tag{3.84}$$

The sampling process consists of first drawing a random number ξ from a uniform distribution between 0 and 1. Then, this number is equated to the CDF and the coordinate is obtained by solving the equation, which is known as sampling a PDF by inversion of the CDF. A different

random number is drawn for each coordinate. This method is not applicable to the radial CDF because equation (3.82) cannot be explicitly solved in terms of R. A rejection-acceptance method is applied to sample the PDF, which is $f(r) \propto R\exp(-R/R_g)$. For the azimuthal and vertical coordinates, it is possible to invert the CDFs in equations (3.83) and (3.84) to obtain the following expressions as a function of ξ. For the azimuthal coordinate, the equation becomes:

$$\phi = 2\pi\xi, \tag{3.85}$$

and for the vertical coordinate:

$$z = z_d\left(\frac{1}{2}\ln\left(\frac{\xi}{1-\xi}\right)\right) \tag{3.86}$$

The sampling process for the gas disc can be summarised as follows. For each particle, 1) sample the radial coordinate R from the radial PDF with the acceptance-rejection method; 2) sample the azimuthal coordinate by drawing a random number ξ from a uniform distribution between 0 and 1 and evaluate equation (3.85); 3) sample the vertical coordinate by drawing a random number ξ from a uniform distribution between 0 and 1 and evaluate equation (3.86), and adjust z_d according to the flaring profile; 4) transform to Cartesian coordinates; 5) assign the particle the circular velocity at R, add a velocity dispersion if desired, and transform to Cartesian components.

3.4 Model Evolution Tests

This section presents the results for the isolated evolution of the galaxy models previously discussed. This section aims to show that the models produce stable configurations for the timescales of interest in the present work.

3.4.1 N-body model

The N-body model is evolved with three levels of resolution. The gas is isothermal at 10^4K and self-gravity is included. The particle numbers, masses, and a label to identify each model are given in Table 3.3.

Table 3.3: N-body Galaxy Model Particle Numbers and Masses

Label	$N_{\rm gas}$	$N_\star$	$N_{\rm bulge}$	m_g [$M_\odot$]	m_d [$M_\odot$]	m_b [$M_\odot$]
4M	2×10^6	2×10^6	78 420	675.0	3825.0	3825.55
32M	30×10^6	2×10^6	78 432	45.0	3825.0	3824.96
100M	100×10^6	2×10^6	78 420	13.5	3825.0	3825.55

Surface Density Maps and Spiral Structure

Figures 3.12 and 3.13 show snapshots of the 4M model simulation and Figures 3.14 and 3.15 present the same data for the 32M simulation at times $t = 0, 149, 299, 468, 597, 747$ Myr. The right and left columns show the gas and stellar surface density maps, respectively.

In both models, spiral structure is clearly formed after 299 Myr. The 32M shows more evident gas features than the 4M model. The number of spiral arms increases with radius. The centre is dominated by a low-number mode whereas the edge has patchier structure. This is visualised in Figure 3.16, which shows the stellar surface density map in a cylindrical projection. The left and right columns show the 4M and 32M maps, respectively, for $t = 447.96$ Myr and $t = 746.59$ Myr. This projection is useful for a qualitative inspection of the spiral arms at different radii. Figure 3.16 shows that both models have qualitatively the same behaviour at both times. At $t = 746.69$ Myr, the map shows approximately 4 to 5 density peaks in the region where $R \approx 3-4$ kpc. At lower radii the structure is blurred by bulge particles, but the gas maps in Figures 3.13 and 3.15 suggest that spiral structure still extends to the central regions. Both the 4M and 32M model, at $R \approx 6$ kpc show 6 density peaks, which are clearly defined in the 32M model. In the 4M simulation, there are clear peaks at $R = 6$ kpc at $\phi \approx 50^\circ$ and $\phi \approx 125^\circ$, but the others are less evident. In both models, the stellar masses and particle numbers are the same and only the gas particle number is varied. It is interesting to note that the model with a higher number of gas particles shows more defined spiral arms. Figure 3.16 shows that the prominent arms have qualitatively the same inclination in both simulations, which indicates that they have similar pitch angles.

Figure 3.17 shows the stellar surface density $\Sigma_\star$ profile as a function of the azimuthal angle ϕ at $R = 3, 5$ and 7 kpc. The surface density decreases with radius, a result of the disc's exponential profile. It shows that the number of modes increases with radius.

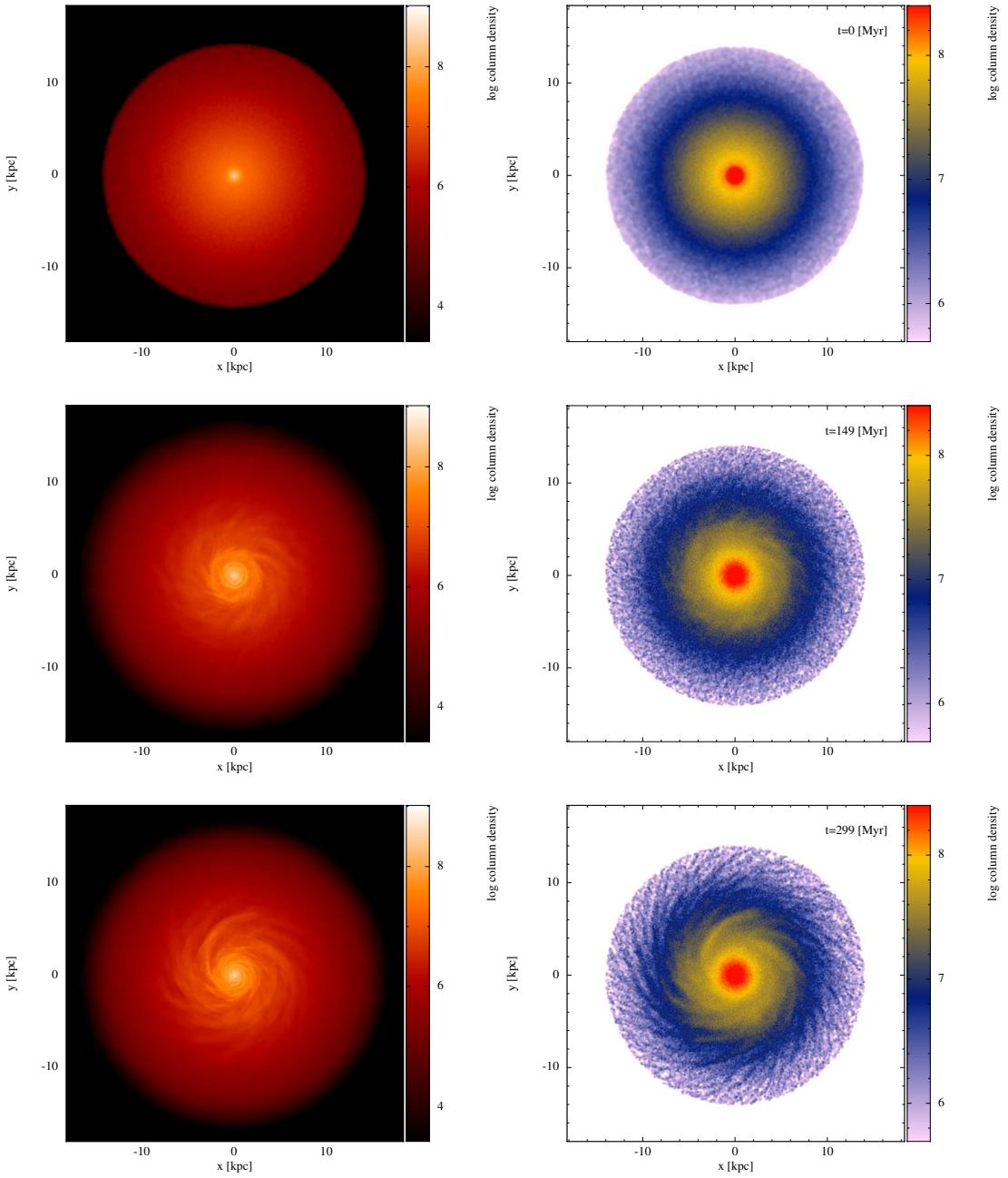

Figure 3.12: Surface density maps for the gas (left panels) and stellar (right panels) components of the 4M model at $t = 0$ Myr (top), $t = 149$ Myr (middle), and $t = 299$ Myr (bottom). Plots obtained with SPLASH (Price, 2007).

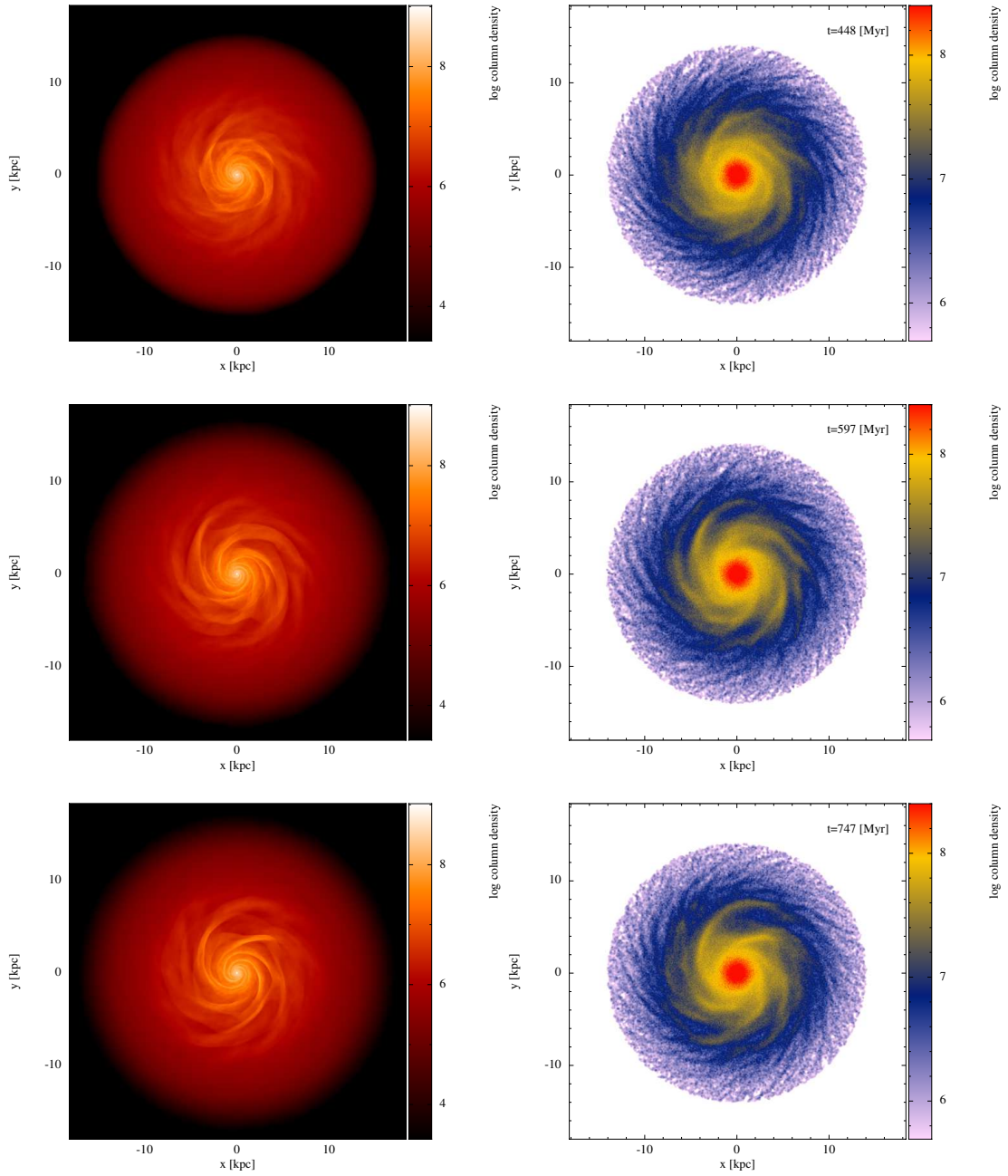

Figure 3.13: Surface density maps for the gas (left panels) and stellar (right panels) components of the 4M model at $t = 448$ Myr (top), $t = 597$ Myr (middle), and $t = 747$ Myr (bottom). Plots obtained with SPLASH (Price, 2007).

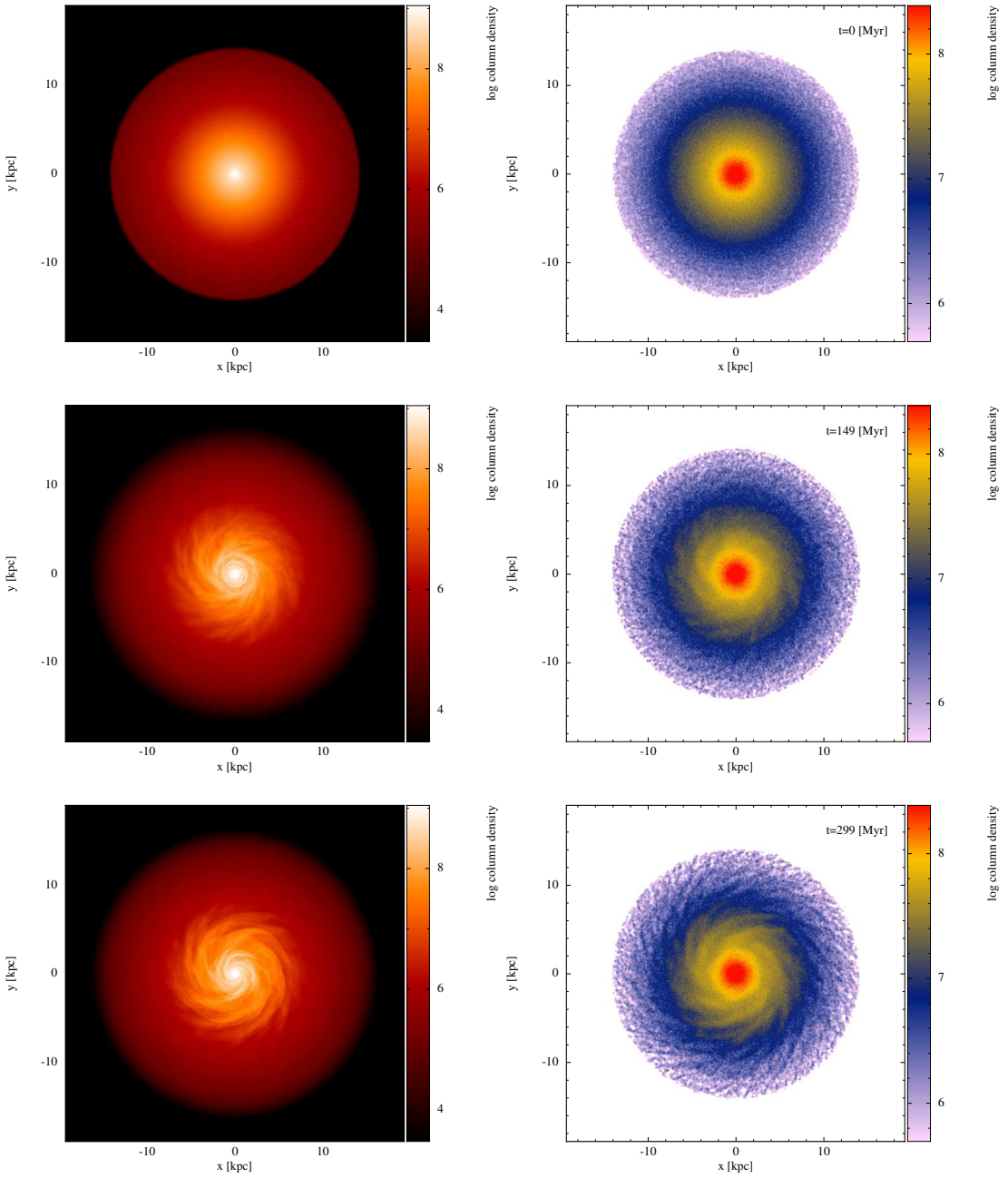

Figure 3.14: Surface density maps for the gas (left panels) and stellar (right panels) components of the 32M model at $t = 0$ Myr (top), $t = 149$ Myr (middle), and $t = 299$ Myr (bottom). Plots obtained with SPLASH (Price, 2007)

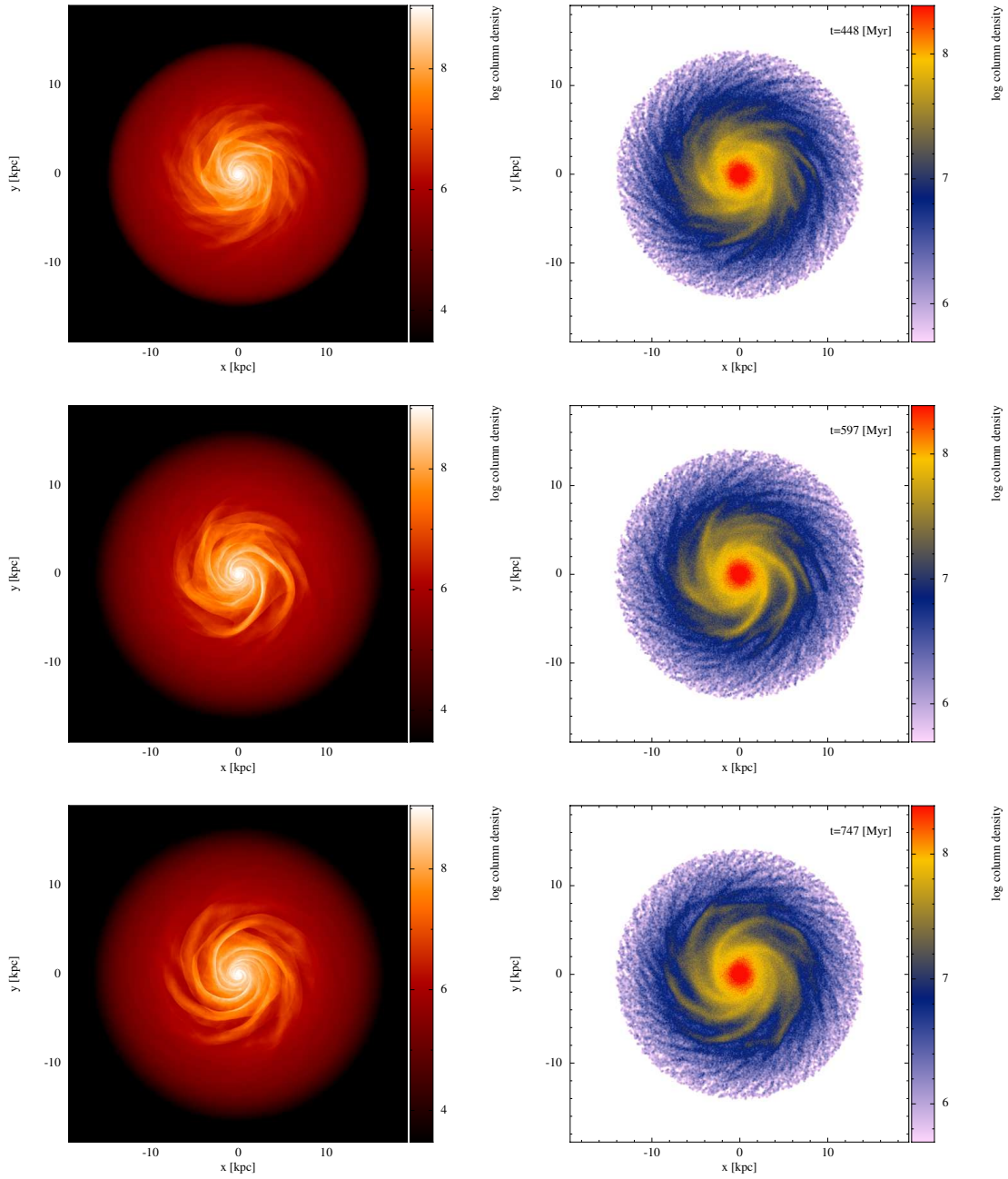

Figure 3.15: Surface density maps for the gas (left panels) and stellar (right panels) components of the 32M model at $t = 448$ Myr (top), $t = 597$ Myr (middle), and $t = 747$ Myr (bottom). Plots obtained with SPLASH (Price, 2007).

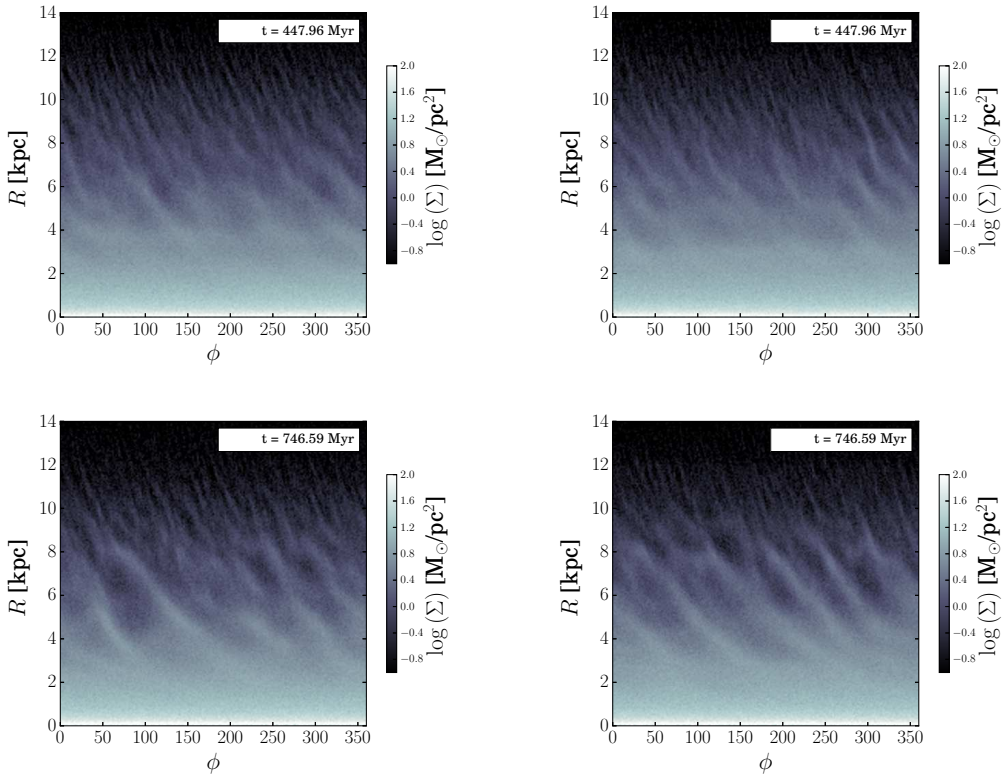

Figure 3.16: Stellar surface density map in the $R-\phi$ cylindrical projection for the 4M model (left column) and the 32M model (right) column. The top panels are at $t = 447.96$ Myr and the bottom panels are at $t = 746.59$ Myr. This mapping of the surface density provides a better visualisation of the location of the spiral arms, the number of arms as a function of azimuth, and the radial extent of the arms.

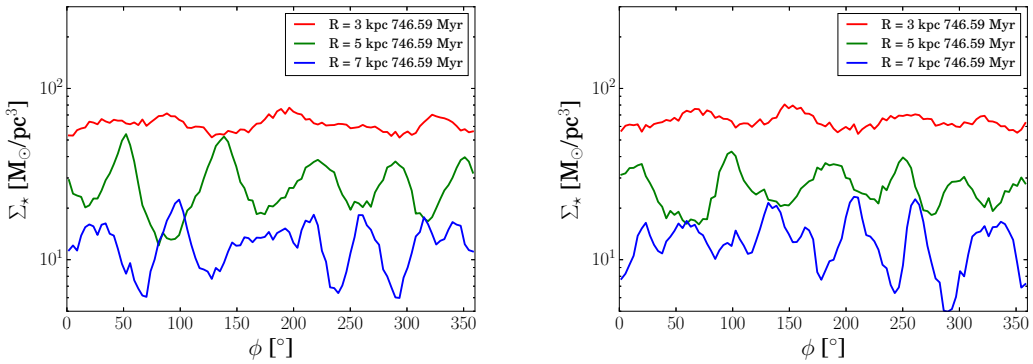

Figure 3.17: Azimuthal stellar surface density $\Sigma_\star(\phi)$ profiles for the 4M (left panel) and 32M (right panel) at $t = 746.59$ Myr for three different radii. The top curve (red) corresponds to $R = 3$ kpc, the middle curve (green) to $R = 5$ kpc, and the bottom curve (blue) to $R = 7$ kpc.

Average Radial and Vertical Density Profiles

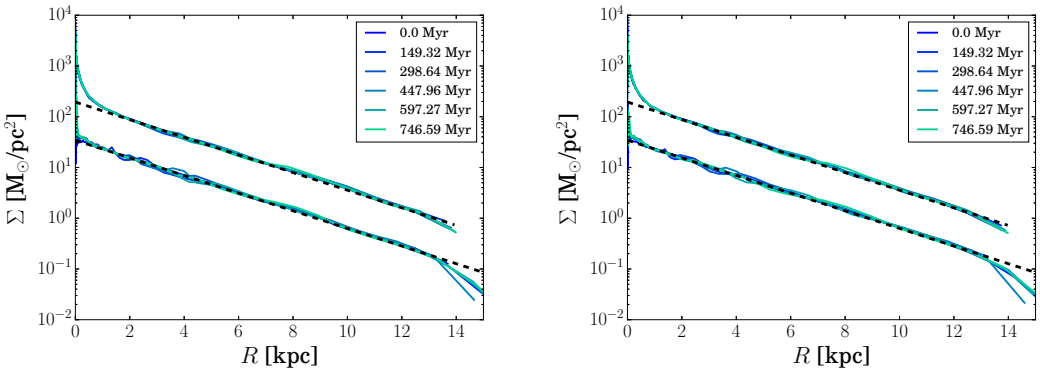

Figure 3.18: Average radial surface density $\Sigma(R)$ profiles for the 4M (left panel) and 32M (right panel) models. The top curve corresponds to the stellar component, which shows a central cusp due to the bulge. The bottom curve corresponds to the gas. The black dashed curve is the target exponential profile given the disc's mass and scale radius.

Figure 3.18 shows the average $\Sigma(R)$ in annular bins for the 4M model in the left panel and for the 32M in the right panel. The lower curve is the gas surface density and the upper curve is the stellar surface density. The black dashed lines are the target exponential density profiles given the mass and scale radius of each component. The central gas surface density peaks around $35\,\mathrm{M}_\odot\,\mathrm{pc}^{-2}$ and the stellar surface density peaks around $10^3\,\mathrm{M}_\odot\,\mathrm{pc}^{-2}$. The central high-density cusp in the stellar density is produced by the central bulge. From $R \approx 2$ kpc, the stellar surface density falls exponentially. On average, Figure 3.18 shows that both models remain close to the target profiles, though some variations appear due to the formation of the arms. There is no significant difference between the low resolution 4M and high resolution 32M models.

Figure 3.19 shows the vertical density profiles at $R = 0$ kpc and $R = 10$ kpc, respectively. These are obtained by taking an annulus 200 pc wide and by binning vertically in the z direction to calculate the average volume density ρ in each bin. The higher-density upper curve corresponds to the stellar component and the lower-density curve, to the gas. The dashed black curve is the initial sech^2 profile (at $R = 0$, the contribution of the bulge is included in the initial profile). The vertical profiles show that the stellar disc becomes denser in the central region. At larger radii, the mid-plane stellar density shows some oscillations around the initial value. In all cases, the gas density profile becomes slightly more compact with a higher mid-plane density. The stellar vertical profile shows more oscillations in the 4M model than

in the 32M model. The mid-plane density at $t = 746.59$ Myr at the two-radii varies slightly between each model, but stays within the same range of values.

Figure 3.20 shows the root mean square value of the particles' vertical positions $z_{\rm rms}$ for both models, which measures the average disc's height. The curve growing from near $z_{\rm rms} = 0$ to almost $z_{\rm rms} = 1$ kpc corresponds to the gas. The almost flat profile near $z_{\rm rms} = 0.2$ kpc corresponds to the stellar disc and the central bump corresponds to the bulge.

Results are similar for both models. The gas disc is settling into a slightly smaller scale height compared to the initial profile, but still follows approximately the same behaviour as a function of radius. This is not unexpected because the initial conditions are not specified according to the exact vertical density profile for hydrostatic balance. The stellar density profile also has some readjustment and becomes denser near the centre, which will drive the gas to a more compact vertical distribution. The gas is initially set in a distribution that alters the original pure N-body system obtained from the McMillan & Dehnen (2007) code, which means that some relaxation is expected.

Regarding the stellar component, the disc and bulge are keeping the initial scale height at most radii. However, it becomes slightly more compact near the edge of the disc. This is consistent with the tests of McMillan & Dehnen (2007) for a Milky Way-type galaxy and it may be a consequence of the assumed initial vertical velocities. At the disc's edge, the halo dominates the potential, but the local velocity distribution was derived assuming that dominant component is the disc, thus not being high enough to compensate for the more dominant halo (McMillan & Dehnen, 2007). This may explain the lower height at large radii. This is not critical as the analysis in this work will be in the galaxy's inner and mid-regions.

Rotation Curve

Figure 3.21 shows the rotation curve of the 4M (left panel) and 32M (right panel) at several times compared to the model curve (dashed curve). The actual curve stays close to the model value, though some variations appear gradually, which may be a consequence of the spiral arms. The gas rotates slightly slower at large radii, which is expected as the rotational equilibrium condition has an additional term due to the radial pressure gradient. This outward force means that the gas should orbit at a lower speed than that predicted by the mass distribution to stay in a circular path. Although this term was not included in the initial conditions

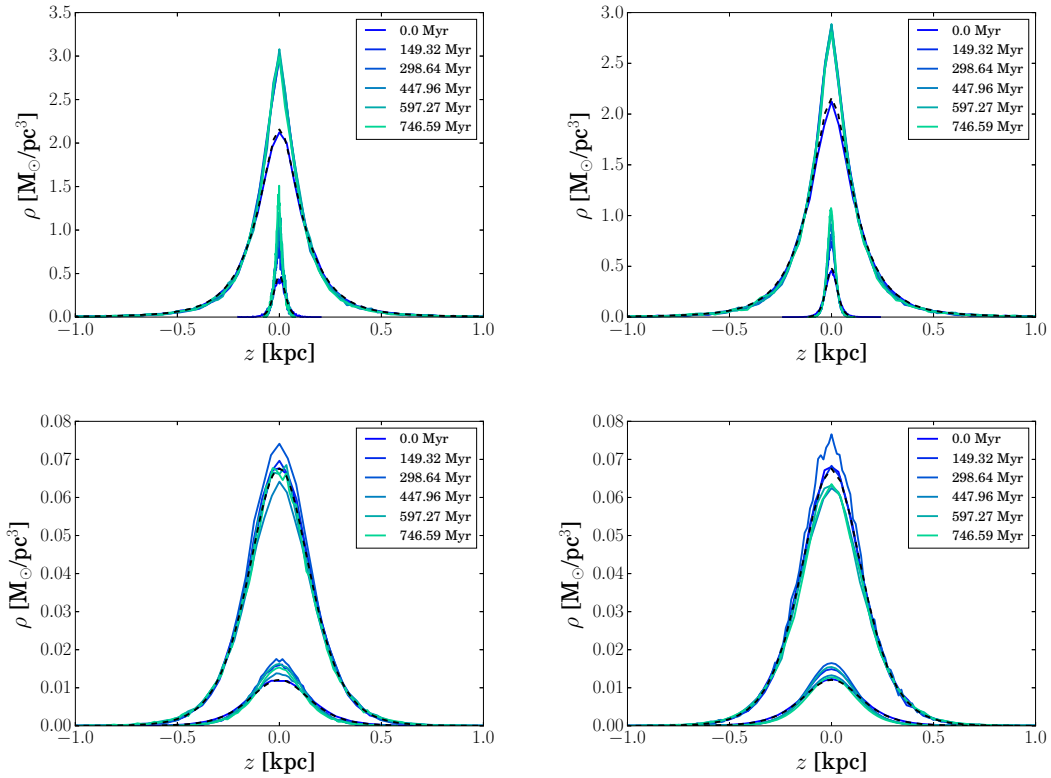

Figure 3.19: Average vertical volume density vertical profiles at $R = 0$ kpc (top), at $R = 5$ kpc (middle), and $R = 10$ kpc (bottom). In each panel, the higher density (upper) curve corresponds to the stellar component and the lower density (lower) curve corresponds to the gaseous component. The left panel corresponds to the 4M model and the right panel to the 32M model.

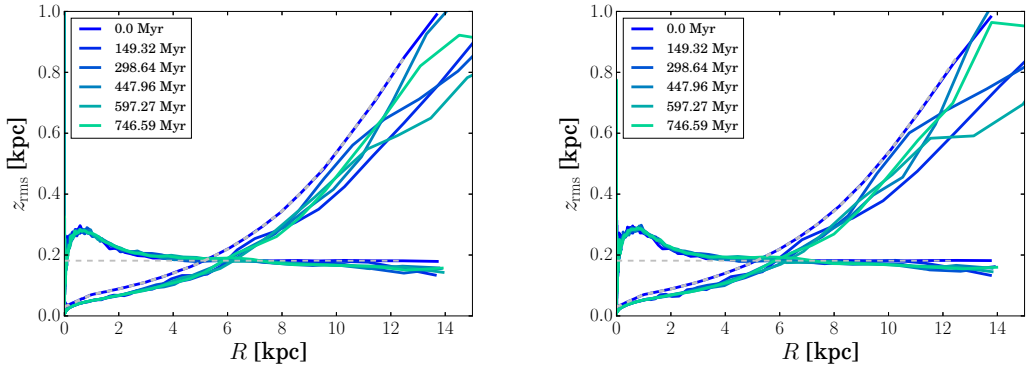

Figure 3.20: Vertical z_{rms} as a function of radius for the 4M (left panel) and 32M (right panel). The flaring profile corresponds to the gas and the nearly flat profile to the stellar component.

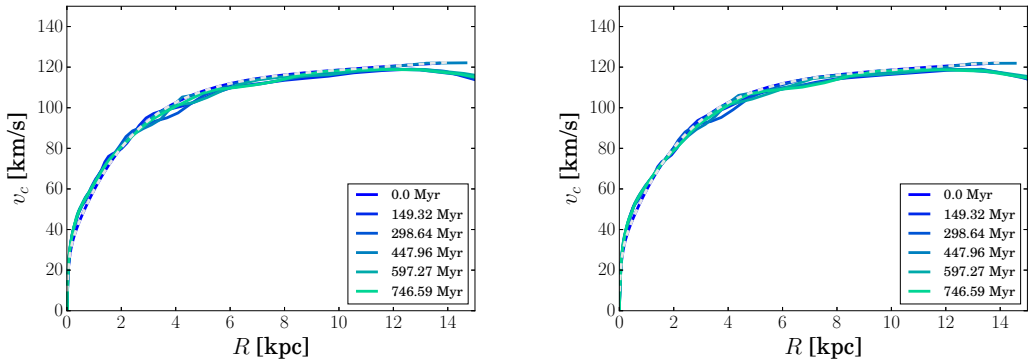

Figure 3.21: Gas rotation curve for the 4M (left panel) and 32M (right panel) models. The dashed curve corresponds to the model curve.

method, these results show that the model relaxes to the actual curve without any noticeable negative effects. In summary, the results of this section show that the N-body model produces a reasonable galaxy model with a flocculent morphology.

3.4.2 Analytic Potential Model

For this simulation, particles are sampled between $R = 0.1$ kpc and $R = 12$ kpc. The inner radius is chosen to avoid small time steps needed in the centre where $v_c(R) \to 0$ and the density is highest and the outer one is chosen to avoid the lower densities of the outer disc. The particle masses are assigned by calculating the mass within these boundaries given the surface density profile and dividing it by the number of particles. The model is evolved isothermally with $T = 10^4$ K without including self-gravity. The spiral potential is set to approximately represent the potential peak-to-peak of the N-body stellar spiral arms. The logarithmic potential and spiral arm parameters used are given in Table 3.2 of §3.2.3. The model galaxy is simulated with two levels of resolution. The particle numbers and masses, and a label identifying each simulation are given in Table 3.4.

Surface Density Maps

The surface density maps for the 2M and 30M models are shown in Figures 3.22 and 3.23, respectively, for the times $t = 156.78, 313.57, 474.08$ Myr. The model is evolved for a shorter time as the spiral structure is already prescribed. Results show that the gas density is enhanced as it passes through the spiral arm. It shows a very regular and well behaved pattern compared to the N-body model.

Table 3.4: Spiral Potential Galaxy Model Particle Numbers and Masses

Label	$N_{\rm gas}$	m_g [$M_\odot$]
2M	2×10^6	642.25
30M	30×10^6	42.82

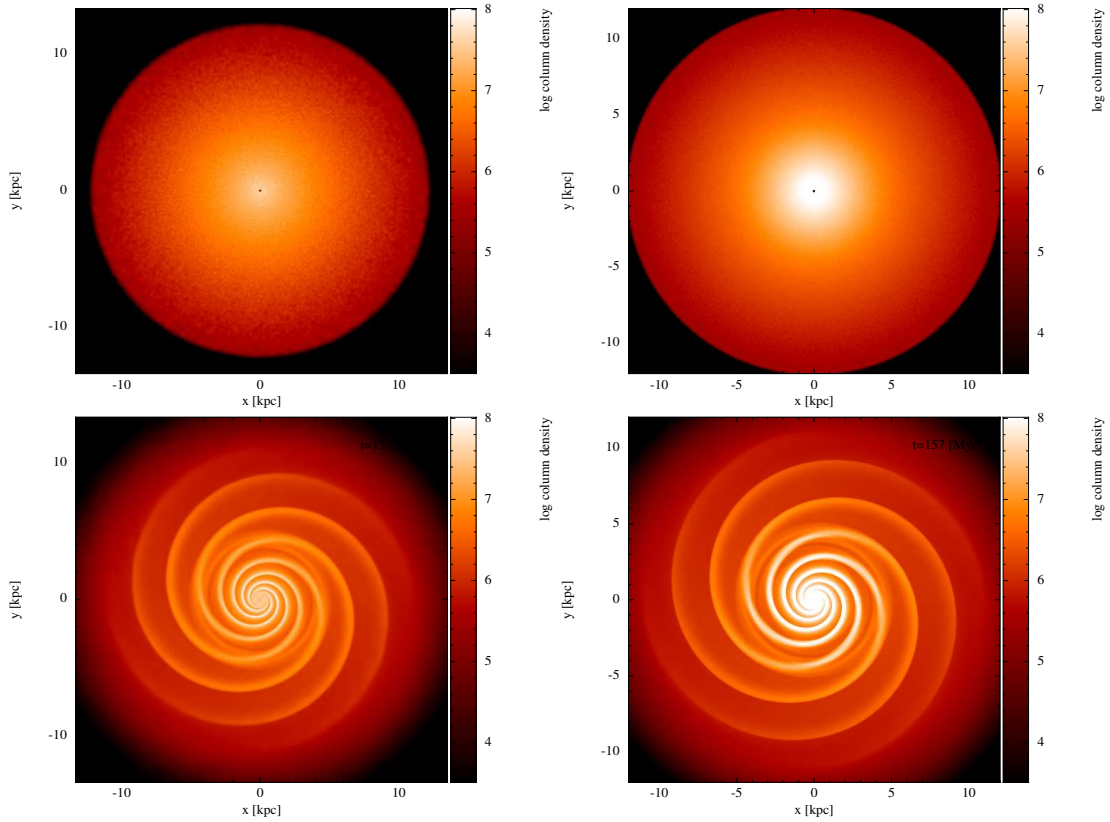

Figure 3.22: Gas surface density maps for the 2M (left column) and 32M (right column) models rendered with SPLASH (Price, 2007). The times are $t = 0$ (top) and $t = 156.78$ (bottom).

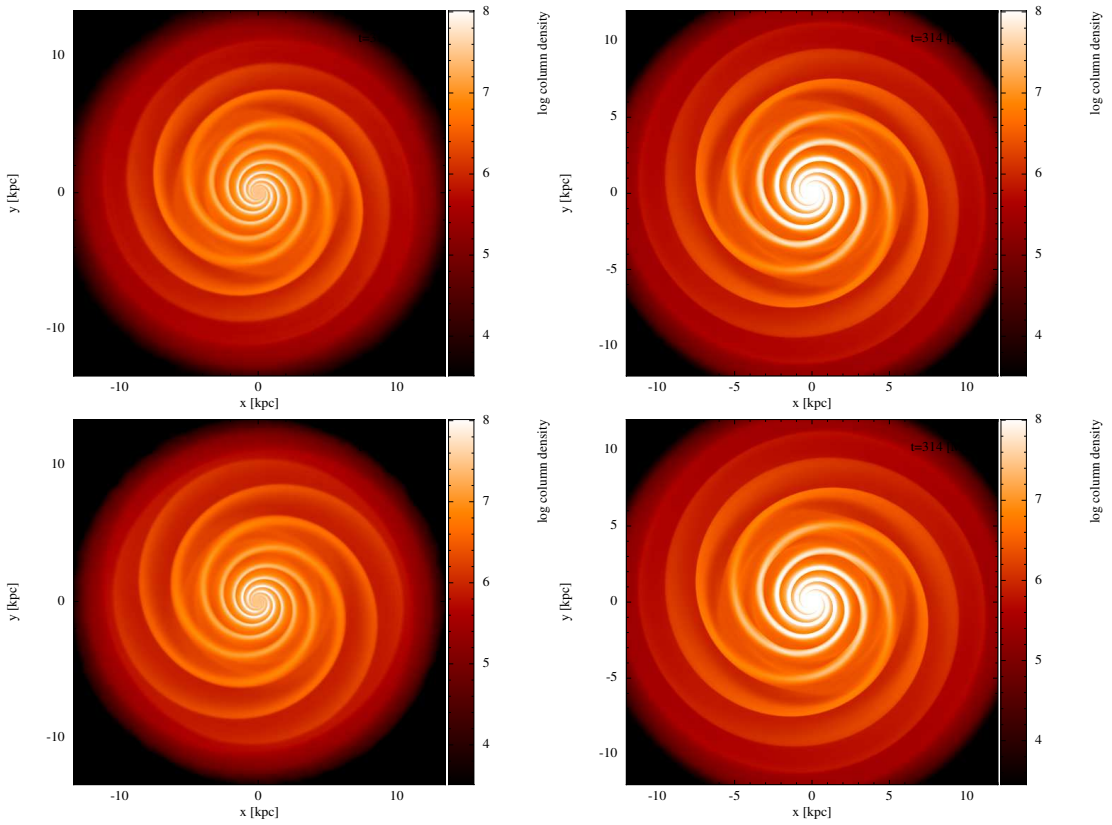

Figure 3.23: Gas surface density maps for the 2M (left column) and 32M (right column) models rendered with SPLASH (Price, 2007). The times are $t = 313.57$ (top) and $t = 474.08$ (bottom).

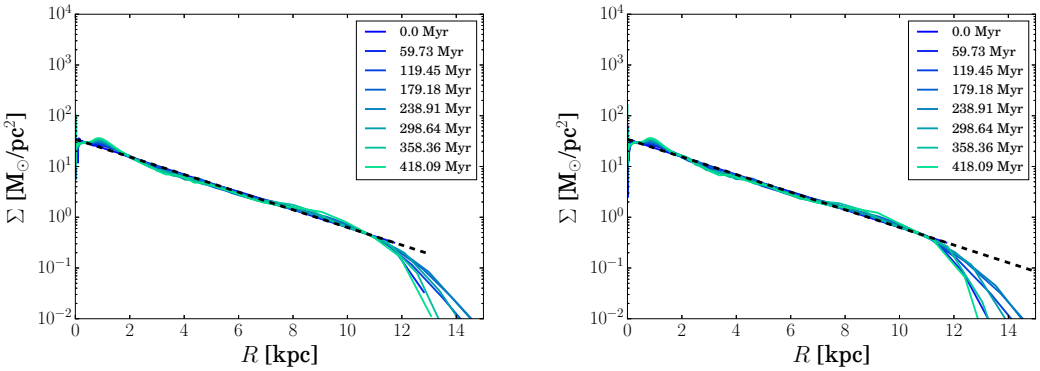

Figure 3.24: Average gas radial surface density $\Sigma(R)$ for the 2M model (left panel) and the 30M model (right panel). The black dashed line is the target exponential profile given the gas disc's parameters.

Average Radial and Vertical Density Profiles

Figure 3.24 shows the average gas surface density profile for the 2M (left panel) and 30M (right panel) models, respectively. The dark dashed line shows the target exponential profile given the gas disc's parameters. These plots show that $\Sigma(R)$ stays close to the target profile. Some variations appear which may be attributed to the effect of the spiral arm structure. Figure 3.25 shows the vertical gas density profile at $R = 0.2$ kpc and $R = 5$ kpc, respectively. The left panels correspond to the 2M model and the right ones to the 30M model. On average, the mid-plane density tends to increase and the profile becomes more compact. This is better visualised in Figure 3.26, which shows $z_{\rm rms}$ as a function of radius. The disc's average height decreases with time and settles at a slightly smaller value, but keeps a similar shape to that of the initial profile. This may be an effect of the spiral potential. The hydrostatic balance solution only used the axisymmetric potential, thus neglecting the vertical force of the arms.

Rotation Curve

Figure 3.27 shows the average rotation curve for the 2M (left panel) and 20M (right panel). The black dashed curve corresponds to the model curve. The rotation curve stays close to target value. The gas rotates slightly slower than the model at larger radius. For $R > 12$ kpc, the velocity shows a significant decrease compared to the model. The initial disc is truncated at $R = 12$ kpc, so this may be the effect of some particles moving outwards as the disc settles in the potential. This is not critical as the analysis will be focused in the inner and middle regions of the galaxy. In summary, these results show that the spiral potential simulations produce a model galaxy with properties consistent with the target density and velocity profiles.

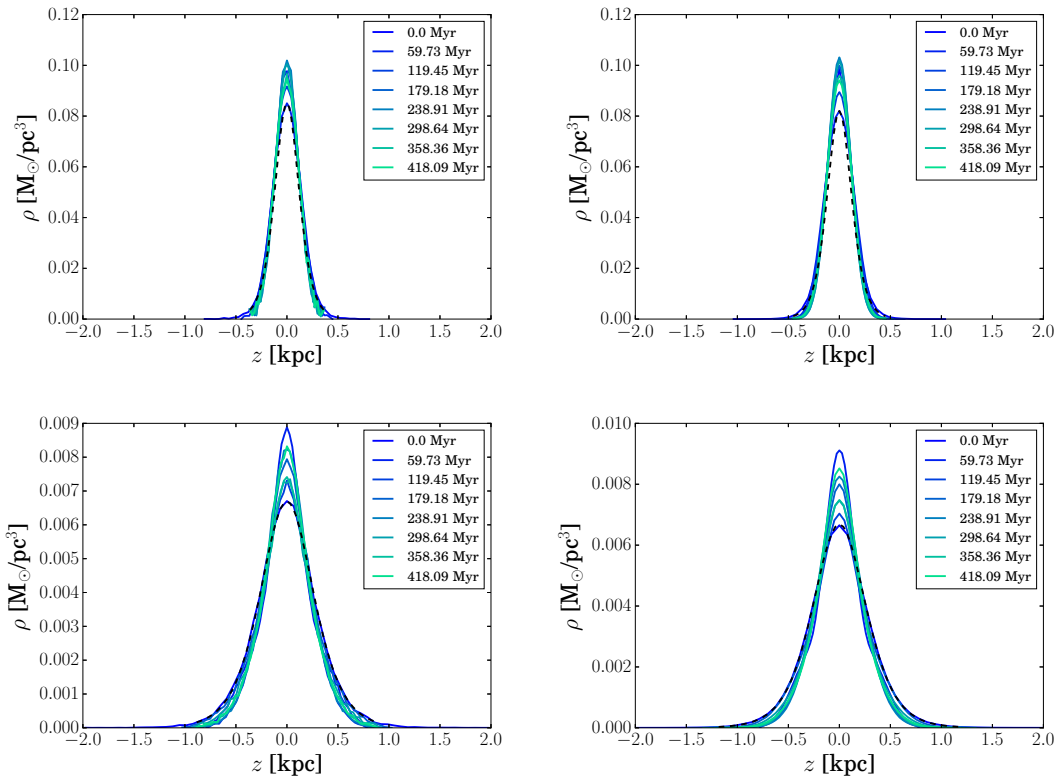

Figure 3.25: Average vertical gas volume density vertical profiles at $R = 0.2$ kpc (top), at $R = 5$ kpc (middle) , and $R = 10$ kpc (bottom). The left column corresponds to the 2M model and the right panel to the 30M model.

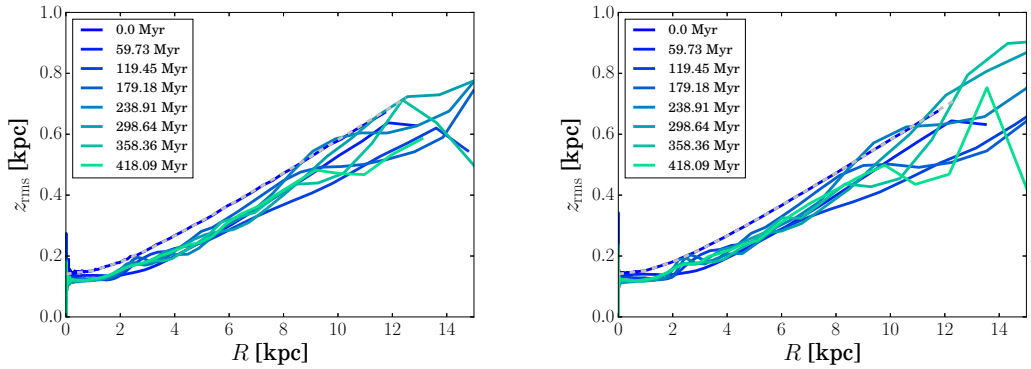

Figure 3.26: Vertical $z_{\rm rms}$ of the gas particles as a function of radius for the 2M model (left panel) and the 30M model (right panel).

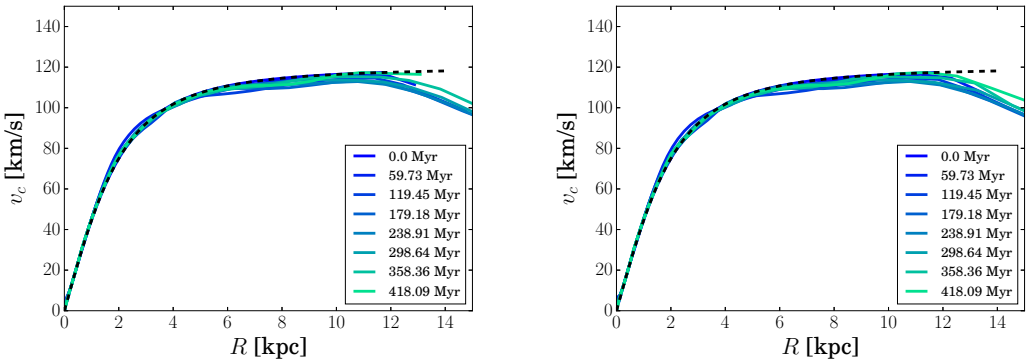

Figure 3.27: Gas rotation curve for the 2M (right panel) and 30M (left panel) models. The dashed curved corresponds to the model curve.

3.5 Final Comments

This section has described the methodology followed to generate initial conditions for a model galaxy with parameters representative of the local spiral M33. Two models were discussed. First, an N-body model obtained from the initial conditions code of McMillan & Dehnen (2007). Then, a model based on analytic potentials of the spiral arms and the axisymmetric components of a galaxy. A method for adding a gas component was also described. Isolated evolution tests showed that the models produce a morphology representative of a spiral galaxy. The N-body model produces a spiral arm morphology with clear arm-to-arm variations that can be related to flocculent galaxies whereas the spiral potential simulation produces a model comparable to a grand-design galaxy. The results of both models will be discussed in the following chapters in simulations that include heating and cooling processes in the ISM.

4

Large-Scale Gas Flows in Spiral Galaxies

The following chapter introduces the analysis of the large-scale flows in the spiral galaxy models developed in the previous chapter. The aim is to explore the characteristic flows through spiral arms. §4.1 introduces the background on previous work on observations and simulations of large-scale flows in galaxies. §4.2 presents results on the isolated evolution of the model galaxies including heating and cooling. §4.3 describes the analysis and results of the gas density and velocities in spiral arm regions. §4.4 presents an analysis of tracing the origin and evolution of gas in spiral arms. §4.5 and 4.6 show the discussion and conclusion, respectively.

4.1 Large-Scale Gas Motions in Spiral Galaxies: driving the formation of molecular clouds

Molecular cloud formation and the triggering of star formation results from the interplay of different mechanisms operating on large galactic scales and small cloud scales (e. g. Elmegreen 2002; Bonnell et al. 2013; Burkert 2017). Neutral gas from the large scales must be processed

into dense structures, where molecular clouds can form. Several mechanisms have been proposed. On the large scales, gravitational instabilities (e. g. Balbus & Cowie 1985) as well as spiral arm shocks (e. g. Roberts 1969) have been suggested as mechanisms that drive strong compressions, where the gas density increases significantly. Because the cooling rate scales with the density, these compressed regions cool quickly, which drives the gas to even higher densities. This process is known as the thermal instability (Field, 1965). Several numerical works have shown that it can be triggered in shock regions (e. g. Koyama & Inutsuka 2000, 2002) as well as in regions of colliding flows (e. g. Hennebelle & Pérault 1999; Hennebelle et al. 2008; Heitsch et al. 2005). The effect can also appear in the presence of magnetic fields (e. g. Hennebelle & Pérault 2000; Stiele et al. 2006). The simulations of Koyama & Inutsuka (2000, 2002); Heitsch et al. (2005) and Heitsch et al. (2008) show that dense regions formed by thermal instabilities can fragment into separate clouds. It is important to study this mechanisms taking into account the full galactic context.

In the gravitational instability scenario, spiral structure grows in the gas disc, which fragments to form giant clouds with mass approximately equal to the Jeans Mass ($M_J \sim c_s^4/(G^2\sigma)$). The clouds tend to form a pattern along the spiral arm analogous to "beads on a string", typically separated by a Jeans length ($\lambda_J = 2c^2/(G\Sigma)$. This scenario predicts cloud masses in the range $10^6 - 10^7\ M_\odot$ (Balbus & Cowie, 1985; Balbus, 1988; Elmegreen, 2002; Inoue & Yoshida, 2018). In the spiral arm shock scenario, as gas flows into a spiral arm it accelerates to the point of moving faster than the local sound speed. Eventually, it forms shock regions, which drive a strong density contrast. The dense gas then can cool efficiently, which can lead to the formation of dense shock fronts (Roberts, 1969; Shu et al., 1972), which can eventually fragment to form clouds (e. g Koyama & Inutsuka 2002; Heitsch et al. 2008). In spiral galaxies, a combination of both mechanisms is likely to occur in the process of molecular cloud formation.

The nature of the underlying spiral potential can have an important effect on the local gas dynamics and hence in the formation of molecular clouds (e. g. Baba et al. 2016, 2017). In the density wave model, the spiral arm is viewed as a rigid pattern rotating with a constant pattern speed. Gas orbiting inside the corotation radius overtakes the arm. As it falls to the spiral potential, it can form shocks as described in Roberts (1969). Outside corotation, the arm overtakes the gas, but it is still possible to form a shock (e. g. Gittins & Clarke 2004). In the Roberts (1969) model, as gas falls into the arm, its radial velocity increases thus moving

slightly outward. After crossing the shock, the radial velocity decreases. This shows that the perturbation is introducing streaming motions in the gas. As it follows its galactic orbit, it eventually leaves the arm. In this model, molecular clouds are formed due to the gas compressions and shocks inside the arm. Several models and simulations predict that the shock will be offset from the potential minimum (e. g. Roberts 1969; Gittins & Clarke 2004; Baba et al. 2016) except in corotation, but the position of the shock depends on the temperature of the gas but also on whether a steady state is achieved (Dobbs, 2007; Sormani et al., 2017). In this scenario, the clouds eventually make their way out of the arm and may be fragmented by shear (Koda et al., 2009).

A second scenario describes spiral arms as dynamic features with variable amplitudes and differential rotation (Goldreich & Lynden-Bell, 1965b). In this scenario, the gas flows into the spiral arm with fairly irregular motions and settles in the potential minimum (e. g. Clarke & Gittins 2006; Baba et al. 2009). The gas may flow from both sides of the arm as a large scale colliding flow, which makes the highest density gas to coincide with the arm's potential minimum (Wada et al., 2011). In addition, (Wada et al., 2011) find that the spiral pattern rotates with the rest of the galaxy, meaning that it is not behaving as a rigidly rotating pattern. However, the gas can leave the arm when the latter dissipates (e. g. Dobbs & Bonnell 2008; Baba et al. 2016).

The above works also show that the spiral arm drives significant streaming motions in the gas flow, however this will be sensitive to the local perturbation and also depends on whether the arm behaves as a steady or a dynamic one. Some works suggest that these motions can affect the formation of molecular clouds. For example, a study of M51 by Meidt et al. (2013) suggests that strong streaming motions will have a stabilising effect on GMCs due to a reduced pressure on the surface of the clouds caused by the relative motion between the cloud and nearby gas. Their results show that clouds in regions with high streaming motions have less star formation activity than other clouds in M51. This means that the gas dynamics driven by the spiral arms have a significant impact on the formation and evolution of molecular clouds (e. g. Meidt et al. 2018).

It is important to study how the large scales connect with the small scales in molecular cloud formation. The spiral arms are structures that play a role in connecting these scales. This chapter analyses the gas dynamics in two types of galaxy models: the N-body and spiral

potential models described in the previous chapter, which can show the differences between steady and dynamic spiral arm scenarios. The simulations in this chapter include heating and cooling. It is noted that the spiral potential has been specified such that the amplitude is approximately similar to those of the N-body model. §4.2 presents results on the surface density maps of the model galaxies. §4.3 shows results on the gas densities, velocities, and velocity dispersions. §4.4 shows results on tracing particle tracks showing the history of position and density as a function of time. §4.5 and §4.6 present a discussion and conclusion, respectively.

4.2 Evolution of the Model Galaxies with Cooling and Heating

This section shows the evolution of the models described in Chapter 3 including the heating and cooling curve described in §2.4 of Chapter 2. The N-body simulation was first allowed to evolve for approximately 747 Myr in isolation with an isothermal gas distribution with $T = 10^4$ K. The simulation at this point is taken as an initial condition for a new simulation with cooling and heating. In the case of the spiral potential simulation, it is allowed to evolve isothermally also at $T = 10^4$ K up to approximately 471 Myr. Then, this is used as an initial condition for a simulation with heating and cooling. The reason for choosing an initial point further in time for the N-body model is that the galaxy required some time to develop spiral structure. The choice for $t \approx 474$ Myr was due to the qualitative appearance of the spiral arms at this point. The results of this chapter are obtained at the same time time interval with respect to the point at which cooling was introduced. When cooling is introduced, the N-body model is simulated with self-gravity whereas the spiral potential model does not include self-gravity. The gravitational softening length of the N-body simulation is $\epsilon = 5$ pc for both gas and stars. A motivation for the latter is that it allows the simulation to follow the gas dynamics for longer timescales as it avoids the formation of collapsing clumps that drive the simulation to very small time steps.

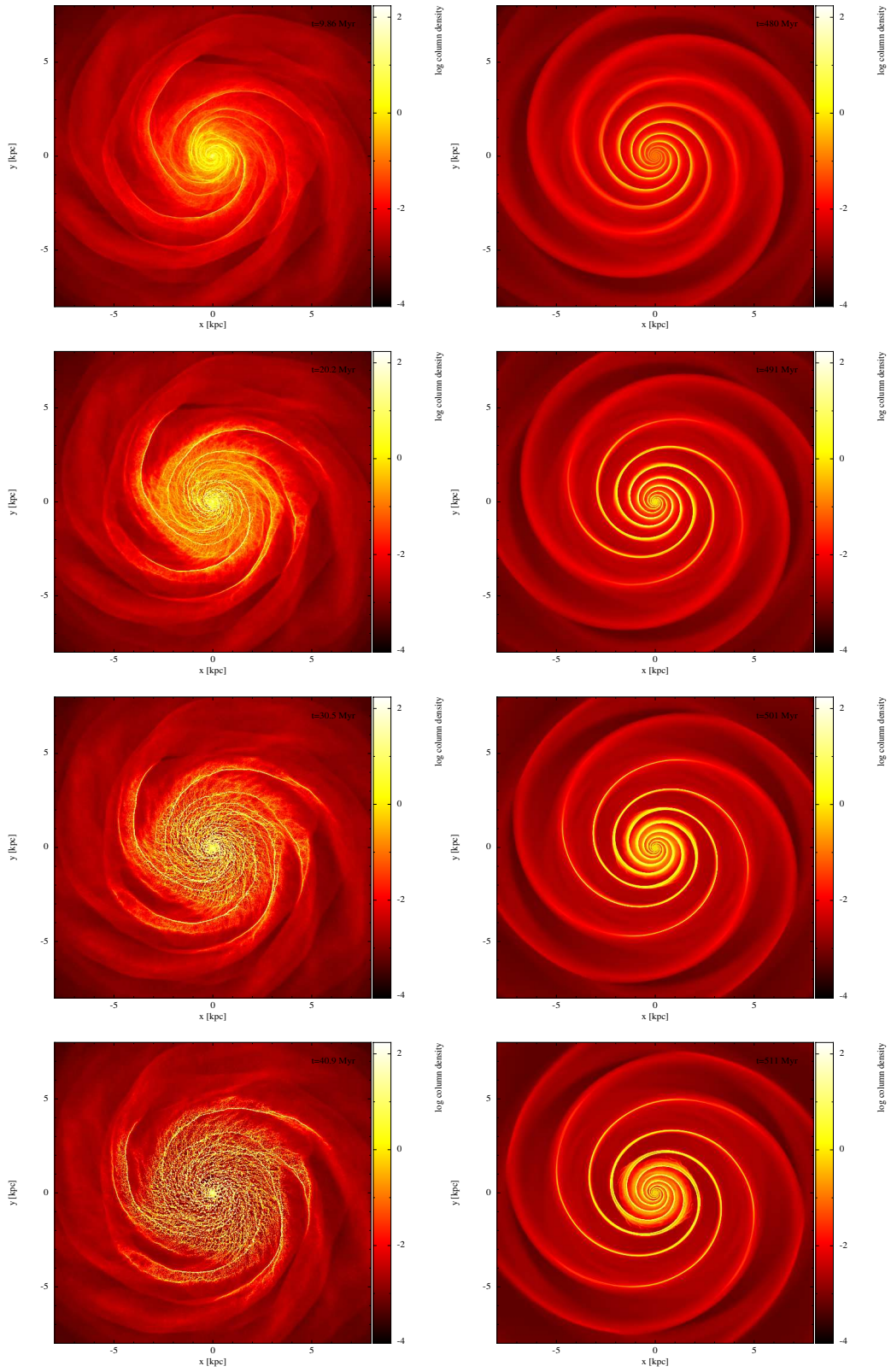

Figure 4.1: Surface density maps showing the evolution of the model galaxies with cooling. The left column corresponds to the N-body simulation and the right column to the spiral potential simulation. The times of the snapshots are $t = 9.86$ Myr (top), $t = 20.22$ Myr (second), $t = 30.53$ Myr (third), $t = 40.86$ Myr (bottom).

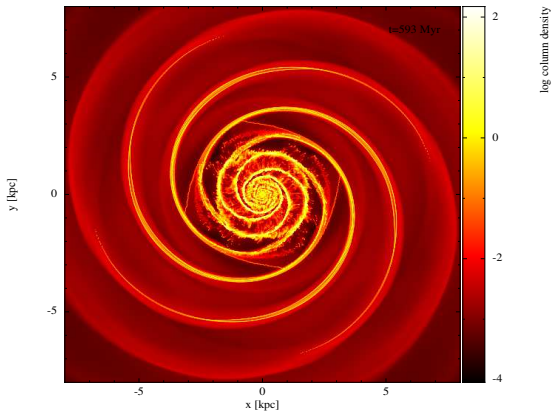

Figure 4.2: Surface density map of the spiral potential simulation at $t = 122.35$ Myr. Not including self-gravity allows to run the simulation for a longer timescale. The map shows how richer structure resembling spurs has developed near the center.

Figure 4.1 shows the evolution of the two models. The left and right columns correspond to the N-body and spiral potential simulations, respectively. The times for each row are $t = 9.86$ Myr (top), $t = 20.22$ Myr (second), $t = 30.53$ Myr (third), $t = 40.86$ Myr (bottom) with respect to the time when cooling was introduced. The galaxy's rotation is counter-clockwise in both models. In the N-body model, the surface density starts to increase near the central regions and spiral arms (top). Because the volume density is highest in these regions, the cooling rate is higher. As time progresses, (second and third panels) it is possible to see the growth of structure in both the arm and inter-arm regions. At $t = 40.86$ Myr (bottom panel), a lot of structure has fragmented into large clouds. These behaviour is expected due to the self-gravity and the lack of feedback and other injection mechanisms.

In the spiral potential simulation, the density increases first in the spiral arms (top panel). The density is higher in these regions, which implies a higher cooling rate. As the system evolves, the density contrast of the spiral arms becomes more evident. However, by $t = 40.86$ Myr it is possible to see that some of the gas originally in the arms has moved into the inter-arm region. For this simulation, it was possible to evolve the model up to $t = 592.71$ Myr, shown in Figure 4.2, which shows richer structure near the central regions. Also notice the formation of structures resembling spurs in the inter-arm regions.

Figure 4.3 shows the density-temperature distribution for both simulations at $t = 20.4$ Myr. The left and right panels correspond to the N-body and spiral potential simulations, respectively. In these plots, the dense phase is defined as gas with $\rho > 10\,\mathrm{M}_\odot\,\mathrm{pc}^{-3}$ (blue box). Most of the gas in this region has a temperature lower than ≈ 200 K. The intermediate phase is

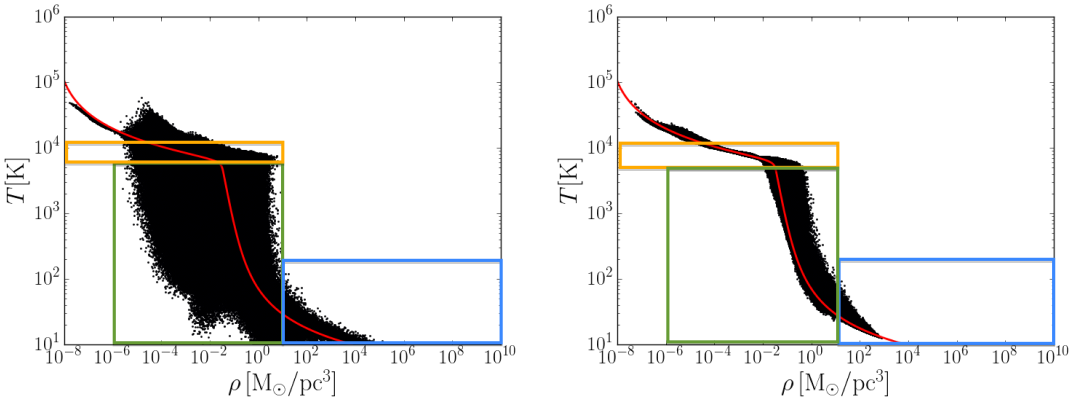

Figure 4.3: The panels show the gas temperature vs. density distribution at $t = 20.4$ Myr for the N-body simulation (left panel) and the spiral potential simulation (right panel). The blue, green, and orange boxes show the selection boundaries for the cold, intermediate, and warm phases. At this time, in the N-body model, 13.8 % of the gas is in the cold phase, 54 % in the intermediate phase, and 30.8 % is in the warm phase. In the spiral potential model, 9.1 % is in the cold phase, 25.5 % is in the intermediate phase, and 64 % is in the warm phase. These gas phase definitions are selected to plot the radial surface density profiles of Figure 4.4.

defined by the region where the density satisfies $10^{-6} < \rho < 10\,\mathrm{M}_\odot\,\mathrm{pc}^{-3}$ and the temperature satisfies $10 < T < 5000$ K. The warm phase corresponds to gas with $\rho < 10\,\mathrm{M}_\odot\,\mathrm{pc}^{-3}$ and with temperature $5000 < T < 12000$ K. The gas in the region with $T > 12000$ K is not included in our analysis because it corresponds mostly to gas close to the vertical and radial edges of the gas distribution. In both simulations, it is less than 2 % of the total gas mass.

The fraction of gas in each of the three phases specified above is computed for $t = 20.4$ Myr and $t = 35.5$ Myr. Tables 4.1 and 4.2 show the values for the N-body and spiral potential simulations, respectively. In the N-body model, the dense gas fraction increases by slightly more than a factor of 2 while the intermediate gas fraction decreases by ≈ 27 %. The warm gas fraction decreases slightly. This suggests that gas from the intermediate phase is passing to the cold phase. In the spiral potential simulation, the dense gas fraction actually decreases slightly while the intermediate gas fraction increases by approximately 36 %. Most of the gas in this model stays within the warm phase, which is about 64 % at the first time and decreases by about 8 % in the time interval considered.

The results are not surprising for the N-body model considering that the self-gravity allows for the formation of denser structures that will cool rapidly. The results for the spiral potential simulation are interesting because they suggest that the compression in the spiral arm is not strong enough to drive the formation of denser gas. Inspection of the snapshot at $t = 20.4$ Myr showed that the densest gas tends to be associated with the spiral arm and is formed inside the

Table 4.1: Gas Mass Fraction by Phases for the N-body Model

t [Myr]	dense phase [%]	intermediate phase [%]	warm phase [%]
20.4	13.8	54.0	30.8
35.5	31.1	39.2	28.3

Table 4.2: Gas Mass Fraction by Phases for the Spiral Potential Model

t [Myr]	dense phase [%]	intermediate phase [%]	warm phase [%]
20.4	9.1	25.5	64.7
35.5	6.8	34.7	57.6

corotation radius. The intermediate phase gas tends to be associated to the inter-arm regions. However, it is difficult to compare with a simulation with a similar potential and physics such as the one in Bonnell et al. (2013) because these authors use a Milky Way potential, which has a faster rotation curve and a corotation radius near the edge of the disc.

Figure 4.4 shows the radial gas surface density plots for the cold, intermediate and warm phases. This is the average surface density in a series of annular bins for each of the gas phases. The top panels shows the profiles at $t = 20.4$ Myr and the bottom panels at $t = 35.5$ Myr. In both simulations, the dense gas tends to decrease quickly with galactocentric distance and the warm gas has a relatively flat distribution. The intermediate gas phase decreases with distance, but at a lower rate than the dense gas.

In the N-body simulation, there is a significant dip in the warm gas profile near 2 kpc at $t = 20.4$ Myr. This behaviour can be explained by the fact that most of the gas is in the intermediate phase in the time interval considered. However, the dip seems to level out as time progresses. These plots show that in this model, the dense gas phase dominates the inner region of the galaxy and the warm phase dominates the outer region.

In the spiral potential simulation, results are slightly different. The warm profile does not change significantly between the two times and dominates the outer region. However, in the cold profile, some oscillations appear which may be a consequence of the spiral arm perturbation. It is interesting to note that at $t = 35.5$ Myr, the intermediate phase dominates over the dense phase. However, at $t = 20.4$ Myr, the dense phase was close to dominating the inner region, which seems that there could be some transient behaviours in the evolution of this phase. The intermediate phase still includes a fraction of gas with $T < 100$ K, which is

fairly cold, but at densities lower than $10\,M_\odot\,pc^{-3}$. This suggests that the inner region is still dominated by fairly cold gas. The spiral potential simulation does not include self-gravity. This may change this results by driving the formation of denser gas as self-gravitating structures collapse.

For most of the disc, the warm gas surface density ranges between $0.1-1\,M_\odot\,pc^{-2}$ (except for the dip at $t = 20.4$ Myr) in both simulations. The central cold gas surface density is higher in the N-body model than in the spiral potential model. At $t = 35.5$ Myr, the cold gas central surface density in the N-body reaches a value close to $10^2\,M_\odot\,pc^{-2}$ whereas in the spiral potential simulation, it stays close to $10\,M_\odot\,pc^{-2}$.

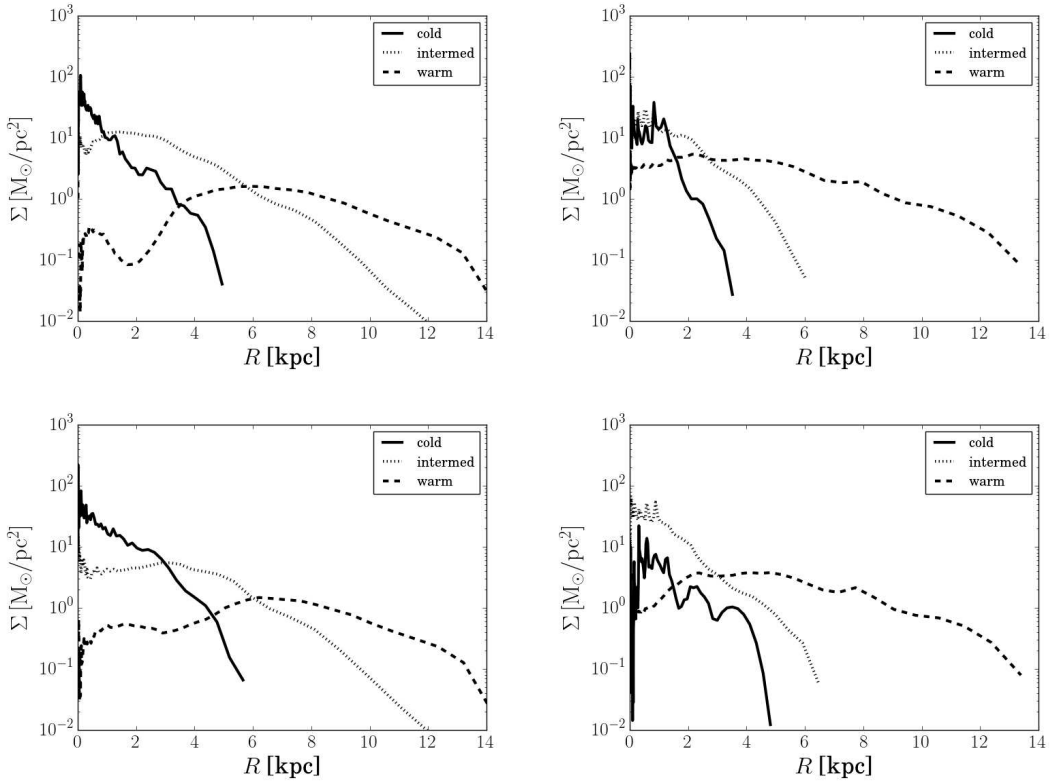

Figure 4.4: Cold (black line), intermediate(dotted), and warm (dashed line) surface density profiles for the N-body model (left column) and spiral potential simulation (right column). The top panels show the profiles at $t = 20.4$ Myr and the bottom panels at $t = 35.5$ Myr.

The global density distribution for both simulations is shown in Figure 4.5 at three times: $t = 9.864$ Myr (blue dots), $t = 20.432$ Myr (green dots), and $t = 31.0 Myr$ (red dots). For the N-body simulation (left panel), at $t = 9.864$ Myr, the distribution is dominated by the warm gas with a peak value at $\rho \approx 10^{-2}\,M_\odot\,pc^{-3}$. A lower peak due to the forming cold

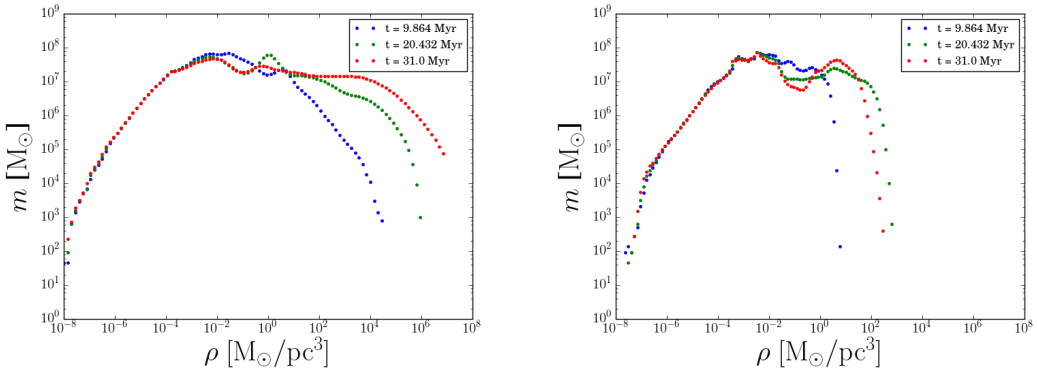

Figure 4.5: Gas density distributions for the N-body model (right panel) and the spiral potential simulation (left panel). The N-body simulation develops a high-density tail in the distribution due to self-gravity. The spiral potential simulation develops a high-density which can be driven by gas shocks and cooling in the arm regions.

phase is barely visible between 1 and $10^2\,M_\odot\,pc^{-3}$. The cold phase peak is clearly marked at $t = 20.4$ Myr near $\rho \approx 1\,M_\odot\,pc^{-3}$ and is less prominent at later times. Due to self-gravity, a tail of high-density gas develops with increasing time. Some of the high-density gas is reaching rather unrealistic values because of the lack of feedback and other injection mechanisms in the simulation. In the spiral potential simulation (right panel), the warm and cold phase peaks have clearly developed at a similar range of values. The dense gas peak in this case falls between 1 and $10^2\,M_\odot\,pc^{-3}$ and is slightly higher than that of the N-body simulation. A higher density phase is clearly developed at 31 Myr; however, it does not develop a high-density tail because self-gravity is not included. At lower densities, the distributions are very similar.

4.3 Gas Dynamics in Spiral Arms

This section aims to explore different diagnostics of the gas dynamics in the vicinity of spiral arms. §4.3.1 shows results on the gas density profiles as a function of azimuth; §4.3.2 presents results on the gas velocity profiles as a function of azimuth; §4.3.3 presents the gas velocity profiles as a function of radius and §4.3.4 presents results on the velocity dispersion profiles.

4.3.1 Azimuthal Gas Density Profiles

A useful way to analyse the gas distribution as a function of position is to map the gas surface density Σ in a cylindrical projection map where the azimuthal coordinate ϕ is in the horizontal axis and the radial coordinate R is in the vertical axis. Figure 4.6 shows the gas surface density map for the N-body simulation (left column) and the spiral potential simulation (right column) at two different times: $t = 20.43$ Myr (top panels) and $t = 34.52$ Myr (bottom panels). In these panels, the galaxy's rotation is to the right-hand side. In the N-body simulation, the results show a richer structure with higher densities associated with the inner spiral structure and the central galaxy. With time, many large clouds have formed in the inner regions ($R < 4$ kpc) due to the effect of self-gravity. The strongest density contrast forms in spiral arm regions up to ≈ 6 kpc. However, there are still some higher density features extending up to 10 kpc. In the spiral potential simulation, the variation of Σ with azimuth is regularly spaced because of the prescribed potential. There are some qualitative similarities to the N-body model in the sense that the higher density contrasts are associated to the inner spiral structure. This is more evident in the top panels. However, as time progresses, the spiral potential simulation does not develop many fragments in the inner regions because of the lack of self-gravity.

Figure 4.7 shows the volume density ρ profiles as a function of azimuth for the N-body (left column) and spiral potential (right column) simulations. The top, middle, and bottom panels of Figure 4.7 correspond to $R = 3, 4, 5, 7$ kpc, respectively. The time of the snapshots is $t = 20.43$ Myr. The data in these figures is chosen in an annulus 50 pc wide centred in the reference radius and within ± 10 pc from the mid-plane. The black curve shows the average stellar surface density, which traces the background spiral arms. Note that in terms of potential, the spiral potential model has been specified such that it has an amplitude similar to those of the N-body model.

In the N-body simulation, at $R = 3$ kpc, there are clear density peaks reaching $\approx 10^3\,\mathrm{M}_\odot\,\mathrm{pc}^{-3}$;

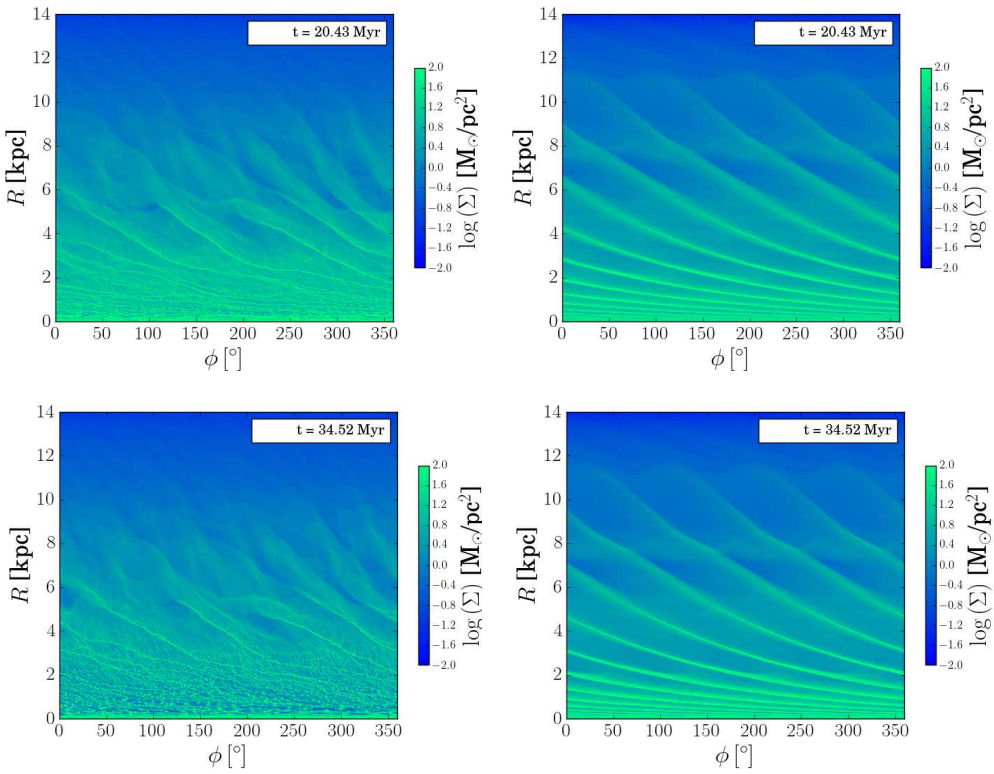

Figure 4.6: Gas surface density maps in cylindrical projection for the N-body (left column) and the spiral potential (right column) simulations. The top panels are for $t = 20.43$ Myr and the bottom panels are for $t = 34.52$ Myr.

however, there are also many local over-densities in the inter-arm regions. In the inter-arm region, the density ranges between 10^{-1} and $10\,\mathrm{M}_\odot\,\mathrm{pc}^{-3}$. At $R = 4$ kpc, it is possible to see some interesting features. For the peaks near $\phi \approx 75°$ and $\phi \approx 150°$, the density peak is not exactly aligned with the stellar surface density maximum. The gas is flowing from left to right, which means that it is forming on the side where the gas is flowing in. However, for the peak near $\phi = 250°$ it is closer to the peak of the arm and for $\phi \approx 300$, the maximum density appears to be on the left-hand side of the corresponding arm. All the density peaks at $R = 4$ kpc reach a maximum between $10^2 - 10^3\,\mathrm{M}_\odot\,\mathrm{pc}^{-3}$ and are followed by a tail of decreasing density until it reaches the low inter-arm value ($\rho \approx 10^{-2} - 10^{-1}\,\mathrm{M}_\odot\,\mathrm{pc}^{-3}$). At $R = 5$ kpc, the density features start to be less prominent. The highest value is around $10\,\mathrm{M}_\odot\,\mathrm{pc}^{-3}$ and the inter-arm density is around $10^{-2}\,\mathrm{M}_\odot\,\mathrm{pc}^{-3}$. The peaks are not necessarily aligned with the background spiral arm peaks. An interesting feature is how the peak around $\phi \approx 225°$ is a mirror image of the one around 125°. For $R = 6$ kpc and $R = 7$ kpc, the density falls to values around $10^{-2}\,\mathrm{M}_\odot\,\mathrm{pc}^{-3}$ and $10^{-3}\,\mathrm{M}_\odot\,\mathrm{pc}^{-3}$. The background potential is dominated by a high number of modes, which is still traced by the gas features.

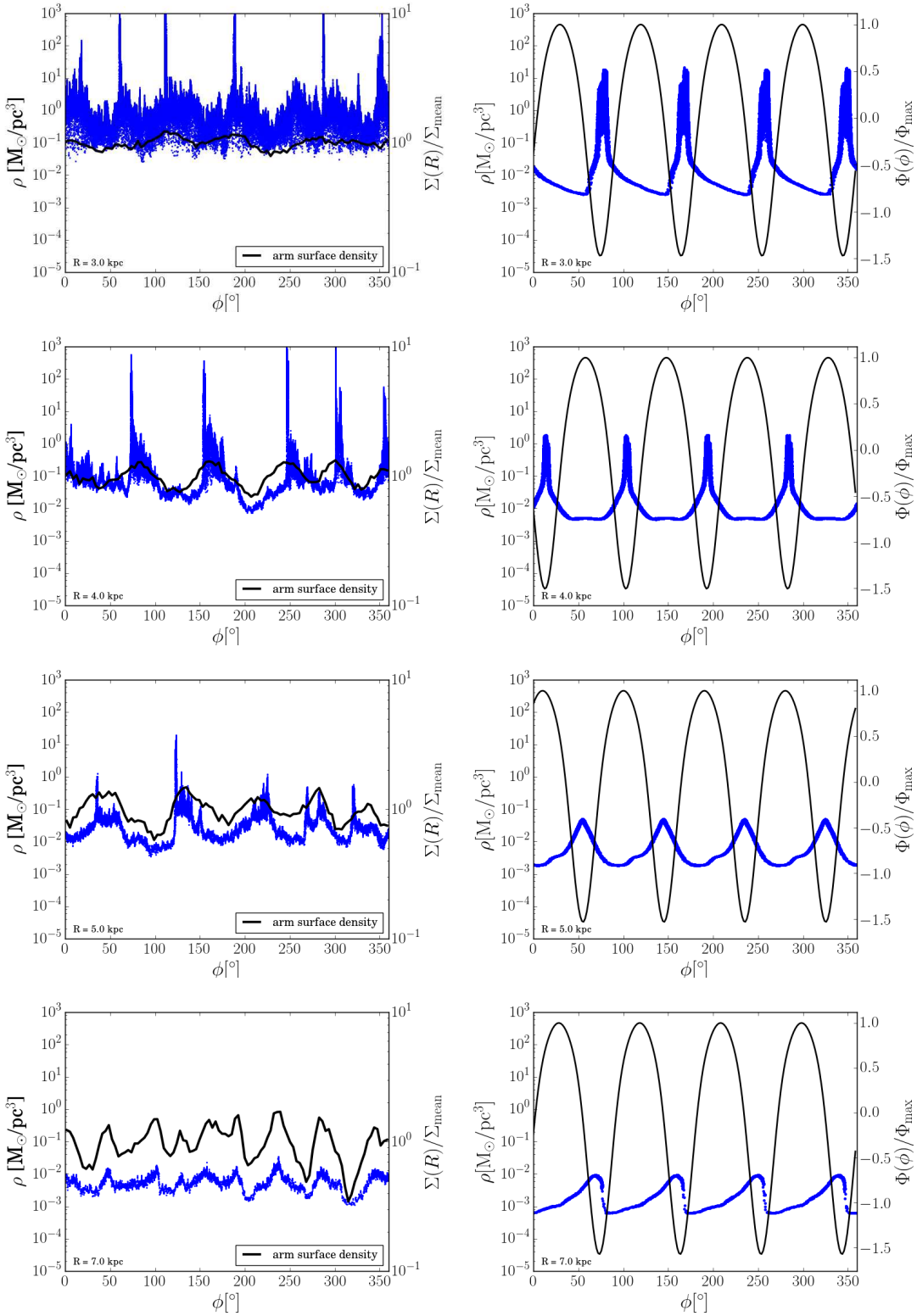

Figure 4.7: Azimuthal gas density profiles for the N-body (left column) and spiral potential (right column) simulations. The panels show the profiles at the following radii: $R = 3$ kpc (top), $R = 4$ kpc (second), $R = 5$ kpc (third), $R = 7$ kpc (bottom). The time is $t = 20.43$ Myr. The particles are chosen in an annulus 50 pc wide centred in the reference radius and within ±10 pc from the mid-plane. In terms of potential, the spiral model (left column) has been specified such that the amplitude is approximately similar to that of the arms in the N-body model.

In the spiral potential simulation, at $R = 3$ kpc (top left of Figure 4.7) the density profile shows four density peaks due to the underlying $m = 4$ spiral. The density peak is forming on the side of the arm where the gas is leaving and reaches a value of $\approx 10\,\mathrm{M}_\odot\,\mathrm{pc}^{-3}$. The minimum inter-arm density is between $(2-4)\times 10^{-3}\,\mathrm{M}_\odot\,\mathrm{pc}^{-3}$. The typical densities are lower than that of the N-body model at the same radius and has a similar behaviour to the $R = 4$ kpc region of this model in the sense that the density decreases more slowly on the left-hand side of the peak. At $R = 4$ kpc of the spiral potential, the density peak is close to the potential minimum as it is near the corotation radius. The density ranges between $\approx 4\times 10^{-3}\,\mathrm{M}_\odot\,\mathrm{pc}^{-3}$ and $\approx 2\,\mathrm{M}_\odot\,\mathrm{pc}^{-3}$. At $R = 5$ kpc, which is outside corotation, the density profile starts to change in shape. The range of densities are not that different to the N-body simulation. At $R = 6$ and $R = 7$ kpc (left panels Figure 4.7), it is possible to see how the density profile is reversed with respect to those at inner radii. Considering that self-gravity is not included, it is interesting that these density values are roughly similar to those of the N-body model.

4.3.2 Gas velocity profiles as a function of azimuth

The radial velocity v_R map in a cylindrical map is shown in Figure 4.8 at times $t = 20.43$ Myr (top) and $t = 34.52$ Myr (bottom). For the N-body simulation (left columns), the map traces well the location of the arms, where a strong velocity contrast forms. Galactic rotation is in the positive ϕ direction. Shocks are forming in the regions of strong velocity contrast. The map shows that the gas can reach $v_R \approx \pm 20$ $\mathrm{km\,s}^{-1}$ depending on its position on the arm. For the spiral potential simulation (right columns), the behaviour is fairly similar but with a more regular structure due to the imposed potential. The velocity contrast is blurred at the around 5 kpc, which is near the corotation radius. The N-body simulation does develop a richer structure in these maps. A similar map for the circular velocity v_ϕ is shown in Figure 4.9 at the same times. In both simulations, it shows the increase of the rotation curve as a function of radius. Most of the velocity deviations occur in the regions of the spiral arms and the gas rotates at different velocities in the arm and inter-arm regions. These differences will be discussed in more detail in the azimuthal profiles shown below.

The radial v_R and azimuthal $v_{\phi(\mathrm{rel})}$ (relative to the mean circular velocity) profiles with respect to ϕ for several radii are shown in Figure 4.10. The profiles are compared to the background spiral arms. The left column shows results for the N-body, which uses the stellar surface density to trace the spiral arms. The right column shows the results for the spiral

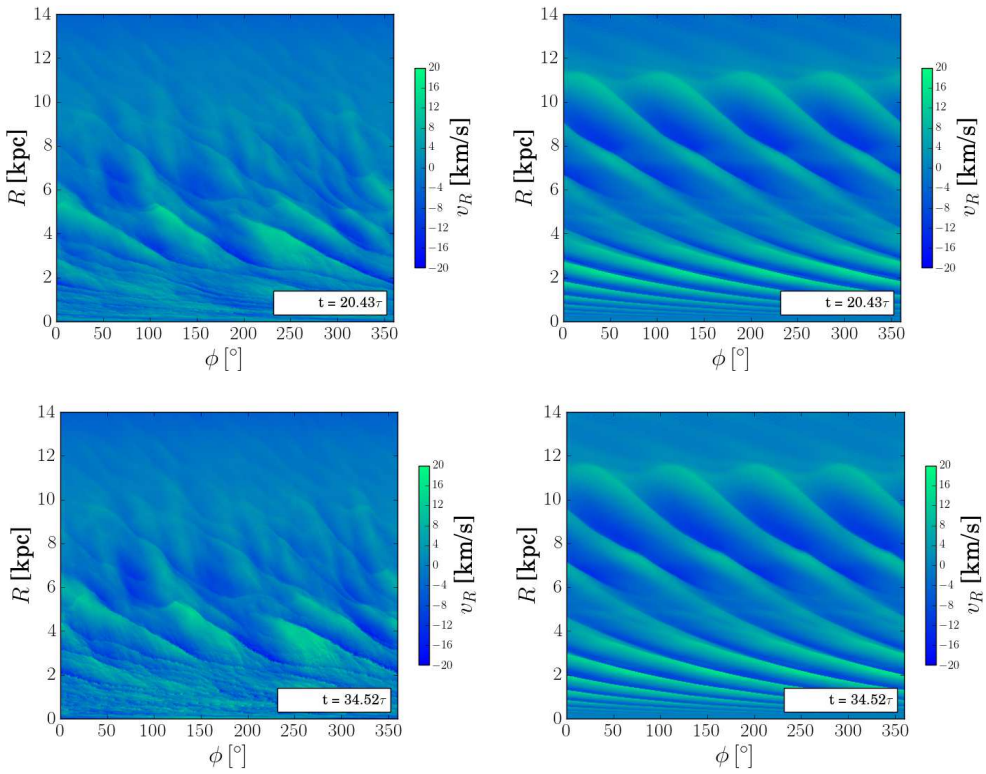

Figure 4.8: Gas radial velocity v_R maps in a cylindrical coordinates projection for the N-body (left column) and the spiral potential (right column) simulations. The top panels are for $t = 20.43$ Myr and the bottom panels are for $t = 34.52$ Myr.

potential simulation, which uses the potential to trace the arms. The time of the snapshots is $t = 20.43$ Myr.

For the N-body simulation, the tendency of the profiles is qualitatively similar for $R = 3, 4$ and 5 kpc (top, second, third panels). The gas moves in the positive ϕ direction. As gas flows into a spiral arm, it gains a positive v_R peaking at $\approx 10 - 15$ km s^{-1} then changes abruptly to negative values. At $R = 3$, it can fall down $v_R \approx -10$ to -15 km s^{-1}. At larger radii, the minimum velocity is ≈ -5 km s^{-1}. In terms of the relative circular velocity $v_{\phi(\mathrm{rel})}$, it can also reach minimum and maximum values of -10 km s^{-1} and 10 km s^{-1} at $R = 3$ kpc. As the radius increases, the oscillation's amplitude tends to decrease. The circular velocity tends to be minimum when the radial velocity is highest. At $R = 7$ kpc, the variation both in v_R and $v_{\phi(\mathrm{rel})}$ is not larger than ± 5 km s^{-1}, but still shows the effect of the local spiral structure.

In the spiral potential simulation, the profiles change gradually with radius. At $R = 3$ kpc, the radial velocity also oscillates between $\approx \pm 15$ km s^{-1}. At $R = 4$ kpc, it oscillates between -10 km s^{-1} and 7 km s^{-1}. It has a lower amplitude at $R = 5$ kpc and it increases again at

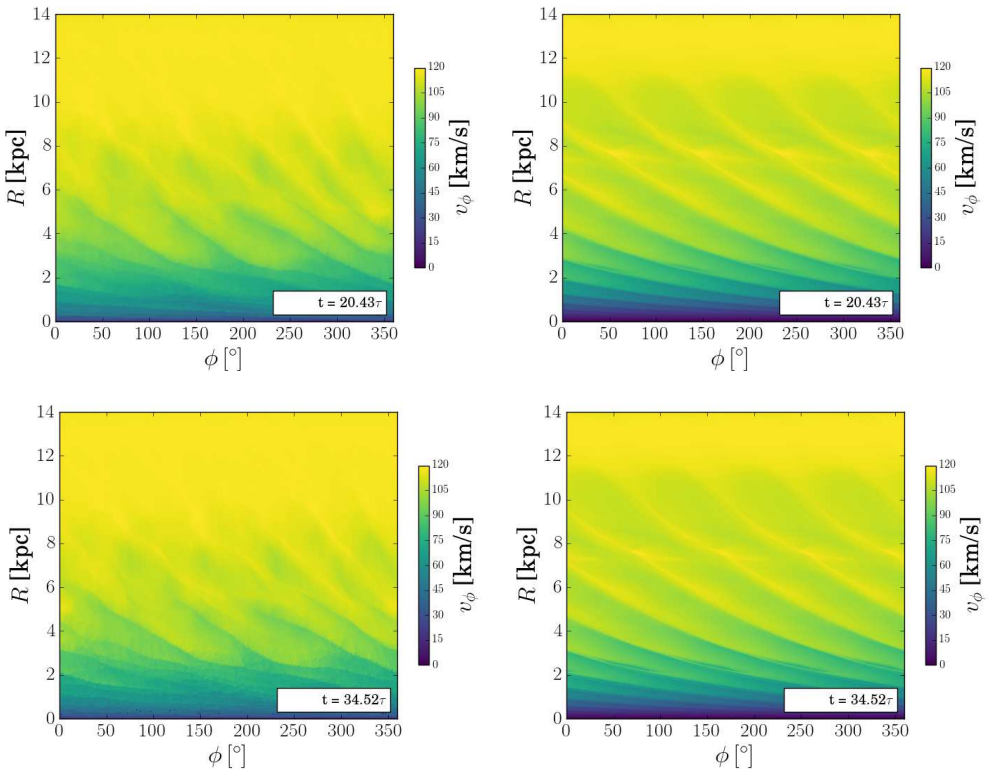

Figure 4.9: Gas azimuthal velocity v_ϕ maps in a cylindrical coordinates projection for the N-body (left column) and the spiral potential (right column) simulations. The top panels are for $t = 20.43$ Myr and the bottom panels are for $t = 34.52$ Myr.

$R = 7$ kpc with minimum and maximum values of -15 and 10 $\mathrm{km\,s^{-1}}$. In terms of $v_{\phi(\mathrm{rel})}$, at $R = 3$ kpc, it oscillates between approximately ± 10 $\mathrm{km\,s^{-1}}$. It falls to around ± 5 $\mathrm{km\,s^{-1}}$ at $R = 4$ kpc and $R = 5$ kpc, and increases slightly at $R = 7$ kpc. The maximum v_R also occurs where $v_{\phi(\mathrm{rel})}$ is lowest. The low velocity perturbations at $R = 5$ kpc are a result of this region being close to corotation.

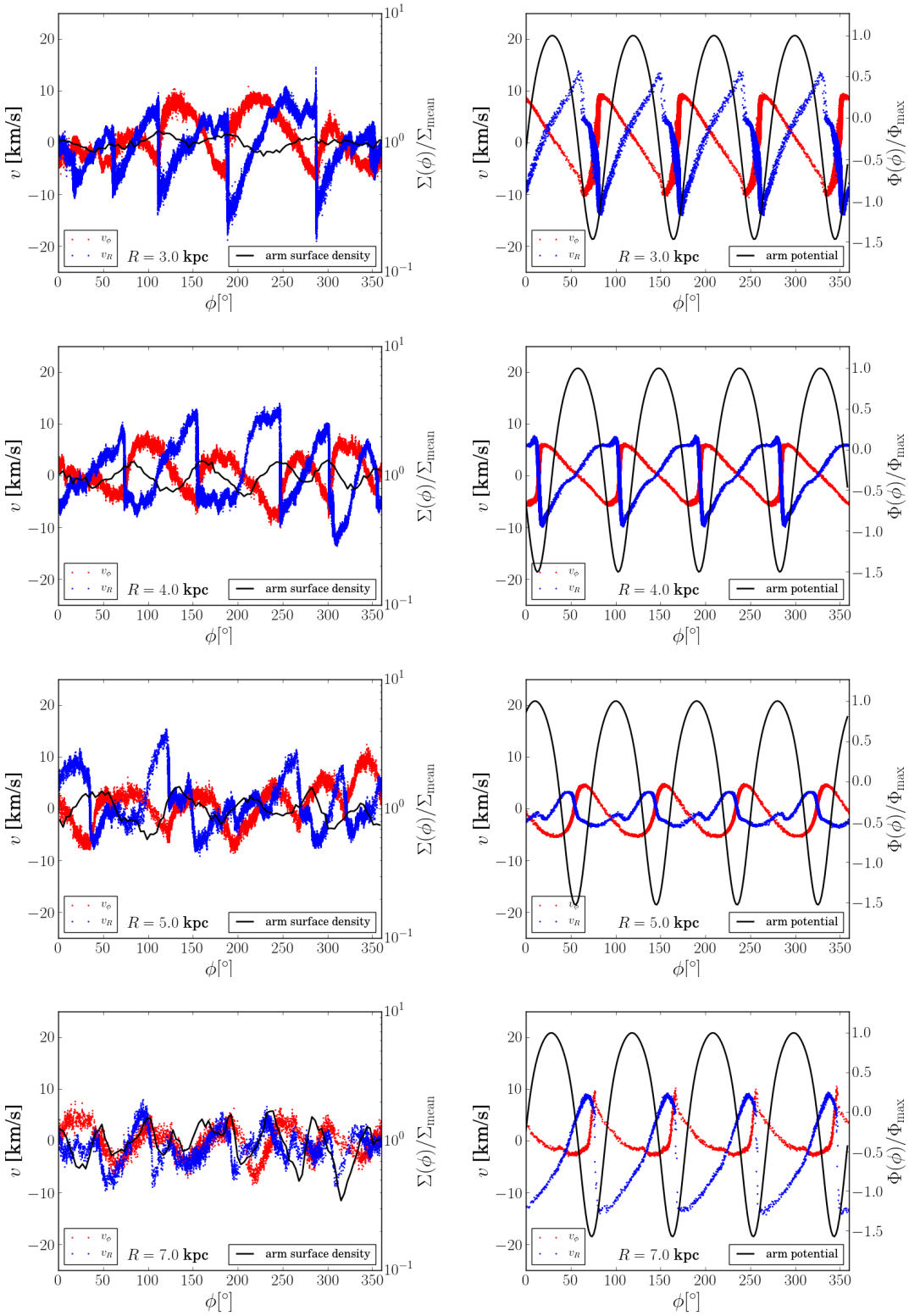

Figure 4.10: Azimuthal gas velocity profiles for the N-body (left column) and spiral potential (right column) simulations. The blue and red dots correspond to v_R and v_ϕ, respectively. The panels show the profiles at the following radii: $R = 3$ kpc (top), $R = 4$ kpc (second), $R = 5$ kpc (third), $R = 7$ kpc (bottom). The time is $t = 20.43$ Myr. The particles are chosen in an annulus 50 pc wide centred in the reference radius and within ±10 pc from the mid-plane.

4.3.3 Gas velocity profiles as a function of radius

The velocity profile as a function of radius is briefly visited in this section. Instead of averaging azimuthally on annular bins, particles are selected in narrow angular regions $\delta\phi = 1.15^\circ$ wide and within ±10 pc in the vertical direction. Four directions are analysed ($\phi = 0^\circ, 90^\circ, 180^\circ, 270^\circ$). For illustration, the results for $\phi = 0$ are shown as the results do not change dramatically between directions.

The radial velocity v_R versus radius is shown in Figure 4.11. The left and right panels correspond to the N-body and spiral potential simulations, respectively. In both models, the spiral structure is introducing oscillations in the radial velocity. There are differences in the profiles due to the difference in the background potential. It is interesting to note that the strong oscillations start to decrease at $R = 4$ kpc. This is close to the corotation radius of the dominant arms in the N-body model and of the spiral perturbation assumed in the potential simulation.

Figure 4.12 shows the circular velocity v_ϕ as a function of radius. For the N-body model (left panel), the profile shows some step-shaped features, particularly one near $R = 2$ kpc. These are associated to gas flowing in the spiral arm regions. The spiral potential simulation (right panel) shows a more periodic behaviour of this step-shaped feature. This stops at around 5 kpc, near the corotation radius, and the shape of the oscillation changes. This is an interesting difference to note between the two models. The spiral perturbation is driving significant streaming motions in the azimuthal direction.

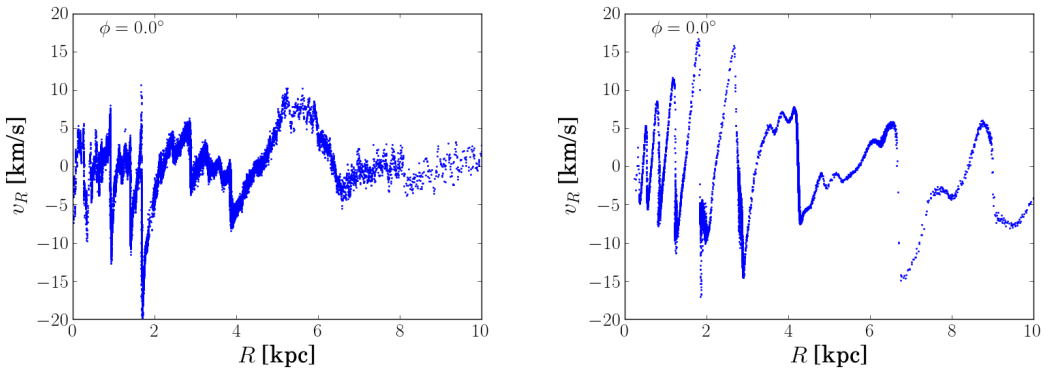

Figure 4.11: Radial velocity v_R profile for the N-body (left panel) and the spiral potential (right panel) at $t = 20.4$ Myr. Particles are selected in a narrow angular region $\approx 1.15°$ wide and within ± 10 pc in the vertical direction. For the dominant arms, the corotation radius is ≈ 4.5 kpc for the N-body simulation. For the spiral potential model, corotation is 4.57 kpc.

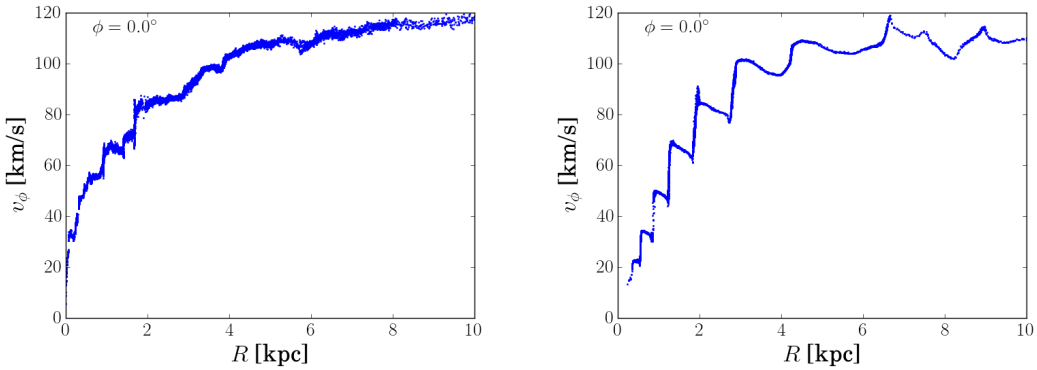

Figure 4.12: Azimuthal velocity v_ϕ profile for the N-body (left panel) and the spiral potential (right panel) at $t =$. Particles are selected in a narrow angular region $\approx 1.15°$ wide and within ± 10 pc in the vertical direction. For the dominant arms, the corotation radius is ≈ 4.5 kpc for the N-body simulation. For the spiral potential model, corotation is 4.57 kpc.

4.3.4 Velocity Dispersion Profiles

Figure 4.13 shows the velocity dispersion map in a cylindrical projection for the N-body (left column) and spiral potential (right column) simulations. The snapshots correspond to the times $t = 20.43$ Myr and $t = 34.52$ Myr. The dispersion is calculated with the magnitude of the gas velocity. These figures show that in both simulations, the highest velocity dispersion tends to be associated with spiral arm regions. It also tends to grow with time, as the spiral regions at $t = 20.42$ Myr show brighter colours. It is interesting to see that the region around the corotation radius in the spiral potential simulation (left column) is marked by an overall lower dispersion (darker colours). The velocity dispersion as a function of azimuth are shown at different radii in Figure 4.14. The left and right columns correspond to the N-body and spiral potential simulations, respectively.

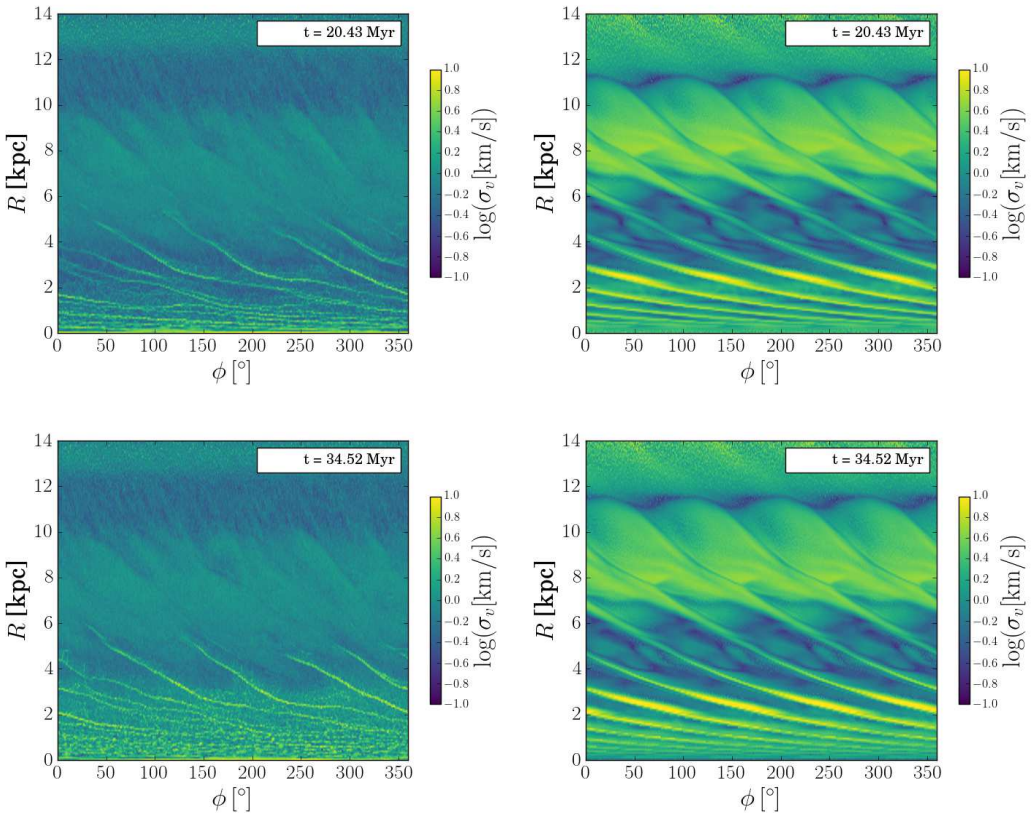

Figure 4.13: Gas velocity dispersion σ maps in a cylindrical coordinates projection for the N-body (left column) and the spiral potential (right column) simulations. The top panels are for $t = 20.43$ Myr and the bottom panels are for $t = 34.52$ Myr.

To generate the plots in Figure 4.14, particles are selected within an annular region spec-

ified by a central radius R, a radial width ΔR, and a vertical width Δz. For convenience, this triad of parameters will be noted as follows: $(R\,[\mathrm{kpc}], \Delta R\,[\mathrm{pc}], \Delta z\,[\mathrm{kpc}])$.

For the N-body simulation, the parameters of these annular regions are specified as follows: $(3.0\,[\mathrm{kpc}], 5.0\,[\mathrm{pc}], 10.0\,[\mathrm{pc}])$; $(4.0\,[\mathrm{kpc}], 10.0\,[\mathrm{pc}], 10.0\,[\mathrm{pc}])$; $(5.0\,[\mathrm{kpc}], 20.0\,[\mathrm{pc}], 10.0\,[\mathrm{pc}])$; $(7.0\,[\mathrm{kpc}], 50.0\,[\mathrm{pc}], 20.0\,[\mathrm{pc}])$. For the spiral potential simulation, these annular regions are specified as: $(3.0\,[\mathrm{kpc}], 5.0\,[\mathrm{pc}], 10.0\,[\mathrm{pc}])$; $(4.0\,[\mathrm{kpc}], 10.0\,[\mathrm{pc}], 20.0\,[\mathrm{pc}])$; $(5.0\,[\mathrm{kpc}], 40.0\,[\mathrm{pc}], 20.0\,[\mathrm{pc}])$; $(7.0\,[\mathrm{kpc}], 50.0\,[\mathrm{pc}], 20.0\,[\mathrm{pc}])$. The regions become wider in both directions with increasing galactocentric radius because of the overall decrease of gas density. At larger R, it is necessary to use bigger regions to obtain adequate plots. The above parameters for both simulations were chosen "by eye" and by inspecting the level in which the plots provided a representative sample of the selected region.

Once the particles are selected, the velocity dispersions are calculated using all the neighbouring particles that fall within a fixed radius around a selected particle. The radius used to obtain the plots in Figure 4.14 is 100pc, which is significantly larger than the typical smoothing lengths of particles in this region. For selected particles close to an edge of the annular region, particles outside the region that fall within the specified radius are still included in the calculation of the dispersion.

In both cases, the highest dispersions are associated with the spiral arms, but the shape of the profile varies between the two. For the N-body simulation, the dispersions are higher at inner radii (top and second left panels). The peak dispersions can be as high as 4 $\mathrm{km\,s^{-1}}$. It is interesting that not all the peaks have similar values in the N-body simulation, which reflects on the variable amplitudes of the spiral arm. At larger radii (third and bottom panel), the dispersion is rather low considering that there is some spiral structure present. For the spiral potential simulation, the dispersion decreases with radius, but at $R = 7$ kpc (bottom panel) it is slightly higher than at $R = 5$ kpc. In this simulation, gas self-gravity is not included, which suggests that the dispersion may be an effect of the gas passage through the arm.

Figure 4.12 shows the velocity dispersion as a function of radius calculated around particles selected in a narrow angular region (1.14° wide) along the $\phi = 0.0$ direction. As in the azimuthal plots, the velocity dispersion is calculated using neighbours within a radius of 100 pc from a selected particle. In the N-body simulation (left panel), the overall dispersion tends to decrease with galactocentric distance. However, there are peaks associated to the spiral

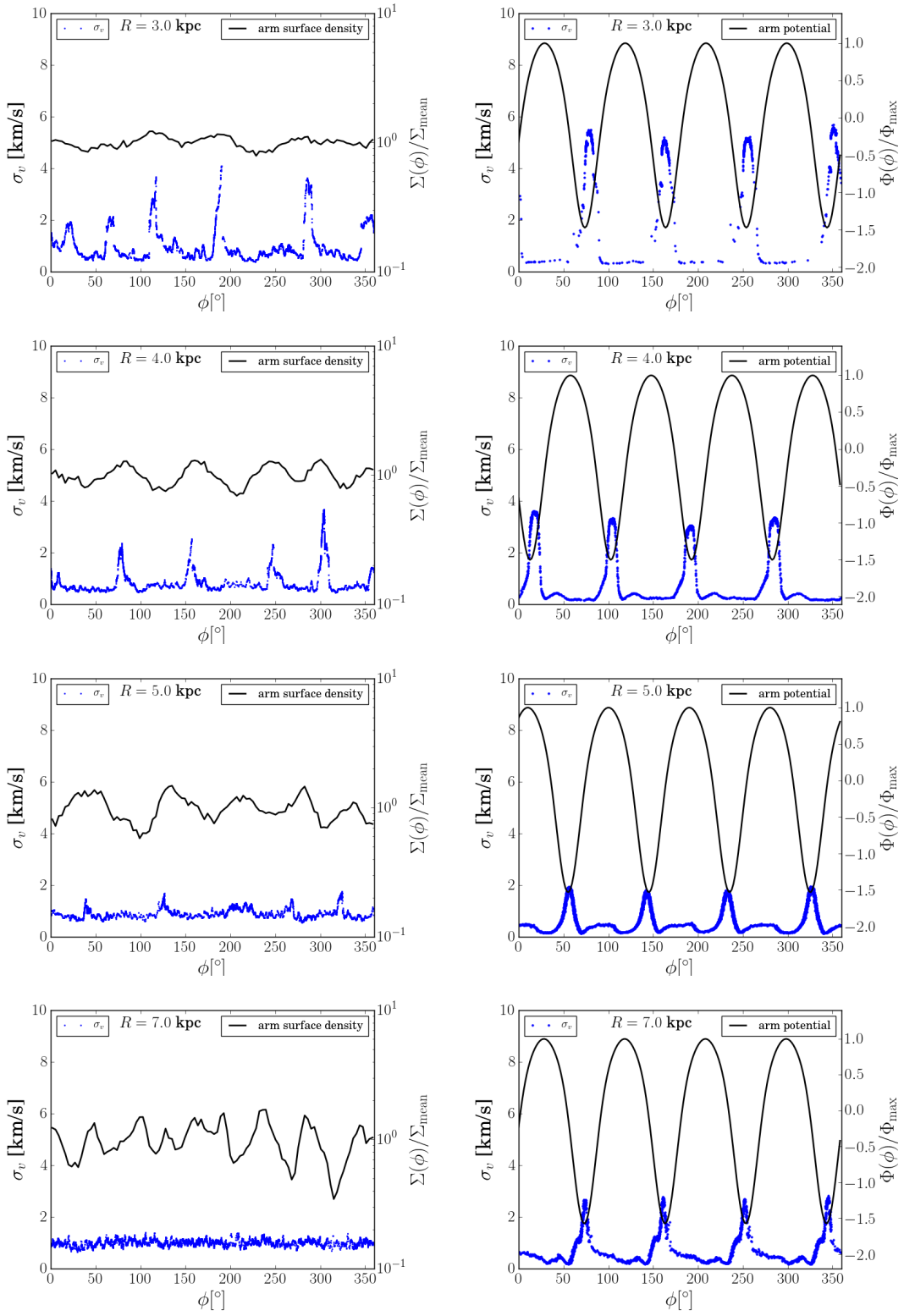

Figure 4.14: Gas velocity dispersion σ as a function of azimuth for the N-body (left column) and spiral potential (right column) simulations. The parameters of the annular regions specified for the plotted particle selection are described in the text. The velocity dispersion is calculated using neighbours within a radius of 100 pc from a selected particle. This length is larger than the typical smoothing lengths of the individual particles. For the dominant arms, the corotation radius is $\approx$ 4.5 kpc for the N-body simulation. For the spiral potential model, corotation is 4.57 kpc.

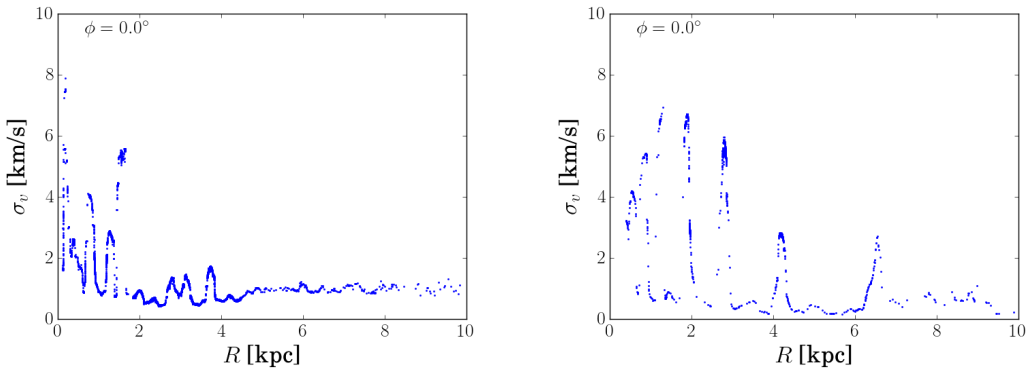

Figure 4.15: Gas velocity dispersion σ as a function of radius for the N-body (left column) and spiral potential (right column) simulations. Particles are selected in a narrow angular region $\approx 0.57°$ wide and within ± 10 pc in the vertical direction. The velocity dispersion is calculated using neighbours within a radius of 100 pc from a selected particle. This length is larger than the typical smoothing lengths of the individual particles. For the dominant arms, the corotation radius is ≈ 4.5 kpc for the N-body simulation. For the spiral potential model, corotation is 4.57 kpc.

structure. There is one particular feature near $R = 2$ kpc reaching a dispersion of almost 6 $\mathrm{km\,s^{-1}}$. This is associated to a dense cloud. A similar analysis in other directions does not show that feature, but gives a similar dispersion profile. In the spiral potential simulation (right panel), the peak σ increases with radius until around 2 kpc, and then decreases with radius. These peaks are associated to spiral arms and have higher values than those in the N-body simulation. These results show that the velocity dispersion has a dependence on the background spiral potential. However, it is possible that in the N-body region the self-gravity is also playing an additional role in driving the dispersion particularly around dense clouds (discussed in Chapter 6).

4.4 Tracing the origin and evolution of gas in spiral arms

In SPH, it is possible to select particles at a given time and then track their evolution as a function of time. This is useful to select the particles inside spiral arms and investigate their origin as well as their future evolution. Figure 4.16 shows the evolution of particles at for N-body simulation (left column) and the spiral potential simulation (right column). The particles are selected at $t = 20.43$ Myr using a density threshold of $10.0\,\mathrm{M}_{\odot}\,\mathrm{pc}^{-3}$. The tracked positions are shown at times $t = 0.0$ Myr (top), $t = 13.38$ Myr (second), $t = 26.77$ Myr (third), $t = 40.16$ Myr (bottom). The time where the particles are selected is located between the second and third panels.

In both simulations, qualitatively there is a fraction of particles at $t = 0.0$ that are located outside the arms and another in denser features tracing an arm. However, in the N-body simulation most of the particles that end in the arms and dense clouds are coming from the upstream side of the arm. In the spiral potential model, the particles' initial positions are widespread around a denser section tracing the shape of the arm. These results that in both models, the gas that ends in dense structures originates on the larger scales.

In the N-body simulation, which includes self-gravity, the sequence shows that in approximately 13 Myr (left column top to second) the gas has condensed into very thin structures tracing the spiral arms. It is interesting to note that there are also some dense structures forming in the inter-arm regions. At $t = 26.77$ Myr and $t = 40.16$ Myr (third and bottom), the gas in the arms has fragmented into denser clouds. Near the centre, there is some less dense gas around denser clouds. In this region, the rotation curve decreases quickly with radius. In the central region, the rotation curve may be close to the profile of solid body rotation, which means that structures in this regions are subject to almost no shear due to rotation. However, as the right panel of Figure 4.12 shows, the spiral potential model still shows important jumps in v_{ϕ} as a function of galactocentric distance near the central region.

In the spiral potential simulation, which does not include self-gravity, the sequence shows that the gas particles proceed from the larger scales and flow into the arm (left top panel to second and third). In contrast to the N-body simulation, the gas that was selected in the arm starts to flow out of it. In the bottom panel, it is possible to see how the gas has spread to a wider spatial distribution showing that the gas is moving out of its densest state. This may be facilitated by the lack of self-gravity in the simulation.

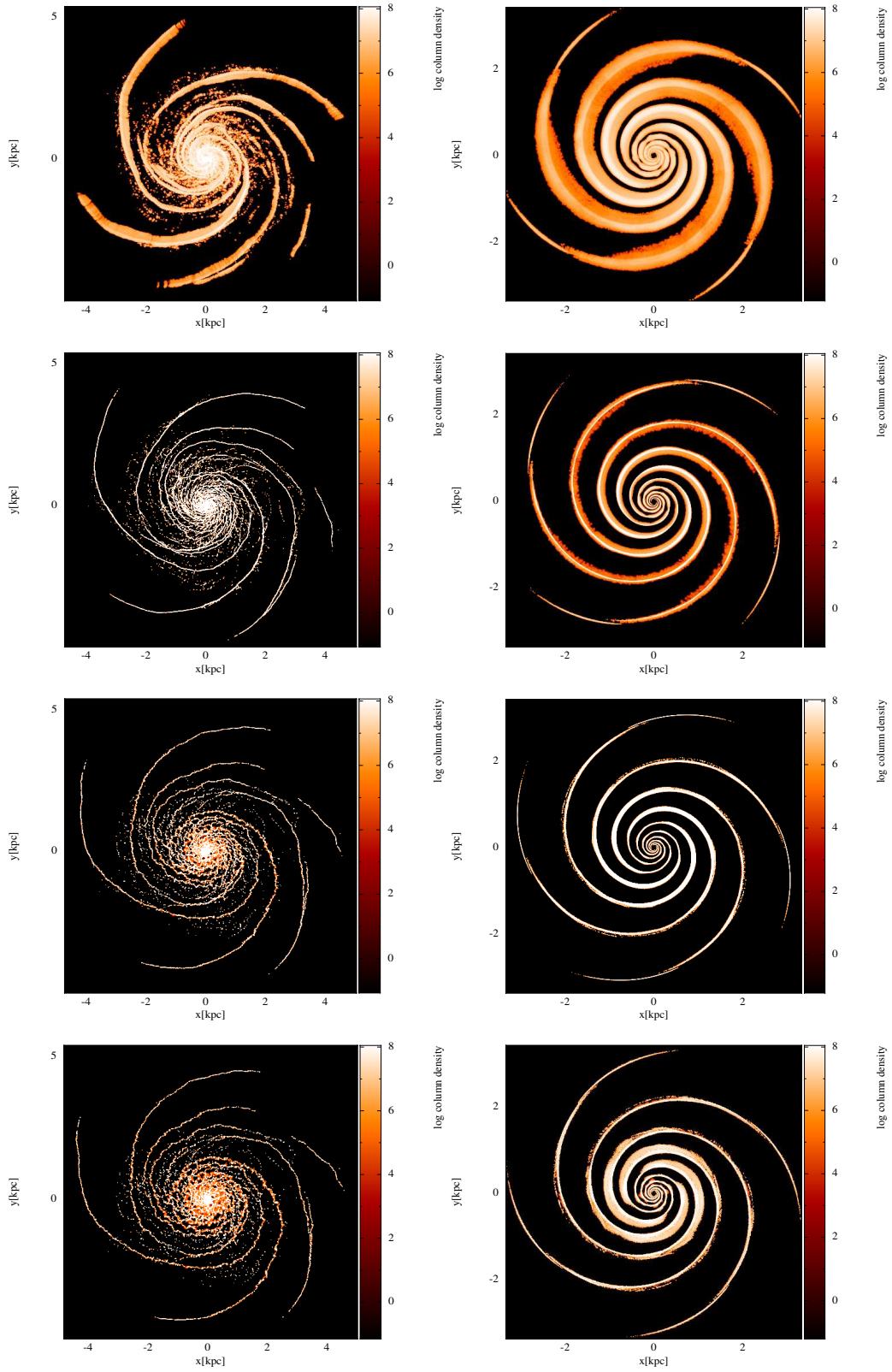

Figure 4.16: Evolution of particles with densities above $10\,M_{\odot}\,pc^{-3}$ selected at $t = 20.4$ Myr. The snapshots show the following times: $t = 0.0$ Myr (top), $t = 13.38$ Myr (second), $t = 26.77$ Myr (third), $t = 40.16$ Myr (bottom).

Figure 4.17 shows the evolution of gas particles in a region just about to enter a spiral arm. The left and right columns correspond to the N-body and spiral potential simulations, respectively. The top panels show the particles' paths in a position map colour coded by their density. The dashed lines are reference circular trajectories. The plots show how the density is enhanced as the gas passes through a spiral arm in both simulations. It is important to note that the gas is not following circular trajectories. As it approaches the arm, it initially moves in an outward direction and then in an inward direction after the gas density has increased. This is consistent with the velocity profiles of §4.3.2, where the gas has $v_R > 0$ before entering and changes sign during the passage.

There are differences in the density evolution between simulation as shown in Figure 4.18. In the case of the N-body simulation, there is a point between 10 and 15 Myr where the density increases by about 2 orders of magnitude. The density keeps increasing for many particles, but oscillates for other particles. The region develops a distribution of densities. However, due to the self-gravity, some gas is reaching high densities $\sim 10^6\,\mathrm{M}_\odot\,\mathrm{pc}^{-3}$. This is rather unrealistic and may be a consequence of the lack of feedback. The spiral potential simulation (right panel of Figure 4.18) shows an interesting behaviour. The density increases to values peaking slightly above $10\,\mathrm{M}_\odot\,\mathrm{pc}^{-3}$ and then decreases slightly. This behaviour shows that gas is compressed as it enters the arm and then expands as it leaves. The left panel of Figure 4.17 shows that the dense particles are spreading over a larger scale, which can be a consequence of the gas leaving the arm. In both simulations, the final density is higher than the density the gas had before entering the arm. These results show that the spiral arms have a role in driving the formation of a dense gas phase.

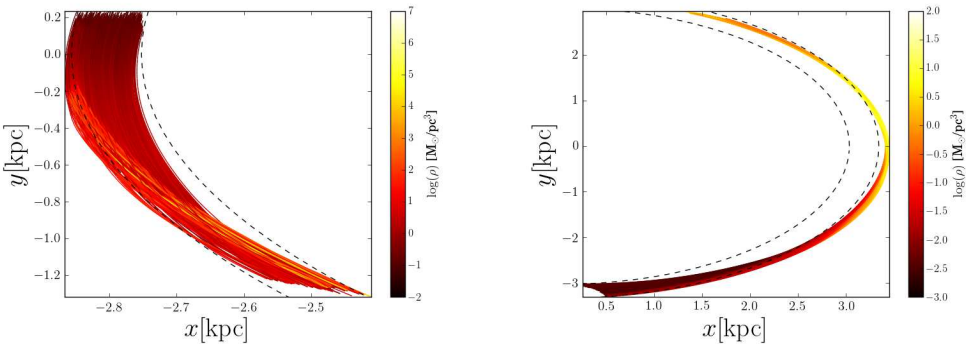

Figure 4.17: Particle trajectories colour coded by density for a selection of particles just about to enter a spiral arm for the N-body (left panel) and spiral potential (right panel) simulations. The particles' motion is in a counterclockwise direction. Results show how the gas density increases and the gas trajectories deviate from circular orbits as the gas flows through a spiral arm. The spiral potential simulation allowed to track the particles for a longer timescale. The trajectories show that particles are oscillating around a reference radius.

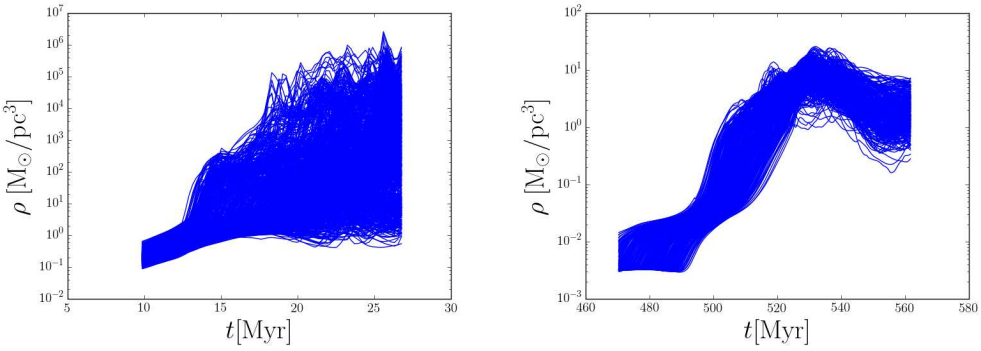

Figure 4.18: Particle densities as a function of time for the same selection of Figure 4.17 for the N-body (left panel) and spiral potential (right panel). In the N-body model, with self-gravity, the density increases significantly as the gas flows through the arm. In the spiral potential model, without self-gravity, the gas reaches a maximum compression and the density decreases as it leaves the arm.

4.5 Discussion

4.5.1 Cold Gas Density Distribution

In §4.2, the results show that the N-body simulation develops a very rich structure whereas the spiral potential simulation does not. Because of the self-gravity, gas in the arms tends to form clouds in a "beads on a strin" fashion. A similar behaviour is observed in the simulations of Renaud et al. (2013). The gas tends to follow well the spiral structure of the galaxy, which is consistent with other N-body with hydrodynamics simulations such as Clarke & Gittins (2006); Baba et al. (2009); Wada et al. (2011); Grand et al. (2012); Mata-Chávez et al. (2014); Baba et al. (2017).

The spiral potential simulation does not develop much structure after the first $\approx$ 40 Myr. However, after approximately 100 Myr, many different structures appear in the inner regions of the galaxy (see Figure 4.2). The morphological features are qualitatively similar to those reported in Dobbs & Bonnell (2006); Bonnell et al. (2013); Smith et al. (2014). These works use a similar potential and SPH and can be compared to the simulations in this work. These features have also been studied in simulations using mesh codes with spiral potentials (e. g. Kim & Ostriker 2002, 2006; Shetty & Ostriker 2006). However, they only develop mostly within $2-3$ kpc from the galaxy's centre. The orbital period at $R = 3$ kpc is $\approx$ 108 Myr. Given the angular frequency relative to the spiral pattern at $R = 3$ kpc, the crossing time of the inter-arm region is approximately 46.5 Myr, which means that the gas has had enough time to pass through about two arms. This may explain the richer structure within 3 kpc, the first arm passage leads to the formation of some dense gas structures and quickly reaches a second arm, where it interacts with more dense gas in the arm.

In both models, most of the dense gas structures form within 5 kpc (corotation is around 4.5 kpc). Because of the exponential gas profile, the inner regions have higher densities, thus higher cooling rates and shorter cooling timescales. This explains why the cold dense gas starts to form from the inner to the outer galaxy. The spiral arms also drive the formation of dense gas.

As described in Chapter 3, observations show that the molecular gas tends to have a steep profile whereas the warm gas tends to have a flatter profile. It is interesting that both simulations also show this behaviour. As shown in Figure 4.4, the dense gas is concentrated in

the inner regions and has a quickly decaying profile whereas the warm gas has a nearly flat profile. The surface density values are consistent with the typical values reported in Bigiel & Blitz (2012). It is interesting that the spiral potential simulation gives a cold gas central density close to the value reported for M33 in Druard et al. (2014).

4.5.2 Gas Dynamics in Spiral Arms

§4.3 presented the density, velocity, and velocity dispersion profiles as a function of azimuth. Roberts (1969) presented a solution for the density and velocity profiles of shocks in spiral arms. In this solution, the density is predicted to jump at the shock and then gradually decrease; the velocity normal to the arm shows the jump due to the shock; the tangent velocity decreases to a minimum near the shock point and then increases. A key point is that Roberts (1969) predicts that as gas enters the arm, the shock occurs before the potential minimum. This has been a subject of discussion in the literature (e. g. Dobbs & Baba 2014).

In the N-body simulation, the gas density behaves in a similar fashion. It increases sharply and decreases gradually after the jump, but this behaviour is less evident at radii larger than ≈ 5 kpc. In several arms, the density peak is located slightly before the arm's density peak, but in some cases it occurs at a different position. This result agrees with the simulations of Clarke & Gittins (2006), although a direct comparison is difficult since they assumed an isothermal and non-gravitating gas. The N-body simulation also agrees with the results of Wada et al. (2011) and Baba et al. (2016). These works do include cooling and self-gravity, although they have less resolution than the simulations of this work.

In the spiral potential simulation, a similar behaviour is seen at smaller radii but without such a strong shock. It is interesting to note that in this simulation the density peak is forming after the potential minimum with respect to the point of inflow. Near the corotation radius, the density peak is close to the minimum. Outside corotation, the position of the peak is reversed. However, in this region, the arm rotates faster than the gas. With respect to the arm, the gas now enters from the opposite direction so the density profile is reversed. The density peak, however, is forming after the potential minimum with respect to the direction of the flow (see Figure 4.7). These results are slightly different to that of Roberts (1969), which predicts that the shock forms before the potential minimum as gas flows into the arm. However, the spiral potential parameters of this thesis are not identical to those of Roberts (1969).

Using a spiral potential, Gittins & Clarke (2004) analysed the behaviour of the gas around the corotation radius using $m = 2$ and $m = 4$ potentials. They find that the shock is offset from the potential minimum and this offset has some dependence with the number of arms. They use semi-analytic as well as numerical codes to model the flow through the potential. Some of their simulations use the SPH method, which can be compared to the spiral potential simulation. For the $m = 4$ potential, Gittins & Clarke (2004) find that the shock forms after the gas passes the potential, which agrees with this simulation. Gittins & Clarke (2004) measure this offset as a function of radius for their models. The spiral potential simulation in this work agrees with their results in the sense that, seen face-on, the offset tends to zero near corotation. A recent study by Sormani et al. (2017) of flow properties around a spiral arm, shows that it is possible to produce shocks forming after passing the minimum when the base flow is supersonic. The result of this section support the idea behind the method proposed by Gittins & Clarke (2004) to constrain the corotation radius by measuring the offset between the shock and the stellar arms. This has been applied in observations by Kendall et al. (2011, 2015).

In terms of the velocity profile, both simulations show a sharp jump in radial velocity where the shock is forming. Where v_R is maximum, the azimuthal velocity is minimum. The pitch angle of the arms is small, so the normal and tangent components are not very different to the v_R and v_ϕ components. The behaviour in the simulations is consistent with the velocity profiles of Roberts (1969). The velocity profiles in our simulations are also consistent with the behaviour of those in the simulations of Baba et al. (2016), which also analyse gas flows in spiral arms.

In terms of the velocity dispersion, the results show that the spiral arms play a significant role in injecting a velocity dispersion to the arm. However, the dispersion may be rather low due to the lack of feedback and other injection mechanisms. The high velocity dispersion regions tend to be associated with the spiral arm regions in both models.

4.5.3 Streaming Motions

The simulations show that the spiral arm regions can add significant streaming motions to gas flowing through the arms. The results show that the velocity perturbation with respect to the circular velocity can be as high as $\pm 15 - 20$ km s^{-1}. However, the velocity shift is sensitive to the model. In the N-body model, it decreases with galactocentric distance. In the spiral

potential model, it decreases near corotation but then tends to increase outside this radius. This is an interesting difference to point between the simulations.

Baba et al. (2016) performed numerical simulations with SPH to study the streaming motions of gas flowing in both dynamic (N-body) and steady (spiral potential) spiral arms. Although the parameters of this work are not the same as theirs as they use a Milky Way model, it is still possible to do a qualitative comparison of the behaviour. In both their N-body and steady spiral models, they find that v_R jumps from a positive value to a negative value as it crosses the potential minimum and that v_ϕ is smallest when v_R is highest. This agrees with the results of the simulations discussed in this chapter. However, they find higher peak to peak variations. It is interesting to note that Figure 4.10 shows a sharp jump in v_R that is not seen in the Baba et al. (2016) model, which may be a result of this thesis using a factor of 6.67 more particles than them. The N-body model agrees with the findings of Wada et al. (2011) and Baba et al. (2009) in the sense that streaming motions tend to be more unorganised. The spiral potential simulation qualitatively agrees with the velocity predictions of Sormani et al. (2017), which also follow a similar tendency to that predicted in Roberts (1969). This simulation also shows that v_R peaks when v_ϕ is minimum which is also a result that can be derived from the velocity predictions in Gittins & Clarke (2004).

An analysis of CO kinematics in M51 by Meidt et al. (2013) shows that there are important radial and azimuthal streaming gas motions. In the radial (galactocentric) component, it has a tendency to increase from $-20\ \mathrm{km\,s^{-1}}$ to $10\ \mathrm{km\,s^{-1}}$ with some oscillations as a function of radius. In the circular component, it oscillates between $\approx -10\ \mathrm{km\,s^{-1}}$ and $\approx 20\ \mathrm{km\,s^{-1}}$. The behaviour of the radial velocity may be a result of an interacting galaxy. Schmidt et al. (2016) analyse the HI kinematics of 10 spiral galaxies from the THINGS survey. Their results show that v_R can have several oscillations around zero. In some cases, there is a net radial component which may be a consequence of an interaction. They report radial velocities typically in the range $\pm 20\ \mathrm{km\,s^{-1}}$, with some exceptions. It is noted that their resolution falls between 100 and 500 pc, depending on each galaxy's distance.

Both simulations show that v_R as a function of radius oscillates around zero. This is observed in some of the galaxies in the sample of Schmidt et al. (2016). The results are consistent with values obtained by Meidt et al. (2013) and Schmidt et al. (2016). In terms of v_ϕ, the spiral potential simulation seems to produce stronger oscillations than the N-body one. It is

interesting to point out that these motions may be sensitive to the underlying potential. However, a limitation of the simulations in this sense is that the N-body stellar component has a noisier representation of the potential, which may also influence the results.

The gas trajectories of Figure 4.17 do show that the gas does not follow exactly circular orbits. This may have implications for surveys using the kinematic distance method to estimate the distance to gas clouds in the Milky Way. This will be discussed in more detail in Chapter 5.

4.5.4 Summary of Comparison with Other Numerical Works

A wide variety of hydrodynamics simulations of spiral galaxies exist in the literature and it is not straightforward to do a direct comparison because of the different parameters used both for N-body and spiral potential simulations. However, it is still possible to make qualitative comparisons with previous work. The N-body simulation broadly agrees with the results of other works such as Dobbs & Bonnell (2008); Clarke & Gittins (2006); Baba et al. (2009); Wada et al. (2011); Baba et al. (2016, 2017) that also present N-body simulations using SPH. The main agreement is that the gas tends to trace the maximum of the stellar density. Compared to previous works, the simulations of this chapter have high mass resolution compared to other large-scale models. An interesting comparison is that the azimuthal density profiles of Figure 4.7 show a more detailed behaviour of the profile compared to those of Wada et al. (2011) and Baba et al. (2016). However, this has been achieved at a higher computational cost, which makes the study of longer timescales more difficult. The velocity profiles are also qualitatively similar to those of Baba et al. (2016) and follow the behaviour of the solutions described in Gittins & Clarke (2004) and Roberts (1969).

The spiral potential simulation agrees with the results of other potential based simulations such as Gittins & Clarke (2004); Dobbs & Bonnell (2006); Dobbs (2007); Baba et al. (2016), which use SPH; and others such as Wada & Norman (1999); Chakrabarti et al. (2003); Wada (2008); Wang et al. (2015), which use mesh-based codes; and Smith et al. (2014), which uses a moving-mesh code. In particular, the simulation agrees with other SPH simulations such as Dobbs (2007); Gittins & Clarke (2004) and Baba et al. (2016) in the sense that the shock forms after the gas passes through the potential minimum. This differs from the Roberts (1969) result and other simulations using mesh codes. However, this may be a result of using an $m = 4$ potential (e. g. Gittins & Clarke 2004) or the fact that it is not in a steady state

(e. g. Dobbs 2007; Kovalenko & Levi 1992). Baba et al. (2016) find that the shock forms after the minimum for an $m = 2$ potential. Their simulations included cooling and heating mechanisms. In this sense, Sormani et al. (2017) show that for cold gas, it is possible to find solutions where the shock forms after passing the minimum. This suggests that the thermal physics assumed affect the solution. The spiral potential simulation presented in this work agrees with Gittins & Clarke (2004) in the sense that the offset between stellar arm and shock can be used to estimate corotation. However, this result may be affected by magnetic fields (e. g. Lee 2014). The velocity profiles agree with those of Baba et al. (2016) in the sense that v_R peaks when v_ϕ is minimum.

4.6 Final Comments

The gas dynamics in two galaxy models were compared to explore the difference between a flocculent and a grand-design galaxy. With cooling and heating included, the models develop a two phase medium where dense clouds resembling molecular clouds form. The dense gas tends to be associated to the spiral arms. The cold and warm gas surface density profiles show that the cold gas forms in the inner regions of the galaxy. The cold gas has a steeply decaying profile and the warm gas has a relatively flat profile, which is consistent with observations. The gas flows in the spiral arm show that the shock region is marked by a sharp jump in the radial velocity. The gas velocity dispersion is enhanced in spiral arms regardless of the potential assumed, though there are some model-to-model variations. The spiral arm structure drives significant streaming motions which results in gas that does not move in precisely circular orbits. The magnitude of the streaming motions is consistent with observations of gas kinematics of a sample of spiral galaxies. In the N-body model, cooling and self-gravity drive the gas to very high-densities; however, in the spiral potential, without self-gravity, the gas is compressed to high densities in the arm, and the density decreases as the gas leaves the arm.

5

Molecular Cloud Streaming Motions and Errors in Kinematic Distances

As described in the previous chapter, the spiral arms introduce significant radial and azimuthal velocity deviations to the gas motions. This has important implications for molecular gas surveys in the Milky Way that calculate distances using the kinematic distance method, which assumes that gas moves in circular orbits. In this chapter, the simulation of gas flowing in a spiral arm derived from the model in Bonnell et al. (2013) is analysed to study the streaming motions that the spiral arm introduces in the clouds' motions around the galaxy. §5.2 outlines the simulation and the cloud identification algorithm. The results on the streaming motions are summarised in §5.3 and their effect in the kinematic distance is analysed in section §5.4. Most of the results of this chapter are based on those published in Ramón-Fox & Bonnell (2018). These are compared with the N-body global simulation, which is described in §5.4.3. A discussion and a summary are given in §5.5 and §5.6.

5.1 Mapping out the Spiral Structure in the Galaxy

As described in Chapter 4, as gas flows into spiral arms, the density increases and coupled to efficient cooling and self-gravity, this can lead to the formation of molecular clouds. Earlier simulations exploring molecular cloud formation such as Dobbs et al. (2006) support this. This suggests that molecular gas will trace spiral structure, which has been observed in CO surveys of nearby galaxies (e. g. Nieten et al. 2006; Rosolowsky et al. 2007; Hughes et al. 2013; Schinnerer et al. 2013). Such extragalactic observations are advantageous as they allow astronomers to measure the position of the gas with respect to an arm, but the large distance to the sources hinders a detailed study of the smaller scales. On the other hand, Milky Way observations allow studies better resolving individual star forming regions. However, the edge-on perspective from Earth complicates the task of mapping these with respect to the large-scale structure.

A reliable mapping of the Galaxy's spiral arms is needed to understand how molecular gas and star formation activity relates to this structure. Additionally, cloud properties such as the size and the mass depend on good distance estimates (e. g. Heyer & Dame 2015). The most common method is the kinematic distance. This assumes that clouds move in circular orbits. Given the Galaxy's circular velocity $v_c(R)$, it is possible to derive a set of equations involving the line-of-sight velocity, $v_c(R)$ and the heliocentric distance to the cloud (e. g. Roman-Duval et al. 2009). This method has the advantage that it can be applied to large distances, but it is less reliable for inside the solar orbit because two different points on the orbit yield the same line-of-sight velocity (described in §5.2.3).

Alternate methods have also been developed. Brunt & Kerton (2002) devised a method using the cloud size-velocity dispersion relation to define a distance calibration. The cloud's velocity dispersion is measured to estimate a physical size, which can be used to estimate a distance given its angular size. Although it can be applied in many Galactic regions, it is rather affected by cloud-to-cloud variations. A highly reliable method is the trigonometric-parallax method (Reid et al., 2009). It uses maser sources in high-mass regions of star formation, which allow the accurate measurement of parallaxes and proper motions. Then, distances are directly calculated. However, it is limited to distances where the parallax angle can still be resolved.

The kinematic distance method still has been widely used in the literature (e. g. Dame

et al. 1986; Blitz & Spergel 1991; Roman-Duval et al. 2009; Wienen et al. 2015; Ragan et al. 2016; Miville-Deschênes et al. 2017). This motivates studies quantifying the method's sources of error and exploring potential improvements. For example, Foster & MacWilliams (2006) proposed an improvement of the estimate by fitting models to HI density and velocity features based on a two-armed model, which may be reasonable for mapping the larger-scale gas distribution. However, recent works indicate that the Galaxy may have a higher number of arms (Vallée, 2017). When dealing with individual molecular clouds, it is necessary to take into account the effect of the cloud-to-cloud velocity dispersion on the line-of-sight velocity. For clouds within 3 kpc from the sun, Stark & Brand (1989) find an average dispersion ≈ 7.8 $\mathrm{km\,s^{-1}}$. Wilson et al. (2011) obtain a typical dispersion of 6.1 $\mathrm{km\,s^{-1}}$ from CO observations of nearby galaxies. Reid et al. (2009) proposed a correction to the kinematic estimate based on observed cloud motions, but this still may be restricted to the particular sample used.

Galaxy simulations are useful for exploring the effect of different spiral arm morphologies on gas streaming motions. Some earlier works have explored both spiral potential (Gómez, 2006; Pohl et al., 2008) and N-body simulations (Baba et al., 2009). These show that errors in the kinematic distance can be larger than 1 kpc, but argue that it is possible to recover the structure with some distortions. However, these works use global models applicable to the large-scale gas distribution, but their resolution limits the conclusions regarding individual molecular clouds. This motivates higher resolution studies following in more detail cloud motions in a spiral arm. This chapter analyses a high-resolution simulation of gas flowing in a spiral arm to study cloud streaming motions and their effect on the kinematic distance method. The simulation is obtained from the simulations in Bonnell et al. (2013).

5.2 Spiral Arm Region and Analysis Methods

5.2.1 Initial Conditions and Region of Simulation

The initial conditions are a high-resolution re-sample of the galaxy-scale simulation of Bonnell et al. (2013). A region of gas about to enter a spiral arm is selected and sampled with a higher resolution. The zoom-in simulation has $N = 31\,454\,976$ particles, each with a mass $m_g = 0.625\ M_\odot$. The total mass is $\approx 1.96 \times 10^7\ M_\odot$. Approximately 53% of the gas is already in the spiral arm region and 47% is about to enter. This allows to study the interaction of inter-arm gas with that already in the arm. The simulation does not include self-gravity, which

allows to focus the computational efforts in the large-scale hydrodynamics over longer time scales, as it avoids the small time steps required in dense collapsing regions.

5.2.2 Cloud Identification: Building a Cloud Catalogue

The following steps are implemented to identify clouds in the simulation. The SPH particles carry information of the local density at a particle's position. The first step is to make a list of all the particles that have densities above a density threshold $\rho_{\rm thresh}$.

The next step is to build a catalogue of the clumps found in this dense gas sample. A friends-of-friends (FOF) algorithm is implemented to achieve this. A version of this algorithm was proposed in Huchra & Geller (1982) to identify and classify galaxy clusters. This method specifies a linking length $l_{\rm link}$ parameter. It starts with the first particle in the list and computes the distance d to the next particle. If $d \leq l_{\rm length}$, then this particle belongs to the same group and a first group ID is created. Then the third particle is checked against the second. Now, if $d > l_{\rm length}$, a new group is created with a new ID. In this case, the third particle clearly does not belong to the first group. However, for an arbitrary particle in the list, the particle has to be checked with previous ones to determine if it is a member of an already defined group. This check is performed by moving backwards in the list. It is very likely that for particles near the end of the list, a previous group will be found first by moving backwards than going all the way to the beginning and check all the list. If the current particle does belong to a previous group, the search is stopped and that group ID is assigned to it. If no matching group is found, the search finishes at the beginning of the list and a new group ID is assigned to the current particle.

This method produces a list of particle properties with their associated group IDs. The next step is to filter out clumps with a number of particles higher than a threshold $N_{\rm min}$. This value is set to $N_{\rm min} = 50$, which is the typical number of neighbours within the compact support length of the SPH kernel. This means that the smallest clump mass is about 31.25 $M_\odot$ given the particle mass in this simulation. The density threshold is set to $\rho_{\rm thresh} = 10\,{\rm M}_\odot\,{\rm pc}^{-3}$ and the linking length to $l_{\rm length} = 1$ pc.

The density threshold ensures that only the dense gas phase is analysed and reduces the number of particles that needs to be checked. The linking length $l_{\rm link}$ can be estimated by the typical particle separation at the threshold density. However, choosing an even smaller linking

length may indirectly set a higher density threshold. As the density increases, the particle separation decreases and a smaller $l_{\rm link}$ will tend to only connect particles in areas of higher density. Conversely, a higher value of $l_{\rm link}$ will tend to connect particles in areas of lower density.

A potential problem with FOF algorithm is that the linking length may affect two clouds whose boundaries are closer than a $l_{\rm link}$. Consider particles in the boundaries of two neighbouring clouds. These boundaries are facing each other. At some point, the distance check will determine that some particles are within a $l_{\rm link}$ thus tagging both clouds as a single structure. However, it may be possible that such a structure is still physically linked by lower density gas discarded by the $\rho_{\rm thresh}$ cut. Then, $l_{\rm link}$ sets the minimum distance between neighbouring clouds.

The final clump list is used to study their physical properties. There are always limitations in cloud identification algorithms, but it provides a starting point to study cloud properties in the simulation.

5.2.3 Overview of the Kinematic Distance Method

According to Roman-Duval et al. (2009), knowing a cloud's line-of-sight velocity $V_{\rm los}$ and its Galactic longitude l allows to calculate its galactocentric radius $R_{\rm cloud}$ and distance D with the following equations:

$$R_{\rm cloud} = R_0 \sin l \left(\frac{V_c(R_{\rm cloud})}{V_\odot \sin l + V_{\rm los}} \right), \tag{5.1}$$

where R_0 is the Sun's galactocentric position and $V_\odot$ is the magnitude of the solar orbital velocity. This assumes that the cloud's motion follows a circular orbit given by the circular velocity $V(R_{\rm cloud})$ at the cloud's position. The distance is then given by

$$D = R_0 \pm \sqrt{R_{\rm cloud}^2 - (R_0 \sin l)^2}. \tag{5.2}$$

The above corresponds to two distances, usually known as the "far" (positive root) and "near" (negative root). The positive case should be used for objects located beyond the tangent point. For $R_{\rm cloud} < R_0$, there are two points where the assumed cloud's orbit intersects the line-of-sight, which means that there are two positions ("near" and "far") where $V_{\rm los}$ is the same. This is known as the kinematic distance ambiguity (Roman-Duval et al., 2009). In a simulation, it is possible to know beforehand what distance to use. This chapter analyses the error assum-

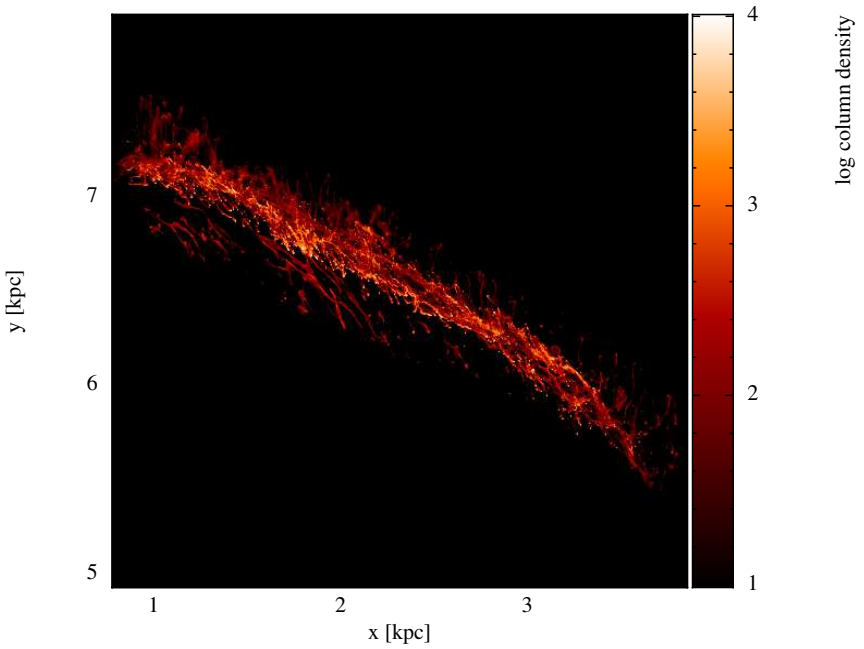

Figure 5.1: Snapshot of the spiral arm region after $t \approx 18.2$ Myr of evolution. It is possible to see that the region has developed a rich substructure of clouds and other morphological gas features.

ing that the correct sign in equation (5.2) is used and does not focus on exploring ways of overcoming the ambiguity.

5.3 Cloud Kinematics and Streaming Motions in the Galaxy

Figure 5.1 shows a snapshot of the spiral arm region simulation at $t \approx 18.2$ Myr of evolution. The identified cloud masses range from $M \approx 31.2\ M_\odot$ to $M \approx 10^4\ M_\odot$. Figure 5.2 plots the radial and azimuthal velocities, v_R and v_ϕ with respect to radius at the same time. These correspond to the centre of mass position and velocity of the clouds. The average velocity of all the gas, including both cold and warm, binned by radius is plotted by comparison (orange triangles).

For the radial velocity, the average value $\bar{v_R}$ shows a significant shift from $v_R = 0$ It has the largest deviation at $R = 7.2$ kpc, where $\bar{v_R} \approx -9$ km s^{-1}. The clouds' radial velocities are scattered between -21.7 to 18.9 km s^{-1}, with an average $\bar{v_R} = -9.3$ km s^{-1}. Their velocities relative to the average motion of the gas ($\delta v_R(\text{cloud}) = v_R(\text{cloud}) - \bar{v_R}(\text{gas})$) are scattered between -18.4 km s^{-1} and 23.9 km s^{-1}. The average relative motion is $\bar{\delta v_R}(\text{cloud}) = -3.4$ km s^{-1}, which shows that the cloud movements, on average, are slightly shifted from the average gas motions. The cloud-to-cloud radial velocity dispersion is $\sigma_R = 6.4$ km s^{-1}. The top panel of Figure 5.3 shows the radial velocity component as a function of position. Most

clouds are moving with $v_R < 0$, but there are some closer to the arm's center moving with positive values.

In the azimuthal direction, the lower panel of Figure 5.2 shows that there is a large scatter in the cloud's velocities. A closer inspection shows two main velocity groups: one with v_ϕ around 220 $\mathrm{km\,s^{-1}}$ and the second v_ϕ near 205 $\mathrm{km\,s^{-1}}$. The average velocity $\bar{v_\phi}$ of all the gas distribution pass between both groups. Figure 5.3 in the bottom panel shows that the clouds in the fast group correspond to the upstream side of the spiral arm where gas is entering. On the other hand, the slow group is on the opposite side where gas may be leaving. The average $\bar{v_\phi}$ of the gas and most of the individual cloud velocities tend to be slower than the rotation curve.

The cloud's azimuthal velocity shows a scatter between 200.8 $\mathrm{km\,s^{-1}}$ and 228.9 $\mathrm{km\,s^{-1}}$ with $\bar{v_\phi} = 214.2$ $\mathrm{km\,s^{-1}}$. The relative motions with respect to the average gas velocity ($\delta v_\phi(\mathrm{cloud}) = v_\phi(\mathrm{cloud}) - \bar{v_\phi}(\mathrm{gas})$) have a scatter between -16.5 $\mathrm{km\,s^{-1}}$ and 18.3 $\mathrm{km\,s^{-1}}$, with an average difference $\delta\bar{v}_\phi(\mathrm{cloud}) = -1.1$ $\mathrm{km\,s^{-1}}$. This shows that the cloud distribution as a whole does not have a large difference with respect to the average gas motion. Nevertheless, there is a cloud group that is rotating faster and another one that is rotating slower than the average gas velocity as shown in Figure 5.2. The azimuthal velocity dispersion is $\sigma_\phi = 6.9$ $\mathrm{km\,s^{-1}}$ and the cloud-to-cloud dispersion of the magnitude of the velocity $v = \sqrt{v_x^2 + v_y^2}$ is $\sigma_v = 7.1$ $\mathrm{km\,s^{-1}}$.

5.4 Error Analysis of the Kinematic Distance

5.4.1 Effect of a Cloud-to-Cloud Velocity Dispersion

A mock catalogue was created to quantify how a cloud-to-cloud velocity dispersion in molecular cloud motions introduces an error in the kinematic distance. Each object was assigned the local circular velocity and then an additional velocity was added from a normal distribution. Three sets were created by adding a dispersion $\sigma_R = 1.0, 5.0$, and 10.0 $\mathrm{km\,s^{-1}}$ in the radial direction. Another three sets were specified by adding an azimuthal dispersion σ_ϕ with the same values. The two directions are analysed independently to understand the error propagated in each component. This will be useful to interpret the results of the actual kinematics in the simulation.

Distances are calculated by assuming an observing point at $\mathbf{R}_0 = \langle -8.0, 0.0, 0.0 \rangle$ kpc that moves at a local circular velocity of 220 $\mathrm{km\,s^{-1}}$. The assumed spiral arm model has 4 arms,

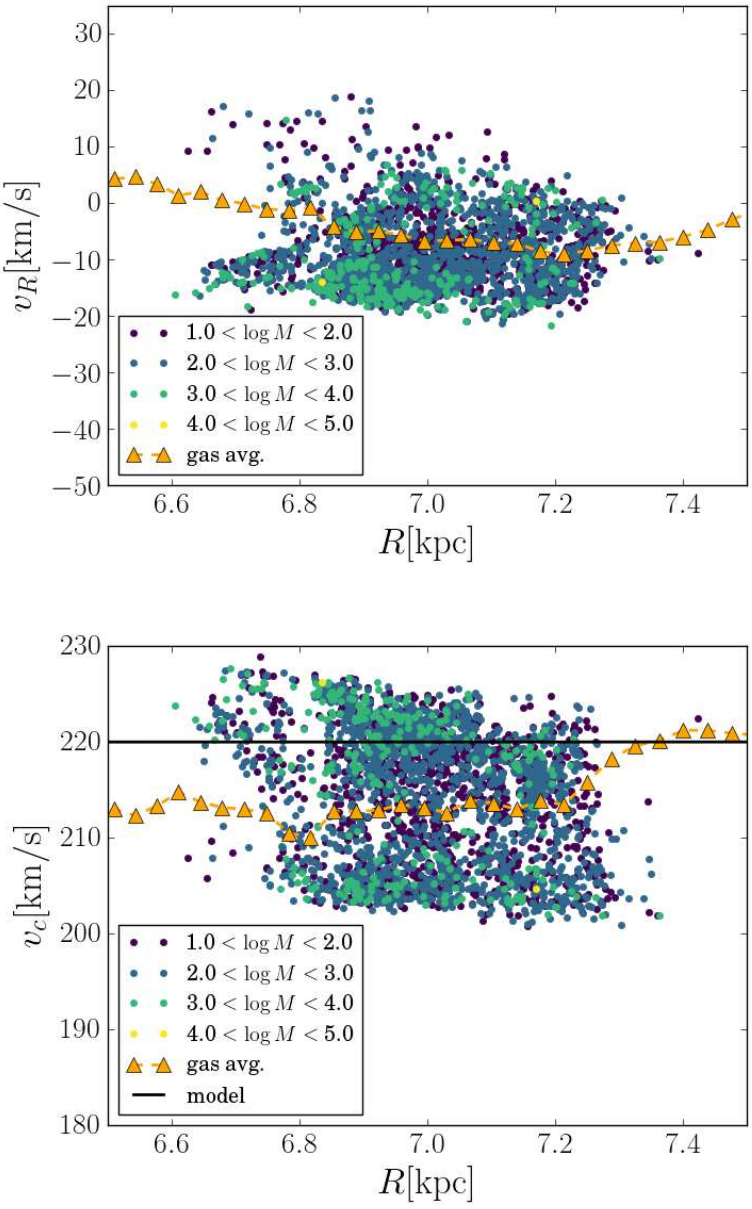

Figure 5.2: Cloud radial velocity (top panel) and azimuthal velocity (bottom panel) colour coded by mass in $M_\odot$ units. The orange triangles show the average of the entire gas distribution including both cold and warm components.

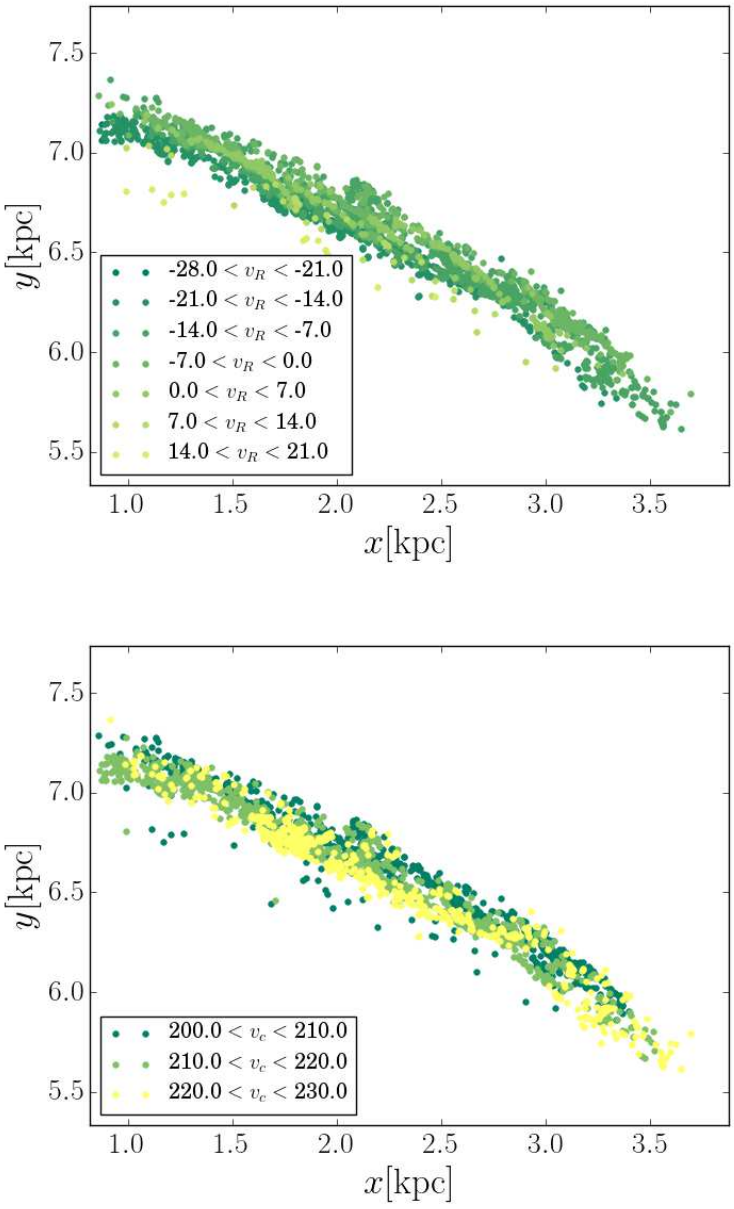

Figure 5.3: Cloud position map colour coded by their radial velocity (top panel) and azimuthal velocity (bottom panel). The galaxy's rotation is in a clockwise direction. Clouds on the left-hand side have a higher azimuthal velocity than those on the right side.

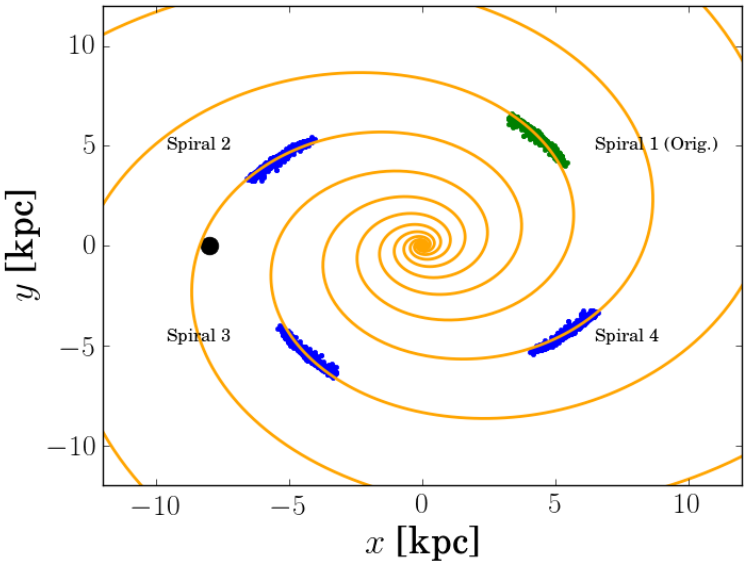

Figure 5.4: Clouds identified in the original simulation are in Spiral I on the upper right corner. The other distributions are copies placed in the equivalent positions with respect to each arm. This allows to analyse the kinematic distance method in different parts of the inner Galaxy. The orange curves trace the spiral arms and the solid black circle is the observing point.

so copies of the positions and velocities of the clouds in the simulated region are placed in the corresponding locations on the other arms, which is visualised in Figure 5.4. This setup is useful for studying the kinematic method in the 1st and 4th Galactic quadrants. For presenting the results for each spiral arm, the region on the upper right of the origin is labelled section 1. The section number increases in a counter-clockwise sense.

The line-of-sight velocity $v_{\rm los}$ as a function of Galactic longitude l for the clouds in each spiral arm is plotted in Figure 5.5. This is calculated from $v_{\rm los} = (\mathbf{V}_{\rm cloud} - \mathbf{V}_0) \cdot \hat{\mathbf{d}}$, where $\mathbf{V}_{\rm cloud}$ is the cloud's velocity, $\mathbf{V}_0$ is the observing point's velocity, and $\hat{\mathbf{d}}$ is a unit vector along the line-of-sight. In the plot in Figure 5.5, the orange points are the $v_{\rm los}$ for clouds moving in circular orbits and the blue points are the actual values from the velocities in the simulation. This indicates that the line-of-sight velocity is not symmetric around the values calculated for circular orbits. For some clouds, the deviation is larger than 10 $\mathrm{km\,s^{-1}}$.

In the case of adding a radial velocity dispersion, the distance errors are largest for sections I and IV, as shown in Figure 5.6. For some clouds the distance is overestimated by ≈ 4 kpc. On the other hand, the addition of an azimuthal velocity dispersion has a more systematic effect. The results are shown in Figure 5.7. The plots are colour-coded by the cloud's relative

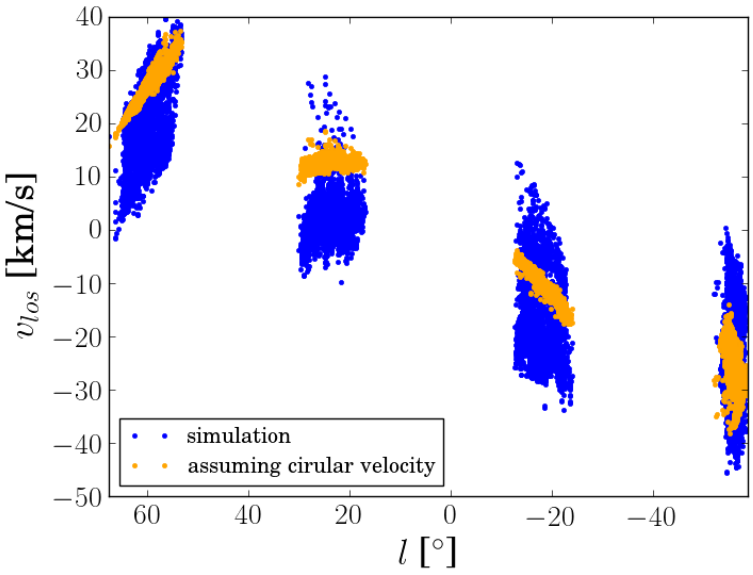

Figure 5.5: Cloud position map colour coded by their radial velocity (top panel) and azimuthal velocity (bottom panel). The galaxy's rotation is in a clockwise direction. Clouds on the left-hand side have a higher azimuthal velocity than those on the right side.

circular velocity with respect to the Galactic rotation: $v_c' = v_c(\text{cloud}) - v_c(\text{gal})$. The distance is overestimated for clouds rotating slower than $v_c(\text{gal})$, while it is overestimated for those rotating faster.

The distance error histogram for the case of a radial velocity dispersion is plotted in the top panel of Figure 5.8. With $\sigma_R = 1.0\ \text{km}\,\text{s}^{-1}$, the standard deviation of the distribution is 0.06 kpc and increases to 0.673 kpc when $\sigma_R = 10\ \text{km}\,\text{s}^{-1}$. In this case, 88% off the clouds have errors within 1 kpc and the distribution ranges from −2.51 kpc to 5.83 kpc. The lower panel of Figure 5.8 plots the error histogram for the azimuthal velocity dispersion. In the case with $\sigma_\phi = 1.0\ \text{km}\,\text{s}^{-1}$, the standard deviation is 0.12 kpc and on the case with $\sigma = 10\ \text{km}\,\text{s}^{-1}$, the deviation increaseses to 0.70 kpc. For the latter, the error values fall between −2.83 kpc and 3.87 kpc.

Given a distance, it is possible to calculate the positions of the clouds in a Cartesian map of the Galaxy with origin at the Galactic centre. The recovered positions can be calculated by

$$\mathbf{R}_{\text{cloud}} = \mathbf{R}_0 + \mathbf{D}, \tag{5.3}$$

where $\mathbf{R}_{\text{cloud}}$ is the cloud's galactocentric position, $\mathbf{R}_0$ is the observing position, and $\mathbf{D}$ is the

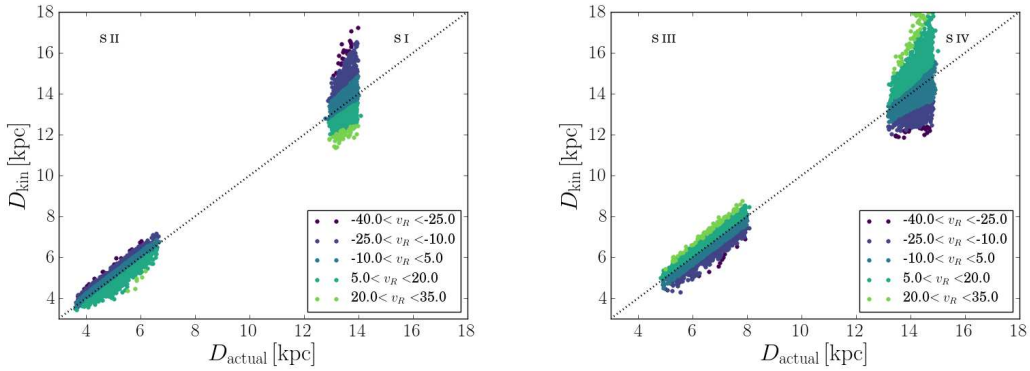

Figure 5.6: Cloud kinematic distance $D_{\rm kin}$ compared to the actual value $D_{\rm actual}$ for an azimuthal scatter around the galaxy's circular velocity of $\sigma_R = 10$ km s^{-1}. Sections I and II are shown in the left panel. Sections III and IV are shown in the right panel. Radial streaming motions introduce larger errors for more distant clouds.

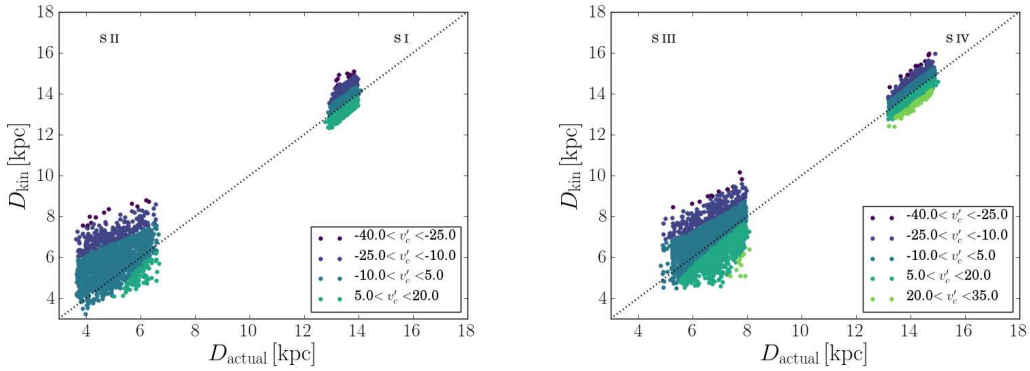

Figure 5.7: Cloud kinematic distance $D_{\rm kin}$ compared to the actual value $D_{\rm actual}$ for an azimuthal scatter around the galaxy's circular velocity of $\sigma_\phi = 10$ km s^{-1}. Sections I and II are shown in the left panel. Sections III and IV are shown in the right panel. Azimuthal streaming motions introduce larger errors for clouds in the nearby arms.

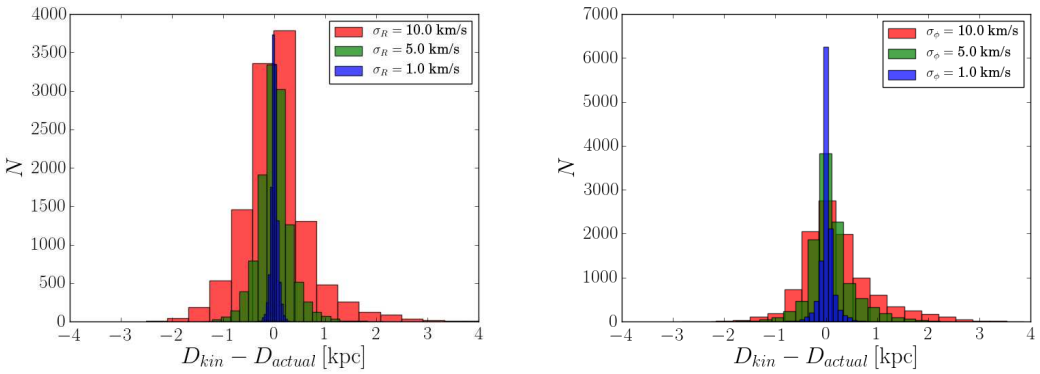

Figure 5.8: Distance error distributions resulting from introducing a radial velocity scatter σ_R (left panel) and an azimuthal velocity scatter σ_ϕ (top panel) to the circular velocity at the cloud's galactocentric position.

distance vector from the observer to the cloud. In cartesian components, this becomes

$$x_{\text{cloud}} = -8.0 + D\cos l, y_{\text{cloud}} = D\sin l, \tag{5.4}$$

for the choice of $\mathbf{R}_0$ previously described and using kpc as a distance unit. Figure 5.9 plots the resulting $(x_{\text{cloud}}, y_{\text{cloud}})$ positions given the calculated kinematic distances. The top panel shows the results for the radial dispersion while the bottom panel plots the case of the azimuthal dispersion. Both panels show the effect of a 10.0 $\text{km}\,\text{s}^{-1}$ dispersion. The recovered cloud positions give a distribution with clear distortions with respect to the original positions.

In Figure 5.9, the top panel shows that sections I and IV have the largest distance errors. These sections lie on a line-of-sight where the contribution of the radial velocity is more important, which may explain the larger errors for these arms. The radial streaming component appears has a lower effect on the clouds in sections II and III. The recovered cloud positions for the case of an azimuthal velocity dispersion are plotted in the bottom panel of Figure 5.9. All the recovered structures show a significant scatter. Those groups in sections II and III have the largest errors, which may be a result of being on a line-of-sight where the projection of the azimuthal component is more important.

This simple analysis shows that a cloud-to-cloud dispersion introduces significant errors in the kinematic distance method. For the cases with the highest velocity dispersion, the error distribution's spread is around 0.6 kpc, which is a non-negligible error considering that an arm's spiral width may be a few 100 pc. A radial dispersion introduces important errors in the kinematic distance, particularly in regions in the opposite side of the Galactic centre.

Another result is that clouds rotating faster than the circular velocity will have their distance overestimated while those rotating slower will have underestimated values.

In view of the kinematics described in §5.3, the above result poses a problem for determining cloud positions in the vicinity of a spiral arm. The simulation shows that clouds in the side closer to the observer are, on average, moving faster than the rotation curve while those further way are rotating more slowly. This means that distances for the nearer clouds would be overestimated while those on the far side underestimated. As shown by the recovered positions, this results in an apparently larger cloud distribution. The average position of the arm is also shifted with respecto to the original one.

5.4.2 Distance Errors derived from a simulated Milky Way Galaxy

This subsection presents the results of analysing the error in the kinematic distance method using the actual cloud velocities from the simulation. These include net radial and azimuthal streaming, which appear as an average shift of the cloud velocity distribution with respect to a circular orbit.

Section I

Figure 5.10 (left panel) plots the kinematic distance with respect to the actual distance for the clouds in this section, which corresponds to the actual region of the simulation. The results show that the distance is overestimated for almost all clouds. The upper right panel of Figure 5.11 shows the histogram of distance errors, which has a systematic offset of ≈ 1 kpc. The error falls between -1 and 2 kpc. Approximately 87% of the clouds have a distance error within 0.5 and 1.5 kpc. In terms of a fractional error, the error ranges between -5% and 16%. The systematic offset towards an overestimated distance may be a consequence of the net inward radial motion of the cloud distribution. In this line-of-sight, the radial component v_R has a larger contribution to $v_{\rm los}$ and opposite to the projection of v_ϕ. This results in a lower line-of-sight velocity compared to that expected from a circular orbit which results in an overestimated distance as v_c at a further distance would match the measured $v_{\rm los}$.

Section II

The results for this section are plotted in the left panel in Figure 5.10, which shows that the kinematic method is overestimating the distance for most of the cloud distribution. The dis-

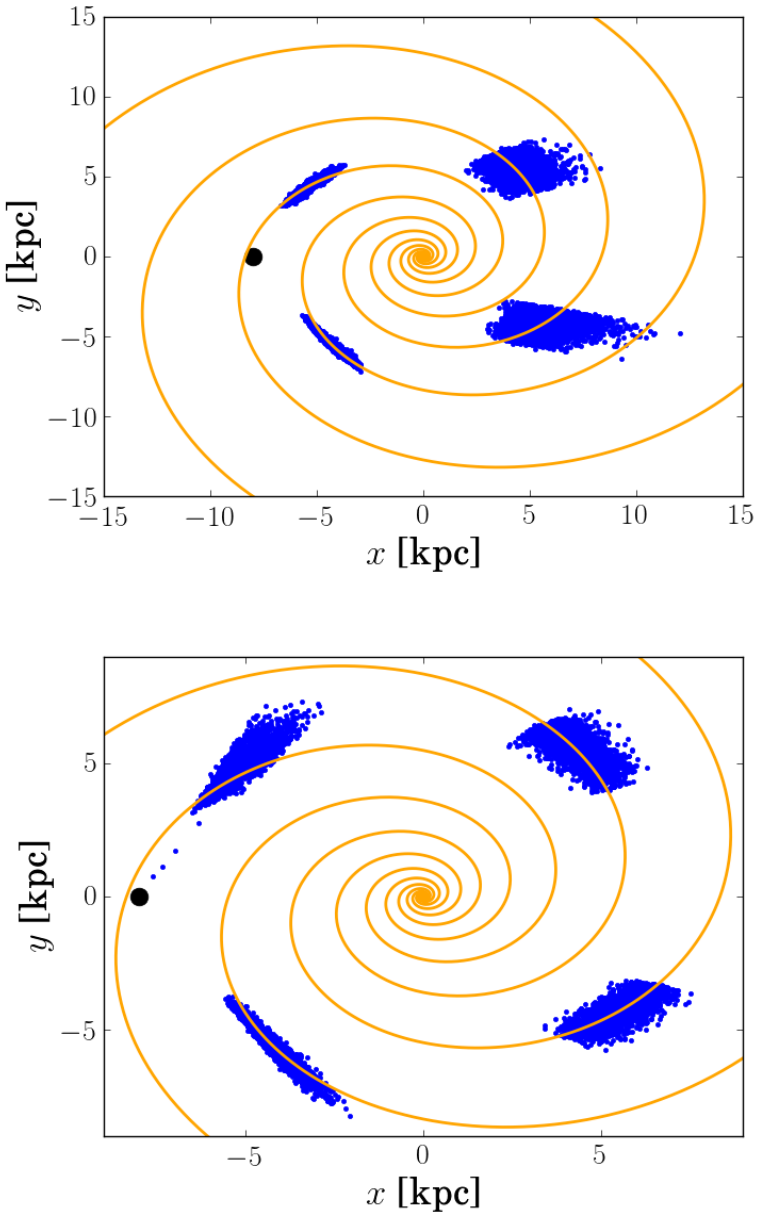

Figure 5.9: Cloud positions recovered from the kinematic distance. The clouds were assigned a velocity corresponding to the local circular velocity plus a component from a cloud-to-cloud velocity dispersion symmetric with respect to the rotation curve. The top panel shows the case for $\sigma_R = 10$ km s^{-1} and the bottom panel the case for $\sigma_\phi = 10$ km s^{-1}.

tance grows with a decreasing actual distance. The error histogram (left panel of Figure 5.11) has a noticeable peak around 2 kpc and a smaller peak near 0.7 kpc. The distribution is approximately centred around 1 kpc, also showing a net systematic shift towards overestimated distances. The max/min error range is −1.0/3.0 kpc. There are a few outliers with errors close to −2 kpc. Approximately 38% of the clouds have errors within 0.5 and 1.5 kpc. This includes the smaller peak of the distribution. About 34% off the clouds are in the range between 1.5 and 2.5 kpc, which includes the larger peak. This shows that around 75% have errors between 0.5 and 2.5 kpc. A fraction of 23% falls between −0.5 and 0.5 kpc. In terms of a fractional error, the distribution ranges from −58% to 80%. This arm section is located in a point where the contribution of v_R to the $v_{\rm los}$ is very low and the projection of v_ϕ is very high. The cloud distribution has an average azimuthal velocity slower than the rotation curve, which explains the overall shift of the distribution. The two velocity groups in the azimuthal component explains the bimodality of the distribution.

Section III

In this region, the error in the distance appears to increase as the actual distance falls. The results are shown in the right panel of Figure 5.10. The error distribution also bimodal and has two peaks, one near 1 kpc and another around −0.5 kpc, as shown in the lower left panel of Figure 5.11. Around 41% of the clouds has errors within −1 kpc and 0 kpc, where one peak is located. Between 1 kpc and 2 kpc, the fraction drops to about 27%, this is where the second peak is located. A similar value is found in the range between 0 and 1 kpc. The fractional error ranges from −28% and 39%. For this section, most of the errors have negative values. The bimodal distribution is a consequence of the two groups in circular velocity.

Section IV

The results for this section are shown in the right panel of Figure 5.10. The error grows with increasing cloud distance. In the error histogram of Figure 5.11 (lower right panel), the distribution shows a systematic offset of ≈ 1 kpc. The error ranges from −2 kpc to $4kpc$. Approximately 58% of the clouds have an error within −1.5 and −0.5 kpc. About 34% falls within the range between −0.5 kpc and 1 kpc. The fractional error falls within −13% to 27%. For this region, $v_R < 0$ which makes the projection of v_ϕ and v_R contribute in the same direction along the line-of-sight. This results in a more negative value of $v_{\rm los}$ compared to

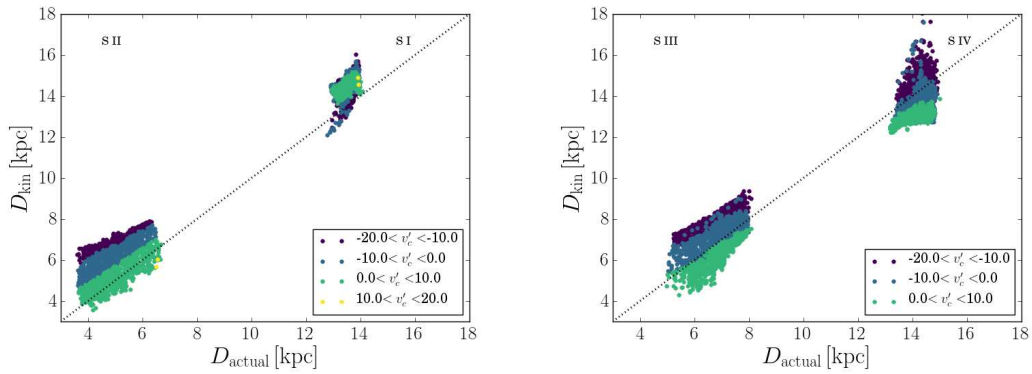

Figure 5.10: Cloud kinematic distance $D_{\rm kin}$ compared to the actual value $D_{\rm actual}$ for an azimuthal scatter around the galaxy's circular velocity of $\sigma_\phi = 10$ km s^{-1}. Sections I and II are shown in the left panel. Sections III and IV are shown in the right panel.

the one expected from a circular orbit. A more negative line-of-sight velocity results in an underestimated distance when using the kinematic estimate because a circular orbit would have to lie at a smaller radius to match the projected velocity. This explains the negative systematic shift of the error distribution.

Recovered Positions

The cloud positions that an imaginary observer would recover from the kinematic distance are plotted in Figure 5.12. These are compared with the original cloud distribution in each region. The orange curves plot the spiral arm curves tracing the actual cloud regions.

In section I, the systematic shift towards overestimated distance results in a recovered distribution at a farther distance compared to the original one. In the spiral of section II, the distribution has an overall shift towards overestimated distances as well. This reflects in an apparent net shift of the centre of the cloud distribution and an artificial increase in its size along the line of sight. A similar effect is observed for section III. In the case of section IV, there is a significant distortion of the geometry of the recovered cloud distribution. However, the behaviour is different to the case of section I. Although most of the clouds of section IV are shifted towards smaller distances, there is still a fraction with overestimated values.

The results of this section shows that average radial and azimuthal deviations from a circular orbit in a group of clouds introduces systematic errors in the kinematic distance. For the values found in the simulation, these can be as large as 1 kpc. This effect was not found in §5.4.1, where the cloud velocity distribution was assumed to be symmetric around the circular

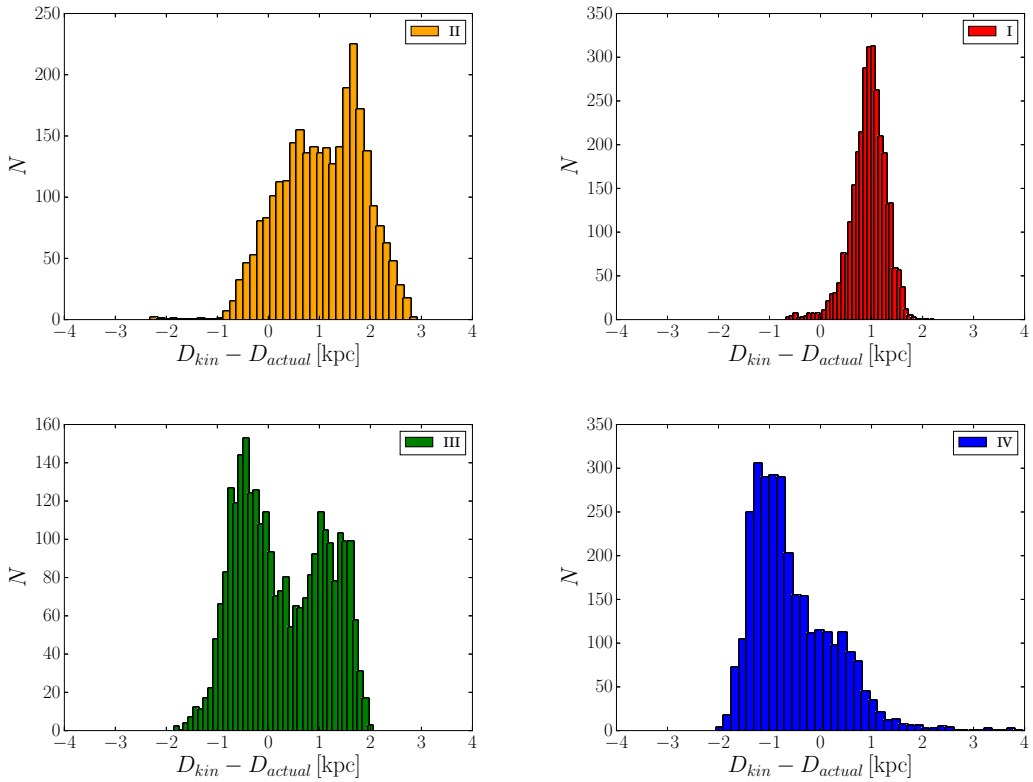

Figure 5.11: Distance error ($D_{\rm kin} - D_{\rm actual}$) distributions per section: section I (upper right), section II (upper left), section III (lower left), section IV (lower right). These are results from the kinematics in the actual simulation, which include both radial and azimuthal streaming motions. The net offset in the distribution of sections I and IV is a consequence of a net inward radial motion and the bimodal behaviour in sections II and III is a result of the two main groups in the azimuthal velocity.

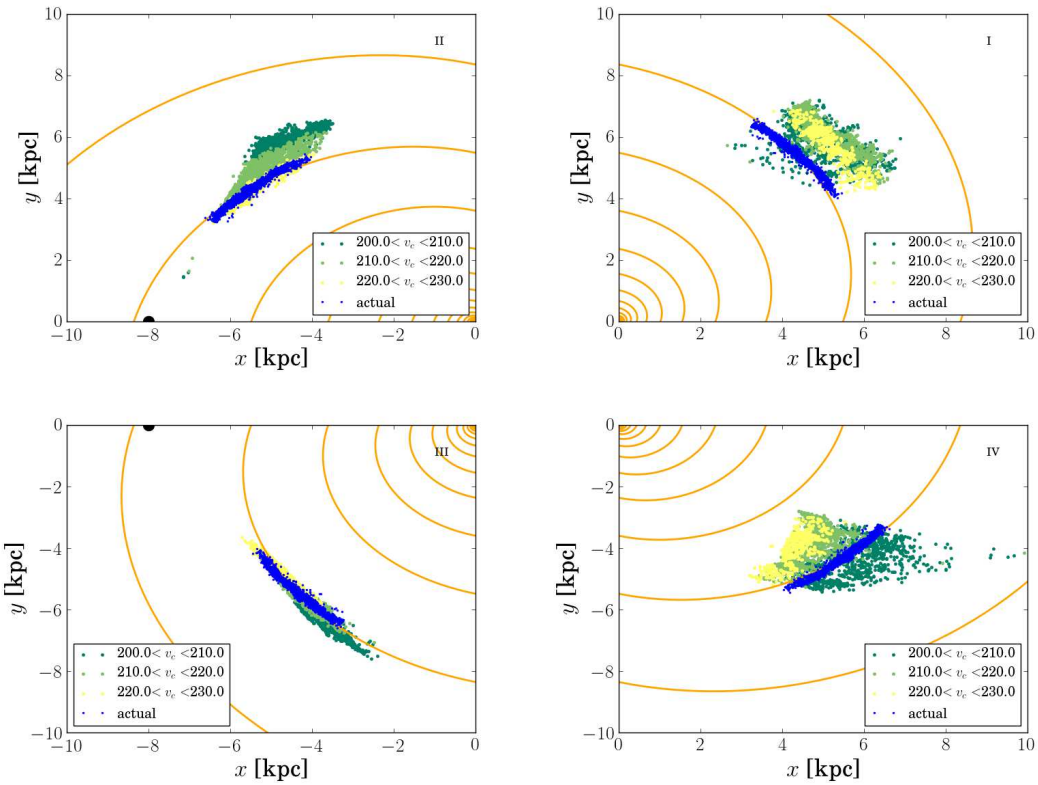

Figure 5.12: Recovered positions maps colour coded by the cloud's azimuthal velocity from the simulation. The solid curves represent the spiral arms tracking the actual cloud distribution. These results show the error introduced by streaming motions in the spiral arm in the recovered positions obtained using the kinematic distance.

velocity. The cloud-to-cloud dispersion propagates into a broader error distribution around the systematic shift.

5.4.3 Comparison with the N-body global model

In this subsection, the kinematic distance analysis described in the previous sections is applied to a snapshot of the 32M global model. Although these results may not be directly applicable to the Milky Way because the global model is based on a different target galaxy, they can give more insight into the limitations of the kinematic estimate. An advantage of the global model is that spiral structure of the galaxy is traced over a wider section of the disc compared to the spiral arm simulation. For this analysis, clouds where identified using a $\rho_{\rm thresh} = 100\,{\rm M}_\odot\,{\rm pc}^{-2}$ and $l_{\rm link} = 1$ pc. A higher density threshold is chosen because the self-gravity drives the formation of higher-density structures.

The radial velocity of the clouds compared to the average radial velocity of the gas (aver-

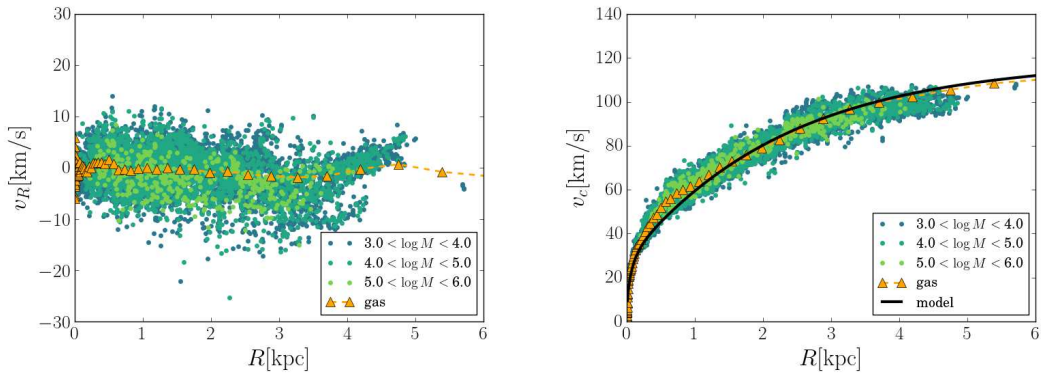

Figure 5.13: Radial velocity v_R (left panel) and circular velocity v_c (right panel) of the cloud distribution identified in the 32M simulation (N-body stellar potential).

aged over annular bins) is shown in the left panel of Figure 5.13. Similarly, the circular velocity compared to the average value of the gas is shown in the right panel of Figure 5.13. The average dispersion of the distribution is close to zero, however most of the clouds are bounded between $v_R \pm 10$ km s^{-1} and for some particular cases it can be close to -20 km s^{-1}. The circular velocity also shows some deviations with respect to the average gas motion. The gas as a whole is rotating slightly faster near the centre of the galaxy, which may be a consequence of some readjustment of the inner mass distribution as the system evolves.

For convenience, an artificial observation point is set at $\mathbf{R}_0 = \langle -8.0, 0.0, 0.0 \rangle$ kpc moving at the local circular velocity $v_c(R_0) \approx 116$ km s^{-1}. This is a purely arbitrary choice for this particular model galaxy. The calculations are limited to clouds with a galactic longitude of $|l| > 15°$ from the point of view of the imaginary observer. For clouds closer to $l = 0$, the projection of the circular velocity is very close to zero (in the Milky Way context, this region is usually known as the zone of avoidance).

The kinematic distance compared to the actual one is plotted in the left panel of Figure 5.14 and the error distribution is plotted in the right panel of Figure 5.14. In the left panel, the points low relatively close to the dotted line where the estimate and actual distances are equal, although there is a noticeable scatter. As the actual distance increases, the kinematic distance tends to be overestimated. The right panel of Figure 5.14 shows that the distribution is not exactly centred at zero. The error ranges between -2.28 kpc and 2.23 kpc and the standard deviation is 0.656 kpc. These results are consistent with those of the spiral arm simulation.

The actual cloud positions are plotted in the top panel of Figure 5.15 and the recovered

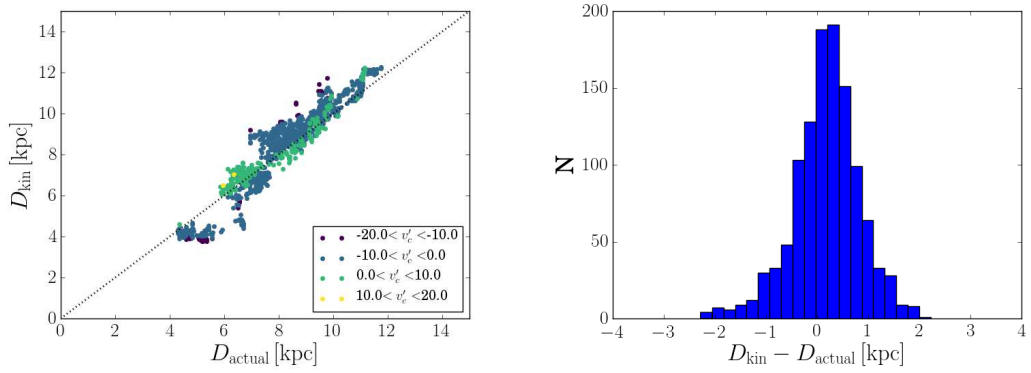

Figure 5.14: Kinematic distance $D_{\rm kin}$ compared to the actual distance $D_{\rm actual}$ (left panel) and distance error distribution (right panel) for clouds identified in the 32M simulation.

positions are plotted in the lower panel of the same figure. In the upper section of the lower panel, the results show that the 4 arms are roughly recovered but with an apparently wider distribution. However, the closest arm to the observed is significantly distorted. For the lower section of the lower panel, the 3 main arms are approximately recovered but with a clearly distorted geometry. A completely spurious group appears around $x = -4$ kpc and between $y = -3$ kpc and $y = -2$ kpc. The distortions in the spiral arm geometry are consistent with those found in the MW spiral arm simulation.

5.5 Discussion

In terms of observational data, Reid et al. (2009) derive a distance using the trigonometric parallax. They also calculate the kinematic distance and compute the difference between the two methods. Their results show errors larger than a kpc for some objects. The analysis in this chapter finds a similar range of errors. Reid et al. (2009) propose a correction to the kinematic estimate based on the motions of the clouds measured in their observations. Although this does improve the method, it still gives large errors for some objects.

Roman-Duval et al. (2009) calculate an uncertainty in the kinematic distance by adding a velocity component ± 15 km s^{-1} with respect to the Galaxy's circular velocity and find relative errors lower than 30%. The results of this chapter find a similar range of values. However, it shows that assuming a cloud-to-cloud velocity dispersion symmetric around the rotation curve may not be applicable in the vicinity of a spiral arm due because the cloud distribution as a whole may have net average deviations from a circular orbit.

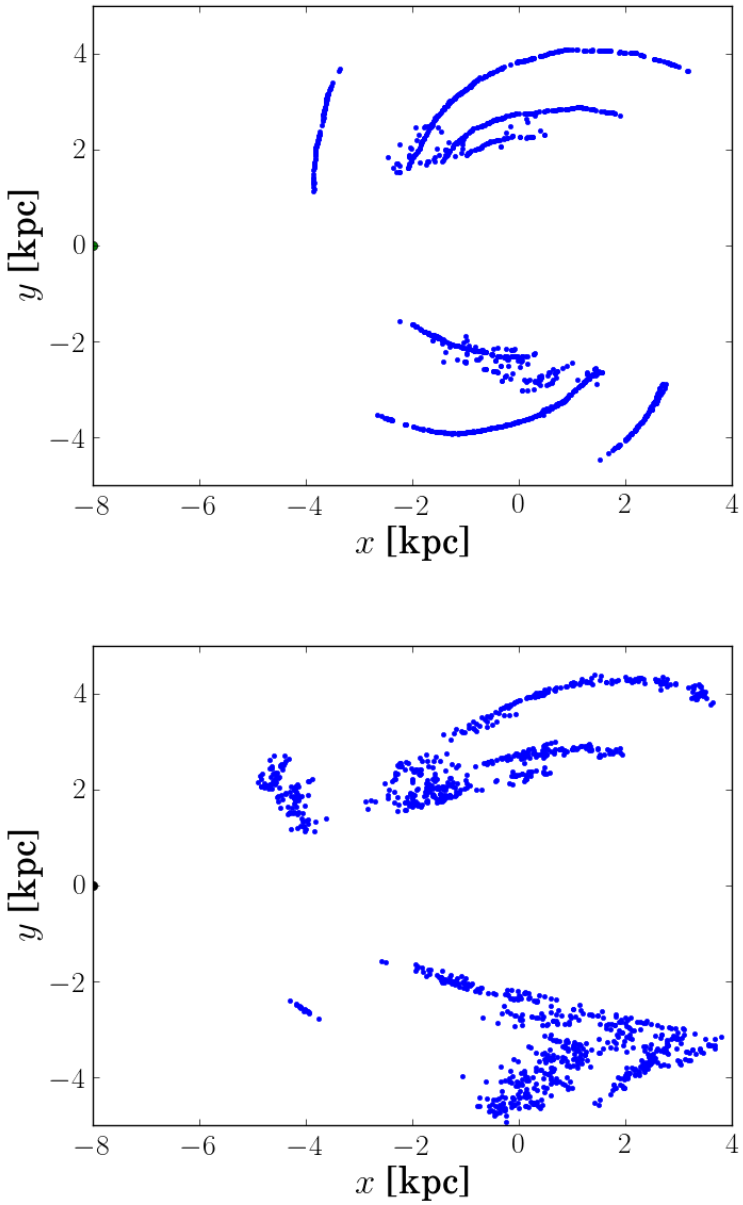

Figure 5.15: Actual cloud positions (top panel) and positions recovered from the kinematic distance estimate (lower panel) for clouds identified in the 32M simulation. The black dot represents the position of the artificial observation point.

Other works, such as Anderson et al. (2012) and Wienen et al. (2015), estimate a distance uncertainty by adding and subtracting a value of $(7-8)$ $\mathrm{km\,s^{-1}}$ to the line-of-sight velocity. Anderson et al. (2012) find a relative error lower than 20%. The added velocity value may be reasonable to account for a cloud-to-cloud velocity dispersion considering the values found in the previous analysis. However, it is still not considering the systematic error introduced by an average streaming motion of the cloud distribution.

From the point of view of simulations, Gómez (2006) performed a similar analysis using a global model of the Milky Way for the global HI gas distribution and concluded that the distance error can be larger than a kpc and is greatest in the lines-of-sight in the direction of spiral arms. The error results in a recovered gas distribution with significant distortions. Baba et al. (2009) obtain a similar result using a global N-body model of the Milky Way galaxy. The errors found in this chapter are comparable to those of Gómez (2006) and Baba et al. (2009). The recovered positions, both in the spiral arm simulation and the global model, show that the inferred spiral structure is considerably altered with respect to the original one.

The spiral arm simulation has the advantage of following with more detail the kinematics of individual clouds. It shows that the spiral introduces average streaming motions that result in systematic errors in the kinematic distance. The analysis of the global N-body model, which includes more realistic spiral arm structure, is consistent with that of the spiral arm simulation.

5.6 Conclusions

The potential of the spiral arm introduces net radial and azimuthal streaming motions in the cloud distribution as a whole, which introduces systematic errors as large as $1kpc$ in the kinematic distance. The cloud-to-cloud velocity dispersion introduces an additional spread in the error distribution of estimated errors. Given the calculated kinematic distances with respect to an imaginary observing point, the recovered positions show significant distortions with systematic offsets with respect to the actual structure. Results from surveys that probe the spatial relationship between molecular clouds and star forming regions with respect to spiral arm structure using the kinematic estimate may be affected by these errors.

6

Molecular Cloud Properties: Mass, Size, Velocity Dispersion

The following chapter introduces the analysis of molecular cloud properties identified in the model galaxies. §6.1 introduces the background on previous work on properties of molecular clouds. §4.2 presents results on the isolated evolution of the model galaxies including heating and cooling. §6.2 presents results on the mass function and the variation of properties with location. §6.3 presents an analysis of the mass-radius relation. §6.4 presents an analysis of the mass-velocity dispersion and the velocity dispersion-size relations; §6.5 and 4.6 show the discussion and conclusion, respectively.

6.1 Overview of Properties of Molecular Clouds

To understand the conditions that trigger star formation, it is necessary to obtain information of the properties and dynamics of the surrounding gas cloud. Since the earliest molecular gas surveys (e. g. Solomon et al. 1979; Dame et al. 1986; Solomon et al. 1987), observers have

measured cloud properties such as the mass, size, surface density, and velocity dispersion focusing mostly on Milky Way clouds. With the increase of observational power, the available data has increased significantly and now allows the study of clouds in both the Milky Way and nearby extragalactic sources (e. g. Rosolowsky 2005; Bolatto et al. 2008; Hughes et al. 2013; Schinnerer et al. 2013; Meidt et al. 2013; Colombo et al. 2014b; Dobbs et al. 2014; Heyer & Dame 2015; Miville-Deschênes et al. 2017).

Molecular cloud masses can be estimated by integrating the observed CO intensity over the observed solid angle of the cloud and applying a CO-to-H_2 conversion factor (e. g. Rosolowsky et al. 2003; Roman-Duval et al. 2010; Miville-Deschênes et al. 2017) or by calculating the virial mass in terms of the measured velocity dispersion (e. g. Solomon et al. 1987; Rosolowsky et al. 2003). The first method depends on the distance which makes it less reliable for Milky Way surveys and assumes that the CO is effectively tracing the H_2. The second method depends only on the observed velocity dispersion, but assumes that the cloud is in virial equilibrium.

Once the mass is estimated, it is possible to characterise the cloud population by obtaining the mass function. Several works have assumed a function of the form (Rosolowsky, 2005; Williams & McKee, 1997):

$$\frac{\mathrm{d}N}{\mathrm{d}M} \propto M^{-\gamma}, \tag{6.1}$$

where N is the number of clouds per bin, M is the cloud mass, and γ is the exponent measuring the function's slope in logarithmic space. In practice, the cumulative function is usually reported in observational surveys and has the form

$$N(>M) = \int \left(\frac{\mathrm{d}N}{\mathrm{d}M}\right) dM \propto M^{-\gamma+1}. \tag{6.2}$$

Solomon et al. (1987) found that $\gamma = 1.5$ for a sample of Milky Way clouds. On the other hand, Rosolowsky (2005) finds that γ varies between 1.53 and 2.29 based on different regions in the Milky Way. The function becomes steeper for the outer Milky Way. Roman-Duval et al. (2010) finds $\gamma = 1.64$ and Miville-Deschênes et al. (2017) finds that $\gamma = 2$ for more recent surveys of the Milky Way. For other Local Group galaxies, Rosolowsky (2005) finds $\gamma = 2.85$ for M33 and $\gamma = 1.71$ for the Large Magellanic Cloud. The result has some sensitivity to the method used to estimate the cloud's mass. For M51, Colombo et al. (2014b) find that γ varies between 1.33 and 2.55 in different regions of this galaxy. The shape of the mass function may indicate local variations in the mechanisms that drive the formation of molecular clouds (Rosolowsky,

2005; Elmegreen & Falgarone, 1996; Vázquez-Semadeni et al., 1997; Wada et al., 2000; Dobbs, 2008).

The physical size of the cloud can be estimated by $R = D \tan \delta\theta$, where R is the size, D is the distance to the cloud, and $\delta\theta$ is the apparent angular size. Because clouds do not necessarily have circular shapes on the sky's plane, Solomon et al. (1987) used a method in which the geometric mean of the characteristic extensions in Galactic latitude and longitude is used to define the angular size. A similar approach is followed by Rosolowsky et al. (2003) and Miville-Deschênes et al. (2017). Roman-Duval et al. (2009) estimate the size by first calculating the cloud's projeced area given the distance and solid angle and then use this quantity to obtain an effective radius: $R = \pi^{-1/2} A^{1/2}$. Some studies suggest that the size distribution follows a power law function given by $dN/dR \propto R^{\alpha}$ (Elmegreen & Falgarone, 1996; Heyer & Dame, 2015).

The mass and size follow a well-defined correlation of the form $M \propto R^{a}$. Solomon et al. (1987) find that $a = 2$; Elmegreen & Falgarone (1996) find $a = 2.38 \pm 0.09$; Roman-Duval et al. (2010) find that $a = 2.36 \pm 0.04$; and a recent survey by Miville-Deschênes et al. (2017) finds that $a = 2.2 \pm 0.2$. All these values are derived from Milky Way surveys. This behaviour is usually interpreted as a result of the interstellar medium having a fractal nature, with a fairly "spongy" nature (Elmegreen & Falgarone, 1996; Roman-Duval et al., 2010). However, it can also be a result of clouds having a constant surface density ($M \propto \Sigma R^2$).

A third property of interest is the cloud's velocity dispersion (e. g. Larson 1981). This has the advantage of being directly measured by observations and is not affected by distance. It also offers a diagnostic of the internal dynamics of a cloud. The mass, size, and velocity dispersion are important in determining whether the dynamical state of the cloud (whether is dominated by kinetic or gravitational energy) (e. g. Heyer & Dame 2015; Dobbs et al. 2014). The analyses of Larson (1979) and Larson (1981) find that the velocity dispersion σ_v and the cloud's size R follow a relation of the form $\sigma_v \propto R^{n}$. Larson (1981) found that $n = 0.38$ for a sample of Milky Way clouds while Solomon et al. (1987) finds that $n = 0.5$. Rosolowsky et al. (2003) find that $n = 0.45 \pm 0.02$ for a sample of M33 clouds and Miville-Deschênes et al. (2017) find that $n = 0.63 \pm 0.30$ for a recent survey of Milky Way clouds. Larson's $\sigma_v - R$ relation is usually interpreted as a consequence of the turbulent nature of clouds and the nearby ISM. Larger scales allow larger turbulent eddies, which results in larger velocities. On the other

hand, the exponent $n = 0.5$ results from assuming that the cloud's kinetic and gravitational energies are equal and that the surface density of clouds is fairly constant (Heyer & Dame, 2015). On the other hand, Heyer & Dame (2015) shows that there is a tighter correlation when σ_v is compared to the product ΣR, where Σ is the surface density of the cloud. Heyer et al. (2009) find that there is a tight relation between $\sigma_v/R^{1/2}$ and Σ.

Several works studying molecular clouds in other galaxies have found evidence of cloud properties varying between galaxies. For example, the study of clouds in the spiral galaxy M64 by Rosolowsky & Blitz (2005) finds that in terms of surface density, size, and some scaling relations, there are some differences with respect to Local Group sources. In M33, Gratier et al. (2012) find that the power of the cloud mass function varies slightly between the inner and outer galaxy. Recent CO observations of M51, M33 and the Large Magellanic Cloud by Hughes et al. (2013) shows that the properties representative of the cloud populations have differences between the galaxies compared. A more detailed analysis of molecular clouds in M51 shows that properties such as the mass, the mass function, and the velocity dispersion vary between different regions of the galaxy. This suggests that there may be an environmental dependence in the mechanisms that drive the formation of molecular clouds (Meidt et al., 2013; Colombo et al., 2014b). From a theoretical perspective, Meidt et al. (2018) have developed analytic models where the cloud dynamics are a result of epicyclic motions driven by the large-scale structure of a galaxy. Their model can predict variations in the $\sigma_v/R^{1/2}$-Σ relation as a function of different galactic models. This motivates hydrodynamic simulations that explore molecular cloud formation and their dynamical properties taking into account the effect of the large-scale structure of the galaxy. It is important to address the effect of different spiral arm models. For example, explore the differences between a strong grand-design perturbation and a more flocculent and transient spiral arm.

This chapter aims to explore the effect of the underlying spiral potential in the properties of molecular clouds. For this purpose, clouds are identified in the N-body and spiral potential simulations using the identification algorithm described in §5.2.2 of Chapter 5. The analysis focuses particularly on the clouds' mass, size, and velocity dispersion and the scaling relations between these quantities. The results and discussion are presented in the following sections.

6.2 Cloud Mass Function and Spatial Location

6.2.1 Cloud Mass Function

The cloud mass function, expressed as a mass histogram with a distribution of the form $f(M) \propto M^{\gamma}$, is shown in Figure 6.1. The left and right columns correspond to the N-body and spiral potential simulations respectively. The top row corresponds to clouds identified using the friends-of-friends algorithm of §5.2.2 with a linking length $l_{\rm link} = 1$ pc, the middle panel to $l_{\rm link} = 2.5$ pc, and the bottom panel to $l_{\rm link} = 5$ pc. In the N-body simulation, the histogram can be represented by a two-power law function; the inner power γ_i is fitted where $M < 1.75 \times 10^5\ M_{\odot}$ and the outer power γ_o is fitted at values greater than this limit. This transition value was chosen from a qualitative inspection of the plots. γ_i varies between -0.72 and -0.23 and γ_0 varies between -3.09 and -2.21. In the spiral potential, the histogram is well represented by a single power law with the exponent γ, which varies between -0.77 and -2.11 depending on the linking length used. Table 6.1 shows the values of the fitted functions as a function of the linking length used for cloud identification.

Figure 6.2 shows the cumulative function as calculated in observational surveys. The left and right columns correspond to the N-body and spiral potential, respectively. It is interesting that the N-body simulations shows a mass function with a behaviour qualitatively similar to those obtained in observations of other galaxies (e. g. Rosolowsky 2005; Colombo et al. 2014b), which observe a similar behaviour transitioning from a lower to a higher slope.

These results provide some insight of the effect of the linking length in the cloud identification. For smaller linking lengths, some large structures may be broken into smaller substructures which results in higher cloud counts at smaller mass bins and lower counts at the higher mass bins. On the other hand, as the length increases, the classification algorithm starts linking structures over larger distances resulting in an increased number clouds in higher mass bins. This effect is clear in the case of the spiral potential simulation. For $l_{\rm link} = 5$ pc, some structures with a mass close to $10^7\ M_{\odot}$ where identified. On an inspection of the positions of identified clouds, it was found that the algorithm using this length had identified a large section of a spiral arm as a single cloud. It is noted that all the properties discussed in this chapter were analysed with the three values of linking length previously described. For the analysis of cloud properties presented in this chapter, the results of $l_{\rm link} = 2.5$ pc are used.

Table 6.1: Power Law Exponents fitted to the Cloud Mass Functions

	N-body model		Spiral Potential
$l_{\rm link}$ [pc]	γ_i	γ_o	γ
1.0	-0.72	-3.09	-2.11
2.5	-0.41	-3.04	-1.06
5.0	-0.23	-2.21	-0.77

For the N-body model, the mass function is fitted by M^{γ_i} for $M < 1.75 \times 10^5\ M_\odot$ and M^{γ_o} for $M \leq 1.75 \times 10^5\ M_\odot$. This threshold was chosen by inspection of the plots. For the spiral potential simulation, the mass function is fitted by M^{γ}.

The number of clouds is sensitive to the cloud definition, as it would be expected. However, it is interesting to note that the qualitative shape of the mass function depends more on the physics involved (self-gravity vs. non-self gravitating cases) as well as the choice of galactic potential model, as suggested by Figure 6.1. In the N-body model, where self-gravity is included, clouds with masses higher than $\sim 10^6\ M_\odot$ are not found. This limit may be explained by the fact that as gas flows through the spiral arm, dense features are formed by shocks and cooling. Then, self-gravity fragments these structures and produces locally dense clouds. This may explain the upper limit seen in the mass function for the N-body model. In the spiral potential simulation, the gas only shocks and cools, but there is no self-gravity included. This allows to form longer structures along the arm and some of these can be quite massive. However, this may also depend on the time chosen to identify the clouds. As the simulation runs, more structure develops, specially as gas moves across different arms along its orbit. The choice of linking length affects the cloud count and thus the fitted γ value, which may affect both observations and simulations. A comparison of these spectra with those of other numerical work is discussed in more detail in §6.5.1.

6.2.2 Cloud Masses as a Function of Position

Figure 6.3 shows a cloud position map colour-coded by mass with $l_{\rm link} = 2.5$ pc. The right and left panels correspond to the N-body and spiral potential simulations, respectively. Both panels are compared at the same time ($t \approx 24$ Myr) from the point where cooling was introduced. In the N-body simulation, the more massive clouds tend to be closer to the centre and associated with spiral arms. Less massive clouds are associated with inter-arm regions. As shown in Chapter 4, gas is flowing into the spiral arms, which drives higher gas densities in these regions. Most of the dense gas remains associated with these structures. Unfortunately, the simulation

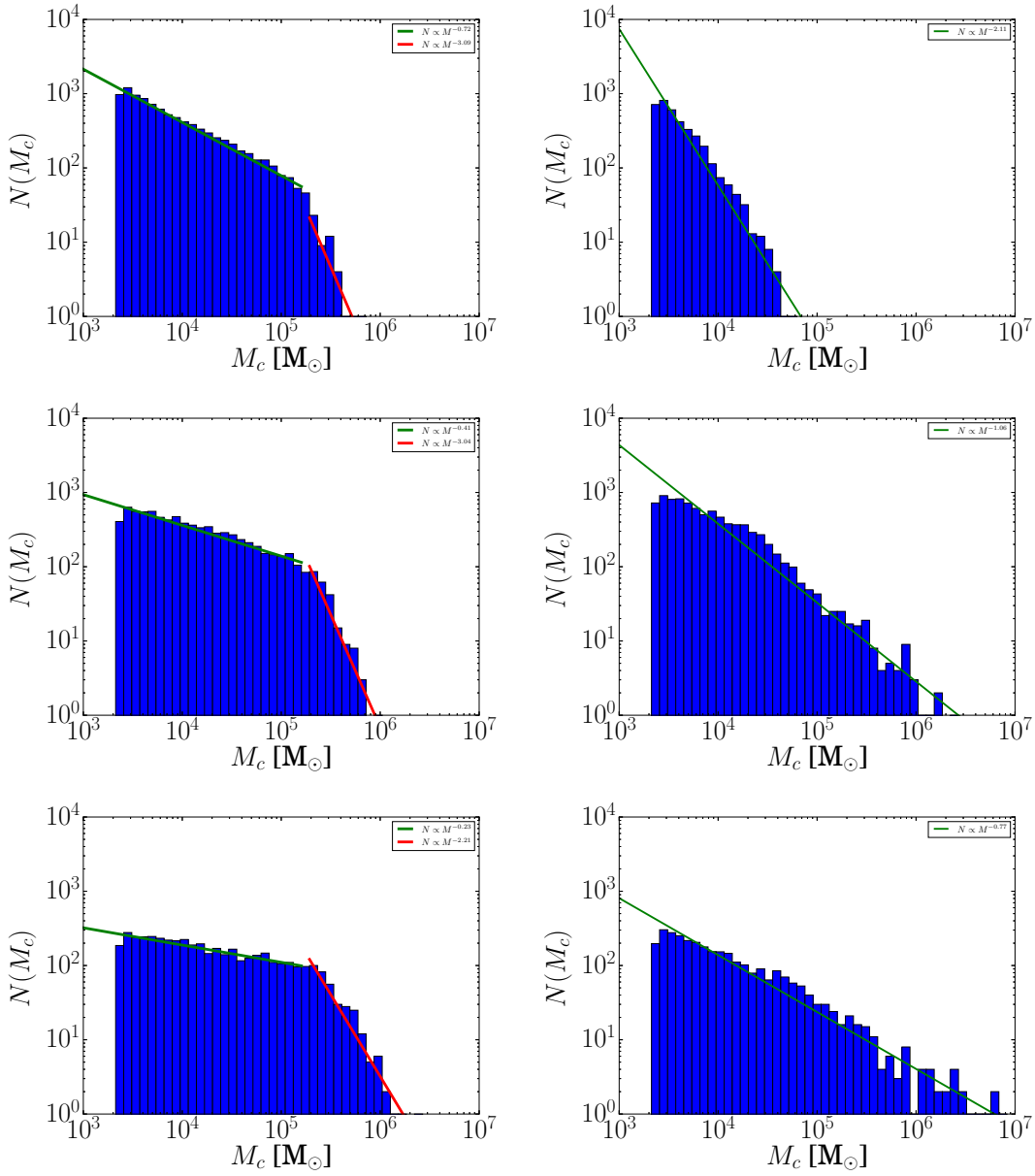

Figure 6.1: Cloud mass histograms: N-body model (left) and spiral potential (right); top $l_{length} = 1$ pc, middle $l_{length} = 2.5$ pc and bottom $l_{length} = 5.0$ pc. These plots correspond to $t \approx 24$ Myr of the simulation.

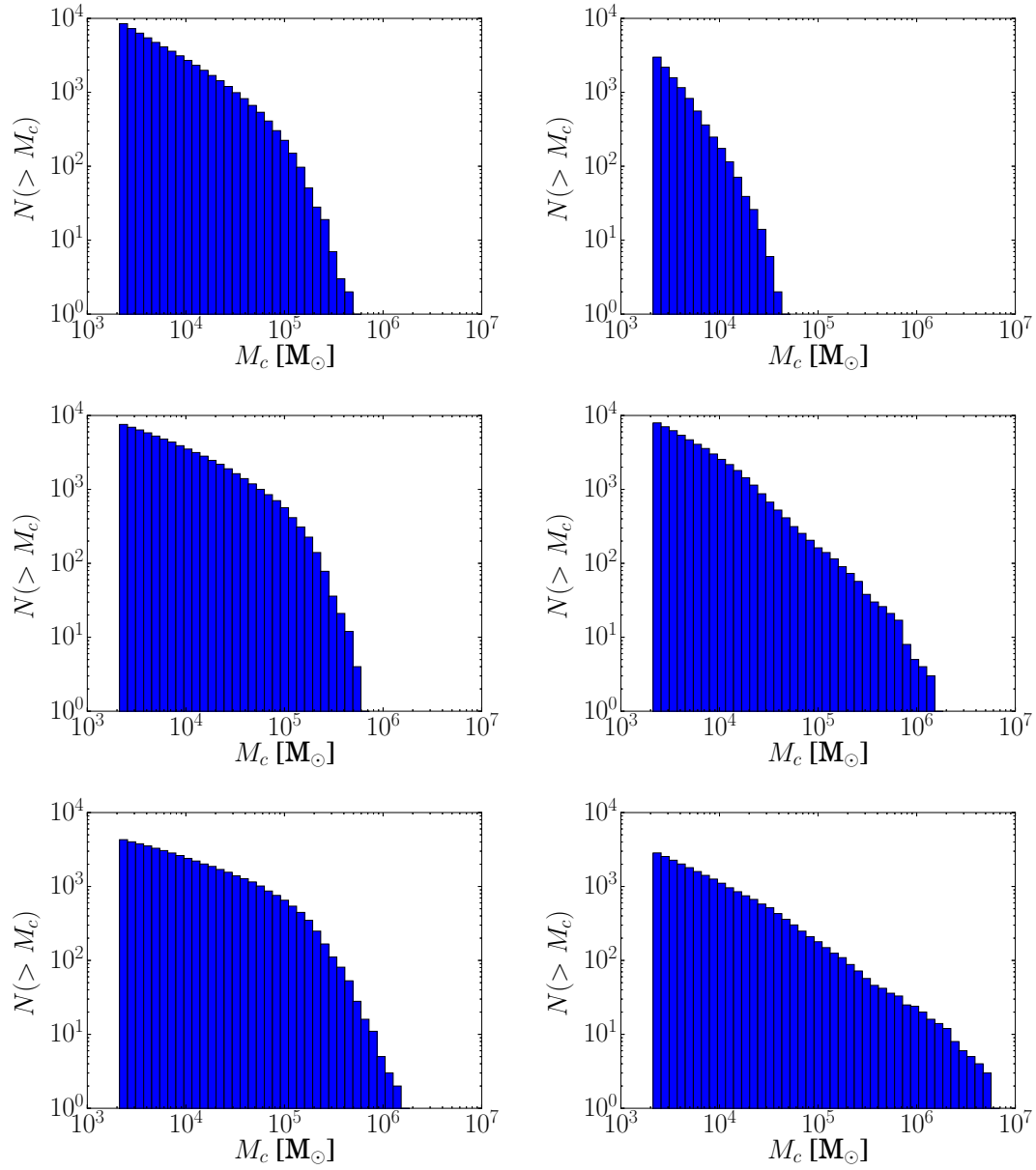

Figure 6.2: Cloud mass function as computed by observers: N-body model (left) and spiral potential (right); top $l_{length} = 1$ pc, middle $l_{length} = 2.5$ pc and bottom $l_{length} = 5.0$ pc. These plots correspond to $t \approx 24$ Myr of the simulation.

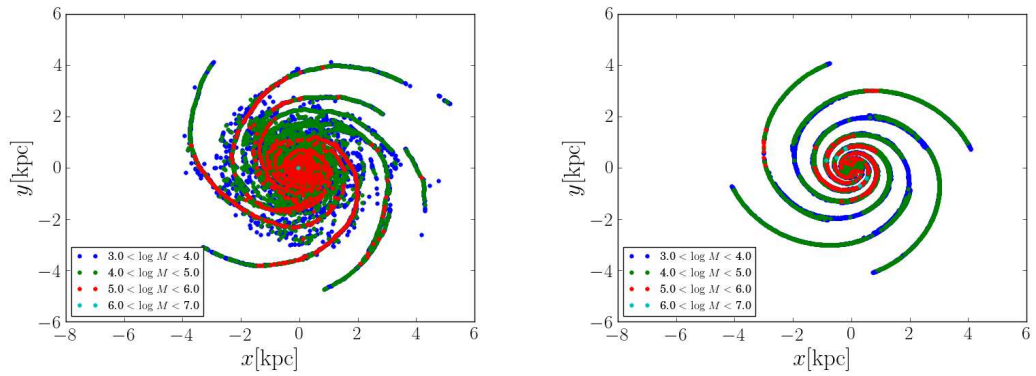

Figure 6.3: Cloud position map coloured by mass: N-body model (left) and spiral potential (right). Clouds were identified with $l_{length} = 2.5$ pc. These plots correspond to $t \approx 24$ Myr of the simulation.

has not been evolved for a sufficiently large timescale to see their long term evolution.

In the spiral arm simulation, the trend is similar but it does show some variation of cloud masses along the arm. This may be the result of an artifact of the cloud definition. There are no inter-arm clouds at this point. As shown in Chapter 4, the gas density increases as gas flows through the arm and should decrease as it leaves due to the expansion in the inter-arm region. The lack of self-gravity may explain the absence of clouds in the inter-arm regions. However, this may also be a consequence of the fact that the model has not been evolved for a longer timescale.

In both simulations, the clouds and the densest gas are formed within a radius of approximately $4-5$ kpc, which is the region inside the co-rotation radius (refer to Chapter 4 for a discussion on the cold gas density distribution). A discussion is presented in §6.5.1.

6.2.3 Cloud Velocities as a Function of Position

Figures 6.4 and 6.5 show a cloud position map coloured by the radial v_R and relative azimuthal $v_{\phi(\mathrm{rel})}$ velocity components, respectively, for each simulation. The clouds are identified with $l_{\mathrm{link}} = 2.5$ pc; $v_{\phi(\mathrm{rel})}$ is the cloud's azimuthal velocity relative to the circular velocity at its position. In the N-body simulation, there is a distribution between positive and negative values of v_R ranging from approximately -20 km s^{-1} to 15 km s^{-1}. In terms of circular velocities, $-24 < v_{\phi(\mathrm{rel})} < 21$ km s^{-1}. In v_R it is possible to see some trends of clouds moving with $v_R < 0$ at regions where gas should be leaving the arm (rotation is counter clock-wise). This tendency is clearer in the middle regions of the cloud distribution. In the azimuthal component, the overall tendency is for clouds to move slower than the rotation curve in most parts of the

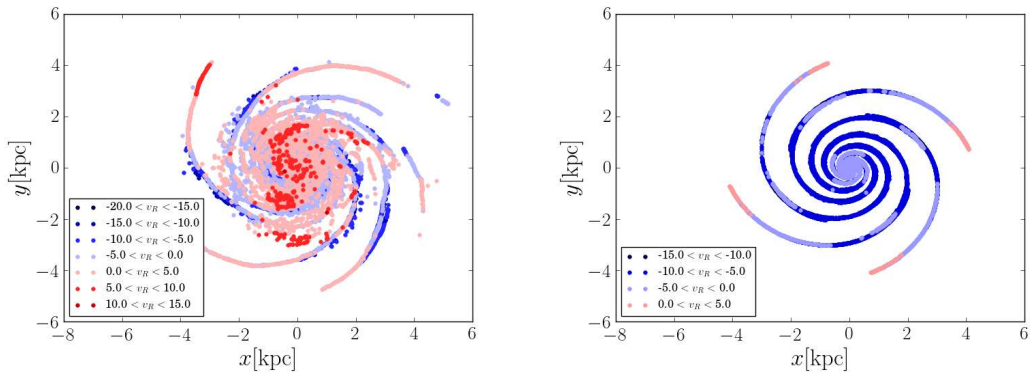

Figure 6.4: Cloud position map coloured by v_R: N-body model (left) and spiral potential (right). Clouds where identified with $l_{length} = 2.5$ pc. These plots correspond to $t \approx 24$ Myr of the simulation.

galaxy, but this tendency reverts in the inner galaxy. It is noted that clouds too close to the galaxy's centre have higher-orbital frequencies and may be affected by a higher shear rate due to the steeper slope of the rotation curve near this region (see Figure 3.5 of Chapter 3). In the spiral potential simulation, v_R ranges from around -15 km s^{-1} to 5 km s^{-1} and is mostly negative for most of the galaxy. The relative azimuthal velocity ranges from -6 to 14 km s^{-1}, and the sign varies with location in the galaxy. A discussion is presented in §6.5.1.

6.3 Mass-Size Relation

Figure 6.6 shows the mass-radius relation for the clouds identified with $l_{\rm link} = 2.5$ pc. The left panel corresponds to the N-body simulation and the right one to the spiral potential simulation. The cloud radius is defined as the root-mean-square (rms) value of the radial positions of the particles with respect to the cloud's centre of mass, which gives a characteristic radius. The points are colour-coded by the sign of the vertical angular momentum L_z. The green-line corresponds to $M \propto R^{2.36}$, which is the mass-radius relation obtained in Roman-Duval et al. (2010) from a survey of Milky Way clouds fitted to the simulated clouds. The grey-line corresponds to fitting a model with a free exponent. The cut at the lower mass end of the distribution introduced a problem for conventional best-fit techniques based on minimising the vertical errors, which tended to bias the exponent to lower values. For this reason, a fit based on minimising the orthogonal errors was obtained with python's scipy implementation of the Boggs & Rogers (1990) method. This certainly improved the result.

For the N-body simulation, the best-fit yields $M \propto R^{2.41}$, which is consistent with the observationally derived value. For the spiral potential simulation, the best-fit gives $M \propto$

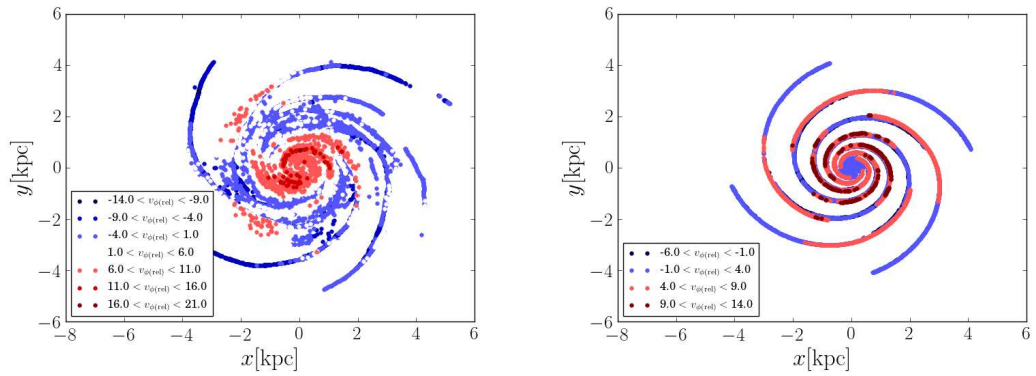

Figure 6.5: Cloud position map coloured by $v_\phi - v_c(R)$: N-body model (left) and spiral potential (right). Clouds where identified with $l_{length} = 2.5$ pc. These plots correspond to $t \approx 24$ Myr of the simulation.

$R^{2.01}$, which is reasonably close but slightly lower. The spiral potential simulation shows less dispersion in the relation compared to the N-body model. However, this could be sensitive to the cloud definition and to the approximation used to define a cloud's characteristic size. It is still interesting that the relation obtained from both simulations is consistent with the observed tendency.

Figure 6.7 shows the mean density profile taking into account the information of all the clouds. The left panel shows results for the N-body model and the right one for the spiral potential simulation. To obtain this plot, the reference for $r = 0$ was taken at the position of the densest particle of each cloud. Then, to obtain the density profile, the particles were split in radial bins. Because the simulation snapshots store the SPH density, it is possible to calculate the mean of the particles densities for each radial bin. The final result is a profile of the mean SPH density per radial bin for each cloud. Given the thousands of clouds identified in the simulations, it is not possible to visualise all the profiles in a single plot. To summarise the information, for each radial bin the median and mean values of all the clouds average density profiles were calculated and plotted as the blue and orange curves respectively. The error bars represent the range between the minimum and maximum values in the distribution of profiles.

The main results are that the mean of the clouds' profiles in the N-body simulation are consistent with a $\rho \propto r^{-1}$ and in the spiral potential the profile tends to be shallower. This density profile means that $M \propto R^2$, which is close to the mass-radius relation obtained. For the spiral potential, the shallow profile indicates a roughly constant surface density profile. This is expected from the fact that gas entering the spiral arm is shocked. The density increases

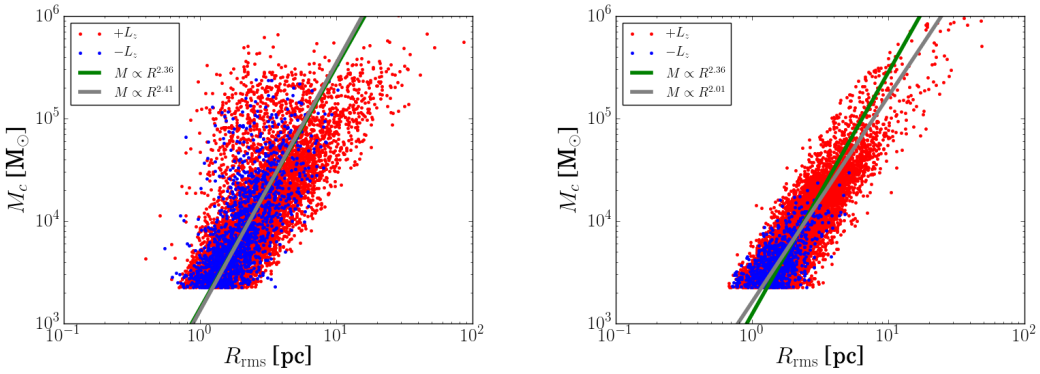

Figure 6.6: Mass-radius relation: grey line, least-squares fit minimising perpendicular offsets; green line, fitting $M \propto R^{2.36}$ minimising perpendicular offsets: N-body model (left) and spiral potential (right). Clouds where identified with $l_{length} = 2.5$ pc. These plots correspond to $t \approx 24$ Myr of the simulation.

and cools down efficiently, but it does not collapse as in the case with self-gravity. However, these plots should be taken with care as the individual cloud profiles may vary from these representative values. A more detailed discussion and comparison with other work is given in §6.5.2.

6.4 Mass-Velocity Dispersion and Velocity-Dispersion Size Relations

6.4.1 Mass-Velocity Dispersion Relation

Figure 6.8 plots the cloud mass with respect to velocity dispersion for the cases with $l_{\rm link} = 2.5$ and 5.0 pc, colour coded by the vertical angular momentum. The left and right columns correspond to the N-body and spiral potential respectively. The velocity dispersion is calculated from:

$$\sigma_v = \bar{v^2} - \bar{v}^2, \tag{6.3}$$

where $v = \sqrt{v_x^2 + v_y^2 + v_z^2}$, which is the magnitude of the particle's velocity. This quantity involves average quantities, which is sensitive to the number of particles. This suggests that lower mass clouds may be more affected by noise due to the lower number of particles sampling the cloud. This motivates to compare the results of using different values of linking lengths. As the linking length is increased, more particles will be associated to a given structure.

The results show that the overall tendency is that the net velocity dispersion grows with increasing mass in both simulations. In the case of the N-body simulation, the results show that the scatter in the relation increases with decreasing cloud mass for the case with $l_{\rm link} = 2.5$.

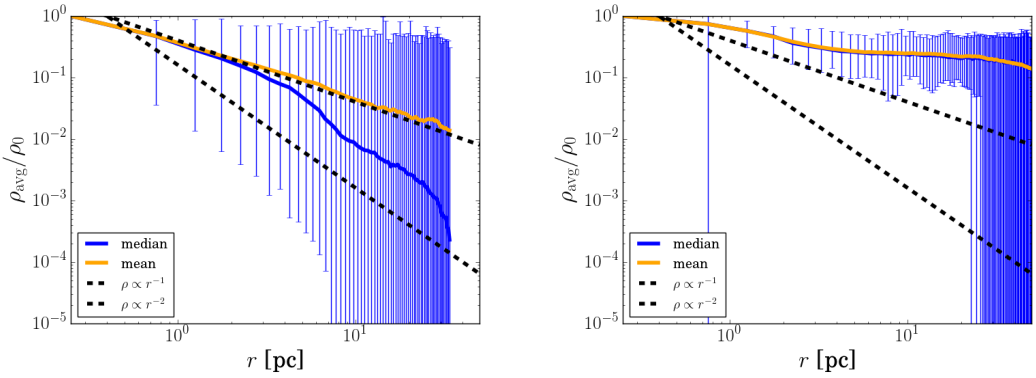

Figure 6.7: Mean particle density profiles of the clouds identified with $l_{length} = 2.5$ pc for the N-body model (left) and spiral potential model (right). The vertical bars represent the range of the density values of the cloud distribution. The lines are the mean and median values.

When the linking length is doubled, the scatter decreases suggesting that it may be an effect associated to the cloud definition. However, the overall tendency is preserved. For the spiral potential simulation, the clouds are approximately scattered in a triangular distribution. This shape does not change significantly when the linking length is increased. This difference may be a consequence of not including self-gravity in the spiral potential simulation.

Figure 6.9 shows the ratio of the velocity dispersion to the sound speed σ_v/c_s as a function of cloud mass and colour coded by the average temperature $T_{\rm avg}$. The left and right panels correspond to the N-body and spiral potential simulations respectively. The sound speed is calculated using the average cloud temperature. These plots make more evident the differences between both simulations. In the N-body simulation, the temperature ranges between approximately 10 and 30 K. The more massive clouds have slightly lower temperatures and higher velocity dispersions, which results in a higher ratio in some cases close to ≈ 10.0. For a significant fraction of clouds, $\sigma_v/c_s > 1$. In the case of the spiral potential simulation, σ_v/c_s is between 1 and 10 for most of the clouds. The lower end of the temperature distribution is slightly higher and $T_{\rm avg}$ ranges between approximately 18 and 27 K. The slightly colder temperatures in the N-body model are a consequence of the self-gravity. This drives gas to higher densities than in the spiral potential simulation (as shown in the density distributions of Chapter 4). A higher density implies a faster cooling rate as it scales with the density squared.

These results are complemented by Figure 6.10, which plots the ratio of the cloud's kinetic energy vs the internal energy $E_K/U_{\rm int}$ as a function of mass for the case with $l_{\rm link} = 2.5$ pc. The kinetic and internal energies are a measure of the cloud's support mechanisms. For $E_K/U_{\rm int} >$

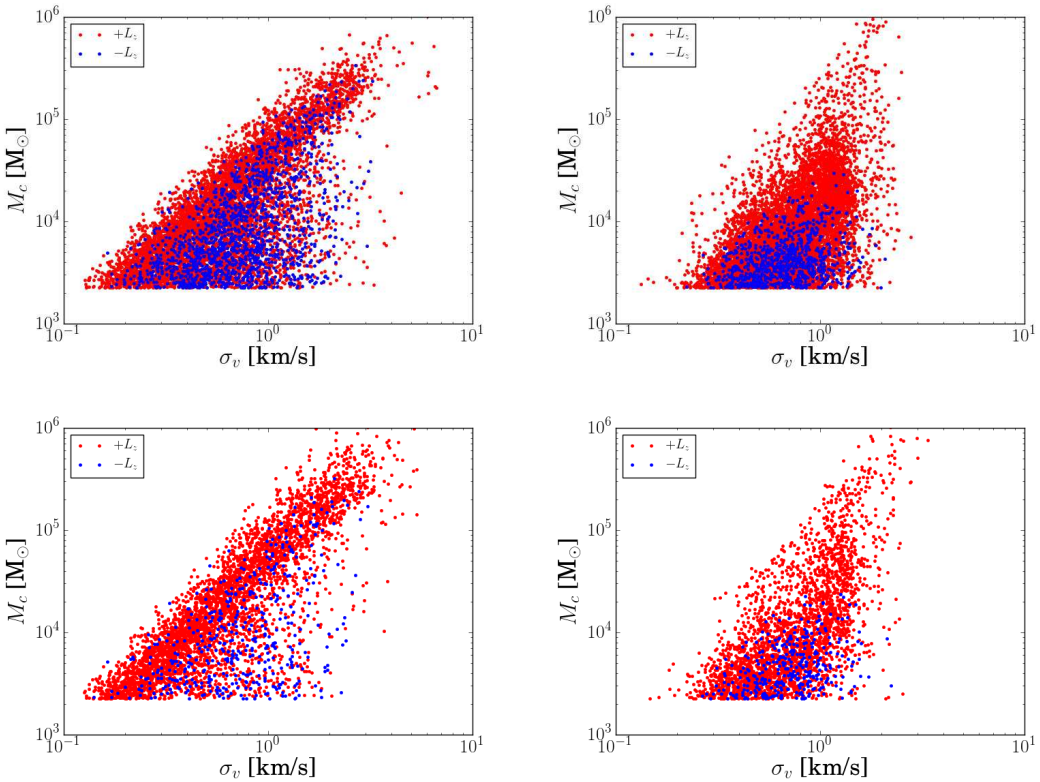

Figure 6.8: Mass-velocity dispersion relation: N-body model (left) and spiral potential (right); top $l_{length} = 1$ pc, and bottom $l_{length} = 5.0$ pc. These plots correspond to $t \approx 24$ Myr of the simulation.

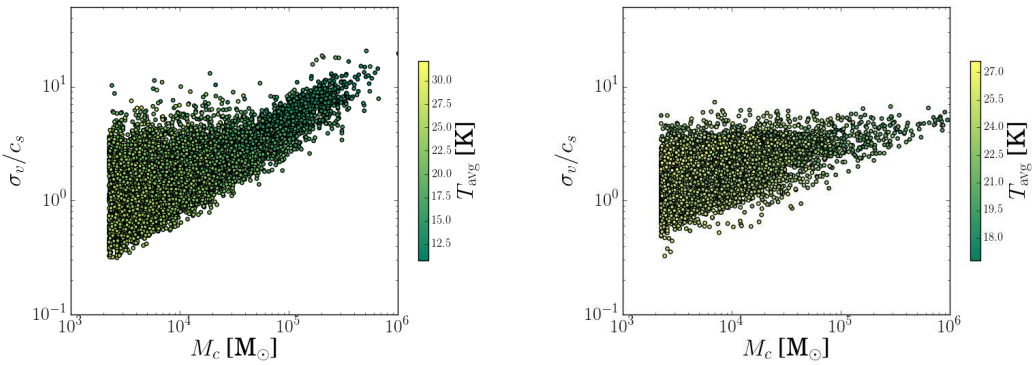

Figure 6.9: σ_v/c_s vs. mass relation colour coded by mean cloud temperature $T_{\rm avg}$ for the N-body model (left) and spiral potential (right). Clouds are identified with a linking length of $l_{length} = 2.5$ pc. The sound speed c_s is calculated from the mean cloud temperature. These plots correspond to $t \approx 24$ Myr of the simulation.

1, the clouds are dominated by kinetic energy; for $E_K/U_{\rm int} < 1$ the clouds are dominated by thermal energy. Figure 6.10 shows that in both simulations the clouds tend to be dominated by kinetic energy in the range of masses studied. The $E_K/U_{\rm int}$ versus cloud mass distributions are similar in shape to those of the σ_v/c_s versus mass. The kinetic and internal energy compared to the gravitational potential energy will be discussed in more detail in §6.4.3.

The results of this section show that in both simulations show that the more massive clouds are associated to larger velocity dispersions and that they tend to be dominated by kinetic energy.

6.4.2 Cloud velocity dispersion-size relation

Figure 6.11 shows the cloud velocity dispersion as a function of the root-mean-square radius of the cloud. The results are shown for clouds identified with $l_{\rm link} = 2.5$ pc. The left and right panels correspond to the N-body and spiral potential simulations respectively. In both cases, three best-fit models have been tested assuming that $\sigma_v = \sigma_0 R^n$. The green line shows the best fit by fixing $n = 0.5$ and fitting only σ_0. The fit is obtained by minimising vertical offsets. This exponent is motivated by Larson's relations. The black line shows the best fit with free parameters, but minimising vertical offsets. The grey line shows the best-fit model minimising orthogonal offsets.

For the N-body simulation, the vertical offsets minimum best-fit yields $n = 0.45$ (black line) and the orthogonal best-fit, $n = 1.06$ (grey line), which is higher from what is expected from Larson's relations. For the spiral potential simulation, the vertical offsets minimum best-

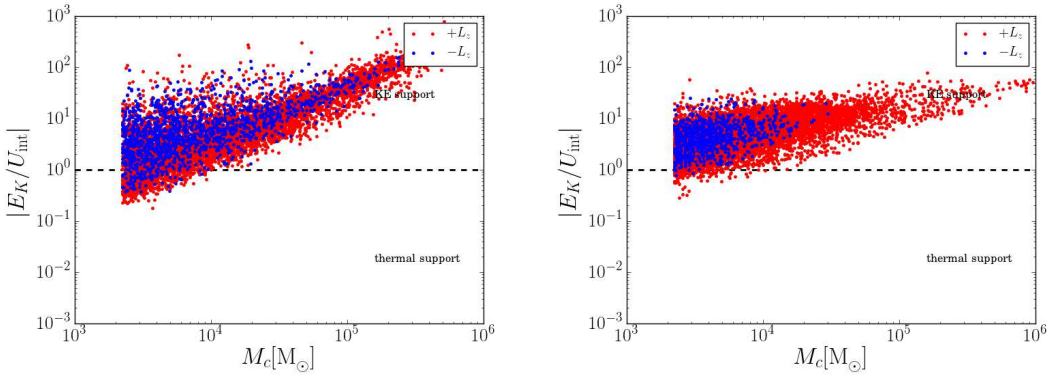

Figure 6.10: Cloud kinetic energy to internal energy ratio $E_k/U_{\rm int}$ vs. mass: N-body model (left) and spiral potential (right). Clouds are identified with $l_{length} = 2.5$. These plots correspond to $t \approx 24$ Myr of the simulation.

fit yields $n = 0.4$ and the orthogonal best-fit, $n = 0.69$, which falls closer to the value of Larson's relations. Inspection of Figure 6.11 shows that the identified clouds do not have a tight correlation in the dispersion-size plane. The cloud-to-cloud scatter is significant, which means that the exponents derived from the fits may be significantly affected by this. The results of Figure 6.11 are sensitive to the cloud definition, particularly in the sense how the characteristic radius is defined.

To reduce the effects of the choice of cloud definition, the velocity dispersion-size relation was explored using the approach in (Bonnell et al., 2013). This consists of taking the positions of the clouds' densest particles as the reference centre. Then several radii are specified and the total velocity dispersion within each radii is calculated. Figure 6.12 shows the results for several radii between 0.5 pc and 100 pc. A slightly higher lower limit was chosen for the spiral potential case. The results on the left panel correspond to the N-body simulation and those on the right panel correspond to the spiral potential simulation. Because for each radii there are dispersion values for all the reference positions considered, the median (blue) and mean (orange) values are plotted. The error bars correspond to the minimum-maximum range of dispersion values calculated at each radii. These values are compared against the $\sigma \propto R^{0.5}$ relation. These plots show that the gas dynamics in the clouds' vicinity are consistent with Larson's relations, although the median and mean values do show a slightly different slope.

The above results show that the kinematics of the simulated clouds are consistent with Larson's velocity dispersion-size relation. However, the values may be rather low compared to the normalisation in Larson (1981). Some previous works have shown that this may be due to

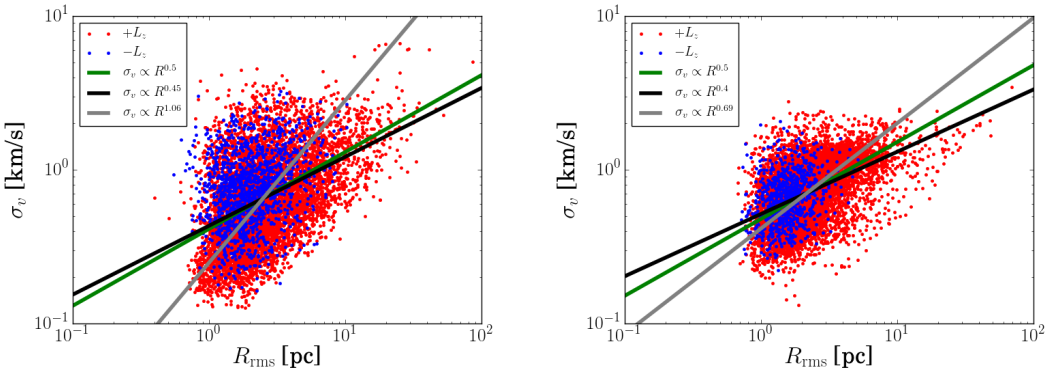

Figure 6.11: Cloud velocity dispersion-radius relation for the N-body (right) and spiral potential (left). The clouds are identified with $l_{length} = 2.5$ pc. The black line corresponds to a least-squares fit minimising the vertical offsets; the grey line corresponds to a least-squares fit minimising the perpendicular offsets; green line corresponds to fitting $\sigma_v \propto R^{0.5}$ by minimising perpendicular offsets.

the lack of feedback injecting additional turbulence. A more detailed comparison with other work in terms of this relation is given in §6.5.3.

6.4.3 Energy Balance in Clouds

Figure 6.13 shows the ratio of kinetic plus internal energy to the gravitational potential energy $|(E_K + U_{\rm int})/U_g|$ of the clouds identified with $l_{\rm link} = 2.5$ pc. The left panel corresponds to the N-body simulation and the right panel to the spiral potential simulation. The gravitational potential energy is calculated from equation:

$$U_g = -\frac{1}{2}\sum_{i=1}^{N}\frac{Gm_i m_j}{|\mathbf{r}_j - \mathbf{r}_i|}, \tag{6.4}$$

where the $1/2$ factor is a correction to account for the fact that the summation calculates the term twice for each pair: $(Gm_i m_j/r_{ij} + Gm_j m_j/r_{ij})$. The simulation offers the advantage of calculating all energy terms directly from the simulation rather than assuming certain approximations such as, for example, spherical symmetry. For the spiral potential simulation, although it is possible to calculate U_g, self-gravity has not been included and this value has to be interpreted with care. Additionally, this simulation is not taking into account the evolution of structures that would eventually collapse due to self-gravity. It is still interesting to note that it shows a similar trend as in the N-body simulation with self-gravity. The results of this section show that clouds have the tendency to be more bound as their mass increases.

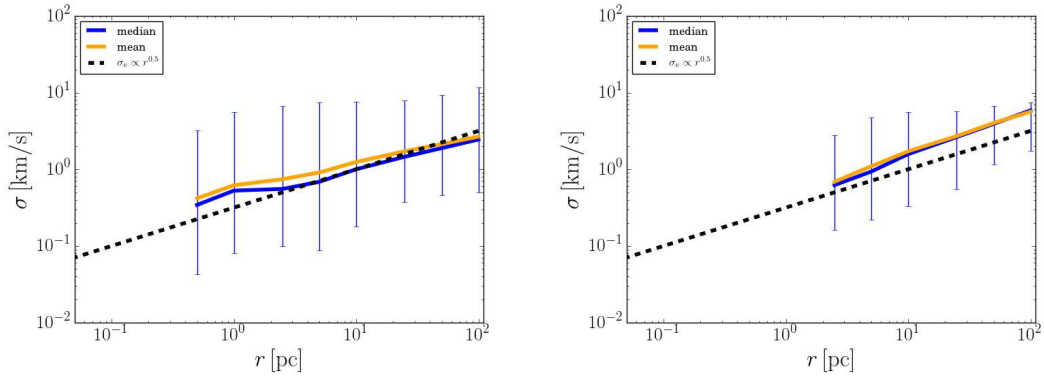

Figure 6.12: Velocity dispersion as a function of radii centred on the densest particles of the clouds identified with $l_{length} = 2.5$ pc for the N-body model (left) and spiral potential model (right). The velocity dispersion is calculated with all the particles enclosed by the specified radius. There is a dispersion value for each reference particle. For an easier visualisation, the vertical bars represent the range of the dispersion values of the cloud distribution. The lines are the mean and median values.

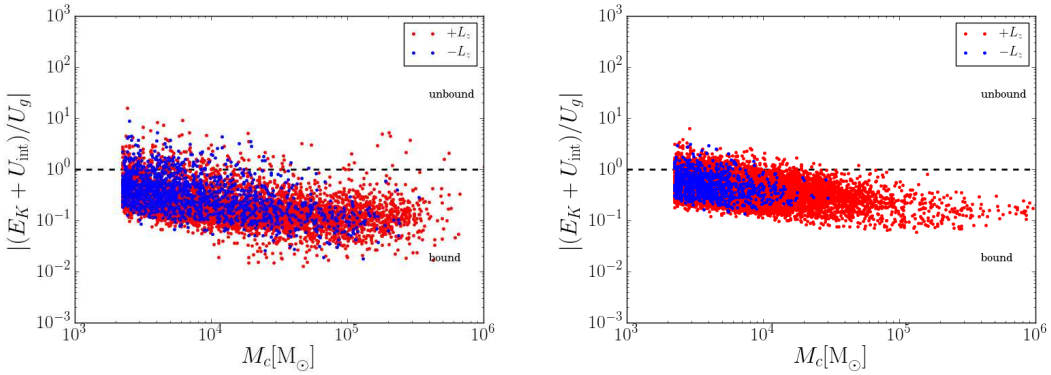

Figure 6.13: Cloud kinetic plus internal energies to gravitational energy ratio $(E_k + U_{int})/|U_g|$ vs. mass for the N-body model (left) and spiral potential (right). Clouds are identified with a linking length $l_{length} = 2.5$ pc.

6.5 Discussion

This chapter has analysed physical properties of gas clouds which have characteristics that can be compared to those of molecular clouds. In this section, a comparison with previous numerical work and observations is discussed.

6.5.1 Cloud Mass Function and Spatial Distribution

The results of §6.2.1 show that the cloud mass spectra is different between the two simulations. For the N-body model, it is well described by a two-power law whereas the spiral potential model is described by a single power law. The fitted slope for the mass function in the spiral potential tends to be lower than that of the N-body model, which reflects on the overall lower exponents in the spiral potential model in Table 6.1.

These mass spectra are comparable with those obtained with other simulations using SPH (e. g. Dobbs & Bonnell 2008; Dobbs 2008; Williamson & Thacker 2012; Williamson et al. 2014; Pettitt et al. 2018) but differ slightly with those presented in mesh simulations (e. g. Shetty & Ostriker 2008; Pan et al. 2015; Khoperskov et al. 2016; Fujimoto et al. 2016; Grisdale et al. 2018). The main difference is that SPH simulations tend to find a higher number of clouds at a lower mass bins than mesh simulations. In the first case, the number of clouds decreases as a function of mass whereas in the second one, the cloud distribution has a bell-shaped function. This may be an effect of the selection algorithm as well as how each method resolves the smallest density features. It is noted that these simulations focus on galaxy models different to the M33 model assumed in the present work.

The N-body simulation can be qualitatively compared to the simulations of Williamson & Thacker (2012) and Williamson et al. (2014), because they use a similar identification method, but use a lower threshold ($7\,\mathrm{M}_\odot\,\mathrm{pc}^{-2}$) and assume a Milky Way model. The second paper compares both feedback and non-feedback models. On the other hand, the present work uses a much higher mass resolution. The cloud masses found in §6.2.1 agree well with the range of masses found by these works. However, these find more massive clouds which results from their lower density threshold. Both works find that $\gamma = -1.5$ and $\gamma = -1.6$ (without feedback), respectively. These are shallower than the values find in the N-body model of this work, but this may be a result of their lower density threshold as well. They also find that the mass function and cloud number does evolve with time, which introduces another parameter to

take into account when comparing.

Pettitt et al. (2018) also obtain mass functions using SPH, but a direct comparison is not possible as they include feedback, the effect of an interacting satellite, a lower resolution of 2×10^3 $M_\odot$, and a lower density threshold for identification. They do include an isolated test that can be qualitatively compared, which shows masses in the range $10^5 - 10^6$ $M_\odot$. For their interacting system, γ varies between -2.9 and -2.2, which is close to the values found in this work. Dobbs & Bonnell (2008) performed N-body simulations, but the gas did not include the self-gravity in the gas. These simulations assumed that a two-phase media composed of fixed fractions of cold and warm gas, assuming an isothermal behaviour for each phase. They obtain shallower distributions with $\gamma = 1.75$ for mostly cold (100 K) gas and $\gamma = 2.05$ for 50% cold (100 K) gas and 50% warm (10^4 K) gas. These are shallower than the present work, and closer to the spiral potential simulation. In terms of observations, the shape of the mass spectra of the N-body model is qualitatively similar to those reported in Rosolowsky et al. (2007) and Colombo et al. (2014b).

The mass function of the spiral potential simulation is qualitatively similar to the simulations of Dobbs (2008); Dobbs & Pringle (2013); Dobbs (2015), which use a very similar spiral potential model. In general, the mass spectra of the spiral potential simulations of this thesis agrees with the cited works. In particular, Dobbs (2008) finds that $\gamma = -2.1$ for a model with no self-gravity. This value agrees with the result with the lowest linking length in the present work. However, Dobbs (2008) used a selection algorithm based on linking structures by surface density calculated on a mesh. Dobbs & Pringle (2013) and Dobbs (2015) find that the mass spectrum is fairly similar even when feedback is included. The maximum mass is more affected by feedback. Dobbs & Pringle (2013) also comment that the spectrum becomes steeper when the surface density threshold of their identification algorithm is increased. An equivalent behaviour is found in this work when the linking length is decreased. As the linking length is decreased, it is able to connect only particles in dense regions where the inter-particle separation is lower, which introduces an artificially higher density cut.

The results of §6.2.2 show that the most massive clouds tend to lie closer to the centre and along the spiral arms and the less massive clouds tend to be along the inter-arm region. Using AMR simulations of a 2-armed disc with a central bar, Fujimoto et al. (2014) show that arms in the spiral arms and bar region tend to have more massive clouds than the outer

disc regions, which agrees with the present results in the spiral arm regions. However, the tendency is slightly reduced when star formation and feedback effects are included (Fujimoto et al., 2016).

In terms of observations, Colombo et al. (2014b) find a similar result for M51, which has a grand-design pattern. In terms of streaming motions, §6.2.3 shows that in both models, there is a tendency for gas clouds at the downstream side of the arm to have negative radial velocities. It is not straight forward to see a tendency for the relative circular velocity. In the N-body model, clouds in the outer-arms appear to be lagging behind the rotation curve, with a similar effect seen in the spiral potential model. However, in the inner galaxy, there is a higher fraction of clouds rotating faster than the rotation curve, which is also seen in the spiral potential model. There is also a significant cloud-to-cloud dispersion. The cloud streaming motions are consistent with the values derived from CO observations of M51 Meidt et al. (2013).

6.5.2 Cloud Mass-Radius Relation

As described in §6.3, the mass-radius relation derived from the simulations is consistent with values reported in observations and other simulations. Other SPH simulations such as those of Dobbs (2007); Dobbs et al. (2011a) and Pettitt et al. (2018), which find that clouds have a relation close to $M \propto R^2$, suggesting a constant surface density. The first two identify clumps based on a surface density classification algorithm while the third uses a FOF algorithm as in this thesis. These works also use global simulations. However, Camacho et al. (2016) find that $M \propto R^3$ for clumps identified by using a similar algorithm in a SPH simulation modelling the collapse of molecular clouds. However, these works differ in how the "radius" of the cloud is defined. For example, Dobbs (2007) and Dobbs et al. (2011a) estimate it assuming that the cloud has circular symmetry in 2D while Camacho et al. (2016) assumes spherical symmetry in 3D. Pettitt et al. (2018) finds the radius by taking as effective area the average of the projected areas in the $x-y$, $x-z$, and $y-z$ planes as described in Fujimoto et al. (2014).

Considering the differences in identification and density thresholds, it is interesting that the mass-radius relation derived in this thesis agrees with Dobbs (2007); Dobbs et al. (2011a); Pettitt et al. (2018). Note that the last two included feedback effects, but their mass resolution is lower than in the simulations of this thesis. As discussed by Pan et al. (2015), the radii derived assuming spherical or circular symmetries overestimates the area for filamentary cloud

structures. In this thesis, such geometries where not assumed, instead the average distance between individual particles and the cloud's centre of mass was used as a characteristic radius and a relation consistent with $M \propto R^2$ was sill obtained. Although the best-fit for the data in §6.3 is closer to the latter, the data are still fairly consistent with $M \propto R^3$ given the scatter. However, this relation may be sensitive to identification methods based on volume density thresholds (Ballesteros-Paredes et al., 2012)

Several AMR works (e. g. Fujimoto et al. 2014; Pan et al. 2015; Fujimoto et al. 2016; Grisdale et al. 2018) have explored the mass-radius relation and in general find a relation close to $M \propto R^3$. However, Pan et al. (2015) and Grisdale et al. (2018) show that when an identification based in synthetic position-position-velocity maps is performed, a lower power closer to two is obtained. Some of these simulations include feedback effects.

The best-fit relation for the N-body simulation is in good agreement with that of the observations of Roman-Duval et al. (2010). The spiral potential model has a best-fit with a slightly lower power, but the Roman-Duval et al. (2010) relation is still consistent with this simulation. This relation has also been verified in earlier observational works such as Falgarone et al. (1991); Elmegreen & Falgarone (1996). These authors interpret the mass-radius relation as a result of a fractal nature of the ISM and a power between 2 and 3 is associated to a "spongy medium" Roman-Duval et al. (2010). However, it is also possible to interpret this relation in terms of the clouds having a density profile of the form $\rho \propto r^{-1}$, which also implies that $M \propto R^2$ (e. g. Ballesteros-Paredes et al. 2012).

In the N-body model, the typical cloud density profile appears to be well represented by $\rho \propto r^{-1}$. The profile is even shallower in the spiral potential model. This is rather different to the $\rho \propto r^{-2}$ model found by Dobbs (2015). However, it is noted that it is not possible to make a direct comparison with Dobbs (2015) because their simulations are specified in a particular kpc-size region of a galaxy, which allows to better resolve the inner cloud structure, and include feedback mechanisms. The simulations of this work may still not have sufficient resolution to properly sample the density profile of the identified clouds, particularly of the lower mass objects.

6.5.3 Cloud Velocity Dispersion Relations with Mass and Radius

In terms of the mass-velocity dispersion relation, as described in §6.4, the N-body model develops a clear correlation between cloud mass and velocity dispersion. The more massive the cloud, the higher the dispersion. Larson (1981) also predicted a similar correlation. The spiral potential simulation produces a less tight correlation. When the velocity dispersion is compared to the average sound speed, the results show that there is a significant fraction of clouds with supersonic dispersion. The Mach number (σ_v/c_s) clearly increases with mass in the N-body simulation whereas in the spiral potential simulation it appears to stay below a certain value slightly lower than 10. In both models, the results show that the more massive clouds tend to be supported by kinetic energy while the less massive clouds tend to be thermally supported. The energy analysis shows that most clouds are gravitationally bound in the range of masses found.

Compared to other SPH simulations, the velocity dispersion in Figure 6.12, which is calculated in spherical regions around the densest particles, is consistent with the range of values found in cite Dobbs & Bonnell (2008) and Dobbs et al. (2006). This calculation is consistent with the values found in Bonnell et al. (2013), which perform a similar calculation. In Figure 6.12, it shows a behaviour closer to $\sigma \propto R^{0.5}$.

When considering individual clouds, the cloud dispersions in Figure 6.11 show results qualitatively similar to other SPH simulations such as Dobbs (2008, 2015); Camacho et al. (2016); Ward et al. (2016); Baba et al. (2017) and Pettitt et al. (2018). A direct comparison is not possible as some of this works include feedback mechanisms and use different galaxy models. Dobbs (2015); Ward et al. (2016); Baba et al. (2017) and Pettitt et al. (2018) find that clouds have velocity dispersions within 10 $\mathrm{km\,s^{-1}}$. All of this works have included feedback effects, but the last two has used a lower resolution than this thesis. Camacho et al. (2016) have found a range between 0.5 and 5 $\mathrm{km\,s^{-1}}$. For both simulations, the range in Figure 6.11 agrees with these works. However, it shows that most of the clouds have a dispersion peaking up to 5 $\mathrm{km\,s^{-1}}$ consistent with Camacho et al. (2016). However, the obtained dispersion-size relation is consistent with the Larson (1981) relation, but the scatter in the cloud data is important and affects the obtained fits.

Global scale AMR simulations such as Fujimoto et al. (2014) and Pan et al. (2015), which do not include feedback, and Khoperskov et al. (2016); Fujimoto et al. (2016) and Grisdale

et al. (2018), which do include feedback, find comparable results to this thesis. However, these codes tend to find a wider range of velocity dispersions, reaching peak values of a few 10 $\mathrm{km\,s^{-1}}$. Notwithstanding, their velocity distributions tend to peak at values less than 10 $\mathrm{km\,s^{-1}}$.

Regarding the dispersion-size relation, both SPH and AMR simulations find relations consistent with Larson (1981) though at a slightly higher slope. For example, Dobbs (2015) finds that $\sigma \propto R^{0.5}$ and Ward et al. (2016) finds a slightly higher power than that reported in Larson (1981). In AMR simulations, Fujimoto et al. (2014) find $\sigma \propto R^{1.1}$ considering only hydrodynamics and self-gravity. Khoperskov et al. (2016) find a power ≈ 0.8, sensitive to the method used to classify the clouds, and including feedback. Grisdale et al. (2018) finds that $\sigma \propto R^{1.88}$ when feedback is not included and $\sigma \propto R^{0.67}$ when it is included. The best-fit relations for the N-body model agree with Fujimoto et al. (2014) and for the spiral potential model with Grisdale et al. (2018). However, these fits and relations may be sensitive to the cloud definition and selection method (e. g. Ballesteros-Paredes et al. 2012; Pan et al. 2015).

In Figure 6.11, the velocity dispersions may be rather low. This may be an effect of not including feedback, which injects energy into clouds. For example, the simulations of Dobbs (2015); Fujimoto et al. (2014) and Grisdale et al. (2018) show that feedback does have an effect in increasing the velocity dispersions. Another effect is the time chosen for cloud identification. For example, Williamson & Thacker (2012) and Williamson et al. (2014) show that cloud properties can evolve over time. Bonnell et al. (2006) show that the velocity dispersion evolves with time as gas flows through the spiral arm. This result has been confirmed in recent simulations by Forgan & Bonnell (2018), which also show that the power in the dispersion-size relation is sensitive to the position across the arm. Nevertheless, a more consistent model of the ISM should include feedback, which was not considered in this thesis.

The cloud identification method can also affect the results. In this thesis, an identification based on the 3D position and density information was applied. However, observers work in position-position-velocity (PPV) space. Pan et al. (2015); Khoperskov et al. (2016) and Grisdale et al. (2018) have studied the differences between using position-density and PPV information, although Khoperskov et al. (2016) compare a method based in a column density rather than a volume density threshold. The general agreement is that using synthetic maps and a PPV classification provides results closer to observed relations. In this thesis, such

methodology was not implemented, making a direct comparison with observations harder. The density threshold can also affect the results. Lowering the threshold will change the characteristic size of the cloud, but will also include gas surrounding the cloud that may be warmer or moving at higher velocities and affect the dispersion calculation.

6.6 Final Comments

In this chapter, molecular cloud properties where studied in the context an N-body and a spiral potential simulations. The cloud mass function differs between simulation. For the N-body one, the function is modelled with a two-power law and is qualitatively consistent with the shape of functions reported in observations. For the spiral potential simulation, the mass function has a shallower profile and it is consistent with other works using a similar potential. The more massive clouds tend to be associated with the central region and the spiral arms of the galaxies, which is consistent with some observations of M51. Clouds have significant streaming motions and the individual kinematics may be sensitive to the underlying potential. Both simulations produce a mass-radius relation consistent with observed values. This result is consistent with a fractal nature of the ISM. The mass-dispersion and dispersion-radius relation are consistent with Larson's relations, but the normalisation may be lower for the simulations presented due to the lack of feedback. This is also complemented by the fact that the most massive clouds are supported by kinetic energy and the less massive clouds by thermal energy. The clouds, in the mass range studied, are gravitationally bound. The results of these simulations show that, in spite of the simple physics included, the cloud properties have a good agreement with observed properties.

7

Conclusion

In this thesis, a series of simulations of the large-scale gas dynamics in spiral galaxies has been explored in order to study its relevance in the formation of molecular clouds. The dynamics in both flocculent and grand-design galaxies have been studied in an N-body and a spiral potential simulation, respectively. The hydrodynamics have been followed using the smoothed particle hydrodynamics method (SPH). In this chapter, the main conclusions and the future work are introduced.

7.1 Concluding Notes

This section presents the main conclusions of this thesis. Chapter 2 introduced the numerical techniques focusing on the N-body techniques and the SPH method implemented for the simulations. Chapter 3 described the formalism behind N-body initial conditions and of fixed-potential simulations. The parameters of the model galaxies were introduced and a series of tests in isolated evolution were presented. In the following subsections, the main conclusions of Chapters 4, 5, and 6.

7.1.1 Large-Scale Gas Flows in Spiral Galaxies

In chapter 4, the gas dynamics in the N-body and the spiral potential simulations were analysed, which may be representative of the behaviours in flocculent and grand-design galaxies, respectively. Heating and cooling is included, which allows to develop a two-phase medium where dense gas structures form, particularly in the spiral arms. The cold gas has a steeply decaying profile, while the warm gas has a fairly flat distribution, which is consistent with observations of spiral galaxies. The azimuthal velocity profiles show that the shock region is sharply marked by a jump in the radial component of the velocity. The gas velocity dispersion is higher in the spiral arms in both models. The spiral arms drive significant streaming motions, which imply that the gas is not moving in circular orbits in their galactic motion. The magnitude of the streaming motions is consistent with observations of a sample of spiral galaxies. In the N-body model, the gas in the arm is driven to high-densities once it enters the arm due to the effect of cooling and self-gravity. in the spiral potential model, the gas reaches a peak density but starts decreasing with time as it leaves the arm.

7.1.2 Molecular Cloud Streaming Motions and Errors in Kinematic Distances

In Chapter 5, a high-resolution simulation of gas flowing in a section of a spiral arm was analysed to study the magnitude of the streaming motions in the flow and their effect in the kinematic distance method. The clouds are identified using a friends-of-friends algorithm applied to particles with densities above a given threshold, which is set to $\rho > 10\,\mathrm{M}_\odot\,\mathrm{pc}^{-3}$. The results show that the spiral arm perturbation introduces net radial and azimuthal streaming motions in a molecular cloud distribution as a whole, which introduces systematic errors as large as ± 1 kpc in the kinematic distance method. The cloud-to-cloud velocity dispersion produces a larger spread in the distribution of distance errors. The recovered positions for an imaginary observer show important distortions in the morphology of the cloud distribution as well as a systematic offset with respect to the actual position of the arm. Surveys probing the relationship between the spiral arms and star formation regions using the kinematic distance method may be significantly affected by these errors.

7.1.3 Molecular Cloud Properties: Mass, Size, Velocity Dispersion

In Chapter 6, the properties of clouds identified using the algorithm described in Chapter 5 using a density threshold of $\rho > 10\,\mathrm{M}_\odot\,\mathrm{pc}^{-3}$. Although the simulation is not following chemical

networks and the formation of H_2, these clouds are representative of molecular clouds. The cloud properties were analysed in the context of an N-body and a spiral potential simulations. The cloud mass function is different between the simulations. For the N-body case, the function is fitted by a two-power law and is qualitatively consistent with the shape of functions reported in some observational surveys. For the spiral potential case, the mass function has a lower slope and it is similar to that of other works using a similar potential. The more massive clouds tend to be located in the central regions a well as in the spiral arms of the model galaxies. A similar tendency has been reported in observations of M51. Clouds have important streaming motions and the individual kinematics may be sensitive to the underlying potential. The clouds in both simulations follow a mass relation consistent with $M \propto R^2$, which is also the tendency identified in simulations. The mass-dispersion and dispersion-size relations are consistent with Larson's relations. The most massive clouds tend to be supported by kinetic energy while the less massive ones by thermal energy. The clouds, in the mass range studied, are gravitationally bound. The cloud properties have a good agreement with observed properties.

7.2 Future Work

This section outlines the ideas for future work. Three main ideas are proposed: explore the rotational properties of molecular clouds, understand what determines star formation rates and efficiency in galaxies, and compare observations and simulations to better understand the physical information that is gained from observed clouds.

7.2.1 Rotational Properties of Molecular Clouds

The rotational properties of molecular clouds are of interest from both observational and theoretical perspectives. Observations in general show that cloud specific angular momentum grows as a function of mass, but the exact behaviour depends on the mechanisms that forms the clouds (e. g. Phillips 1999; Rosolowsky et al. 2003). Observations compiled by Phillips (1999) show that large clouds rotational angular velocity vectors either aligned or anti-aligned with the axis of the Milky Way, with not very different proportions. Smaller substructures tend to have more random directions Phillips (1999). However, the observations of GMCs in M33 by Rosolowsky et al. (2003) show that clouds tend to have a rotation aligned with the axis of the galaxy, but there is a fraction of clouds ($\approx$ 40%) with a retrograde orientation. Simulations by Tasker & Tan (2009) and Dobbs (2008) show that collisional effects can explain why

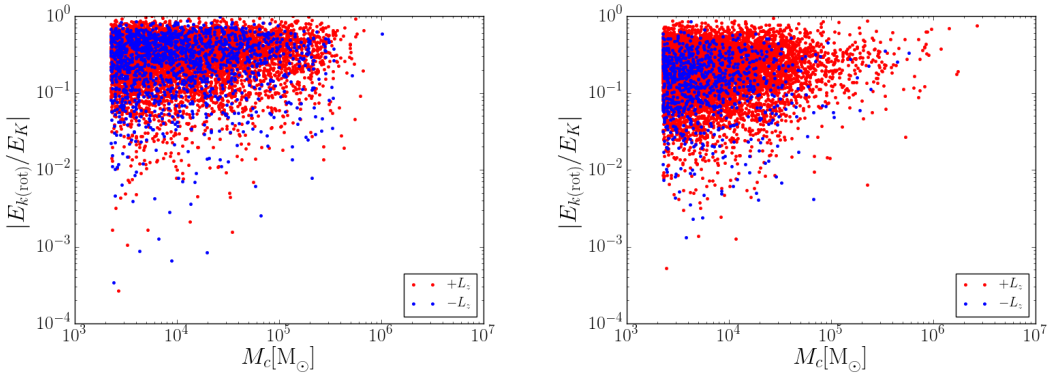

Figure 7.1: Ratio of rotational kinetic energy to total kinetic energy $E_{k(\mathrm{rot})}/E_K$ for clouds identified with a linking length $l_{length} = 2.5$ pc for the N-body model (left) and spiral potential model (right). This shows that there is a fraction of clouds with high rotational energy fractions.

a fraction of clouds has a retrograde orientation. The simulations developed in this work can be used to explore the angular momentum and rotational properties and explore the effect of the different spiral arm morphologies. It will be interesting to obtain cloud velocity gradients, which is the main diagnostic of rotation in observations, and measure if it is purely driven by rotation or there are additional kinematic effects present. It is interesting to determine what is the fraction of clouds dominated by rotational kinetic energy (see Figure 7.1 for preliminary results).

7.2.2 What determines the star formation rates and efficiency in galaxies?

The star formation rate and efficiency are useful for parametrising the star formation process in molecular clouds. Observations show that efficiencies are relatively low, which implies that the conversion of gas to stars is rather inefficient given the measured cloud properties (e. g. Heiderman et al. 2010). Turbulence has been proposed as a mechanism that can maintain cloud stability on a large scale, but at the same time drive strong compressions on the smaller scales (Mac Low & Klessen, 2004). These regions can reach sufficiently high densities to trigger star formation. A problem with this mechanism is that it decays within a dynamical timescale. Therefore, injection mechanisms are needed to sustain it in a giant cloud. It can be driven either externally, by accretion or collisions, and it can be driven internally, by stellar feedback. Another mechanism is magnetic support, although it is not entirely clear if this is an important mechanism given that observations show that clouds are typically slightly supercritical (Dobbs et al., 2014; Crutcher, 2012). Another possibility, according to observations of M51 by Meidt et al. (2013), is the effect of strong streaming motions in the gas surrounding a cloud, which

would affect the external pressure balance.

It is interesting to address this problem in the context of galaxy-scale simulations. The simulations developed in this work could be used to explore the effect of the large-scale flows in driving the turbulent motions of the cloud. Additionally, it is possible to explore the streaming motion mechanism proposed by Meidt et al. (2013). As a longer term idea, it would be interesting to follow a similar approach to Bonnell et al. (2013) of taking a section of gas in a spiral arm and re-simulate it with higher resolution to follow with more detail the evolution of individual clouds. This approach would allow to explore internal effects that regulate the star formation efficiency.

7.2.3 Molecular Cloud Properties: Comparing Observations with Simulations

Observations by Hughes et al. (2013); Colombo et al. (2014b) show that molecular cloud properties have variations between galaxies and also between regions of an individual galaxy. However, these properties may be sensitive to the observational tracers used and the cloud definition assumed. This still suggests that there may be an environmental dependence on the physical mechanisms that are driving the formation of molecular clouds. The nature (grand-design vs. flocculent) of the underlying spiral arms can also have an effect on the properties of the clouds. It is interesting to take the results of Chapter 6 and analyse them from the point of view of synthetic observations. This would permit a better comparison with observational results. It will be interesting to compare these results with observations of recent surveys such as BIMA (Regan et al., 2001), THINGS (Walter et al., 2008), PAWS (Schinnerer et al., 2013), and surveys of the Milky Way (e. g. Miville-Deschênes et al. 2017).

A

Supernova Injection

Sink particles can be used as sources of feedback. Energy and momentum can be injected in the neighbouring gas. In this work, a module was developed to inject feedback due to supernovae exploding in simulations of galactic scales. Some of the concepts are based in the work developed in Lucas (2015).

Two parameters are defined are to determine if a sink becomes a source of supernova feedback: a critical mass $M_{\rm crit}$ and a critical age $\tau_{\rm SN}$. These are free input parameters specified by the user at the beginning of the simulation. When a sink is created, its creation time $t_{\rm creation}$ is saved. The age of the sink is defined as $\Delta t_{\rm creat} = t_{\rm actual} - t_{\rm creation}$, where $t_{\rm actual}$ is the current time of the simulation. When $\Delta t_{\rm creat} > \tau_{\rm SN}$ or the mass accreted by the sink is larger than $M_{\rm crit}$, the sink is tagged for supernova feedback injection.

The initial conditions for the supernova region are taken from a spherical glass distribution. This has a uniform density profile, which is obtained by running a particular type of set up that ensures that the inter-particle distance is roughly equidistant. The number of particles inserted

is determined depending on the mass of the particles in the global simulation in order to ensure that the inserted particles have the same mass. The positions of the SN particles relative to the centre of the explosion are loaded at the beginning of the simulation.

If a sink has been tagged for injection, it enters a subroutine that first places the distribution of particles such that their positions are $\mathbf{r}_{\rm inserted} = \mathbf{r}_{\rm sink} + \delta\mathbf{r}$, where $\mathbf{r}_{\rm sink}$ is the current position of the sink and $\delta\mathbf{r}$ is the particle position relative to the centre of the explosion loaded from the spherical glass distribution. The ejected mass $m_{\rm ejected}$ is the sum of the masses of the injected particles.

The total amount of energy injected $E_{\rm injected}$ is 10^{51} [erg] plus an additional amount from particles killed just before the SN insertion. The latter step ensures that particles that have not been accreted near the sink are removed to avoid potential effects of introducing a distribution of highly energetic particles with a few low energy particles in between. The injected energy is then split into a thermal fraction $E_{\rm therm,injected} = f_{\rm therm} E_{\rm injected}$, and a kinetic fraction $E_{\rm kin,injected} = f_{\rm kin} E_{\rm injected}$, where $f_{\rm therm}$ and $f_{\rm kin}$ are the fractions of thermal and kinetic energies, respectively, and should satisfy $f_{\rm therm} + f_{\rm kin} = 1$.

The injection speed is given by $v_{\rm inj} = (2 f_{\rm kin} E_{\rm injected}/m_{\rm ejected})^{1/2}$, assuming that all particles receive the same kinetic energy injection. For simplicity, the velocity vector is radially outward from the centre of the explosion: $\mathbf{v} = v_{\rm inj}\mathbf{r}/|\mathbf{r}|$. The specific internal energy of the particles is set to $u_{\rm inj} = f_{\rm therm} E_{\rm injected}$.

The particles are given initial time steps which are a fraction of the crossing time of an estimate of the local smoothing length based on the average density of the inserted distribution. This is just an estimate and the time step will be adapted as soon as they enter the error checking and time step limiter parts of the code. Once the particles are inserted, their smoothing lengths are obtained with the iterative scheme described in equations (2.73), (2.74) and (2.75) of §2.2.3. A full implementation of this method is left for future work.

Bibliography

Agertz, O., Lake, G., Teyssier, R., Moore, B., Mayer, L., & Romeo, A. B. 2009, MNRAS, 392, 294, 0810.1741

Agertz, O. et al. 2007, MNRAS, 380, 963, astro-ph/0610051

Aguilar, L. A. 1991, Rev. Mex. de Física, 38, 701

Anderson, L. D., Bania, T. M., Balser, D. S., & Rood, R. T. 2012, ApJ, 754, 62

Athanassoula, E., Fady, E., Lambert, J. C., & Bosma, A. 2000, MNRAS, 314, 475, astro-ph/9912467

Audit, E., & Hennebelle, P. 2005, A&A, 433, 1, astro-ph/0410062

Audouze, J., & Tinsley, B. M. 1976, ARA&A, 14, 43

Baba, J., Asaki, Y., Makino, J., Miyoshi, M., Saitoh, T. R., & Wada, K. 2009, ApJ, 706, 471

Baba, J., Morokuma-Matsui, K., Miyamoto, Y., Egusa, F., & Kuno, N. 2016, MNRAS, 460, 2472, 1604.06879

Baba, J., Morokuma-Matsui, K., & Saitoh, T. R. 2017, MNRAS, 464, 246, 1609.00097

Bahcall, J. N., & Soneira, R. M. 1980, ApJS, 44, 73

Balbus, S. A. 1988, ApJ, 324, 60

Balbus, S. A., & Cowie, L. L. 1985, ApJ, 297, 61

Ballesteros-Paredes, J., D'Alessio, P., & Hartmann, L. 2012, MNRAS, 427, 2562, 1209.3346

Balsara, D. S. 1995, Journal of Computational Physics, 121, 357

Banerjee, R., Klessen, R. S., & Fendt, C. 2007, ApJ, 668, 1028, 0706.3640

Barnes, J. 1994 (Cambridge University Press), 403

Barnes, J., & Hut, P. 1986, Nature, 324, 446

——. 1989, ApJS, 70, 389

Barnes, J. E. 1996 (Springer), 275

Bate, M. 1995, PhD thesis, PhD thesis, Univ. Cambridge, (1995)

Bate, M. R. 2018, MNRAS, 475, 5618, 1801.07721

Bate, M. R., Bonnell, I. A., & Price, N. M. 1995, MNRAS, 277, 362

Benz, W., Bowers, R. L., Cameron, A. G. W., & Press, W. H. . 1990a, ApJ, 348, 647

Benz, W., Cameron, A. G. W., & Melosh, H. J. 1989, Icarus, 81, 113

Benz, W., Cameron, A. G. W., Press, W. H., & Bowers, R. L. 1990b, ApJ, 348, 647

Bigiel, F., & Blitz, L. 2012, ApJ, 756, 183, 1208.1505

Binney, J. 1980, MNRAS, 190, 873

Binney, J., & Merrifield, M. 1998, Galactic Astronomy (Princeton University Press)

Binney, J., & Tremaine, S. 2008, Galactic Dynamics (Princeton University Press)

Blitz, L., & Shu, F. H. 1980, ApJ, 238, 148

Blitz, L., & Spergel, D. N. 1991, ApJ, 370, 205

Boggs, P. T., & Rogers, J. E. 1990, 112, 186

Bolatto, A. D., Leroy, A. K., Rosolowsky, E., Walter, F., & Blitz, L. 2008, ApJ, 686, 948, 0807.0009

Bonnell, I. A., Dobbs, C. L., Robitaille, T. P., & Pringle, J. E. 2006, MNRAS, 365, 37

Bonnell, I. A., Dobbs, C. L., & Smith, R. J. 2013, MNRAS, 430, 1790

Bouché, N. et al. 2007, ApJ, 671, 303

Bournaud, F., Elmegreen, B. G., Teyssier, R., Block, D. L., & Puerari, I. 2010, MNRAS, 409, 1088, 1007.2566

Brunt, C. M., & Kerton, C. R. 2002, ApJL, 430, L41

Bruzual A., G., & Charlot, S. 1993, ApJ, 405, 538

Bryan, G. L. et al. 2014, ApJS, 211, 19, 1307.2265

Burkert, A. 2017, ArXiv e-prints, 1709.02112

Camacho, V., Vázquez-Semadeni, E., Ballesteros-Paredes, J., Gómez, G. C., Fall, S. M., & Mata-Chávez, M. D. 2016, ApJ, 833, 113, 1609.09112

Camm, G. L. 1950, MNRAS, 110, 305

Casoli, F., & Combes, F. 1982, A&A, 110, 287

Chakrabarti, S., Laughlin, G., & Shu, F. H. 2003, ApJ, 596, 220, astro-ph/0306472

Churchwell, E. et al. 2009, PASP, 121, 213

Clarke, C., & Carswell, R. 2007, Principles of Astrophysical Fluid Dynamics (Cambridge University Press)

Clarke, C., & Gittins, D. 2006, MNRAS, 371, 530, astro-ph/0607019

Cohen, R. S., Cong, H., Dame, T. M., & Thaddeus, P. 1980, ApJL, 239, L53

Cohen, R. S., Dame, T. M., & Thaddeus, P. 1986, ApJS, 60, 695

Colling, C., Hennebelle, P., Geen, S., Iffrig, O., & Bournaud, F. 2018, ArXiv e-prints, 1809.01037

Colombo, D. et al. 2014a, ApJ, 784, 3, 1401.1505

——. 2014b, ApJ, 784, 4

Colombo, D., Rosolowsky, E., Ginsburg, A., Duarte-Cabral, A., & Hughes, A. 2015, MNRAS, 454, 2067, 1510.04253

Corbelli, E. 2003, MNRAS, 342, 199

Corbelli, E., & Salucci, P. 2000, MNRAS, 311, 441

Corbelli, E., Thilker, D., Zibetti, S., Giovanardi, C., & Salucci, P. 2014, A&A, 572, A32

Courant, R., & Hilbert, D. 1962, Methods of Mathematical Physics Vol. II (Interscience Publishers)

Cowie, L. L. 1981, ApJ, 245, 66

Cox, D. P. 2005, ARA&A, 43, 337

Cox, D. P., & Gómez, G. C. 2002, ApJS, 142, 261

Cox, D. P., & Smith, B. W. 1974, ApJL, 189, L105

Crutcher, R. M. 2012, ARA&A, 50, 29

Cuddeford, P. 1991, MNRAS, 253, 414

——. 1993, MNRAS, 262, 1076

Daddi, E. et al. 2010, ApJ, 714, L118

Dale, J. E. 2015, New Astronomy Reviews, 68, 1, 1508.06054

Dale, J. E., Ercolano, B., & Bonnell, I. A. 2012, MNRAS, 424, 377, 1205.0360

Dame, T. M., Elmegreen, B. G., Cohen, R. S., & Thaddeus, P. 1986, ApJ, 305, 892

Dame, T. M., Hartmann, D., & Thaddeus, P. 2001, ApJ, 547, 792, astro-ph/0009217

Das, M., & Jog, C. J. 1996, ApJ, 462, 309

Dawson, J. R., Ntormousi, E., Fukui, Y., Hayakawa, T., & Fierlinger, K. 2015, ApJ, 799, 64

De Becker, M. 2013, Bull. de la Soc. Roy. de Sciences de Liege, 82, 33

de Vaucouleurs, G. 1959, ApJ, 130, 728

de Vaucouleurs, G., de Vaucouleurs, A., Corwin, Jr., H. G., Buta, R. J., Paturel, G., & Fouqué, P. 1991, Third Reference Catalogue of Bright Galaxies. Volume I: Explanations and references. Volume II: Data for galaxies between 0^h and 12^h. Volume III: Data for galaxies between 12^h and 24^h.

Dehnen, W. 1999, AJ, 118, 1201

——. 2001, MNRAS, 324, 273, astro-ph/0011568

Dehnen, W., & Aly, H. 2012, MNRAS, 425, 1068, 1204.2471

Dobbs, C., & Baba, J. 2014, PASA, 31, e035, 1407.5062

Dobbs, C. L. 2007, PhD thesis, PhD thesis, Univ. of St. Andrews, (2007)

——. 2008, MNRAS, 391, 844, 0809.1942

——. 2015, MNRAS, 447, 3390

Dobbs, C. L., & Bonnell, I. A. 2006, MNRAS, 367, 873

——. 2008, MNRAS, 385, 1893, 0801.3562

Dobbs, C. L., Bonnell, I. A., & Pringle, J. E. 2006, MNRAS, 371, 1663

Dobbs, C. L., Burkert, A., & Pringle, J. E. 2011a, MNRAS, 417, 1318

——. 2011b, MNRAS, 413, 2935, 1101.3414

Dobbs, C. L., Glover, S. C. O., Clark, P. C., & Klessen, R. S. 2008, MNRAS, 389, 1097, 0806.4312

Dobbs, C. L. et al. 2014, Protostars and Planets VI, 3, 1312.3223

Dobbs, C. L., & Pettitt, A. 2014 (Springer), 147–156

Dobbs, C. L., & Pringle, J. E. 2013, MNRAS, 432, 653, 1303.4995

Dobbs, C. L., Pringle, J. E., & Burkert, A. 2012, MNRAS, 425, 2157, 1206.4904

Dosch, A., & Zank, G. P. 2016, Transport Processes in Space Physics and Astrophysics (Springer)

Draine, B. T. 2011, Physics of the interstellar and intergalactic medium (Princeton University Press)

Druard, C. et al. 2014, A&A, 567, A118, 1405.5884

Duarte-Cabral, A., & Dobbs, C. L. 2016, MNRAS, 458, 3667, 1603.02470

——. 2017, MNRAS, 470, 4261, 1706.05421

Durier, F., & Dalla Vecchia, C. 2012, MNRAS, 419, 465, 1105.3729

Dyson, J. E., & Williams, D. A. 1997, The physics of the interstellar medium

Eckart, C. 1960, Physics of Fluids, 3, 421

Eddington, A. S. 1916, MNRAS, 76, 572

Einasto, J. 1965, Trudy Astrofizicheskogo Instituta Alma-Ata, 5, 87

——. 1969, Astronomische Nachrichten, 291, 97

Elmegreen, B. G. 1979, ApJ, 231, 372

——. 2002, ApJ, 577, 206, astro-ph/0207114

Elmegreen, B. G., & Elmegreen, D. M. 1983, MNRAS, 203, 31

Elmegreen, B. G., & Falgarone, E. 1996, ApJ, 471, 816

Englmaier, P. 2000, in Reviews in Modern Astronomy, Vol. 13, Reviews in Modern Astronomy, ed. R. E. Schielicke, 97

Evans, II, N. J. et al. 2009, ApJS, 181, 321, 0811.1059

Falgarone, E., Phillips, T. G., & Walker, C. K. 1991, ApJ, 378, 186

Field, G. B. 1965, ApJ, 142, 531

Forgan, D. H., & Bonnell, I. A. 2018, MNRAS, 481, 4532, 1809.06601

Foster, T., & MacWilliams, J. 2006, ApJ, 644, 214

Foyle, K., Courteau, S., & Thacker, R. J. 2008, MNRAS, 386, 1821

Freeman, K. C. 1970, ApJ, 160, 811

Freeman, K. C. 1978, in IAU Symposium, Vol. 77, Structure and Properties of Nearby Galaxies, ed. E. M. Berkhuijsen & R. Wielebinski, 3–10

Friedli, D., & Benz, W. 1993, A&A, 268, 65

——. 1995, A&A, 301, 649

Fujimoto, M. 1966, AJ, 71, 856

Fujimoto, Y., Bryan, G. L., Tasker, E. J., Habe, A., & Simpson, C. M. 2016, MNRAS, 461, 1684, 1606.04981

Fujimoto, Y., Tasker, E. J., Wakayama, M., & Habe, A. 2014, MNRAS, 439, 936, 1401.1212

Fukui, Y. et al. 1999, PASJ, 51, 745

Genzel, R. et al. 2010, MNRAS, 407, 2091

Gingold, R. A., & Monaghan, J. J. 1977, MNRAS, 181, 375

——. 1982, Journal of Computational Physics, 46, 429

Gittins, D. M., & Clarke, C. J. 2004, MNRAS, 349, 909, astro-ph/0312562

Glover, S. C. O., & Mac Low, M.-M. 2007a, ApJS, 169, 239, astro-ph/0605120

——. 2007b, ApJ, 659, 1317, astro-ph/0605121

Goldreich, P., & Lynden-Bell, D. 1965a, MNRAS, 130, 97

——. 1965b, MNRAS, 130, 125

Goldsmith, D. W., Habing, H. J., & Field, G. B. 1969, ApJ, 158, 173

Gómez, G. C. 2006, AJ, 132, 2376

Gould, R. J., & Salpeter, E. E. 1963, ApJ, 138, 393

Grand, R. J. J., Kawata, D., & Cropper, M. 2012, MNRAS, 426, 167

Gratier, P. et al. 2012, A&A, 542, A108, 1111.4320

——. 2010, A&A, 522, A3

Grisdale, K., Agertz, O., Renaud, F., & Romeo, A. B. 2018, MNRAS, 479, 3167, 1801.03104

Habart, E., Walmsley, M., Verstraete, L., Cazaux, S., Maiolino, R., Cox, P., Boulanger, F., & Pineau des Forêts, G. 2005, Space Science Reviews, 119, 71

Hague, P. R., & Wilkinson, M. I. 2015, ApJ, 800, 15

Hausman, M. A. 1982, ApJ, 261, 532

Heggie, D. C. 2005, ArXiv Astrophysics e-prints, astro-ph/0503600

Heiderman, A., Evans, II, N. J., Allen, L. E., Huard, T., & Heyer, M. 2010, ApJ, 723, 1019, 1009.1621

Heitsch, F., Burkert, A., Hartmann, L. W., Slyz, A. D., & Devriendt, J. E. G. 2005, ApJL, 633, L113, astro-ph/0507567

Heitsch, F., Hartmann, L. W., & Burkert, A. 2008, ApJ, 683, 786, 0805.0801

Hennebelle, P. 2018, A&A, 611, A24, 1709.07619

Hennebelle, P., Banerjee, R., Vázquez-Semadeni, E., Klessen, R. S., & Audit, E. 2008, A&A, 486, L43, 0805.1366

Hennebelle, P., & Iffrig, O. 2014, A&A, 570, A81, 1405.7819

Hennebelle, P., & Pérault, M. 1999, A&A, 351, 309

——. 2000, A&A, 359, 1124

Hernández-López, I., Athanassoula, E., Mújica, R., & Bosma, A. 2009, Rev. Mex. A. A. (Serie de Conferencias), 37, 160

Hernquist, L. 1987, ApJS, 64, 715

——. 1990, ApJ, 356, 359

——. 1993, ApJS, 86, 389

Hernquist, L., & Katz, N. 1985, ApJS, 149, 135

Heyer, M., & Dame, T. M. 2015, ARA&A, 53, 583

Heyer, M., Krawczyk, C., Duval, J., & Jackson, J. M. 2009, ApJ, 699, 1092, 0809.1397

Hollenbach, D., & Salpeter, E. E. 1971, ApJ, 163, 155

Hopkins, P. F., Quataert, E., & Murray, N. 2011, MNRAS, 417, 950, 1101.4940

——. 2012, MNRAS, 421, 3488, 1110.4636

Huchra, J. P., & Geller, M. J. 1982, ApJ, 257, 423

Hughes, A. et al. 2013, ApJ, 779, 46

Hut, P. 1983, AJ, 88, 1549

Iffrig, O., & Hennebelle, P. 2015, A&A, 576, A95, 1410.7972

Inoue, S., & Yoshida, N. 2018, MNRAS, 474, 3466, 1706.01895

Jeans, J. H. 1915, MNRAS, 76, 70

Jurić, M. et al. 2008, ApJ, 673, 864, astro-ph/0510520

Kalberla, P. M. W., & Dedes, L. 2008, A&A, 487, 951

Kalberla, P. M. W., & Kerp, J. 2009, ARA&A, 47, 27

Kawamura, A. et al. 2009, ApJS, 184, 1, 0908.1168

Kendall, S., Clarke, C., & Kennicutt, R. C. 2015, MNRAS, 446, 4155, 1411.5792

Kendall, S., Kennicutt, R. C., & Clarke, C. 2011, MNRAS, 414, 538, 1101.5764

Kennicutt, Jr., R. C. 1989, ApJ, 344, 685

——. 1998a, ARA&A, 36, 189, astro-ph/9807187

——. 1998b, ApJ, 498, 541

Khoperskov, S. A., Vasiliev, E. O., Ladeyschikov, D. A., Sobolev, A. M., & Khoperskov, A. V. 2016, MNRAS, 455, 1782, 1508.04966

Kim, W.-T., & Ostriker, E. C. 2002, ApJ, 570, 132, astro-ph/0111398

——. 2006, ApJ, 646, 213, astro-ph/0603751

King, I. R. 1990, in The Milky Way as a Galaxy, ed. I. King, G. Gilmore, & P. C. van der Kruit, 161–183

Klessen, R. S., & Glover, S. C. O. 2016, Star Formation in Galaxy Evolution: Connecting Numerical Models to Reality, Saas-Fee Advanced Course, Volume 43. ISBN 978-3-662-47889-9. Springer-Verlag Berlin Heidelberg, 2016, p. 85, 43, 85, 1412.5182

Klessen, R. S., & Hennebelle, P. 2010, A&A, 520, A17, 0912.0288

Klyping, A., Zhao, H., & Somerville, R. S. 2002, ApJ, 573, 597

Koda, J. et al. 2009, ApJL, 700, L132, 0907.1656

Kovalenko, I. G., & Levi, V. V. 1992, A&A, 264, 406

Koyama, H., & Inutsuka, S.-I. 2000, ApJ, 532, 980, astro-ph/9912509

Koyama, H., & Inutsuka, S.-i. 2002, ApJL, 564, L97

Kruijssen, J. M. D., & Longmore, S. N. 2014, MNRAS, 439, 3239, 1401.4459

Kuijken, K., & Dubinski, J. 1995, MNRAS, 277, 1341

Lada, C. J., Lombardi, M., & Alves, J. F. 2010, ApJ, 724, 687, 1009.2985

Larson, R. B. 1979, MNRAS, 186, 479

——. 1981, MNRAS, 194, 809

Lattanzio, J. C., Monaghan, J. J., Pongracic, H., & Schwarz, M. P. 1985, MNRAS, 215, 125

Lee, C. W., Lee, H. M., Ann, H. B., & Kwon, K. H. 1999, ApJ, 513, 242

Lee, W.-K. 2014, ApJ, 792, 122, 1407.5215

Lequeux, J. 2005, The Interstellar Medium (Cambridge University Press)

Lin, C. C., & Shu, F. H. 1964, ApJ, 140, 646

Lindblad, P. O. 1960, Stockholms Observatoriums Annaler, 21

Lubow, S. H., Balbus, S. A., & Cowie, L. L. 1986, ApJ, 309, 496

Lucas, W. E. 2015, PhD thesis, PhD thesis, Univ. of St. Andrews, (2015)

Lucy, L. B. 1977, AJ, 82, 1032

Mac Low, M.-M., & Klessen, R. S. 2004, Reviews of Modern Physics, 76, 125, astro-ph/0301093

Madau, P., & Dickinson, M. 2014, ARA&A, 52, 415, 1403.0007

Mata-Chávez, M. D., Gómez, G. C., & Puerari, I. 2014, MNRAS, 444, 3756, 1408.3670

McKee, C. F., & Ostriker, J. P. 1977, ApJ, 218, 148

McMillan, P. J., & Dehnen, W. 2007, MNRAS, 378, 541, astro-ph/0703534

Meidt, S. E. et al. 2018, ApJ, 854, 100, 1712.06364

——. 2013, ApJ, 779, 45, 1304.7910

Merritt, D. 1985, AJ, 90, 1027

Merritt, D., Graham, A. W., Moore, B., Diemand, J., & Terzić, B. 2006, AJ, 132, 2685, astro-ph/0509417

Miville-Deschênes, M.-A., Murray, N., & Lee, E. J. 2017, ApJ, 834, 57

Molinari, S. et al. 2014, Protostars and Planets VI, 125, 1402.6196

Monaghan, J. J. 1992, ARA&A, 30, 543

——. 1997, Journal of Computational Physics, 136, 298

——. 2002, MNRAS, 335, 843, astro-ph/0204118

——. 2005, Rep. Prog. Phys., 68, 1703

Monaghan, J. J., & Gingold, R. A. 1983, Journal of Computational Physics, 52, 374

Monaghan, J. J., & Lattanzio, J. C. 1985, A&A, 149, 135

Morrison, P. J. 1998, Rev. Mod. Phys., 70, 467

Navarro, J. F., Frenk, C. S., & White, S. D. M. 1997, ApJ, 490, 493

Nelson, R. P., & Papaloizou, J. C. B. 1993, MNRAS, 265, 905

Nieten, C., Neininger, N., Guélin, M., Ungerechts, H., Lucas, R., Berkhuijsen, E. M., Beck, R., & Wielebinski, R. 2006, A&A, 453, 459

Osipkov, L. P. 1979, Soviet Astronomy Letters, 5, 42

Osterbrock, D. E., & Ferland, G. J. 2005, Astrophysics of Gaseous Nebulae and Active Galactic Nuclei (University Science Books)

Padoan, P., Pan, L., Haugbølle, T., & Nordlund, Å. 2016, ApJ, 822, 11, 1509.04663

Pan, H.-A., Fujimoto, Y., Tasker, E. J., Rosolowsky, E., Colombo, D., Benincasa, S. M., & Wadsley, J. 2015, MNRAS, 453, 3082, 1508.01647

Parzen, E. 1962, Ann. Math. Stat., 33, 1065

Pettitt, A. R. 2015, PhD thesis, PhD thesis, Univ. of Exeter, (2015)

Pettitt, A. R., Egusa, F., Dobbs, C. L., Tasker, E. J., Fujimoto, Y., & Habe, A. 2018, MNRAS, 480, 3356, 1807.09980

Pettitt, A. R., Tasker, E. J., Wadsley, J. W., Keller, B. W., & Benincasa, S. M. 2017, MNRAS, 468, 4189, 1704.04127

Pety, J. et al. 2013, ApJ, 779, 43

Phillips, J. P. 1999, A&AS, 134, 241

Plummer, H. C. 1911, MNRAS, 71, 460

Pohl, M., Englmaier, P., & Bissantz, N. 2008, ApJ, 677, 283

Portail, M., Wegg, C., Gerhard, O., & Martinez-Valpuesta, I. 2015, MNRAS, 448, 713, 1502.00633

Press, W. H. 1986, in Lecture Notes in Physics, Berlin Springer Verlag, Vol. 267, The Use of Supercomputers in Stellar Dynamics, ed. P. Hut & S. L. W. McMillan, 184

Price, D. J. 2004, PhD thesis, University of Cambridge

——. 2007, PASA, 24, 159

——. 2008, Journal of Computational Physics, 227, 10040

——. 2012, Journal of Computational Physics, 231, 759, 1012.1885

Price, D. J., & Bate, M. R. 2007, MNRAS, 377, 77

Price, D. J., & Monaghan, J. J. 2004, MNRAS, 348, 139, astro-ph/0310790

Price, D. J. et al. 2017, ArXiv e-prints, 1702.03930

Puerari, I. 1993, PASP, 105, 1290

Ragan, S. E., Moore, T. J. T., Eden, D. J., Hoare, M. G., Elia, D., & Molinari, S. 2016, MNRAS, 462, 3123

Ramón-Fox, F. G., & Bonnell, I. A. 2018, MNRAS, 474, 2028, 1711.01154

Regan, M. W., Thornley, M. D., Helfer, T. T., Sheth, K., Wong, T., Vogel, S. N., Blitz, L., & Bock, D. C.-J. 2001, ApJ, 561, 218, astro-ph/0107211

Regan, M. W., & Vogel, S. N. 1994, ApJ, 434, 536

Reid, M. J. et al. 2009, ApJ, 700, 137

Renaud, F. et al. 2013, MNRAS, 436, 1836, 1307.5639

Revaz, Y., Pfenniger, D., Combes, F., & Bournaud, F. 2009, A&A, 501, 171, 0801.1180

Rice, W. K. M., Paardekooper, S.-J., Forgan, D. H., & Armitage, P. J. 2014, MNRAS, 438, 1593, 1311.7355

Roberts, W. W. 1969, ApJ, 158, 123

Roman-Duval, J., Jackson, J. M., Heyer, M., Johnson, A., Rathborne, J., Shah, R., & Simon, R. 2009, ApJ, 699, 1153

Roman-Duval, J., Jackson, J. M., Heyer, M., Rathborne, J., & Simon, R. 2010, ApJ, 723, 492, 1010.2798

Rosenblatt, M. 1956, Ann. Math. Stat., 27, 832

Rosolowsky, E. 2005, PASP, 117, 1403, astro-ph/0508679

Rosolowsky, E., & Blitz, L. 2005, ApJ, 623, 826, astro-ph/0501387

Rosolowsky, E., Engargiola, G., Plambeck, R., & Blitz, L. 2003, ApJ, 599, 258, astro-ph/0307322

Rosolowsky, E., Keto, E., Matsushita, S., & Willner, S. P. 2007, ApJ, 661, 830

Rosolowsky, E., & Leroy, A. 2006, PASP, 118, 590, astro-ph/0601706

Rosswog, S. 2009, New Astronomy Review, 53, 78

Rubin, V. C., Ford, Jr., W. K., & Thonnard, N. 1980, ApJ, 238, 471

Rybicki, G. B., & Lightman, A. P. 2004, Radiative processes in astrophysics (Wiley-VCH)

Saitoh, T. R., & Makino, J. 2009, ApJL, 697, L99, 0808.0773

Sakamoto, S., Hasegawa, T., Handa, T., Hayashi, M., & Oka, T. 1997, ApJ, 486, 276

Saraiva Schroeder, M. F., Pastoriza, M. G., Kepler, S. O., & Puerari, I. 1994, A&A Supp. Series, 108, 41

Schaller, M., Gonnet, P., Chalk, A. B. G., & Draper, P. W. 2016, ArXiv e-prints, 1606.02738

Schaye, J. et al. 2015, MNRAS, 446, 521

Schinnerer, E. et al. 2013, ApJ, 779, 42

Schmidt, M. 1959, ApJ, 129, 243

Schmidt, T. M., Bigiel, F., Klessen, R. S., & de Blok, W. J. G. 2016, MNRAS, 457, 2642, 1601.01689

Schoenberg, I. J. 1946, Q. Appl. Math., IV, 45

Schuessler, I., & Schmitt, D. 1981, A&A, 97, 373

Scoville, N. Z., & Hersh, K. 1979, ApJ, 229, 578

Seigar, M. S. 2011, ISRN Astronomy and Astrophysics, 2011

Seigar, M. S., Block, D. L., Puerari, I., Chorney, N. E., & James, P. A. 2005, MNRAS, 359, 1065, astro-ph/0502587

Sérsic, J. L. 1963, Boletin de la Asociacion Argentina de Astronomia La Plata Argentina, 6, 41

Shetty, R., & Ostriker, E. C. 2006, ApJ, 647, 997, astro-ph/0605142

——. 2008, ApJ, 684, 978, 0805.3996

Shu, F. H. 1969, ApJ, 158, 505

Shu, F. H., Milione, V., Gebel, W., Yuan, C., Goldsmith, D. W., & Roberts, W. W. 1972, ApJ, 173, 557

Sie Kam, Z., Carignan, C., Chemin, L., Amram, P., & Epinat, B. 2015, MNRAS, 449, 4048

Silk, J. 1997, ApJ, 481, 703, astro-ph/9612117

Slyz, A. D., Devriendt, J. E. G., Bryan, G., & Silk, J. 2005, MNRAS, 356, 737, astro-ph/0411383

Smilgys, R., & Bonnell, I. A. 2016, MNRAS, 459, 1985, 1604.02048

——. 2017, MNRAS, 472, 4982, 1709.08948

Smith, R. J., Glover, S. C. O., Clark, P. C., Klessen, R. S., & Springel, V. 2014, MNRAS, 441, 1628

Sofue, Y. 2017, PASJ, 69, R1, 1608.08350

Sofue, Y., Honma, M., & Omodaka, T. 2009, PASJ, 61, 227, 0811.0859

Sofue, Y., & Rubin, V. 2001, ARA&A, 39, 137

Solomon, P. M., Rivolo, A. R., Barrett, J., & Yahil, A. 1987, ApJ, 319, 730

Solomon, P. M., Scoville, N. Z., & Sanders, D. B. 1979, ApJL, 232, L89

Sormani, M. C., Sobacchi, E., Shore, S. N., Treß, R. G., & Klessen, R. S. 2017, MNRAS, 471, 2932, 1707.00301

Sparke, L. S., & Gallagher, III, J. S. 2000, Galaxies in the universe : an introduction, 416

Spitzer, Jr., L. 1942, ApJ, 95, 329

Springel, V. 2005, MNRAS, 364, 1105

Springel, V. 2010, MNRAS, 401, 791

Springel, V. 2010, ARA&A, 48, 391

Springel, V., & Hernquist, L. 2002, MNRAS, 333, 649, astro-ph/0111016

Stahler, S. W., & Palla, F. 2004, The Formation of Stars (Wiley-VCH)

Stark, A. A., & Brand, J. 1989, ApJ, 339, 763

Stephens, A. W., & Frogel, J. A. 2002, AJ, 124, 2023

Stiele, H., Lesch, H., & Heitsch, F. 2006, MNRAS, 372, 862

Stone, J. M., & Norman, M. L. 1992, ApJS, 80, 753

Strömgren, B. 1939, ApJ, 89, 526

Tasker, E. J. 2011, ApJ, 730, 11, 1101.1534

Tasker, E. J., & Bryan, G. L. 2006, ApJ, 641, 878, astro-ph/0512027

——. 2008, ApJ, 673, 810, 0709.1972

Tasker, E. J., & Tan, J. C. 2009, ApJ, 700, 358, 0811.0207

Tasker, E. J., Wadsley, J., & Pudritz, R. 2015, ApJ, 801, 33, 1501.00277

Teuben, P. 1995, in Astronomical Society of the Pacific Conference Series, Vol. 77, Astronomical Data Analysis Software and Systems IV, ed. R. A. Shaw, H. E. Payne, & J. J. E. Hayes, 398

Timmermann, R., Bertoldi, F., Wright, C. M., Drapatz, S., Draine, B. T., Haser, L., & Sternberg, A. 1996, A&A, 315, L281

Toomre, A. 1964, ApJ, 139, 1217

Vallée, J. P. 2005, AJ, 130, 569

——. 2017, The Astronomical Review, 13, 113, 1711.05228

van der Kruit, P. C., & Freeman, K. C. 2011, ARA&A, 49, 301, 1101.1771

van der Kruit, P. C., & Searle, L. 1981, A&A, 95, 105

Vandenbroucke, B., & De Rijcke, S. 2016, Astronomy and Computing, 16, 109, 1605.03576

Vázquez-Semadeni, E., Ballesteros-Paredes, J., & Rodríguez, L. F. 1997, ApJ, 474, 292, astro-ph/9607175

Vázquez-Semadeni, E., Gómez, G. C., Jappsen, A. K., Ballesteros-Paredes, J., González, R. F., & Klessen, R. S. 2007, ApJ, 657, 870

Wada, K. 2008, ApJ, 675, 188, 0710.0407

Wada, K., Baba, J., & Saitoh, T. R. 2011, ApJ, 735, 1, 1104.1287

Wada, K., & Norman, C. A. 1999, ApJL, 516, L13

Wada, K., Spaans, M., & Kim, S. 2000, ApJ, 540, 797, astro-ph/0005330

Wadsley, J. W., Veeravalli, G., & Couchman, H. M. P. 2008, MNRAS, 387, 427

Walch, S. et al. 2015, MNRAS, 454, 238, 1412.2749

Walter, F., Brinks, E., de Blok, W. J. G., Bigiel, F., Kennicutt, Jr., R. C., Thornley, M. D., & Leroy, A. 2008, AJ, 136, 2563, 0810.2125

Wang, H.-H., Klessen, R. S., Dullemond, C. P., van den Bosch, F. C., & Fuchs, B. 2010, MNRAS, 407, 705, 1004.5593

Wang, H.-H., Lee, W.-K., Taam, R. E., Feng, C.-C., & Lin, L.-H. 2015, ApJ, 800, 106, 1412.6203

Ward, R. L., Benincasa, S. M., Wadsley, J., Sills, A., & Couchman, H. M. P. 2016, MNRAS, 455, 920, 1510.08187

Ward-Thompson, D., & Whitworth, A. P. 2011, An Introduction to Star Formation (Cambridge University Press)

Wendland, H. 1995, Advances in Computational Mathematics, 4, 389

Whittle, P. 1958, J. Roy. Stat. Soc., 20, 334

Wienen, M. et al. 2015, A&A, 579, A91

Williams, J. P., de Geus, E. J., & Blitz, L. 1994, ApJ, 428, 693

Williams, J. P., & McKee, C. F. 1997, ApJ, 476, 166

Williamson, D. J., & Thacker, R. J. 2012, MNRAS, 421, 2170, 1201.2152

Williamson, D. J., Thacker, R. J., Wurster, J., & Gibson, B. K. 2014, MNRAS, 442, 3674, 1404.5526

Wilson, C. D. et al. 2011, MNRAS, 410, 1409

Wolfire, M. G., Hollenbach, D., McKee, C. F., Tielens, A. G. G. M., & Bakes, E. L. O. 1995, ApJ, 443, 152

Wong, T., & Blitz, L. 2002, ApJ, 569, 157

Yoda, T. et al. 2010, PASJ, 62, 1277, 1101.3547

Zwicky, F. 1937, ApJ, 86, 217